THE ROLE OF LOW DENSITY LIPOPROTEIN RECEPTOR-RELATED PROTEINS FOR WNT SIGNAL TRANSDUCTION DURING EARLY FOREBRAIN DEVELOPMENT

DISSERTATION

zur Erlangung des akademischen

Grades des Doktors der

Naturwissenschaften (Dr. rer. nat.)

eingereicht im Fachbereich Biologie, Chemie, Pharmazie

der Freien Universität Berlin

vorgelegt von

Fabian Alexander PAUL

aus Frankfurt am Main

2017

Diese Arbeit wurde in der Zeit von August 2012 bis Dezember 2016 unter der Leitung von Professor Dr. Thomas Willnow und Dr. Annette Hammes am Max-Delbrück-Centrum für Molekulare Medizin in Berlin-Buch durchgeführt.

1. Gutachter: Prof. Dr. Thomas Willnow

2. Gutachter: Prof. Dr. Ursula Koch

Disputation am 23.11.2017

Contents

1 Introduction **1**

1.1 Principles of forebrain development 1

1.1.1 Signaling pathways involved in telencephalic formation 1

1.1.1.1 Induction of the prospective forebrain 1

1.1.1.2 Neurulation and dorsoventral patterning of the forebrain 2

1.1.2 Structural organization of the neuroepithelium 3

1.2 The low density lipoprotein receptor (LDLR) family 5

1.2.1 LDLR family members and their structural hallmarks 5

1.2.2 Diverse implications of LRPs in development and disease 6

1.2.3 LRP4 9

1.2.4 LRP5 and LRP6 10

1.3 The WNT signaling pathway 11

1.3.1 Various functions of the WNT pathway during embryogenesis 11

1.3.2 The WNT-frizzled receptor complex 13

1.3.3 LRP5/6 as crucial components of the WNT machinery 14

1.3.4 LRP4 as a potential modulator of WNT signaling 15

2 Aim **17**

3 Material and Methods **19**

3.1 Material 19

3.1.1 Technical equipment 19

3.1.2 Consumables and kits 19

3.1.3 Chemicals and reagents 20

3.1.4 Buffers and solutions 21

3.1.5 Media 22

3.1.6 Antibodies 22

3.1.7 Oligonucleotides (Primers) 23

3.1.8 Riboprobes for ISH 23

3.2 Molecular biology methods 24

3.2.1 Cloning 24

3.2.1.1 Amplification of DNA segments by PCR . . . 24
3.2.1.2 Gel electrophoresis of DNA/RNA . . . 24
3.2.1.3 Determination of DNA/RNA concentration . . . 24
3.2.1.4 Digest of DNA with restriction enzymes . . . 25
3.2.1.5 Purification of DNA/RNA solutions . . . 25
3.2.1.6 Ligation of DNA fragments . . . 26
3.2.1.7 Transformation of Escherichia coli with DNA . . . 26
3.2.1.8 Cryopreservation of bacteria strains (+DNA plasmids) . . . 27
3.2.1.9 Blue-white screen for colony selection . . . 27
3.2.1.10 Isolation of plasmid DNA from bacteria . . . 27
3.2.1.11 Sequencing of DNA . . . 27
3.2.2 Protein Immunoblot . . . 28
3.2.2.1 Preparation of tissue lysates . . . 28
3.2.2.2 Determination of protein concentration . . . 28
3.2.2.3 SDS polyacrylamide gel electrophoresis . . . 28
3.2.2.4 Immunoblotting (Western blot) . . . 28
3.2.3 Genotpying . . . 29
3.2.3.1 Isolation of genomic DNA from tissue . . . 29
3.2.3.2 Genotyping by PCR . . . 29
3.2.3.3 PCR programs *Lrp4*, *Lrp5*, *Lrp6* and *TCF/Lef1-GFP* genotyping . . . 30
3.2.3.4 Genotyping by X-Gal staining . . . 30
3.3 Animal experiments . . . 30
3.3.1 Mouse husbandry and breeding . . . 30
3.3.2 $Lrp4^{mitt}$ functional null mouse line . . . 31
3.3.3 $Lrp5^{tm1Lex}$ functional null mouse line . . . 31
3.3.4 $Lrp6^{Gt(Ex187)Byg}$ functional null mouse line . . . 32
3.3.5 *TCF/Lef:H2B/GFP* transgenic reporter mouse line . . . 32
3.3.6 $Lrp4^{mitt}; Lrp5^{tm1Lex}$ compound mutant mouse line . . . 32
3.3.7 $Lrp4^{mitt}; Lrp6^{Gt(Ex187)Byg}$ compound mutant mouse line . . . 32
3.3.8 Dissection of mice and fixation of specimen . . . 33
3.3.9 Whole embryo culture (WEC) preparation . . . 33
3.3.10 Fluorophore labeling of WNT3a proteins . . . 33
3.3.11 Alexa488-WNT3a uptake experiments . . . 33
3.4 Histology and staining . . . 35

3.4.1 Embedding of tissue and sectioning 35
3.4.2 Nomenclature of section levels 35
3.4.3 Immunohistochemistry 36
3.4.3.1 Fluorescent immunohistochemistry on sections 36
3.4.4 *In situ* hybridization 37
3.4.4.1 Generation of digoxigenin-labeled riboprobes 37
3.4.4.2 *In situ* hybridization on sections 37
3.4.4.3 Whole-mount *in situ* hybridization 38
3.4.5 TUNEL assay 39
3.4.6 X-Gal staining on cryo-sections 39
3.4.7 X-Gal staining on whole embryos 39
3.5 Quantification and statistical analysis 40
3.5.1 MPM-2 quantification 40
3.5.2 Alexa488-WNT3a uptake analysis 40

4 Results **43**

4.1 Expression patterns of *Lrp4* and *Lrp5/6* overlap in the developing forebrain . . . 43
4.1.1 *Lrp4* starts to be expressed at E9.5 in the dorsolateral region of the forebrain 43
4.1.2 *Lrp5* mRNA is widely expressed in the developing forebrain 45
4.1.3 *Lrp6* is ubiquitously expressed in neural progenitors between E8.5 and E10.5 47
4.2 *Lrp4;Lrp5* compound mutants are embryonic lethal at E10.5 48
4.2.1 Statistics of genotype distribution for embryos of $Lrp4^{+/-};Lrp5^{+/-}$ timed matings 48
4.2.2 Embryonic resorption of $Lrp4^{-/-};Lrp5^{-/-}$ embryos occurs at E10.5 49
4.2.3 *Lrp4;Lrp5* compound mutant embryos display a delayed neural tube closure 50
4.3 $Lrp6^{-/-}$ and $Lrp4^{-/-};Lrp6^{-/-}$ embryos exhibit impaired growth 52
4.3.1 Ratio of *Lrp4;Lrp6* compound mutants embryos matched the expected Mendelian ratio 52
4.3.2 $Lrp6^{-/-}$ neural tube closure defect is also exhibited in $Lrp4^{-/-};Lrp6^{-/-}$ embryos 53
4.3.3 Somitogenesis phenotype of *Lrp6* single mutants persists in *Lrp4;Lrp6* compound mutant embryos 55
4.3.4 $Lrp6^{-/-}$ and $Lrp4^{-/-};Lrp6^{-/-}$ mutants are smaller than littermate embryos . . 57
4.4 *Lrp4;Lrp6* compound mutants develop excrescences in the neuroepithelium . . . 64

4.4.1 Neuroepithelial excrescences can be detected from E9.5 onwards 64
4.4.2 The number of mitotic cells is increased in neuroepithelial excrescences . 67
4.4.3 *Lrp6*$^{-/-}$ embryos and *Lrp4; Lrp6* compound mutants exhibit patches of apoptotic cells within the neuroepithelium 69
4.4.4 Excrescences within the neuroepithelium were accompanied by structural abnormalities 72
4.4.5 Columnar organization of the pseudostratified neuroepithelium is dispersed within *Lrp4*$^{-/-}$*; Lrp6*$^{-/-}$ excrescences 75
4.5 WNT signaling pathway is affected in the developing forebrain of *Lrp6* single mutants and *Lrp4; Lrp6* compound mutant embryos 79
4.5.1 BMP4 signaling pathway is not affected in telencephalon of E10.5 *Lrp4*$^{-/-}$ embryos 79
4.5.2 SHH source in the floor plate and expression of downstream *Nkx2.1* is unchanged in *Lrp4*$^{-/-}$ and *Lrp6*$^{-/-}$ embryos 81
4.5.3 *Wnt1* and *Wnt3a* expressing domains are still present in embryos deficient for LRP6 83
4.5.4 WNT target gene expression is downregulated in *Lrp6*$^{-/-}$ embryos and partially rescued in *Lrp4*$^{-/-}$*; Lrp6*$^{-/-}$ mutant embryos 85
4.6 Immunostainings reveal further differences of *Lrp6*$^{-/-}$ and *Lrp4*$^{-/-}$*; Lrp6*$^{-/-}$ embryos in WNT target gene expression 88
4.6.1 WNT/ β-catenin downstream target cyclin-D1 is up-regulated in *Lrp4; Lrp6* compound mutants and severely down-regulated in *Lrp6*$^{-/-}$ embryos 88
4.6.2 At E10.5, reduction of cyclin-D1 levels in the neuroepithelium of LRP6 deficient embryos is less pronounced 91
4.6.3 LRP6 deficient embryos show increased levels of PAX6 in the neuroepithelium 94
4.6.4 *TCF/Lef:H2B-GFP* reporter strain was crossed to the *Lrp* mouse lines to visualize Wnt/β-catenin signaling activity in the neuroepithelium 97
4.7 WNT3a uptake is markedly reduced in *Lrp6*$^{-/-}$ embryos 99
4.7.1 At E8.5 the uptake of WNT3a in dramatically reduced in LRP6 deficient embryos 99
4.7.2 While WNT3a uptake at E9.5 is still impaired in *Lrp6*$^{-/-}$ embryos, *Lrp4; Lrp6* compound mutants exhibit increased uptake of WNT3a 103

5 Discussion **109**

5.1 *Lrp4;Lrp5* and *Lrp4;Lrp6* compound mutant embryos serve as models to study common and distinct functions of LRP4 and LRP5/6 during forebrain development 110

5.2 Generation of *Lrp4;Lrp5* compound mutants revealed embryonic lethality at E10.5 and delayed closure of the anterior neuropore 111

5.3 *Lrp6*$^{-/-}$ embryos and *Lrp4;Lrp6* compound mutants have a growth deficit 113

5.4 *Lrp4;Lrp6* compound mutant embryos develop neuroepithelial excrescences . . . 115

5.5 WNT pathway is affected in *Lrp6* single mutants and *Lrp4;Lrp6* compound mutant embryos but not in *Lrp4*$^{-/-}$ 117

5.6 Further evidence that WNT readout is reduced in *Lrp6*$^{-/-}$ and to some extent compensated in *Lrp4*$^{-/-}$;*Lrp6*$^{-/-}$ neuroepithelium of the prospective forebrain . . . 118

5.7 WNT3a uptake of *Lrp6* single mutant embryos is markedly reduced, whereas WNT3a binding reduction seems to be reversed in *Lrp4;Lrp6* compound mutants 120

5.8 Summary and hypothetical models for WNT pathway regulation in the neuroepithelium during early embryonic forebrain development 122

5.9 Critical assessment of the results and future perspectives 125

A Appendix **127**

A.1 List of Algorithms 127

A.2 List of Figures 127

A.3 List of Tables 130

A.4 Curriculum vitae (CV) 131

A.5 Bibliography 132

Abstract

The formation of the forebrain is a very complex developmental process that is highly dependent on proper orchestration and integration of various signaling pathways. The WNT signaling pathway is one of the key regulators for establishing regional identity during early forebrain development. For proper WNT signal transduction the highly homologous low density lipoprotein receptor-related proteins LRP5 and LRP6 (LRP5/6) are required as co-receptors of the Frizzled receptor complex. Recently, LRP4 has been shown to act on LRP5/6 function to modulate WNT signal transduction during the development of various non-neuronal tissues. My aim was to shed light on common and distinct functions of LRP4 and LRP5/6 regarding their role of transducing and integrating WNT signaling during early forebrain development. I could show that all three LRP candidates are expressed during critical developmental stages of the mouse forebrain. From E9.5 onwards, *Lrp4* and *Lrp5/6* are co-expressed in the dorsolateral domain of the developing Telencephalon. To investigate gene interactions that contribute to the integration of WNT signal transduction, I generated and analyzed *Lrp4;Lrp5* and *Lrp4;Lrp6* compound mouse mutants, respectively. I could reveal distinct functions of LRP5 and LRP6 in interplay with LRP4, since *Lrp4;Lrp5* compound mutant embryos but not *Lrp4;Lrp6* compound mutants develop embryonic lethality at E10.5. Regarding WNT dependent forebrain development, my results deliver lines of evidence that LRP6 is essential for WNT signal transduction in neural progenitor cells (NPCs) during early forebrain development. WNT downstream targets are markedly downregulated in *Lrp6* single mutant embryos at E9.5 and E10.5. Intriguingly, this reduction in WNT target gene expression was partially reversed in the dorsolateral domain of the prospective forebrain of *Lrp4;Lrp6* compound mutant embryos. The impact on the WNT pathway mediated by LRP4/LRP6 deficiency was also reflected by reporter activity in NPCs on a *TCF/Lef:H2B-GFP* reporter background. Furthermore, I could show for the first time that *Lrp4;Lrp6* compound mutants develop excrescences in the neuroepithelium that result from locally increased neural progenitor proliferation. These neuroepithelial excrescences displayed elevated levels of WNT downstream target gene expression compared to Lrp6 single mutant embryos. In addition, I could reveal that WNT3a uptake in NPCs of the forebrain of Lrp6 single mutant embryos was markedly reduced at E9.5, whereas *Lrp4;Lrp6* compound mutants showed increased WNT3a uptake at sites where neuroepithelial excrescences were located. Thus, I conclude that LRP4 and LRP6 are crucial components of the canonical WNT pathway in respect of balancing the proliferative activity of neuronal progenitor cells in the developing forebrain. Moreover, it shows that a cell-specific receptorsome is essential for NPCs to interpret the diverse extracellular signals and ensure fine-tuned spatial and temporal control of morphogen signals during early forebrain formation.

Zusammenfassung

Die Entwicklung des Vorderhirns ist einer der komplexesten Vorgänge während der Embryogenese. Jede neuronale Progenitorzelle (NPZ) des Neuroepithels muss dabei Signale verschiedener Signaltransduktionswege erkennen und korrekt interpretieren. Der WNT-Signalweg ist von entscheidender Bedeutung für die Festlegung regionaler Zellspezifizierung während der frühen Vorderhirnentwicklung. Für die korrekte Weiterleitung von WNT Signalen agieren die sehr ähnlichen Low Density Lipoprotein Receptor-related Proteine LRP5 und LRP6 (LRP5/6) als Co-Rezeptoren des Frizzled-Rezeptorkomplexes. Kürzlich konnte gezeigt werden, dass bei der Entwicklung nicht neuronalen Gewebes LRP4 auf die Funktion von LRP5/6 einwirken und somit die WNT-Signaltransduktion modulieren kann. Mein Ziel bestand darin gemeinsame und unterschiedliche Funktionen von LRP4 und LRP5/6 in Bezug auf ihre Rolle in der WNT-Signalkaskade während der frühen Vorderhirnentwicklung zu untersuchen. Ich konnte nachweisen, dass alle drei LRP Kandidaten während der entscheidenden Entwicklungsphase des frühen Telencephalons der Maus ab E9.5 koexprimiert werden. Um mögliche Geninteraktionen untersuchen zu können, welche ausschlaggebend für die Interpretation der WNT-Signale sein kann, habe ich doppeldefiziente Mäuse für *Lrp4;Lrp5* und *Lrp4;Lrp6* generiert und analysiert. Darüber hinaus konnte ich eine distinkte Rolle von LRP5 und LRP6 im Zusammenspiel mit LRP4 aufdecken, da *Lrp4;Lrp5* Doppelmutanten eine embryonale Letalität bei E10.5 entwickelten, *Lrp4;Lrp6* Doppelmutanten hingegen nicht. Bezüglich WNT abhängiger Vorderhirnentwicklung konnte ich belegen, dass LRP6 ein essentieller Bestandteil der WNT-Signaltransduktion in neuronalen Vorläuferzellen des Vorderhirns ist. In *Lrp6* Einzelmutanten war die Expression von WNT Zielgenen in NPZ deutlich reduziert bei E9.5 und E10.5. Interessanterweise konnte diese verminderte Expression im Vorderhirn von *Lrp4;Lrp6* Doppelmutanten teilweise aufgehoben werden, so dass WNT Zielgene im dorsolateralen Bereich des Telencephalons wieder detektierbar waren. Dieser Einfluss auf die Vermittlung von WNT Signalen in *Lrp4;Lrp6* Doppelmutanten konnte durch Einkreuzen der *TCF/Lef:H2B-GFP* Reportermaus-Linie verifiziert werden. Des Weiteren konnte ich erstmals zeigen, dass *Lrp4;Lrp6* Doppelmutanten auf Grund von lokal erhöhter NPZ-Proliferation neuroepitheliale Auswüchse entwickelten. Diese Wucherungen wiesen eine erhöhte Expression von WNT Zielgenen auf. Mit Hilfe von WNT3a Aufnahme-Assays war ich in der Lage nachzuweisen, dass die Aufnahme von WNT3a in LRP6 defizienten NPZ des Vorderhirns massiv reduziert war, jedoch in den neuroepithelialen Auswüchsen der *Lrp4;Lrp6* Doppelmutanten wiederum erhöht. Daher folgere ich, dass LRP4 und LRP6 essenzielle Bestandteile des WNT-Signalweges darstellen, die benötigt werden, um die Balance der NPZ Proliferation im sich entwickelnden Vorderhirn zu gewährleisten. Darüber hinaus wird deutlich wie wichtig eine zellspezifische Rezeptorzusammensetzung ist, wenn es um die zeitliche und räumliche Interpretation von Signalen während der Hirnentwicklung geht.

“Willst du dich am Ganzen erquicken,

so mußt du das Ganze im Kleinsten erblicken”

Johann Wolfgang von Goethe

1 Introduction

1.1 Principles of forebrain development

The adult mammalian forebrain is one of the most complex organic structures and therefore it is a challenging endeavor to elucidate the underlying mechanisms for its formation during embryogenesis. The forebrain comprises the Telencephalon and the Diencephalon, which are the most anterior segments of the mammalian brain. This division of the brain is essential for processing sensory information, perception, memory, emotions, conscious thinking and controlling motor activity. The developmental process of this tremendously complex structure from a rather simple neuroepithelial sheet to the complicated neuronal network of cells that process all the information is still not fully understood. However, early events in forebrain development are highly conserved in vertebrates and many studies undertaken in frog, chick and mice have unraveled principles that are essential for the induction of the forebrain and early patterning. During the initial specification of the forebrain, integration of signals from multiple signaling centers is required to establish regional identity of neural progenitor cells (NPCs). In addition, these extracellular signals are crucial for keeping the balance of NPC proliferation and differentiation as well as coordinating cell migration.

1.1.1 Signaling pathways involved in telencephalic formation

1.1.1.1 Induction of the prospective forebrain There are three fundamental steps during early embryonic development that contribute to the formation of the prospective forebrain. First, during gastrulation ectodermal cells need to adopt a neural character and form the neuroectoderm. Further, cells located in the anterior division of the neuroectoderm must acquire rostral identity. And finally, regional patterning events need to establish specific domains of neural progenitors of the prospective forebrain [47, 170, 198]. Anterior ectoderm is initially obstructed to acquire neural identity by bone morphogenetic protein (BMP) signals from posterior mesodermal tissue. The neuroectoderm forms when it receives BMP inhibiting signals mediated by chordin and noggin [202]. The BMP inhibiting factors are secreted by the anterior visceral endoderm (AVE), which acts as a gastrula organizer crucial for establishing anterior brain structures [144, 170]. The newly formed neuroectoderm gives rise to the neural plate, which comprises another important signaling center – the anterior neural ridge (ANR). Fibroblast growth factor (FGF) signaling (i.e. FGF8) from the ANR represents yet another prerequisite to establish the prospective forebrain region [42, 76]. FGF and WNT antagonists (sFRP and DKK) signals from the ANR are considered to antagonize the WNT activity from

the nonaxial mesoderm, which has a posteriorizing effect [76, 97]. Further, FGF8 is required to induce telencephalic marker in the anterior segment of the neural plate [161, 177]. The WNT antagonizing signals from the ANR (anterior) and the WNT signals from the paraxial mesoderm (posterior) establish a gradient along the anterior-posterior axis that is required for proper regional specification along this axis [102, 132].

1.1.1.2 Neurulation and dorsoventral patterning of the forebrain Primary neurulation is the process in which the neural plate transforms into the neural tube. The neural plate cells receive signals from the surrounding tissue to proliferate on the edges, invaginate and bend dorsally to form a U-shaped neural groove [164]. Finally, the neural groove closes as the neural folds are brought together at the dorsal midline to form the neural tube [157]. The most anterior division of the newly formed neural tube comprises the prosencephalon. Within the forebrain three distinct midline structures are established that act as morphogen signaling centers and contribute to regional patterning of the neural progenitor cells (as depicted in Figure 1.1.1). The ventral midline (floor plate) is the source of sonic hedgehog (SHH) that acts as a ventralizing factor regarding progenitor specification [72, 198]. The dorsal midline (roof plate) secretes WNT and BMP molecules that act in an antagonistic fashion to SHH signals from the floor plate and are therefore referred to as dorsalizing factors [66]. The third midline structure is the anterior midline – also referred to as ANR – that is the main source of FGF signaling in the forebrain [63]. In addition, all midline cells are less proliferative and therefore contribute to the formation of the telencephalic vesicles as the forebrain separates into two hemispheres (see also Figure_1.1).

However, more importantly forebrain midline structures are required establish a dorsoventral morphogen gradient in the anterior neural tube that helps to specify progenitor cell fate according to their location along the dorsoventral axis. SHH that is secreted from floor plate cells establishes a morphogen gradient along the dorsoventral axis, which leads to high SHH concentrations ventrally and low SHH concentrations dorsally. This morphogen code enables progenitor cells within the neural tube to interpret the extracellular SHH signals and express target genes that lead to a ventral or dorsal cell fate depending on the morphogen concentrations [49]. On the other hand, the roof plate cells in the ventral midline of the forebrain form an organizer that secretes BMP and WNT signals, which act antagonistically to the ventral SHH signals [150]. However, BMP signaling seems to play a minor role in dorsoventral patterning events during forebrain formation. It is required to establish the choroid plexus, but seems dispensable for progenitor specification along the dorsoventral axis [43]. Further,

it has been shown that BMP4 is required to restrict the FGF domain to rostral regions by downregulating its expression [110].

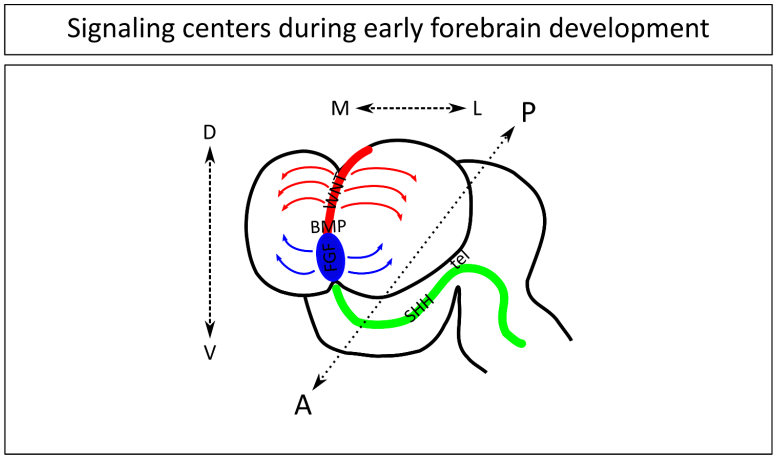

Figure 1.1: Signaling centers during early forebrain development

Schematic model of the developing anterior neural tube at E9.5 (rostrolateral view) and important signaling centers for forebrain formation. FGF expressing organizer at the rostral midline (in the ANR) is depicted in blue. BMP and WNT signals are expressed in the dorsal roof plate (illustrated in red). In the ventral midline SHH is processed from floor plate cells (indicated in green). A-P: Anterior - posterior, D - V: Dorsal-ventral, M - L: Medial-lateral.

Besides BMP factors, various WNT proteins are expressed in the dorsal midline of the forebrain [142]. WNT signals from the roof plate antagonize SHH signaling from the floor plate cells to specify the fate of neural progenitors that are located dorsally. However, the morphogen range of WNT factors is less pronounced than the SHH coverage. In the forebrain, WNT signaling from the dorsal midline also promotes growth of dorsal structures such as the cerebral cortex and the optic tectum [136, 214]. Further, WNT signals from the roof plate are required to form the cortical hem and the hippocampus. Disruption of WNT components such as WNT3a, LRP6 or LEF1 incomplete hippocampus formation due to failure of proliferation and specification of neural progenitor cells [51, 105, 213].

1.1.2 Structural organization of the neuroepithelium

After the neural tube has formed, the neural stem cell-like progenitors compose the highly polarized structure of the neuroepithelium (NE). The apical side of the neural progenitor cells (NPCs) faces inward to the ventricle, whereas the basal side is in contact with the pial surface and faces outward [100]. The apical-basal polarity of the NPCs within the NE is reflected by their protein expression profiles at the respective sides. The apical side of NPCs for instance

exclusively expresses transmembrane receptors such as CD133 and several tight junction proteins (i.e. Occludin, Claudin-5 or ZO-1) at the lateral plasma membrane [1, 199]. Further, the tight junctions at the apical side help to maintain the neuroepithelial cell polarity [58]. On the other hand, the basal side of NPCs comprises anchor proteins such as Integrin alpha6 to attach the NE to the basal lamina [58, 199].

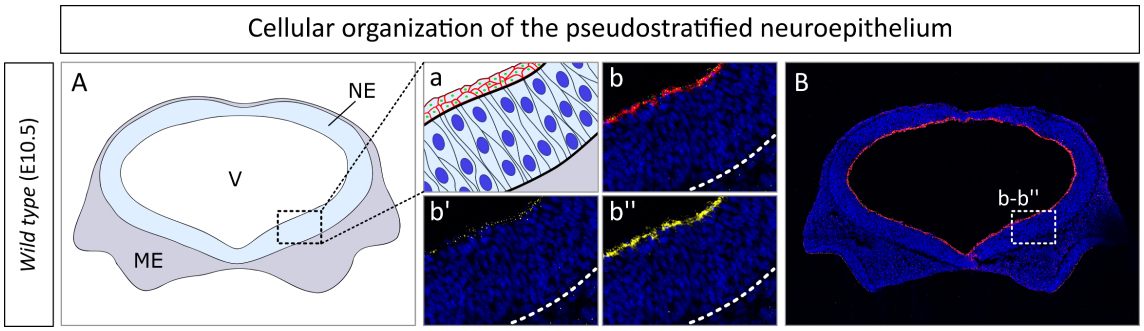

Figure 1.2: Cellular organization of the pseudostratified neuroepithelium

(A) Schematic of a E10.5 coronal section of the embryo head: Neuroepithelium (NE) depicted in light blue; mesenchyme (ME) illustrated in gray; ventricle (V). **(a)** Schematic of the cellular organization of the NE: On the apical side tight junctions are illustrated in red and the primary cilia are depicted in green. Neuroepithelial progenitor cells (NPCs) are light blue and cell nuclei are colored dark blue. **(B)** Immunostaining of a E10.5 coronal section. Cell nuclei in blue (DAPI), tight junctions in red (ZO-1), primary cilia in green (ARL13b). **(b)** Magnified inset showing ZO-1 (red) and ARL13b (green) on the apical surface of the NPCs. **(b')** Immunostaining of apical marker ARL13b (yellow). **(b")** Immunostaining of apical marker ZO-1 (yellow). White-dotted line delineates basal side of the NE.

Although the NE comprises several layers of cell nuclei and it appears as if it would consist of multiple cellular layers, in fact the NE is organized as a pseudostratified columnar epithelium and forms only a single layer of NPCs. Therefore, it is also referred to as the pseudostratified neuroepithelium. That implies that each NPC within the NE extends from the apical side to the basal surface resulting in a bipolar morphology that stretches up to 100µm [126]. According to their cell cycle stage cell nuclei migrate along the apical-basal axis [79, 199]. During G1-phase nuclei move towards the basal side, where the nuclei remain during S-phase. After completion of the S-phase the cell nuclei migrate back to the apical side, undergo mitosis and divide [126]. This interkinetic nuclear migration reflects the cell cycle progression of the NPCs that undergo symmetric division (i.e. one NPC divides into two daughter NPCs). When NPCs start to differentiate (at E10.0-E10.5) they divide asymmetrically, resulting in one basal progenitor and a radial glia cell [58]. However, as long as NPCs are not differentiating, the NE retains the organization of a pseudostratified epithelial layer.

1.2 The low density lipoprotein receptor (LDLR) family

1.2.1 LDLR family members and their structural hallmarks

The low density lipoprotein receptor-related proteins (LRPs) are an evolutionary well-conserved group of cell-surface receptors with multiple biological functions [121]. The low density lipoprotein receptor (LDLR) was the first to be discovered and gave its name to the whole protein family. LDLR is essential for lipid metabolism and homeostasis of cholesterol levels, since it is involved in the uptake of cholesterol-containing low density lipoprotein (LDL) particles [55]. Since the discovery of LDLR several structurally related proteins were found and assigned to the LRP family that are in fact not only involved in lipid metabolism. There are seven core members (LDLR, LRP1, LRP1B, LRP2, LRP4, LRP8 and APOER2) that are structurally closely related and three (LRP5, LRP6 and SORLA) that are more distantly related family members [70]. Structural hallmarks of the LRP family members can be found in the extracellular domain in which all LRPs share a common modular structure. The LRP core members share a distinct module (some even have multiple copies of that module) that consists of complement-type repeats (CTRs), epidermal growth factor (EGF)-type repeats and YWTD-motif containing β-propellers (see Figure 1.3). The CTRs function primarily as ligand binding sites (Russell 1989), whereas theβ-propeller structure is involved in pH-dependent ligand release in endosomes [155]. Compared to other LRP candidates, LRP1 and LRP2 for instance have larger extracellular domains that contain multiple copies of the described module. In the more distantly related LRP family members the module is either inverted (in LRP5 and LRP6) or the module is interrupted by motifs (SORLA) that are not common in other LRPs. However, all LRPs have a single transmembrane domain that anchors the receptors to plasma membrane domain [120]. Another trait that is common amongst all LRPs is the relatively short intracellular domain (ICD). However, the sequence homology between the cytoplasmic tail of all LRP family members is less pronounced compared to the similarity of the extracellular domains. The ICD of the LRPs is essential for the physiological function of the receptors, since it contains regulatory phosphorylation sites as well as motifs important for endocytic activity [106]. It has been reported that NPxY, di-leucine and YxxΦ motifs of the LRP-ICD are involved in endocytosis [25], whereas PxxP and the PDZ binding motifs are involved in protein interaction [201]. Although the ICDs of the LRP family members are rather short, there is growing that LRPs play important roles as signaling receptors of various signal transduction pathways [27, 106].

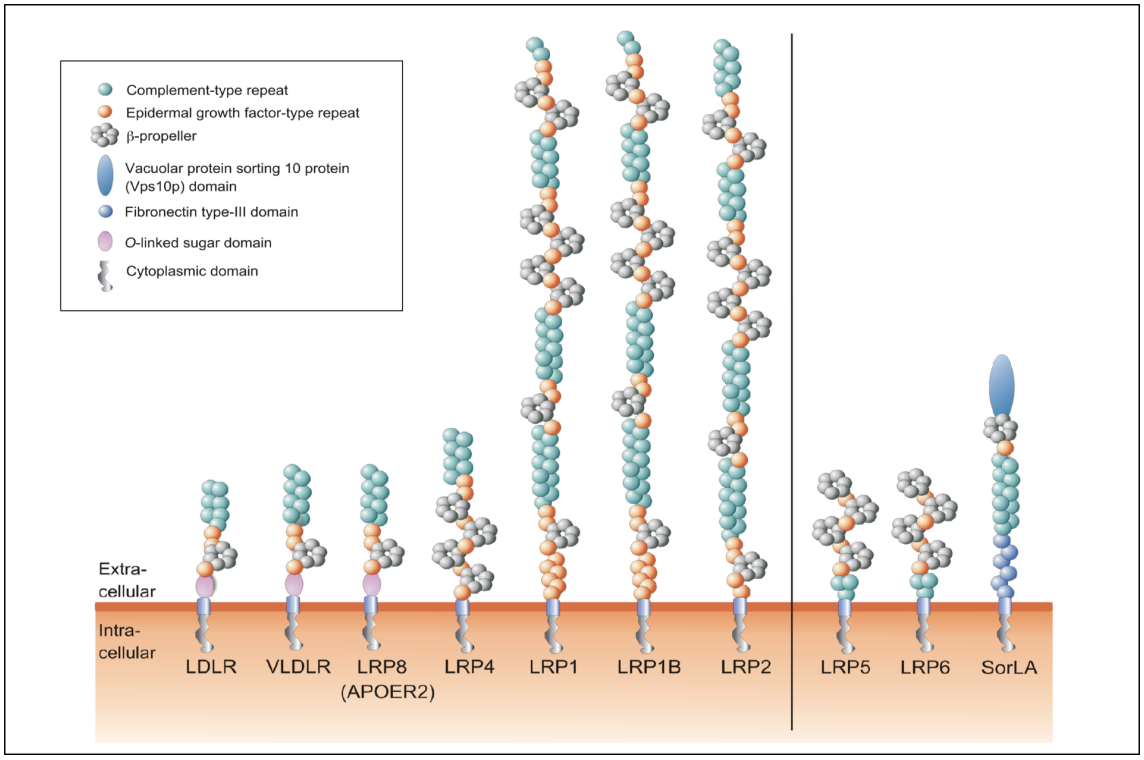

Figure 1.3: The low density lipoprotein receptor (LDLR) family

Organization of the structural domains of LDLR family members. More distantly related receptors on the right (order according to the molecular weight). LRP: Lipoprotein receptor-related protein, SorLA: sortilin-related receptor, VLDLR: Very low-density lipoprotein receptor. *Adapted from Willnow et al., 2007 [197]* .

1.2.2 Diverse implications of LRPs in development and disease

As the complexity of the extracellular domain of LRPs including various binding motifs already suggests, LRP family members can bind multiple ligands. Besides lipoproteins, LRPs have been shown to bind vitamins, hormones, proteins of the extracellular matrix and signaling molecules [121]. This reflects the multitude of biological functions that LPRs are associated with. The analysis of several loss-of-function mutations of the LRP family members shed light on their role in diseases and developmental defects. A list of loss-of-functions mutations for the LRP candidates is summarized in Table 1.1+1.2. Impaired function of LRPs have been linked to various human diseases. For instance, a genetic mutation in LDLR leads to hypercholesterolemia, which is caused by elevated cholesterol levels in the blood. This genetic disorder leads to accelerated deposition of cholesterol in the walls of arteries and increases the risk of developing atherosclerosis [15]. Another prevalent human disease has been associated with the physiological role of LRP family members. Recently it was reported that LRP1, LRP2 and SORLA can have a protective function in Alzheimer's disease. It seems

that they prevent amyloid plaque formation through acting on intracellular trafficking of the amyloid precursor protein [107, 121, 197]. Further implications of LRP family members in human diseases are referred to in Subsection 1.2.3+1.2.4. The concept that lipoproteins are essential for embryogenesis has been demonstrated long ago. Human mutations in 7-dehydrocholesterol reductase and desmosterol reductase causing the Smith-Lemli-Opitz syndrome and Desmosterolosis helped to shed light on the implications of lipoprotein metabolism in developmental processes. These syndromes cause various neurological impairments, facial abnormalities and a general developmental delay [78]. However, most developmental impairments due to lack of LRP family members are not linked to defective lipoprotein metabolism. Loss-of-functions models of various LRP family members not only revealed their role in embryogenesis but also their ability to bind signaling molecules. Whereas loss of LDLR does not lead to developmental deficits, the loss of other LRP family members has severe consequences on embryogenesis (see also Table 1.1+1.2). For instance, VLDLR and LRP8 have an impact on brain formation. By binding to the neuronal guidance factor Reelin, these LRP candidates act on neural migration in the developing brain [33, 181]. Consequently, loss-of-function models for VLDLR and LRP8 develop dysplasia in the cerebellum as well as layering defects in the cortex and disturbed hippocampal morphology [181]. Homozygous VLDLR mutations in humans leads to a hypoplastic cerebellum [13]. Embryos with inactivated *Lrp1* gene are die during midgestation, probably due to defective liver formation [71, 153]. Likewise, LRP1B is essential for embryogenesis as its loss leads to an early embryonic lethality. However, the definite function of LRP1B in embryonic development remains open [36]. A crucial role in early forebrain development was assigned to LRP2, which is expressed at the apical surface of the neuroepithelium. *Lrp2* loss-of-function mutants display severe malformations of the forebrain as well as facial dysgenesis [195]. It has been shown by Christ et al. that a delayed induction of *Shh* expressing cells in the rostral diencephalic ventral midline (RDVM) – a major forebrain organizer – is delayed and fails to induce Shh target genes that are important for forebrain specification [27]. This leads to improper separation of the forebrain hemispheres and results in expanded lateral ventricles [168]. Mutations in the human LRP2 gene leads to microforms of holoprosencephaly and Donnai-Barrow syndrome with failure to establish the corpus callosum as well as facial and ocular abnormalities [94, 154]. Like the above mentioned LRP family members, LRP4 as well as LRP5 and LRP6 play important roles during development and are also associated with human disorders. Their implications in development and disease are subject of the following sections (Subsection 1.2.3+1.2.4). An overview of the phenotypes that were reported for mutations for LDLR family members is depicted in Table 1.1+1.2.

Gene:	Species:	Mutation:	Phenotype:	Authors:
LRP1	Mouse	targeted gene disruption	Embryonic lethality, impaired formation of liver	Herz et al. [71], Roebroek et al. [153]
LRP1B	Mouse	targeted gene disruption	Early embryonic lethality	Dietrich et al. [36]
	Human	sporadic	Esophageal squamous cell carcinoma, non-small-cell lung cancer	Liu et al. [109] Sonoda et al. [167]
LRP2 (megalin; Ce-LRP1)	Mouse	targeted gene disruption	Defects in development of forebrain, spinal cord and optic nerve, impaired maturation of reproductive organs, renal dysfunction	Willnow et al. [195] Hammes et al. [65] Spoelgen et al. [168] Wicher and Aldskogius [194] Ortega et al. [139]
	Zebrafish	ENU mutagenesis	Glaucoma, myopia, pronephric tubular clearance defects	Kur et al. [101] Veth et al. [184]
	C. elegans	spontaneous mutant	Molting defect, larval growth arrest, defective vulva development	Yochem et al. [204] Kamikura and Cooper [93]
	Human	Familial, autosomal recessive	Donnai-Barrow Syndrome (proteinuria, brain malformation, diaphragmatic hernia), microform of HPE	Kantarci et al. [94] Rosenfeld et al. [154]
LRP4 (MEGF7)	Mouse	ENU mutagenesis, spontaneous mutant, targeted disruption	Impaired limb formation, renal agenesis, impaired orofacial development, reduced bone growth, neuromuscular junction defects	Johnson et al. [88] Simon-Chazottes et al. [163] Weatherbee et al. [191] Kim et al. [99] Zhang et al. [207] Choi et al. [26] Karner et al. [95] Ohazama et al. [138]
	Cattle	spontaneous mutant	Mulefoot disease (syndactyly)	Duchesne et al. [40] Drogemuller et al. [39]
	Human	Familial, autosomal recessive	Cenani-Lenz syndrome (limb and kidney malformations)	Li et al. [107]
LRP5	Mouse	targeted gene disruption	Low bone mass, hypercholesterolemia, impaired insulin secretion, impaired retinal vascularization, impaired mammary development	Kato et al. [96] Fujino et al. [50] Lindvall et al. [108] Ye et al. [203]
	Human	familial, autosomal recessive	Osteoporosis-Pseudoglioma Syndrome (reduced bone mass, persistent embryonic eye vascularization)	Gong et al. [57]
	Human	familial, autosomal recessive	Familial exudative vitreoretinopathy	Toomes et al. [180]

Table 1.1: (a) List of loss-of-function models of LDLR protein family

Gene:	Species:	Mutation:	Phenotype:	Authors:
LRP6 (Arrow)	Mouse	targeted gene disruption	Abnormal pattering of body axis, neural tube and limb defects, orofacial abnormalities, cardiac neural crest and outflow tract defects, hypoplasia of neocortex, ocular coloboma, neuroretinal patterning defect	Pinson et al. [146] Zhou et al. [214] Zhou et al. [215]; Song et al. [165]; Song et al. [166]
	Xenopus	spontaneous mutant	Impaired dorsal axis and neural crest formation	Tamai et al. [69]
	Human	familial, autosomal dominant	Autosomal dominant early coronary artery disease	Mani et al. [117]
	D. melanogaster	spontaneous mutant	Inhibition of Wingless-dependent patterning	Wehrli et al.[193]
LRP8 (APOER2)	Mouse	targeted gene disruption	Dysplastic hippocampus and cerebellum, impaired retinal synaptic connectivity	Trommsdorff et al.[181] Trotter et al. [182]
VLDLR	Mouse	targeted gene disruption	Dysplastic cerebellum, abnormal cortical layering, absent rostral migratory stream	Trommsdorff et al. [181] Andrade et al. [5] Hack et al. [64]
	Chicken	spontaneous mutant	Impaired vitellogenesis, female sterility	Bujo et al. [17]
	Human	familial, autosomal recessive	Cerebellar hypoplasia, ataxia, mental retardation	Boycott et al. [13] Ozcelik et al. [140]
Yolkless	D. melanogaster	X-ray induced mutant	Impaired vitellogenesis, female sterility	DiMario and Mahowald [37]

Table 1.2: (b) List of loss-of-function models of LDLR protein family (*Adapted from Willnow et al., 2012* [196])

1.2.3 LRP4

The cell surface receptor low density lipoprotein receptor-related protein 4 (LRP4) was originally named multiple epidermal growth factor repeat containing protein 7 (MEGF7) and was discovered in a screen for cDNA containing EGF- and CR- domains that is expressed in the central nervous system [129]. Mice that are deficient for LRP4 are perinatal lethal and display impaired limb formation and develop polysyndactyly likely due to abnormal WNT signaling in the apical ectodermal ridge, which plays a key role in limb patterning [88]. Furthermore, loss of LRP4 leads to renal agenesis, impaired orofacial development and aberrant mammary placode formation [3, 26, 88, 95, 138, 163]. Mutations within the human LRP4 gene lead to kidney malformations, complex syndactyly and growth retardation, which is also referred to as Cenani-Lenz syndrome [107]. LRP4 has been shown to bind several factors that are involved

in different signaling pathways, such as WISE (SOSTDC-1), DKK (Dickkopf-related protein 1), AGRIN [3, 7, 26, 99, 138, 207] and is also proposed as a regulator for WNT signal transduction (see Subsection 1.3.4). LRP4 is required for the formation and maintenance of the neuromuscular junction (NMJ), which is essential for efferent signaling to the skeletal muscles. Thus, impaired signaling from motor neuron synapses might be the cause of the perinatal lethality of *Lrp4* loss-of-function mice, due to respiration failure [88]. LRP4 directly binds AGRIN and mediates it to the tyrosine kinase receptor MuSK (Muscle-Specific Kinase) complex. AGRIN is required to phosphorylate MuSK in order to induce NMJ formation [99, 207, 191]. Alternatively, LRP4 was suggested to play a role in canonical Wnt signaling as negative regulator to antagonize LRP6-mediated pathway activation [2, 3, 4, 137, 138]. The WNT-dependent role of LRP4 is furhter described in Subsection 1.3.4.

1.2.4 LRP5 and LRP6

The low density lipoprotein receptor-related proteins 5 and 6 (LRP5/6) are closely related and share a high degree of similarity regarding their structure and amino acid sequence. However, compared to other LRP family members they display structural differences in their extracellular domain (ECD). Contrary to the other LRP family members, the ECD of LRP5 and LRP6 shows reverse arrangement of the EGF- and CR-motifs (see Figure 1.3). On the other hand, the intracellular domain (ICD) does not contain an NPxY-motif, whereas this common to the ICDs of all other LRP family members [25]. LRP5 and LRP6 are expressed in many tissues and very often overlap in their expression pattern. Both receptors can be detected in the heart, skeletal muscle, liver and kidney [14] and during different stages of embryonic development they are almost ubiquitously expressed [146, 166, 215]. As essential components of the WNT signaling transduction cascade (see Subsection 1.3.3) they are important for many different developmental aspects. However, studies with loss-of-function mutants revealed that loss of LRP6 leads to many different impairments during embryo formation, whereas *Lrp5* deficient embryo develop normally [68, 73]. It appears that LRP6 can fully compensate for the loss of LRP5 during embryogenesis. However, LRP5 is required in the adult organism, since *Lrp5* null mice show a decreased bone mineral density [73]. In humans, LRP5 mutations are associated with a form of osteoporosis termed OPPG (Osteoporosis-Pseudoglioma syndrome) [57]. Mouse embryo that lack LRP6 function are perinatal lethal and display severe developmental defect affecting the axial skeleton, formation of the limbs and the tail as well as urogenital malformations and brain defects [146]. The embryonic phenotypes observed in *Lrp6* loss-of-function mutants resemble observed phenotypes in WNT loss-of-function models, suggesting

an essential role for LRP6 in respect of WNT signal transduction during embryo development (see also Subsection 1.3.3) . Further details on LRP5/6 function as co-receptors of Frizzled are described in Subsection 1.3.3.

1.3 The WNT signaling pathway

The WNT signaling pathway controls a multitude of processes during embryonic development as well as in the adult organism. WNT signal transduction is involved in the regulation of fundamental mechanisms that include cell proliferation, determination of cell fate as well as cell polarity during embryogenesis and homeostatic stem cell self-renewal various adult tissues [30, 112]. The Wnt1 gene was initially discovered by Nusse and Varmus in 1982 as they identified the proto-oncogene Int-1 (original name of Wnt1) that was activated in mouse mammary tumor virus proviral DNA, when breast tumors were virally induced [135]. Since then myriads of findings were published that revealed WNT signaling as an evolutionary well-conserved signal transduction pathway that controls a vast number of physiological processes among vertebrates and invertebrates [30, 112, 134, 131, 187]. Therefore, understanding of the complexity of the WNT pathway has steadily risen and many components have been identified that play important roles in the WNT signal transduction cascade (described in Subsection 1.3). Accordingly, many mutations that affect WNT pathway components have be discovered and helped to unravel the implications of WNT signaling in birth defects as well as in cancer such as colon cancer and melanoma and neurodegenerative diseases [30, 112, 116]. At present, WNT factors are suggested to activate three different WNT pathways: The canonical WNT/ß-catenin cascade as well as the ß-catenin-independent planar cell polarity (PCP) pathway and WNT/Ca2+ pathway, which are both referred to as non-canonical WNT signaling. However, the canonical WNT signaling pathway is best known of these three and is also the primary subject this introduction.

1.3.1 Various functions of the WNT pathway during embryogenesis

As mentioned above WNT signaling is essential for various aspects of embryogenesis and is involved during virtually every stage of development of the vertebrate and invertebrates [172, 187]. WNT signal transduction has been reported to be involved in the regulation of fundamental developmental mechanisms that include primary embryonic axis formation, segmentation, organogenesis as well as stem cell proliferation [134, 131, 187]. Whereas most developmental implications of WNT pathway components were originally discovered by genetic

studies in Drosophila and Xenopus, in the past decades *in vivo* studies of mouse mutants as well as *in vitro* experiments with mammalian cells shed light on function of the WNT pathway in development and differentiation in mammals [187]. Here, I want to highlight experiments conducted in mice that unraveled implications of WNT signaling components in the course of mammalian embryogenesis. WNT proteins are approximately 40 kDa in size and contain many conserved cysteines [133]. So far, 19 different WNT factors have been identified that are all expressed during mammalian development [116]. Interestingly, these WNTs seem to have distinct as well as common functions during embryogenesis although they exhibit spatial and temporal overlapping expression. However, loss-of-function mouse models revealed that some WNT proteins seem to have a more prominent role in mammalian development. For instance, loss of WNT3 causes an early gastrulation phenotype and the embryo axis is not formed [111]. On the other hand, Wnt3a mutants display severe developmental defects in dorsolateral neural tube that leads to loss of the hippocampus. In addition, they display disrupted somitogenesis that causes a tailbud defect [62, 81, 173]. WNT1 is another ligand that is important for brain formation, as it was shown that loss-of-function mutation for Wnt1 leads to failure of midbrain and cerebellum formation [123, 122]. Interestingly, generation of Wnt1 and Wnt3a double deficient mutants revealed that there is a synergistic gene interaction leading to a more drastic developmental phenotype in the neural tube [81]. In contrast, there are also WNTs that play only a minor role in embryonic development like WNT8b or WNT16. Loss-of-function mutation for WNT16 leads to a slightly reduced bone mineral density [211] and Wnt8a null mice seem to have no developmental defects but display an abnormal gene expression in the telencephalon [48]. However, not only loss of the ligands can lead to defective WNT signaling during development. Many receptors have been revealed to play a role in WNT signal transduction. Frizzled (FZD) proteins are seven-transmembrane receptors that comprise the largest group of WNT receptors. There are ten mammalian FZD proteins that have variable impact on the formation of the mammalian embryo [82, 206]. For instance, FZD4 and FZD8 have been associated with the formation of the kidneys and uteric growth (INT_Ye), whereas FZD3 and FZD6 are required for proper midbrain development [171]. Among others, LRP5 and LRP6 are also important receptors for WNT signal transduction and play an essential role during embryogenesis. The function of LRP5 and LRP6 in development is described in greater depth in Subsection 1.2.4.

1.3.2 The WNT-frizzled receptor complex

Over the past decades, our understanding of the WNT signaling transduction cascade has enormously increased. Besides identification of a multitude of WNT binding transmembrane receptors that transduce extracellular WNT signals, various proteins have been linked to the complex intracellular transduction process. The complexity of the WNT pathway becomes apparent by only looking at variety of ligands that the WNT factors comprise. By now, 19 WNT proteins have been identified [116]. The number of cell surface receptors that are capable of binding WNT factors is even greater. To introduce the basic concept of canonical WNT signaling, I want to concentrate on the core elements of the pathway and elucidate their function in the WNT transduction cascade. Figure 1.4 summarizes the principle of WNT signal transduction to illustrated the detailed processes that will be discussed in the following passage.

In absence of WNT proteins, the co-activator beat-catenin in the cytoplasm is constantly degraded by the so-called β-catenin degradation complex, which comprises AXIN (a scaffolding protein), APC (the tumor suppressor Adenomatous polyposis coli) and GSK3 (glycogen synthase kinase 3). GSK3 phosphorylates the amino terminal of β-catenin, which subsequently leads to recognition by β-Trcp1 (β-transducin repeat containing protein). β-Trcp1, acting as a subunit of the ubiquitin protein ligase complex, induces ubiquitination of β-catenin, which is then degraded by the proteasome [68]. This continuous degradation prevents β-catenin from entering the nucleus, where TCF/Lef (T-cell factor/lymphoid enhancer-binding factor) binds to the DNA and inhibits expression of WNT downstream targets [68].

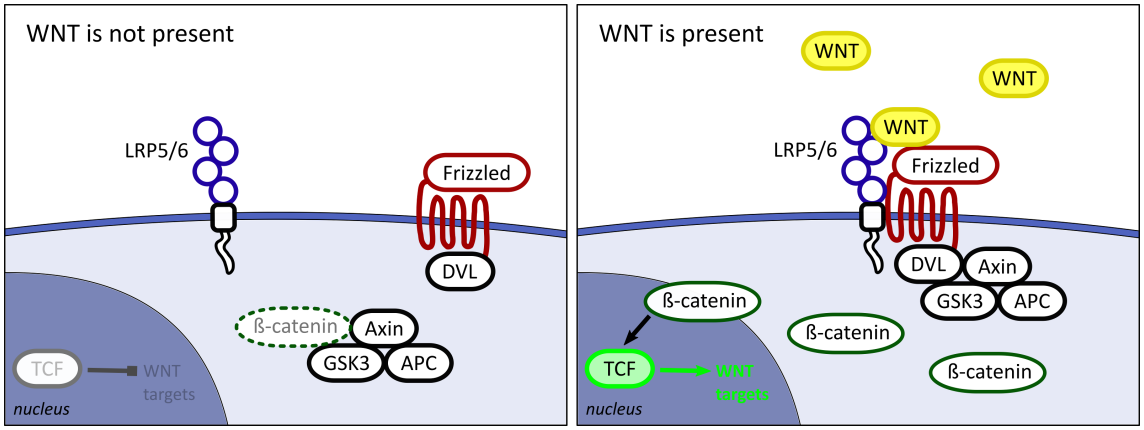

Figure 1.4: Schematic model of WNT signaling transduction

(In absence of WNT) When WNT factors are not present, the β-catenin degradation complex (Axin, GSK3, APC) prevents accumulation of β-catenin in the cytosol. Consequently, β-catenin cannot enter the nucleus and WNT targets genes are not activated. **(In presence of WNT)** When WNT proteins are present, LRP5/6 forms a complex with FZD. WNTs bind to the receptor complex and DVL recruits the β-catenin degradation complex, which is no longer able to degrade β-catenin. As a consequence, intracellular β-catenin level rises, which enables β-catenin to enter the nucleus, initiate *TCF/Lef* transciption and activate WNT target gene expression.

In presence of WNT proteins, the G protein–coupled receptor Frizzled (FZD) and its co-receptors LRP5 and LRP6 (LRP5/6) form a complex, which binds the ligands with their extracellular domains. When the LRP-FZD receptor complex is formed, the scaffolding protein Dishevelled (DVL) is recruited to the intracellular domain of the complex. Subsequently, LRP6 gets phosphorylated and the β-catenin degradation complex binds to DVL and is therefore inhibited. Ultimately, the inhibition of β-catenin degradation complex implies accumulation of β-catenin in the cytosol and the co-activator can enter the nucleus. In the nucleus β-catenin forms a complex with TCF/Lef, which in turn leads to activation of WNT downstream target expression [16, 133, 134].

1.3.3 LRP5/6 as crucial components of the WNT machinery

As described above (Subsection 1.3.2) LRP5 and LRP6 are co-receptors of FZD and essential for WNT signal transduction. FZD proteins comprise a large group of seven-pass transmembrane receptors and have overlapping function, which often leads to compensation when function of a single FZD members is lost [112] (as described Subsection 1.3.2). Between the two LRP co-receptors, LRP6 plays a more prominent role and is essential for embryonic development, whereas loss of LRP5 does not lead to impaired embryogenesis (as described in Subsection 1.2.4). However, LRP5 and LRP6 partially display redundant functions in the course of development as the *Lrp5;Lrp6* compound mutants do not survive towards blasto-

cyst implantation [98]. The formation of the ternary LRP-FZD complex upon binding of WNT factors seems to be a crucial step, since WNT itself seems to be a suboptimal ligand for LRP6 [12]. The subsequent phosphorylation of the intracellular domain (ICD) of LRP6 is crucial for proper WNT signal transduction (as described in Subsection 1.3.2). The ICD of LRP6 contains five PPPSP (Pro-Pro-Pro-Ser/Thr-Pro) repeats that are required to be phosphorylated for successful β-catenin signaling [174]. There are several proline-directed kinases that are able to phosphorylate the PPPSP motif of LRP6 and thus facilitate WNT signal transduction. GSK3 for instance mediates the PPPSP phosphorylation of LRP6 and on the other is a crucial component of the β-catenin degradation complex. Thus, GSK3 combines an opposing roles in WNT signal transduction as both a negative and a positive regulator [174]. However, there are also other membrane-associated kinases that are capable of mediating LRP6 phosphorylation [22].

1.3.4 LRP4 as a potential modulator of WNT signaling

In recent years, another LRP family member attracted the attention of the WNT research community. LRP4 was reported to have a modulatory role on LRP5/6 function and can therefore act on WNT signaling transduction events during embryogenesis [3, 4, 137, 138]. Ohazama et al. were the first to report on the interplay of LRP4 and the WNT inhibitor WISE (also known as SOSTDC1 - Sclerostin domain-containing protein 1) regarding tooth development [137]. They could show that WISE binds BMP and is then bound by LRP4, which then acts inhibitory on the LRP-FZD complex and therefore modulates WNT signal transduction [137, 138]. In another study, Ahn and others showed that LRP4 is involved in induction and formation of other skin appendages namely the mammary glands. They revealed that in LRP4 deficient mice increased WNT signaling leads to retarded placode induction and changes in distribution and number of mammary placodes [3]. Further, they could demonstrate for LRP4 that in interplay with WISE it antagonizes LRP5/6 function and thus modulated WNT signal transduction [3][3, 4, 137, 138]. In Figure 1.5 a schematic of the proposed model (adapted from Ahn et al. [3]) for LRP5/6 modulation by LRP4 in interplay with a WNT antagonist is illustrated. These findings related LRP4 function as a modulator of WNT signaling to the development of skin appendages, but whether this is a common function of LRP4 that also applies to the formation of other tissues remains to be elucidated.

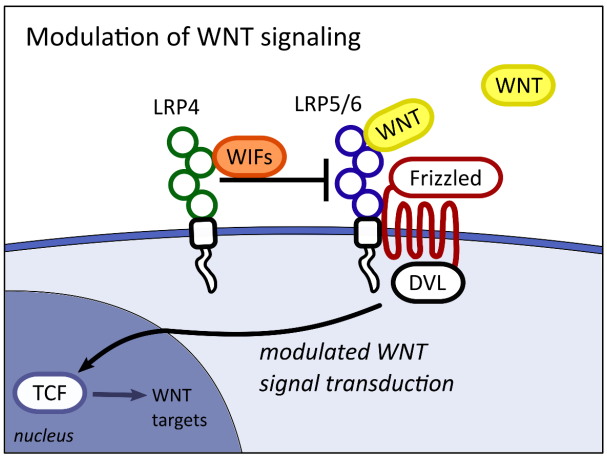

Figure 1.5: Schematic of proposed model for LRP4 modulation of the LRP-FZD complex

In interplay with an WNT antagonist (e.g. WISE), LRP4 acts inhibitory on the LRP-FZD receptor complex. Thus, LRP5/6 binding capacity for WNT factors is decreased, which consequently modulates WNT downstream target expression. Model adapted from *Ahn et al., 2013* [3].

2 Aim

The development of the forebrain needs tightly regulated orchestration of various signaling pathways to achieve the transformation from a simple neuroepithelial layer of progenitor cells to a complex three-dimensional brain structure at later stages. The SHH pathway is essential for forebrain induction and pattering, but also the opposing WNT signals from the roof plate are of crucial function for proper forebrain formation. LRP family members have been shown to contribute to the transduction of both SHH and WNT signals. Whereas LRP2 is required to establish proper SHH signaling during early forebrain formation, LRP5/6 as co-receptors of FZD are essential for the WNT signal transduction cascade. My aim was to shed light on the function of LRP5/6 during forebrain formation as transcripts of both *Lrp5* and *Lrp6* can be detected in the telencephalon from early on. Further I intended to investigate the role of LRP4 (which is also expressed during early forebrain) as a potential modulator of LRP5/6 function in the course of telencephalic development. So far, the concept that LRP4 acts in a modulatory fashion on LRP5/6 has only been demonstrated for non-neuronal tissue development. Thus, I intended to examine whether LRP4 plays a simliar role in the developing brain. To study common and distinct functions of LRP4 and LRP5/6 regarding their implications for transducing and integrating WNT signaling during early forebrain development, I generated double deficient mouse models for *Lrp4;Lrp5* and *Lrp4;Lrp6*. Thereby, I also aimed to unravel potential gene interactions of *Lrp4* and *Lrp5/6* to contribute to further understanding of the mechanisms, which modulate WNT signal transduction in regard of forebrain formation.

3 Material and Methods

3.1 Material

3.1.1 Technical equipment

Device/equipment:	Manufacturer:
ABI PRISM 7000 Sequence Detection System	Applied Biosystems (Foster City, USA)
ABI PRISM 377 Sequencer	Applied Biosystems (Foster City, USA)
Agilent 2100 Bioanalyzer	Agilent Technologies (Santa Clara, USA)
Centrifuge 5415 R	Eppendorf (Hamburg, Germany)
Cryo-Star HM 560 Cryostat	Microm UK Ltd. (Bicester, UK)
GenoPlex Gel documentation System	VWR International (Darmstadt, Germany)
Gel Electrophoresis Chamber	Renner GmbH (Dannstadt, Germnany)
GFL 1083 Shaking Waterbath	GFL (Großburgwedel, Germany)
Genova Plus Life Science Spectrophotometer	Jenway (Staffordshire, UK)
Lnyx 4000 Centrifuge (Sorvall)	Thermo Fisher Scientific (Waltham, USA)
LSM 710 Confocal Laser Scanning Microscope	Carl Zeiss AG (Oberkochen, Germany)
Luminescent Image Analyzer LAS-1000 plus	FujiFilm (Minato, Japan)
MS2 Minishaker Vortexer	IKA (Staufen, Germany)
Multitron Standard Incubation Shaker	Infors HT (Bottmingen, Switzerland)
NanoDrop ND-1000 Spectrophotometer	Thermo Fisher Scientific (Waltham, USA)
Optima MAX-XP Ultracentrifuge	Beckman Coulter (Wien, Austria)
Orbital Shaker KS 501D	IKA (Staufen, Germany)
Power Pack P25	Biometra (Göttingen, Germany)
Rotary microtome HM355S	Microm UK Ltd. (Bicester, UK)
Shake 'n' Stack Hybridization Ovens	Thermo Fisher Scientific (Waltham, USA)
SONOPULS Ultrasonic homogenizer	Bandelin (Berlin, Germany)
Stereoscope SteREO Discovery.V8	Carl Zeiss AG (Oberkochen, Germany)
Thermomixer Comfort	Eppendorf (Hamburg, Germany)
Thermocycler TAdvanced	Biometra (Göttingen, Germany)

Table 3.1: List of technical equipment

3.1.2 Consumables and kits

Consumeables/kit:	Manufacturer:
BCA Protein Assay Reagent	Thermo Fisher Scientific (Waltham, USA)
BigDye Terminator Sequencing Kit	Applied Biosystems (Foster City, USA)
BioRad Protein Assay	BioRad (München, Germany)
High Pure PCR Product Purification Kit	Roche (Basel, Switzerland)
PureLink® HiPure Plasmid Midiprep Kit	Life Technologies (Carlsbad; USA)
RNeasy Mini - RNA Isolation Kit	Qiagen (Hilden; Germany)
SuperSignal West Pico Chemiluminescent Substrate	Thermo Fisher Scientific (Waltham, USA)
SuperSignal West Femto Maximum Sensitivity Substrate	Thermo Fisher Scientific (Waltham, USA)
TACS 2 TdT DAB *in situ* Apoptosis Detection Kit	Trevigen Inc. (Gaithersburg, USA)

Table 3.2: List of consumables and kits

3.1.3 Chemicals and reagents

Chemical/ reagent:	Manufacturer:
2-Mercaptoethanol	Sigma Aldrich (St. Louis, USA)
Agarose (Ultrapure)	Invitrogen (Carlsbad, USA)
Albumin Bovine Serum (BSA)	Sigma Aldrich (St. Louis, USA)
Ampicillin	Carl Roth GmbH (Karlsruhe, Germany)
Anti-DIG-AP Fab fragments	Roche (Basel, Switzerland)
Aqua-PolyMount	Polysciences Inc. (Eppelheim, Germany)
BM purple	Roche (Basel, Switzerland)
Bromodeoxyuridine (BrdU)	Sigma Aldrich (St. Louis, USA)
Deoxycholate	AppliChem (Darmstadt, Germany)
Dextran sulfate	AppliChem (Darmstadt, Germany)
Digoxigenin-labeled NTPs	Roche (Basel, Switzerland)
Disodium phosphate (Na_2HPO_4)	Carl Roth GmbH (Karlsruhe, Germany)
DNA ladder (1kb plus)	Invitrogen Corporation (Carlsbad, USA)
dNTPs	Peqlab (Erlangen, Germany)
Ethidium bromide (EtBr)	Invitrogen Corporation (Carlsbad, USA)
Ethanol (EtOH)	Carl Roth GmbH (Karlsruhe, Germany)
Ethylenediaminetetraacetic acid (EDTA)	Carl Roth GmbH (Karlsruhe, Germany)
Formamide	Invitrogen Corporation (Carlsbad, USA)
Glycerol	Thermo Fisher Scientific (Waltham, USA)
Glycine (Gly)	Carl Roth GmbH (Karlsruhe, Germany)
Hydrochloric acid (HCl)	Carl Roth GmbH (Karlsruhe, Germany)
Isopropyl-ß-D-thiogalactopyranosid (IPTG)	Thermo Fisher Scientific (Waltham, USA)
Isopropyl alcohol	Sigma Aldrich (St. Louis, USA)
Lithium chloride (LiCl)	Sigma Aldrich (St. Louis, USA)
Magnesium chloride ($MgCl_2$)	Carl Roth GmbH (Karlsruhe, Germany)
Normal donkey serum (NDS)	Sigma Aldrich (St. Louis, USA)
Normal goat serum (NGS)	Sigma Aldrich (St. Louis, USA)
Paraformaldehyde (PFA)	Carl Roth GmbH (Karlsruhe, Germany)
Phenol-Chloroform	AppliChem (Darmstadt, Germany)
PolyMount (Aqua)	Polysciences Inc. (Eppelheim, Germany)
Polysorbate 20 (Tween 20)	Carl Roth GmbH (Karlsruhe, Germany)
Potassium chloride (KCl)	Carl Roth GmbH (Karlsruhe, Germany)
Restriction enzymes	New England Biolabs (Ipswich, USA)
RNase inhibitor	Roche (Basel, Switzerland)
Sodium acetate (NaAc)	Merck (Darmstadt, Germany)
Sodium citrate	Carl Roth GmbH (Karlsruhe, Germany)
Sodium chloride	Carl Roth GmbH (Karlsruhe, Germany)
Sodium diphosphate	Carl Roth GmbH (Karlsruhe, Germany)
Sodium hydroxide (NaOH)	Carl Roth GmbH (Karlsruhe, Germany)
Sodium tetraborate decahydrate	Carl Roth GmbH (Karlsruhe, Germany)
Tissue Tek O.C.T.	Sakura Finetek Inc. (Torrance, USA)
Transcription buffer	Roche (Basel, Switzerland)
Triethanolamine (TEA)	Carl Roth GmbH (Karlsruhe, Germany)
Tris-aminomethane (TRIS)	Merck (Darmstadt, Germany)
Triton X-100	Merck (Darmstadt, Germany)
X-Gal (BCIG) solution	Sigma Aldrich (St. Louis, USA)

Table 3.3: List of chemicals and reagents

3.1.4 Buffers and solutions

Buffer/ solution:	Manufacturer:
Blocking buffer (immunostainings)	20 % goat or donkey serum in PBTr
Blocking buffer (WB)	5 % powdered milk blotting grade (w/v) in TBST
Dialysis buffer	150 mM NaCl, 10 mM Tris, 10 % (v/v) glycerin, with pH 7.5
Denhardt's (100 x)	5 g Ficoll, 5 g PVP, 5 g BSA (Sigma), in 250 mL dH_2O
DNA-loading buffer (10 x)	10 mM Tris, 1 mM EDTA, 50 % (v/v) glycerin 0.25 % (w/v) bromphenol blue, with pH 8.0
IVT solution mix	1.5 μg purified DNA, 2 μL transcription buffer (1x), 1 μL DIG-NTP labeling mix (1x), 0.5 μL RNase inhibitor (1U), 1.5 μL RNase polymerase (3U),12.5 uL dH_2O
Hot Shot Buffer	2 mL 1 M NaOH, 20 .5 M EDTA in 50 mL dH_2O
Hybridization Solution (100 mL)	50 mL Formamide (deionized) (50%), 20 mL 50% (v/v) Dextran sulfate, 1 mL 100 x Denhardt's (10%), 2.5 mL yeast tRNA (10 mg/ mL) (10%), 6 mL 5 M NaCl (0.3 M), 2 mL 1 M Tris-HCl, pH 8 (20 mM), 1 mL 0.5 M EDTA (5 mM), 1 mL 1 M $NaPO_4$, pH 8 5 mL 20% Sarcosyl (10 mM), 11.5 mL DEPC-H_2O
Lämmli buffer (4 x)	450 mM Tris-HCl, 40 % (v/v) glycerin, 8 % (w/v) SDS, 0.01 % (w/v) bromphenol blue, with pH 6.8
Low TE buffer	10 mM Tris-HCl, 1 mM EDTA, with pH 8.0
Lysis buffer (Mini prep)	200 mM NaOH, 1 % (w/v) SDS
Neutralization buffer (Mini prep)	3 M potassium acetate, with pH 5.5
NTMT(100 mL)	2 mL 5 M NaCl (100 mM), 10 mL 1 M Tris-HCl, pH 9.5 (100 mM) 5 mL 1 M $MgCl_2$ (50 mM), 0.1 mL Tween 20, 82.9 mL dH_2O
Ponceau S solution	0.1 % (w/v) Ponceau S, 5 % (v/v) acetic acid
PBS	1.5 M NaCl, 80 mM Na_2HPO_4, 20 mM NaH_2PO_4
PBTw	PBS + 0.1 % (v/v) Tween-20
PBTr	PBS + 0.1 % (v/v) Triton-X100
PFA 4 %	4 % paraformaldehyde (w/v) in PBS
Resuspension buffer (Mini prep)	50 mM Tris-HCl, 10 mM EDTA, 100 µg/ml RNase, with pH 8
RIPA Buffer	3 mL 5 M NaCl (150 mM), 1 mL 0.5 M EDTA with pH 8.0 (5 mM), 5 mL 1 M Tris with pH 8.0 (50 mM), 1 mL NP-40 (IGEPAL CA-630) (1.0 % - v/v), 5 mL of 10 % sodium deoxycholate (0.5 % - v/v), 1 mL of 10 % SDS (0.1 % - v/v), in 84 mL dH_2O
Sonication buffer	15 % (w/v) sucrose, 50 mM Tris, 50 mM EDTA, 1 mM PMSF, 0.1 % lysozyme; pH 8
TAE	40 mM Tris-HCl pH 8, 1 mM EDTA, 20 mM glacial acetic acid
TBS (10 x)	250 mM Tris-HCl, 1.37 M NaCl, 27 mM KCl, with pH 7.4
TBST	1 x TBS + 0.1 % (v/v) Tween-20
Tris-glycine running buffer (5 x)	125 mM Tris, 1.25 M glycine, 0.1 % (w/v) SDS; pH 8.3
Tris-glycine transfer buffer (10 x)	181.6 mM Tris, 1.49 M glycine
X-gal washing Buffer	500 λ of Igepal Ca-30 (0.1 % - v/v), 0.25 mL of 10 % deoxycholate solution (0.05 % - v/v), 500 mL PBS
X-gal staining solution (50 mL)	1.25 mL 200 mM potassium ferrocyanide solution (5 mM) 1.25 mL 200 mM potassium ferricyanide solution (5 mM) 45.8 mL X-gal washing buffer 1.2 mL X-gal substrate (40 mg X-gal/ 1 mL DMF)

Table 3.4: List of buffers and solutions

3.1.5 Media

Medium:	Composition/ manufacturer:
DMEM medium	Dulbecco's Modified Eagle Medium (DMEM) (Gibco)
DMEM+B medium	DMEM (Gibco), 10% bovine serum albumin (BSA)
LB agar	15 g/L agar in LB medium
LB medium	10 g/L bacto-tryptone, 5 g/L bacto-yeast extract, 10 g/L NaCl, with pH 7.2
SOC medium	20 g/L bacto-peptone, 5 g/L bacto-yeast extract, 0.5 g/L NaCl, 0.17 g/L KCl, 0.95 g/L MgCl2, 3.6 g/L glucose, with pH 7.0

Table 3.5: List of media

3.1.6 Antibodies

Antigen:	Raised in:	Dilution:	Obtained from:
MPM-2	mouse	1:1500	Millipore (05-368)
GFP	chicken	1:200	Abcam (ab13970)
PAX6	rabbit	1:100	Biolegend (901301)
TUJ-1	mouse	1:1000	Covance (MO15013)
SOX2	rabbit	1:100	Abcam (ab97959)
cleaved-Caspase-3	rabbit	1:1000	Cell Signaling (CST #9661)
N-Cadherin	rabbit	1:100	Cell Signaling (CST #13116)
N-Cadherin	mouse	1:100	Santa Cruz (sc-8424)
β-Catenin	guinea pig	1:1500	Dr. Niccolo Zampieri
β-Catenin	rabbit	1:200	Abcam (ab16051)
Vimentin	rabbit	1:200	Abcam (ab92547)
ARL13b	rabbit	1:1000	Proteintech (17711-1-AP)
ZO-1	mouse	1:1000	Invitrogen (ZO1-1A12)
Cyclin-D1	rabbit	1:100	Abcam 16663)
LRP6	rabbit	1:100	Abcam (ab134146)
phospho-Histone-H3	rabbit	1:1000	Millipore (06-570)
Tubulin	mouse	1:1000	Sigma Aldrich (T9026)

Table 3.6: List of primary antibodies

Antigen:	Conjugate:	Dilution:	Obtained from:
guinea pig IgG	Alexa488 Alexa546 Alexa555	1:1000 (IHC)	Life Technologies
mouse IgG			
rabbit IgG			
chicken IgG			
mouse IgG	HRP	1:4000 (WB)	SLife Technologies
rabbit IgG			

Table 3.7: List of secondary antibodies

3.1.7 Oligonucleotides (Primers)

All oligonucleotides were ordered from Eurofins MWG Operon (Berlin, Germany). Stock solutions of all primers (100 µM) were kept at -20 °C for longterm storage. Working solutions with 10 µM concentration were kept at 4°C for up to 4 weeks.

Index #:	Primer name:	Sequence (5' to 3'):	T_m (in °C):
1	L4Hpmf_corr	GGT GAG GAG AAC TGC AAT GT	57,0
2	Lrp4-G_pp9-rev	TGA GTC AAG GTC ACA CCC ATC	60,0
3	β-geo F	CAA ATG GCG ATT ACC GTT GA	55,3
4	β-geo R	TGC CCA GTC ATA GCC GAA TA	57,3
5	Tcrd F	CAA ATG TTG CTT GTC TGG TG	55,3
6	Tcrd R	GTC AGT CGA GTG CAC AGT TT	57,3
7	CD4 mix F	GCA CGG ATG TCT CAG ATC AAG AGG	64,4
8	CD4 mix R	CGG GAT CAT CGC TCC CAT ATA TG	62,4
9	CD_LRP5_neo_F	GCC TTC TAT CGC CTT CTT GAC	59,8
10	CD_LRP5_gen_F	AAA CTG TGA CAG GCT GTG GGA AGT	62,7
11	CD_LRP5_gen_R	GCC GCA CAC ACC ACC AAA CTA TAA	62,7
12	Hadj_F	ACA ACA AGC GCT CGA CCA TCA C	62,1
13	Hadj_R	AGT CGA TGC CCT TCA GCT CGA T	62,1
14	Hadj_oIMR7338	CTA GGC CAC AGA ATT GAA AGA TCT	59,3
15	Hadj_oIMR7339	GTA GGT GGA AAT TCT AGC ATC ATC C	61,3
16	LRP4 ISPNfwd	TAC CAT CGA AGC ATC TCG GC	59,4
17	LRP4 ISPNrvs	TTC GTG TTT CCA GCC TGT GT	57,3
18	Lrp5 ISP3 for	ATG CCG GCG GAG TGA AG	57,6
19	Lrp5 ISP3 rev	GAG TAG AAA GGC TCC CTC GG	61,4
20	Lrp6 ISP3 for	CCC TTT TCT TTC TTC TCG CGG	59,8
21	Lrp6 ISP3 rev	CCA GTA AAG CTT CCG CTC CT	59,4

Table 3.8: List of primers

3.1.8 Riboprobes for ISH

Riboprobe:	Cut with RE:	Polymerase:	Provided by:
Axin2	Xba I	T7	Thomas Willnow
Bmp4	EcoR I	SP6	Elizabeth Robertson
Id3	EcoR I	SP6	Thomas Willnow
Lef1	Bgl I	T7	Thomas Willnow
Lrp4	Pst I	T7	Fabian Paul
Lrp5	Spe I	T7	Fabian Paul
Lrp6	Sac I	SP6	Fabian Paul
Nkx2.1	EcoR I	T3	Thomas Willnow
Shh	Hind III	T3	Thomas Willnow
Wnt1	Sal I	T7	Thomas Willnow
Wnt3a	EcoR I	T3	Ed Monuki

Table 3.9: List of ISH riboprobes

3.2 Molecular biology methods

3.2.1 Cloning

3.2.1.1 Amplification of DNA segments by PCR Polymerase chain reaction (PCR) is a common method in molecular biology to enzymatically amplify specific sequences of deoxyribonucleic acid (DNA) from composite nucleic acid [158]. This *in vitro* procedure involves a cyclic repetition of separating the source/sample DNA strands, binding of the specifically designed oligonucleotides and elongation of DNA segments that are in between the two primer sites. By repeating these steps for several times, an exponential multiplication of the desired DNA sequence is achieved [127]. In a subsequent step the specific DNA sequence can be visualized and/or isolated and purified for further procedure. In this study, PCR was performed to determine the genotypes of genetically modified mice that were used in the experiments and to amplify specific DNA sequences for cloning procedure. PCR products for cloning were generated by using Phusion high-fidelity DNA polymerase (New England Biolabs). The following cycling setting were used: 1.) Initial denaturation for 5 minutes at 98°C, 2.) denaturation for 20 seconds at 98°C, 3.) annealing for 30 seconds at 62-72°C, 4.) elongation for 30 seconds per 1 kb sequence at 72°, 5.) final elongation for 10 minutes at 72°C. Steps 2.) to 4.) were repeated for 30-35 cycles. Genotyping PCR programs are listed in Subsection 3.2.3.3.

3.2.1.2 Gel electrophoresis of DNA/RNA Gel electrophoresis can be used to separate differently sized DNA or RNA fragments (which are negatively charged) by applying an electric field to the gel matrix. In this study, gel electrophoresis was performed to separate and/or isolate DNA/RNA from PCR, restriction enzyme digests and *in vitro* transcriptions. According to the molecular weight of the DNA/RNA, 0.8-2.5% agarose gels (in TAE buffer) were used as matrix. 0.5µg/mL Ethidium bromide was added to the gel to ensure visualization of the DNA/RNA fragments under UV-light. The voltage was set to 120V and the gels ran for 20-30 minutes. By exposure to UV-light the DNA/RNA bands were detected. The gel was photographed and if required DNA fragments were cut and purified using High Pure PCR Product Purification Kit (Roche) according to manufacturer's instruction.

3.2.1.3 Determination of DNA/RNA concentration For rough estimation of DNA/RNA concentration the bands on gels were compared to bands of known concentration and same/similar length from the DNA/RNA ladder. For exact DNA/RNA concentration measurements a Nanodrop spectrophotometer (Thermo Fisher Scientific) was used according to manufacturer‘s instructions.

3.2.1.4 Digest of DNA with restriction enzymes Enzymatic digestion with restriction enzymes that cut at specific sites within the genomic sequence is an essential tool for cloning experiments. For complete digestion of plasmids or DNA fragments the amount of the restriction enzyme was determined by applying the formula listed below. A DNA-enzyme solution mix (including the respective enzyme buffer) was set up according to manufacturers instructions (New England Biolabs). Subsequently, the DNA-enzyme mix was digested for 2-3 hours at 37°C with constant shaking at 800rpm. All enzymes and buffers were obtained from New England Biolabs (USA). In this study, restriction enzyme digestion was used to linearize plasmids containing riboprobes before *in vitro* transcription and to cut amplified product of *Lrp4* genotyping PCR.

Algorithm 1 Equation to calculate amount of restriction enzyme for DNA cutting

$$U = m_p \cdot \frac{L_{Ref}}{L_p} \cdot \frac{n_p}{n_{Ref}}$$

m_p: mass of the plasmid; L_p: length of the plasmid; n_p: number of cut interfaces on plasmid; L_{Ref}: length of the reference DNA; n_{Ref}: number of cut interfaces on reference DNA; U: Units of the enzyme (1U is set as the amount of enzyme that cuts 1µg of λ-DNA in one hour)

3.2.1.5 Purification of DNA/RNA solutions High Pure PCR Product Purification Kit (Roche) was used for purification/isolation of DNA from gels and solutions. RNA was purified using RNeasy Micro Kit (Qiagen). Apart from that, increased DNA/RNA yield was sometimes achieved by purifying with phenol-chloroform extraction and subsequent ethanol precipitation. Phenol-chloroform extraction is a biochemical method to isolate nucleic acid from protein. Phenol-chloroform is added in a ratio of 1:1 to the solution. The suspension gets vortexed and centrifuged at 15.000x g for 10 minutes. From the resulting two-phase solution, the aqueous phase containing the DNA is taken and precipitated as follows. Ethanol precipitation is a method to isolate/concentrate DNA or RNA from aqueous solutions. The pH gets reduced by adding sodium acetate (pH 5.2) to a final concentration of 0.3M. Then two volumes of ice-cold (-20°C), pure ethanol are added and the solution gets vortexed. To facilitate the precipitation of the nucleic acid, the solution is put to -80°C for 30 minutes and subsequently

centrifuged for 10-15 minutes at 4°C with maximum speed. The supernatant is discarded and the pellet gets air-dried for 10-15 minutes. Afterwards the pellet is resuspended in 20µL RNase-free water and stored at -20°C.

3.2.1.6 Ligation of DNA fragments For inserting DNA fragments into the target vectors, insert and vector DNA (backbone) were cut with appropriate restriction enzymes and subsequently purified. For 20µL ligation solution, 100ng of backbone DNA were mixed with appropriate amount of insert DNA. The following formula was used to calculate amount of insert DNA:

Algorithm 2 Formula to calculate amount of insert DNA for ligation

$$Mass\,insert\,(ng) = \frac{5x\,mass\,vector\,(ng)\,\cdot\,length\,insert\,(bp)}{length\,vector\,(bp)}$$

Besides vector DNA and insert DNA, the ligation mix consisted of ligation buffer (2uL) and 1U of T4 DNA ligase (both New England Biolabs). The ligation reaction was performed at room temperature for 2 hours or at 4°C overnight. Afterwards, the ligase was inactivated by incubation at 65°C for 10-15 minutes. 2uL of the ligation solution were used to transform to electrocompetent Escherichia coli. See also Subsection 3.2.1 for the selection method of successfully integrated insert DNA into the vector.

3.2.1.7 Transformation of Escherichia coli with DNA Electrocompetent Escherichia coli (DH5a or XL1blue strain) were used for transformation with purified plasmids or DNA from ligation reactions. Bacteria were made competent for transformation as described by Chung and Miller [29]. Electrocompetent DH5a or XL1blue cells were thawed on ice prior to transformation. 20ng of plasmid DNA or 2uL from a ligation reaction mixed with 50uL of competent bacteria. The suspension was transferred to pre-chilled electroporation cuvettes and electroporated at 1.8kV. Immediately after successful electroporation the bacteria suspension was taken up in 1mL pre-warmed SOC medium and kept 1 hour at 37°C for recovery. Subsequently, the desired amount of cell suspension was plated on LB agar plates with appropriate selection antibiotic agent.

3.2.1.8 Cryopreservation of bacteria strains (+DNA plasmids) Long-term storage of plasmids with inserted DNA fragments was achieved by freezing bacterial cultures containing the respective vectors. 1mL of an overnight culture of DH5a or XL1blue Escherichia Coli was mixed with 1mL pure glycerol and immediately frozen to -80°C.

3.2.1.9 Blue-white screen for colony selection For selection of bacterial colonies after a ligation reaction the blue-white screening technique was used as follows. The blue-white screen is a screening method that allows detection of recombinant bacteria that integrated the insert DNA to the backbone. For this, the vector has a β-galactosidase cassette spanning the multiple cloning site (MCS). Integration of the insert DNA into the MCS interrupts the β-galactosidase sequence and inactivates β-Gal expression. The chromogenic substrate X-Gal and IPTG as an inducer of β-galactosidase expression are added to the LB agar plates for selection. Only bacterial colonies that incorporated the vector with the insert DNA at the MCS appear white, whereas self-ligated vectors appear blue. 2uL of X-Gal stock solution (40ug/mL) and 0.1mM IPTG were added to 1mL LB medium that contained the appropriate antibiotic agent. Bacteria solution was plated on LB agar plates and after overnight incubation at 37°C white colonies were picked for further procedure.

3.2.1.10 Isolation of plasmid DNA from bacteria For screening of bacterial colonies after transformation, 5-100mL of LB medium (depending on desired DNA yield) with respective antibiotic agent were inoculated with a single colony picked from the agar plates. This culture suspension was incubated overnight at 37°C with constant shaking. On the next day, the cells were centrifuged with 6000x g for 20 minutes. The bacterial pellet was resuspended and the DNA was isolated with the appropriate Plasmid DNA Kit (Thermo Fischer Scientific) according to manufacturer's instructions. After measuring the DNA concentration (see Subsection 3.2.1.3) the plasmid DNA was stored at -20°C.

3.2.1.11 Sequencing of DNA DNA sequencing was conducted by using BigDye Terminator Cycle Sequencing Kit (Applied Biosystems) as described by manufacturer. The amplification process included the following steps: 1.) initial denaturation at 96°C for 60 seconds, 2.) denaturation at 96°C for 10 seconds, 3.) annealing at 50-55°C for 5 seconds, 4.) elongation at 60°C for 4 minutes. Steps 2.) to 4.) were repeated for 30 cycles. Subsequently, the amplified DNA was purified with Sephadex G-50 (Amersham Bioscience) and sequenced with an ABI PRISM 377 DNA Sequencing system (Applied Biosystems). Alternatively sequencing of DNA

was conducted by LGC Genomics GmbH (Berlin). Results were analyzed by using Lasergene SeqMan Version 10.0 (DNASTAR).

3.2.2 Protein Immunoblot

3.2.2.1 Preparation of tissue lysates Dissections for tissue collection were conducted in PBS on ice. After removal, the tissue was immediately snap-frozen in liquid nitrogen and stored at -80°C when not processed directly. The tissue sample was sonicated in RIPA buffer to extract the proteins from the cells. By subsequent centrifugation, cell debris and nuclei were separated from the proteins in solution. The supernatant was taken to a new tube for further procedure.

3.2.2.2 Determination of protein concentration The protein concentration was measured by using either the BioRad Protein Assay (BioRad) or BCA Protein Assay Reagent (Thermo Fisher Scientific) according to manufacturer's instructions. A series of defined concentrations of bovine serum albumin (BSA) were measured to generate a standard curve. According to the protein content of the BSA samples plotted in the standard curve, the protein concentration of the sample was extrapolated.

3.2.2.3 SDS polyacrylamide gel electrophoresis Sodium dodecyl sulfate polyacrylamide gel electrophoresis (SDS-PAGE) is a biochemical method to separate a mixture of substances by their molecular weight. Defined amounts of protein solution were applied onto 8-12% gradient SDS polyacrylamide gels (Lonza). Prior to electrophoresis, 50-100µg of the protein sample were boiled in Lämmli buffer containing 10% 2-mercaptoethanol at 95°C for 5 minutes. In the subsequent electrophoresis step, the proteins were separated along the electrical field. The voltage was set to 90 V and running time was about 2-3 hours. SeeBlue Plus2 pre-stained Protein Standard (Thermo Fisher Scientific) served as a marker. In the following step, the gels were applied to immunoblotting.

3.2.2.4 Immunoblotting (Western blot) After SDS-PAGE, all proteins on the gel were transferred to a nitrocellulose membrane (Amersham Bioscience) by using a trans-blot electrophoretic transfer chamber (Bio-Rad Laboratories) according to manufacturer's instructions. The protein transfer was conducted at 400mA for 1-2 hours or at 50mA overnight. Subsequently, the nitrocellulose membrane was stained with Ponceau S solution to visualize the protein bands and thus verify successful protein transfer. Before the primary antibody could

be applied, the membranes were blocked with blocking buffer for 1 hour while constantly shaking. Primary antibodies were diluted to desired concentration in blocking buffer. Membranes were incubated overnight in the primary antibody solution at 4°C while constantly shaking. On the following day, nitrocellulose membranes were washed with TBST (3x for 15 minutes) and incubated in secondary antibody solution (HRP conjugated AB, 1:4000 in blocking buffer) for 1-2 hours. After that, the membranes were washed again 3x with TBST for 15 minutes. Finally, the protein bands were detected by adding SuperSignal West Pico/Femto Chemiluminescent Substrate (Thermo Fisher Scientific) detection solution and subsequent visualization with the Luminescent Image Analyzer LAS-1000 plus (FujiFilm).

3.2.3 Genotpying

3.2.3.1 Isolation of genomic DNA from tissue Adult mice that were kept in the mouse facility were subjected to an ear punch biopsy to collect tissue for genotyping. For genotype detection of mouse embryos, the yolk sac of each embryo was collected during dissections. Both adult and embryonic tissue was processed to extract the DNA as follows. The tissue samples were transferred to 90-300µL HotShot buffer (depending on the size of tissue) and boiled at 95°C for 20-30 minutes. Subsequently, the samples were centrifuged at maximum speed for 5-10 minutes and the supernatant was neutralized by adding 10% neutralization buffer. The isolated DNA solution was stored at 4°C until genotyping was performed.

3.2.3.2 Genotyping by PCR PCR (as described in Subsection 3.2.1.1) was used to genotype mouse tissue samples. Oligonucleotide pairs that to specifically amplify genomic sequences to discriminate genetically modified alleles (Subsection 3.3.2-3.3.7) from *wild type* alleles were designed. For each genetically modified mouse line specific primer sets (see list of primers: Subsection 3.1.7) and corresponding PCR cycling conditions (see list of PCR programs: Subsection 3.2.3) were used.

3.2.3.3 PCR programs *Lrp4*, *Lrp5*, *Lrp6* and *TCF/Lef1-GFP* genotyping

***Lrp4* PCR:**	**Temp.:**	**Time (min):**
1) First Denaturing	95°C	→ 3:00
2) Denaturing	95°C	→ 0:20
3) Annealing	60°C	→ 0:20
4) Extension	72°C	→ 0:30
→ *Cycles*	*40 x*	*step 2-4)*
5) Final Extension	72°C	→ 5:00
6) Incubation	8°C	→ ∞
→Digestion with HpyCH4V at 37°C for 2 h		
→*WT* band at 165 bp →*MT* band at 236 bp		

***Lrp5* PCR:**	**Temp.:**	**Time (min):**
1) First Denaturing	95°C	→ 3:00
2) Denaturing	95°C	→ 0:20
3) Annealing	55°C	→ 0:20
4) Extension	72°C	→ 0:30
→ *Cycles*	*35 x*	*step 2-4)*
5) Final Extension	72°C	→ 5:00
6) Incubation	8°C	→ ∞
→*WT* band at 220 bp →*MT* band at 150 bp		
→*HET* bands at 150 bp and 220 bp		

Table 3.10: PCR programs for genotyping *Lrp4 and Lrp5* samples

***Lrp6* PCR:**	**Temp.:**	**Time (min):**
1) First Denaturing	95°C	→ 3:00
2) Denaturing	95°C	→ 0:20
3) Annealing	52°C	→ 0:20
4) Extension	72°C	→ 0:40
→ *Cycles*	*35 x*	*step 2-4)*
5) Final Extension	72°C	→ 5:00
6) Incubation	8°C	→ ∞
→Generates only mutant band (β-geo)		
→*MT* band at 160 bp (to identify *HET*)		

***TCF/Lef1-GFP*:**	**Temp.:**	**Time (min):**
1) First Denaturing	95°C	→ 3:00
2) Denaturing	95°C	→ 0:25
3) Annealing	57°C	→ 0:25
4) Extension	72°C	→ 0:35
→ *Cycles*	*35 x*	*step 2-4)*
5) Final Extension	72°C	→ 5:00
6) Incubation	8°C	→ ∞
→Generates transgenic band at 530 bp		
→ Internal positive control at 324 bp		

Table 3.11: PCR programs for genotyping *Lrp6 and TCF/Lef1-GFP* samples

3.2.3.4 Genotyping by X-Gal staining Homozygotic $Lrp6^{Gt(Ex187)Byg}$ were identified by X-Gal staining of the yolk sac [2, 61, 73]. For this, yolk sacs were collected and transferred to tubes containing PBS. The yolk sacs were washed with X-Gal washing buffer for 20 minutes and subsequently transferred to tubes containing the X-Gal staining solutions. To facilitate the staining reaction, the tubes were incubated at 37°C. After 15-30 minutes, the staining intensity was sufficient to discriminate between heterozygous and homozygous samples. The staining process was stopped by transferring the yolk sacs to X-Gal wash buffer.

3.3 Animal experiments

3.3.1 Mouse husbandry and breeding

All mice were kept at species-appropriate conditions and handled according to the regulations in the German animal protection act (Tierschutzgesetz: TierSchG §1-11). Mice were exposed to a fixed day-and-night cycle with artificial light from 6 a.m. to 6 p.m. Timed matings were

set up right before the light-cycle ended (approximately at 6 p.m.) to obtain embryos at defined developmental stages. Detection of a vaginal plug in the morning indicated conception during the dark-cycle (active phase of mice) and was referred to as day E0.5 (embryonic day 0.5). All dissections to collect embryos at a given timepoint were conducted at around noon. Thus, the nomenclature of embryonic stages indicates the days after conception (e.g. E9.5 – id est ten and a half days after conception). Dissections were carried out regarding to German animal protection act. All genetically modified mouse lines were maintained on a C57BL/6N (black6) inbred background. C57BL/6N mice that were not carrying any genetically modified alleles are referred to as *wild type*.

3.3.2 *Lrp4^{mitt}* functional null mouse line

The *Lrp4^{mitt}* mouse line was created by the laboratory of Lee Niswander and was kindly provided by Scott Weatherbee and Robert Krumlauf [191]. The *Lrp4^{mitt}* mouse line was generated by ENU induced point mutations [156]. The mitten (*Lrp4^{mitt}*) allele contains two different point mutations in its coding region. One which is located C-terminally to the LA domains, leading to a premature stop codon. This ultimately results in the deletion of most of *Lrp4* encoded protein. Another early stop codon is caused by a splice site mutation [191]. Several other studies used this mouse line as a model for LRP4 loss of function analysis [2, 56, 99]- for further details see Subsection 1.2.3. In this study, *Lrp4^{mitt}* heterozygotes are referred to as *Lrp4$^{+/-}$* and likewise *Lrp4^{mitt}* homozygotes termed *Lrp4$^{-/-}$* mice.

3.3.3 *Lrp5^{tm1Lex}* functional null mouse line

The *Lrp5^{tm1Lex}* mouse line was generated by a gene targeting approach by Matthew Warman and Bart Williams, who generously provided this mouse line for this study [73]. A targeting vector containing an IRES-β-Gal-MC1-neo cassette was designed to be inserted in exon1 and inactivate *Lrp5* gene expression. β-Galactosidase expression under the control of the endogenous *Lrp5* promoter was expected to be detected in cells that express LRP5. However, detection of β-Gal expression was not possible. Therefore, RT-PCR was conducted to screen for *Lrp5 wild type* transcripts and immunoreactivity for LRP5 protein was performed. Both *Lrp5* transcripts and LRP5 protein could not be found in *Lrp5^{tm1Lex}* mice, confirming that this mouse line is a functional null mutant [73]. Several studies reported use of these mice to study implications by loss of LRP5 [6, 31, 54] - for further details see Subsection 1.2.4. In the following *Lrp5^{tm1Lex}* mice are referred to as *Lrp5$^{+/-}$* (heterozygotes) and *Lrp5$^{-/-}$* mice (homozygotes).

3.3.4 *Lrp6*$^{Gt(Ex187)Byg}$ functional null mouse line

The *Lrp6*$^{Gt(Ex187)Byg}$ functional null mouse line was created by William Skarnes [146] and obtained from BayGenomics via the Jackson Laboratories. *Lrp6*$^{Gt(Ex187)Byg}$ functional null mutation was achieved by insertion of gene trap vector containing the sequence of the first 321 amino acids of LRP6 in frame with a β-Galactosidase-Neomycin cassette. Northern blot analysis revealed that a truncated non-functional transcript was encoded by this allele [146]. *Lrp6* expression could be traced by detecting β-Galactosidase activity Subsection 4.1.3. The loss of function *Lrp6*$^{Gt(Ex187)Byg}$ mouse line was investigated in several other studies [61, 86, 165] - as further described in Subsection 1.2.4. In this study, mice that carried one *Lrp6*$^{Gt(Ex187)Byg}$ allele (heterozygotes) are termed *Lrp6*$^{+/-}$ mice, whereas embryos that had both alleles with the *Lrp6*$^{Gt(Ex187)Byg}$ mutation (homozygotes) are referred to as *Lrp6*$^{-/-}$ embryos.

3.3.5 *TCF/Lef:H2B/GFP* transgenic reporter mouse line

The *Tg(TCF/Lef1-HIST1H2BB/EGFP)*^{61Hadj} transgenic reporter mouse line was created by Anna-Katerina Hadjantonakis and was obtained from the Jackson Laboratories (MGI:4881498). *TCF/Lef:H2B-GFP* transgenic mice express an H2B-EGFP fusion protein under the control of six copies of *TCF/Lef* DNA binding sites and an *Hspa1b* promoter [44]. In this study, the *TCF/Lef:H2B-GFP* transgenic mouse line was used to visualize WNT/β-signaling in neuroepithelial cells of the investigated Lrp-mouse models Subsection 4.6.4. Mice that carry one allele of the *TCF/Lef:H2B-GFP* reporter are referred to as *Gfp*$^{+/-}$ (e.g. *Lrp4*$^{+/-}$;*Gfp*$^{+/-}$).

3.3.6 *Lrp4*^{mitt};*Lrp5*^{tm1Lex} compound mutant mouse line

To generate *Lrp4*^{mitt};*Lrp5*^{tm1Lex} functional null compound mutant embryos, *Lrp4*$^{+/-}$;*Lrp5*$^{+/-}$ adult mice were combined in timed matings. See Subsection 4.2 for genotypic distribution that resulted from these matings. *Lrp4*^{mitt};*Lrp5*^{tm1Lex} functional null compound mutants are referred to as *Lrp4*$^{-/-}$;*Lrp5*$^{-/-}$ embryos.

3.3.7 *Lrp4*^{mitt};*Lrp6*$^{Gt(Ex187)Byg}$ compound mutant mouse line

Lrp4^{mitt};*Lrp6*$^{Gt(Ex187)Byg}$ functional null compound mutant embryos were generated by combining two *Lrp4*$^{+/-}$;*Lrp6*$^{+/-}$ adult mice in timed matings. In Subsection 4.3.1 genotypic distribution that resulted from these matings are shown. *Lrp4*^{mitt};*Lrp6*$^{Gt(Ex187)Byg}$ functional null compound mutants are referred to as *Lrp4*$^{-/-}$;*Lrp6*$^{-/-}$ embryos.

3.3.8 Dissection of mice and fixation of specimen

Pregnant females from timed matings were dissected according to the detected plug date to obtain embryos at the desired embryonic stage. The uterus was removed and immediately transferred to ice-cold (4°C) PBS to anaesthetize the embryos and preserve tissue integrity. The embryos were dissected out of the uterus and the somites were counted to match the developmental stage. Subsequently, the specimens were transferred to pre-chilled 4% paraformaldehyde solution (PFA). Dependent on the developmental stage of the embryos fixation varied from 2 hours to overnight at 4°C (under constant shaking). After fixation, the specimens were washed with PBS and further processed or transferred to pure methanol and stored at -20°C.

3.3.9 Whole embryo culture (WEC) preparation

Whole embryo cultures were used to conduct WNT3a uptake experiment with E8.5 and E9.5 embryos. The uterus containing the embryos was excised and immediately transferred to 37°C pre-warmed DMEM+B medium (+10% BSA). Subsequently, embryos were removed from the uterus and transferred to fresh DMEM+B medium at 37°C. For the uptake experiments the embryo dishes were transferred to a primary cell incubator (Binder) and incubated up to 2 hours at 37°C with 5% CO_2.

3.3.10 Fluorophore labeling of WNT3a proteins

Prior to the WNT3a uptake experiments, the recombinant WNT3a proteins had to labeled with a fluorophore. For all uptake experiments, recombinant murine WNT3a (PeproTech) was labeled with Lightning Link Rapid DyLight 488 (Innova Biosciences) to generate green fluorescent Alexa488 coupled WNT3a molecules (referred to as Alexa488-WNT3a or WNT3a-A488). Labeling procedure was performed according to manufacturer's instructions.

3.3.11 Alexa488-WNT3a uptake experiments

Whole embryo culture uptake experiments were conducted to assess *ex vivo* capability of neuroepithelial cells to bind and incorporate WNT3a protein. As described in Subsection 3.3.9, the embryos were dissected and transferred to DMEM+B medium. Subsequently, the yolk sac of the embryos was incised and for E9.5 embryos the diencephalon was cut open at the dorsal midline to allow the ligand to access all neuroepithelial cells. The prepped embryos were transferred to petri dishes (22.1mm in diameter) with DMEM+B medium that contained

2.5µM A488-WNT3a. The petri dishes were placed in an incubator (Binder) set at 37°C with 5% CO_2 level. The specimens were incubated for 2 hours and every 15 minutes the dishes were shaken to guarantee equal distribution of the labeled WNT3a molecules. After 2 hours, the embryos were washed in PBS and immediately transferred to 4°C pre-chilled 4% PFA. After 2-3 hours of fixation at 4°C, the specimens were washed 3x in PBS and subsequently put in 30% sucrose/PBS solution at 4°C. About 1-2 hours later when dehydration was complete, the embryos sank to the bottom and were embedded in O.C.T. as described in Subsection 3.4.1. The embryo samples were sliced with a cryostat and coronal cryo-sections were stained and analyzed as described in Subsection 3.5.2.

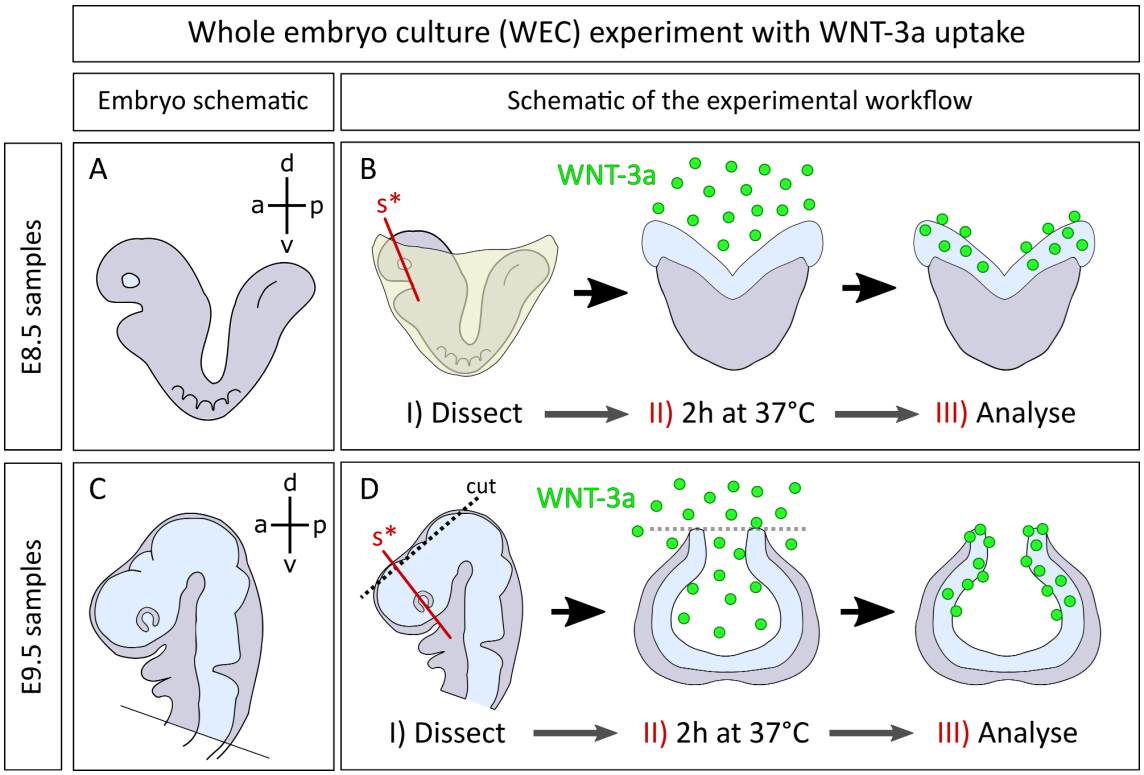

Figure 3.1: Schematic of the experimental design for the *in vitro* uptake assay of WNT3a-A488 For the WNT3a uptake experiments, the embryos were dissected and incubated in WNT3a-A488 containing medium **(A)** Lateral view of schematic embryo at E8.5. **(B)** Experimental workflow: Embryos were dissected, incubated with WNT3a-A488 containing culture medium and subsequently analyzed. **(C)** Lateral view of schematic embryo at E9.5 (head). **(D)** To perform the WNT3a uptake assay at E9.5, the neural tube had to be cut dorsally to ensure WNT3a-A488 could access neuroepithelial tissue. Apart from that, the workflow was the same as for E8.5 embryos. [s* red line) indicates section plane in II) + III)].

3.4 Histology and staining

3.4.1 Embedding of tissue and sectioning

Embryos were embedded in TissueTek OCT mounting medium (Sakura) as follows. After fixation, the samples were washed with PBS for 15-30 minutes (depending on embryonic stage). The specimens were then transferred to 15% sucrose/PBS solution and constantly shaken (100rpm) at 4°C. When the embryos completely submerged, the solution was changed to 30% sucrose/PBS. The dehydration process was completed, when the embryos sunk to the bottom of the well. Subsequently, the specimens were transferred to an embedding mold and OCT mounting medium was added. After alignment of the embryo, the mold was transferred to -78°C cold, pure methanol to rapidly freeze the sample. Cryo-blocks were sealed in an air-tight plastic bag and stored at -80°C until cut. Before cryo-samples were sliced, OCT blocks were placed in the cryostat chamber to equilibrate to -20°C. Specimens were sliced with an HM 560M cryostat (Microm). The object temperature was set to -12°C and knife temperature was cooled to -25°C. E8.5 embryos were sliced at 9µm, E9.5 samples were cut at 10-11µm and E10.5 embryos were sliced to 12µm thick sections. All cryo-sections were stored at -20°C until processed further.

3.4.2 Nomenclature of section levels

All coronal sections are indicated by a section plane index to allocate sections on the rostro-caudal axis. For each micrograph of a coronal section in this document, the section plane is indicated in the lower left corner (e.g. E9.5 sp1 indicates the most rostral coronal section of an E9.5 embryo – as shown in (Figure 3.2-B)).

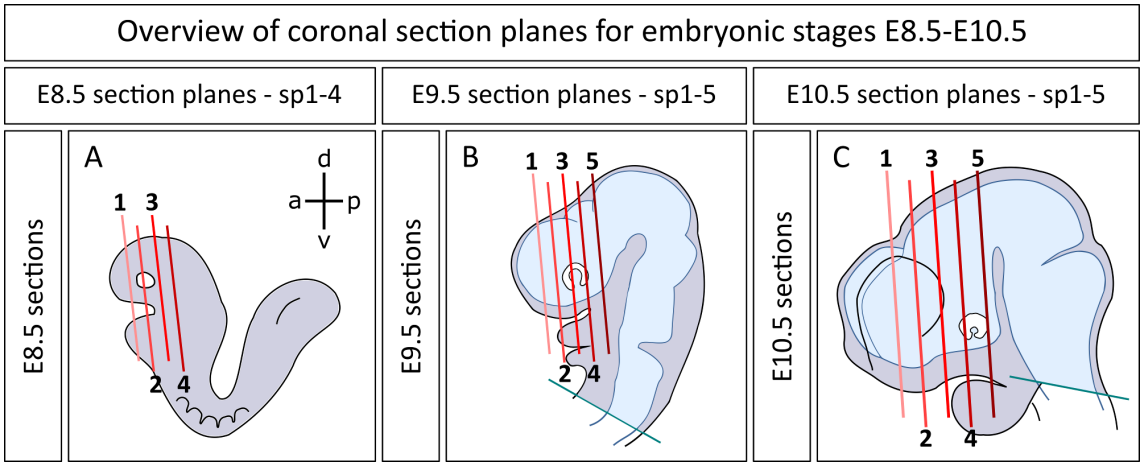

Figure 3.2: Schemtic overview of coronal section planes along the anterior-posterior axis **(A)** Lateral view of an E8.5 embryo indicating section planes sp1-sp4 (a-p: anterior-posterior, d-v: dorsal-ventral). **(B)** Lateral view of an E9.5 embryo head indicating section planes sp1-sp5. **(C)** Lateral view of an E10.5 embryo head indicating section planes sp1-sp5.

3.4.3 Immunohistochemistry

3.4.3.1 Fluorescent immunohistochemistry on sections Immunohistochemical staining (IHC) was used on tissue sections to visualize spatial distribution of specific proteins. Frozen sections were removed from -80°C freezer and air-dried for 1 hour. Slides were transferred to a Coplin jar and washed in PBS for 10-15 minutes to remove excess OCT. Subsequently, sections were fixed with 4 % PFA for 10 minutes. Slides were washed once in PBS and two times in PBS+0.1 % Triton-X100 (PBTr) for 10 minutes each. After that, sections were blocked with 20 % normal donkey serum (NDS) in PBTr for 3-4 hours at ambient temperature. Subsequently, sections were circled with a water-repellent agent (PAP pen) and placed horizontally in a humid box. In the next step, the primary antibody solution (see Subsection 3.1.6 for concentrations) was administered and the sections were incubated at 4°C overnight. On the following day, the primary antibody solution was discarded and slides were washed 5x with PBTr for 20 minutes at RT. Next, the sections were again circled with PAP pen and placed in the humid box to apply the secondary antibody solution (see Subsection 3.1.6 for concentrations). After 1 hour of incubation at RT, the slides were washed again with PBTr 2x for 10-15 minutes. Nucleic counterstain was achieved by incubation in a 300 nM DAPI solution for 5 minutes. After two final washing steps in PBTr for 10 minutes at RT, the sections were dried and mounted with fluorescent mounting medium (Dako). Slides were stored at 4°C to minimize fading of the fluorophores.

3.4.4 *In situ* hybridization

3.4.4.1 Generation of digoxigenin-labeled riboprobes After linearizing the riboprobe's cDNA containing plasmid (as described in Subsection 3.2.1.4) with the appropriate restriction enzyme (see Subsection 3.1.8), *in vitro* transcription (IVT) was performed. For details see IVT solution mix in Subsection 3.1.4. Digoxigenin-(DIG-)labeled riboprobes were generated by using DIG labeling Kit (Roche) according to manufacturer's instructions. Subsequently, the RNA-probes were purified as described in Subsection 3.2.1.5. Concentration of the riboprobes was detected with Nanodrop and gel electrophoresis was conducted for verifying the size of the RNA-probes. Finally, 1 % RNase-inhibitor was added to the riboprobes solution and probes were stored at -20°C.

3.4.4.2 *In situ* hybridization on sections RNA *in situ* hybridization (ISH) is a biochemical method to detect ribonucleic acid on tissue section or in cells. In this study, ISH was used to detect mRNA expression on forebrain embryo sections and whole embryo samples (see Subsection 3.4.4). The RNA-probes were generated as described in Subsection 3.4.4. Before the ISH protocol was started, the cryo-sections were air-dried at RT for 1 hour. After that, the slides were transferred to a Coplin jar with PBS and excess OCT was washed off for 10 minutes. Subsequently, sections were post-fixed in 4% PFA for 10 minutes at RT. Again, the slides were washed with PBS 2x for 10 minutes and then transferred to proteinase-K solution (see Subsection 3.1.4) and incubated for 5-10 minutes. Sections were washed with PBS 2x for 10 minutes and then again fixed with 4% PFA for 10 minutes at RT. Subsequently, slides were washed again with PBS for 10 minutes and then transferred to PBS+0,1%Tween-20 (PBTw). Another washing step with PBTw for 10 minutes followed and then sections were dehydrated in 70% ethanol for 5 minutes at RT. Subsequently, the sections were air-dried until completely dry. Riboprobes were diluted in hybridization solution (see Subsection 3.1.4) at a concentration of 0,8-1ng/µL and pre-heated to 95°C for 5 minutes. The dried slides were placed horizontally in a humid box (filled with 50mL of 50%-formamide solution) and 150-200µL hybridization solution (including riboprobes) per slide was applied. Immediately, sections were covered with Hybri-Slips (Sigma-Aldrich) to prevent evaporation during hybridization process. The humid box was then transferred to a pre-heated hybridization oven and incubated overnight at 65°C. Solution I and Solution II (see Subsection 3.1.4) were also pre-heated to 65°C overnight. On the next day, the slides were transferred to a Coplin jar with solution I (65°C) and Hybri-Slips were carefully removed. Sections were washed 2x in Solution I for 30 minutes at 65°C and subsequently incubated 2x in Solution II for 30 minutes at 65°C. After that, 3x washing steps

in MABT solution were conducted at RT. Subsequently, sections were blocked in ISH-Blocking solution (see Subsection 3.1.4) for 3-4 hours at RT. Anti-digoxigenin-AP Fab-fragments were diluted 1:3000 in blocking solution and applied to slides. Sections were incubated in Fab-fragment solution overnight at 4°C. On the next day, antibody solution was removed and slides were washed 5x for 20 minutes at RT. Finally, sections were 2x incubated in NTMT solution for 10 minutes at RT and transferred to ISH-Staining solution until staining was clearly visible. Staining process was stopped by transferring slides to a Coplin jar with PBS. After another 2x washing in PBS for 10 minutes, the sections were air-dried and mounted in Aqua Poly-Mount.

3.4.4.3 Whole-mount *in situ* hybridization Whole-mount *in situ* hybridization was used to visualize RNA expression in E8.5 embryos. After dissection, the embryos were fixed in 4% PFA overnight. On the next day, embryos were washed 3x in PBSTw for 5-10 minutes. Subsequently, a dehydration series up to pure MeOh was performed in 10 minute-steps (25-50-75-90-100% MeOH) and embryos were stored at -20°C until further processed. For ISH, the samples were rehydrated from pure MeOH to PBS (100-90-75-50-25% MeOH, then PBS) in 5-10 minute-steps. Embryos were transferred to a 12-well plate and washed 2x with PBTw for 5-10 minutes and subsequently bleached in 6% H_2O_2/PBTw for hour at 4°C (in the dark). After washing 2x with PBTw for 5-10 minutes, the samples were permeabilized with proteinase-K solution (see Subsection 3.1.4) for 10 minutes at RT. The embryos were washed again in PBTw for 10 minutes and re-fixed in 4% PFA for 20 minutes at RT. PFA was removed and samples were washed 2x with PBTw for 5-10 minutes. Subsequently, the embryos were incubated in hybridization solution (see Subsection 3.1.4) for 3-4 hours at 65°C. After that, specimens were incubated overnight at 65°C in hybridization solution containing the appropriate riboprobe at 0,8-1ng/µL concentration (on nutator). On the following day, hybridization solution was removed and the embryos were washed 2x at 65°C in Solution I and then Solution II for 30 minutes each. Samples were washed 3x with PBTw for 10 minutes at RT and then blocked for 3-4 hours in PBTw containing 20% sheep serum and 1% BSA (WMISH Blocking). Finally, the embryos were incubated overnight at 4°C in anti-digoxigenin-AP Fab-fragments diluted 1:3000 in WMISH blocking solution. On the next day, the antibody solution was removed and the samples were washed 5x in PBTw for 10-20 minutes. Afterwards, the embryos were washed 2x with NTMT solution for 10-20 minutes and finally transferred to ISH-Staining solution. Staining process was individually stopped by transferring samples to NTMT, when staining intensity was reached (1-5 hours). After removal of ISH-Staining solution, the em-

bryos were washed 3x in NTMT for 5-10 minutes. This was followed by incubation in low-pH PBTw (pH5.2) for 3-5 hours at RT. Embryos were re-fixed in 4% PFA for 20 minutes and dehydrated in a series of graded MeOH solutions (25-50-75-90-100% MeOH) for 5-10 minutes each. Optional: Clearing was achieved by rehydrating the samples (form MeOH to PBS as described above) and subsequent incubation in glycerol (step-wise from 25%, 50% to 80% glycerol/PBS, 5-10 minutes each). The embryos were either stored at 4°C (glycerol) or -20°C (MeOH) for up to several months.

3.4.5 TUNEL assay

Terminal deoxynucleotidyl transferase dUTP nick end labeling (TUNEL) is a biochemical method to detect DNA fragmentation during apoptosis by labeling 3´- hydroxyl ends generated by DNA breaks (nick ends). In this study, TUNEL assay was used on tissue sections to detect apoptotic cells. For this, the 2 TdT DAB *In Situ* Apoptosis Detection Kit (Trevigen) was used according to manufacturer's instructions.

3.4.6 X-Gal staining on cryo-sections

X-Gal (5-bromo-4-chloro-3-indolyl-β-D-galactopyranoside) staining is a biochemical method to visualize activity of β-Galactosidase with a chromogenic substrate that is hydrolyzed to an insoluble blue compound in presence of active β-Gal enzyme. In this study, X-Gal staining was used to detect β-Galactosidase expression under the control of the *Lrp6* promoter to indirectly visualize *Lrp6* expressing cells. X-Gal staining on embryo sections was performed exclusively on OCT cryo-sections. For this, sections were removed from -20°C and equilibrated to 4°C in PBS. Sections were re-fixed in 4% PFA for 10 minutes and rinsed with PBS+ (+2mM MgCl2) for 10-20 minutes at 4°C. Subsequently, sections were washed in X-Gal washing buffer (see Subsection 3.1.4) for 10-20 minutes at 4°C. Finally, sections were transferred to X-Gal staining solution (see Subsection 3.1.4) and incubated at 37°C for 30 minutes or to conserve tissue integrity at 4°C for several hours. Staining process was stopped by removed X-Gal solution and washing sections in X-Gal washing buffer for 10 minutes at 4°C. After that, slides were washed in PBS+ for 10 minutes, air-dried and mounted in Aqua Poly-Mount.

3.4.7 X-Gal staining on whole embryos

X-Gal staining on whole embryos was processed analogously to X-Gal staining procedure on sections. After fixation of the embryos, the samples were washed in PBS+ and transferred to X-

Gal washing buffer. Then embryos were submerged in X-Gal staining solution and stained at 37°C or RT until the desired staining intensity was reached. Subsequently, staining process was stopped by transferring the embryos to X-Gal washing buffer. Finally, embryos were washed with PBS+ and stored at 4°C. As described in Subsection 3.4.4 clearing with glycerol was optional.

3.5 Quantification and statistical analysis

3.5.1 MPM-2 quantification

To quantify mitotic cells within the neuroepithelium, neural progenitor cells that stained positive for mitosis marker MPM-2 (see Subsection 3.1.6) were counted manually on six coronal sections of the forebrain. The mean values of MPM-2 cell count for each section was calculated and correlated to the length of the inner outline (in µm) of the neural tube (lining of the apical side of the neuroepithelium). The values were then transformed to reflect the relative values of average count of MPM-2 positive cells per 100µm (values on y-axis of graphs in Figure 4.15). These values were averaged for all sections per individual to have one data-point per analyzed embryo (data-points displayed in the diagrams of Figure 4.15). MPM-2 quantification of the regions with neuroepithelial excrescences was performed in an analogue fashion. The regions that clearly exceeded the normal thickness of the neuroepithelium (along the apical-basal axis) were defined as excrescences and MPM-2 positive cells were counted separately. These values were correlated to the length of the apical outline of the neuroepithelium along the excrescence (see Figure 4.15 B).

3.5.2 Alexa488-WNT3a uptake analysis

Quantification of the results from WNT3a-A488 uptake experiments was performed in an automated fashion. For this, I wrote a script (source code in Algorithm 3) in ImageJ to automatically count the Alexa488 positive vesicles (defined as particles bigger than 2 pixels2) within a manually defined area of the neural folds/neuroepithelium (as shown in Figure 4.33 C-D). Moreover, it was possible with this script to detect the area of all A488-positive vesicles. Thus, one can extrapolate the average size of an Alexa488-WNT3a positive vesicle. The automated vesicle detection was performed with 5 sections per embryo at E8.5 and 6 sections per embryo at E9.5. The number of vesicles of all sections was averaged. Further, the absolute values of A488-positives vesicles were correlated to the measured neuroepithelial area of each embryo to have relative values for better comparability.

Algorithm 3 Script for quantification of WNT3a-A488 positive vesicles

Sourcecode of FIJI macro for quantification of WNT3a-A488 positive vesicles

```
run("8-bit");
run("Invert");
run("Subtract Background...", "rolling=10 light disable");
setAutoThreshold("Default");
//run("Threshold...");
setThreshold(0, 220);
//setThreshold(0, 220);
setOption("BlackBackground", false);
run("Convert to Mask");
run("Watershed");
run("Restore Selection");
run("Analyze Particles...", "size=2-Infinity show=Masks display clear");
run("Measure");
dir = getDirectory("image");
  name=getTitle;
  path = dir+name;
saveAs("PNG", "C:\\Users\\fapaul\\Desktop\\"+name);
close();
dir = getDirectory("image");
  name=getTitle;
  path = dir+name;
saveAs(path+"_inv");
close();
   index = lastIndexOf(name, ".");
   if (index!=-1) name = substring(name, 0, index);
   name = name + ".xls";
   saveAs("Measurements", dir+name);
selectWindow("Results");
run("Close");
```

4 Results

4.1 Expression patterns of *Lrp4* and *Lrp5/6* overlap in the developing forebrain

Many studies have addressed to what extent the low-density lipoprotein receptors LRP4 [107, 138, 148] as well as LRP5 and LRP6 (referred to as LRP5/6) [73, 87, 146] are involved in skeletal development and reported in detail on their role in limb formation (see also Section 1.2.3+1.2.4). It could be shown that the observed skeletal malformations in mice that are deficient for these LRP family members appear due to defective WNT signal transduction [73, 87, 138, 137, 142]. However, comparatively little is known about their function in brain development and especially the formation of the forebrain [60, 66, 148]. Thus, I wanted to shed light on the implications of LRP4 and LRP5/6 in WNT signaling dependent development of the murine telencephalon. At first, I used *in situ* hybridization (ISH) analyzes to detect the mRNA expression profiles of *Lrp4* and *Lrp5*/6 in the neural tube at early developmental stages that are crucial timepoints for forebrain formation.

4.1.1 *Lrp4* starts to be expressed at E9.5 in the dorsolateral region of the forebrain

Whole mount *in situ* hybridization experiments revealed that *Lrp4* was not detected in mouse embryos at E8.5 (n=5) (Figure 4.1 A). However, one day later in development - at E9.5 (n=5) - expression of *Lrp4* transcripts could be demonstrated in the rostral neural tube by using ISH on coronal embryo sections. *Lrp4* is expressed in a broad domain of dorsolateral region of the forebrain, whereas the ventral midline was always void *Lrp4* transcripts (Figure 4.1 C-F). It continues to be expressed in the dorsolateral domain of the developing telencephalon at E10.5 and E11.5 (n=6). In the ventral midline and the adjacent ventrolateral region of the prospective forebrain *Lrp4* could not be detected (Figure 4.1 G-J). At later developmental stages (E12.5-E18.5) *Lrp4* is widely expressed in the brain, whereas its strongest expression was detected peri-ventricularly along the lateral ventricles and a subset of cells within the prospective thalamus (Figure 4.1 K-M).

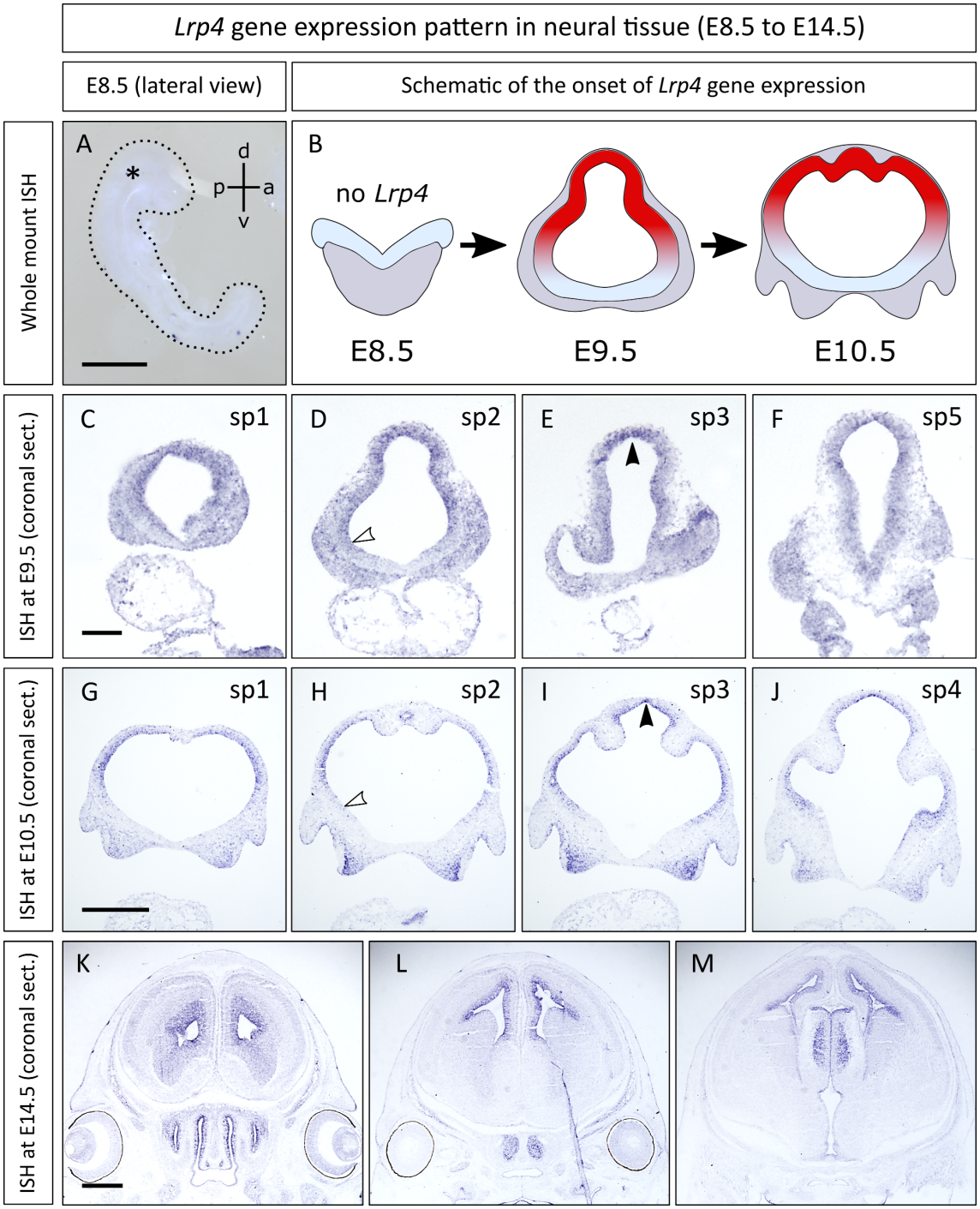

Figure 4.1: *Lrp4* starts to be expressed between E8.5 and E9.5 in the neural tube

(A) *Lrp4* mRNA expression could not be detected at E8.5 [whole embryo at E8.5 (lateral view), asterisk marks the head, dorsoventral- (d-v) and anteroposterior axis (a-p) are indicated, scalebar: 100 µm]. **(B)** Schematic of the onset of *Lrp4* transcript expression (indicated in red). **(C-F)** On E9.5 sections (19s) *Lrp4* mRNA could be visualized by ISH – *Lrp4* is expressed in the dorsal lateral domain of the neural tube. (white arrowhead: ventral border of *Lrp4* expression, black arrowhead: dorsal midline, scalebar: 100 µm). **(G-J)** At E10.5, *Lrp4* continues to be expressed in the forebrain - the ventral midline is void of *Lrp4* transcripts (white arrowhead indicating the ventral border of *Lrp4* expression, scalebar: 500 µm). **(K-M)** At later stages, expression of *Lrp4* can be detected adjacent to the lateral ventricles and in the thalamus (scalebar: 500 µm).

4.1.2 *Lrp5* mRNA is widely expressed in the developing forebrain

In contrast to *Lrp4*, expression of *Lrp5* could already be detected in E8.5 mouse embryos (n=4) by using whole mount ISH. *Lrp5* mRNA is first expressed in the dorsal tips of the neural folds (Figure 4.2 A). At E9.5 (n=3), *Lrp5* expression profile extends to the entire scale of the neural tube (Figure 4.2 C-F). However, at later stages (E10.5, n=4) *Lrp5* appeared to be less expressed in the roof plate and the adjacent lateral domain of the dorsal neural tube compared to its expression levels in the lateral and ventrolateral region of the forebrain (Figure 4.2 G-J). *In situ* hybridization data of *Lrp5* transcripts (n=6) at later developmental stages (E12.5-E18.5) revealed an expression pattern similar to the *Lrp4* mRNA profile. *Lrp5* was found to be widely expressed in brain tissue, whereas the highest expression levels were detected in the ventricular zone of the lateral ventricles. The distinct cell population within the thalamus primorium that expresses *Lrp4* was not found to express *Lrp5* transcripts in a similar fashion (Figure 4.2 K-M). However, from E9.5 onwards a remarkable overlap of *Lrp4* and *Lrp5* expression could be revealed, which indicates a potential interaction of these LRP family members.

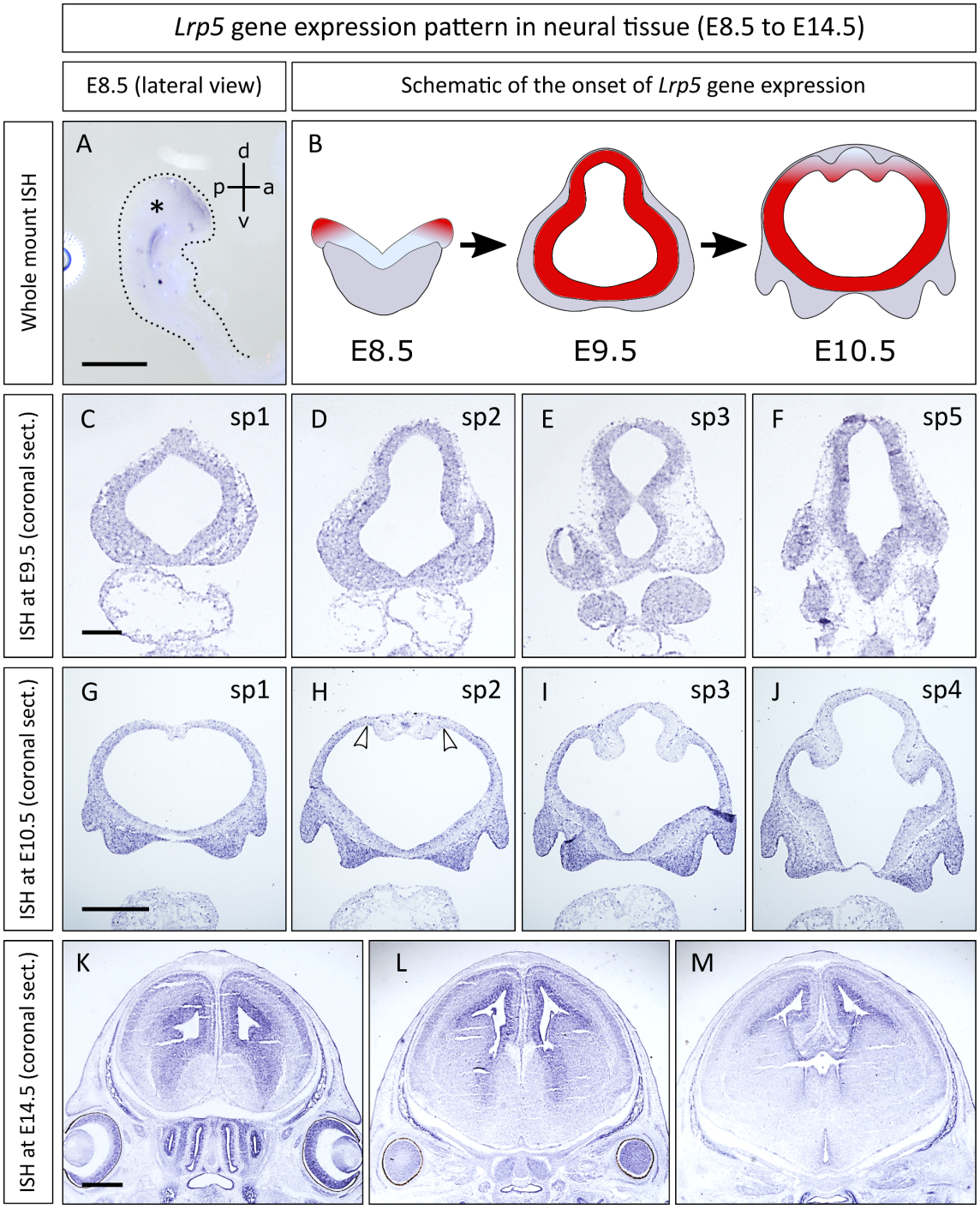

Figure 4.2: *Lrp5* starts to be expressed at E8.5 in the neural folds

(A) Whole mount *in situ* hybridization at E8.5 shows *Lrp5* expression in the neural folds [whole embryo at E8.5 (lateral view), asterisk marks the head, dorsoventral (d-v) and anteroposterior axis (a-p) are indicated, scalebar: 100 µm]. **(B)** Schematic of the onset of *Lrp5* mRNA expression (indicated in red). **(C-F)** ISH on sections at E9.5 (19s) indicate that *Lrp5* is widely expressed in the neural tube (scalebar: 100 µm). **(G-J)** At E10.5, *Lrp5* continues to be expressed in neuroepithelial cells (white arrowheads mark the dorsal area within *Lrp5* is less expressed, scalebar: 500 µm). **(K-M)** At E14.5, strongest expression of *Lrp5* can be found adjacent to the lateral ventricles. (scalebar: 500 µm).

4.1.3 *Lrp6* is ubiquitously expressed in neural progenitors between E8.5 and E10.5

Since the inserted gene trap vector of the $Lrp6^{Gt(Ex187)Byg}$ mouse line includes a β-galactosidase reporter gene under control of the endogenous *Lrp6* promoter (see Subsection 3.3.4), it was feasible to determine gene expression of *Lrp6* by using X-Gal staining (see Subsection 3.2.3.4) on $Lrp6^{Gt(Ex187)Byg}$ heterozygous embryos. It turned out that *Lrp6* is ubiquitously expressed in the neural folds of E8.5 embryos (n=8) (Figure 4.3 A-C). All other X-Gal staining experiments including *Lrp6* heterozyous embryos between E8.5 and E12.5 revealed that *Lrp6* is expressed in all neural cells during these developmental stages (n=12) (Figure 4.3 A-G), which was in line with previously publised data [216].

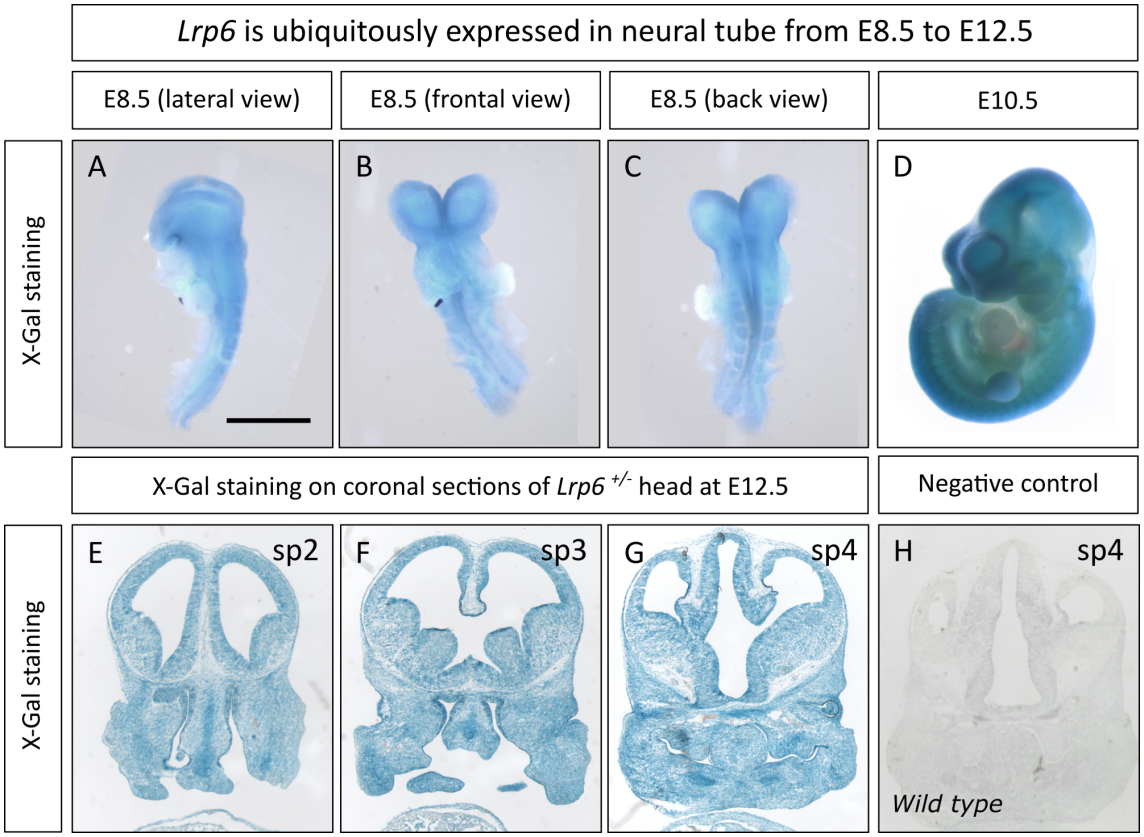

Figure 4.3: *Lrp6* is ubiquitously expressed in neural tissue between E8.5 and E12.5

(A-C) At E8.5, *Lrp6* is expressed in the neural folds (whole mount $Lrp6^{+/-}$ embryos, (scalebar: 500 µm). **(D)** Whole mount X-Gal stained $Lrp6^{+/-}$ embryo at E10.5 (lateral view). **(E-G)** X-gal staining on coronal sections at E12.5 confirmed that *Lrp6* continues to be expressed ubiquitously in the developing brain. **(H)** *Wild type* littermates were used as negative controls and never showed an X-Gal color response.

4.2 *Lrp4;Lrp5* compound mutants are embryonic lethal at E10.5

I could show that from E9.5 onwards, *Lrp4* and *Lrp5* gene expression profiles overlap to a great extent in the neuroepithelium of the developing telencephalon. To dissect common and distinct functions of these LRP candidates during forebrain formation and to reveal potential gene interaction, I decided to generate *Lrp4;Lrp5* double deficient embryos and analyzed these compound mutants from E9.5 onwards.

4.2.1 Statistics of genotype distribution for embryos of $Lrp4^{+/-};Lrp5^{+/-}$ timed matings

Lrp4;Lrp5 compound mutant embryos were generated by breeding two $Lrp4^{+/-};Lrp5^{+/-}$ adult mice - referred to as *Lrp4;Lrp5* (or *Lrp4;5*) timed matings - (Figure 4.4 A-C) or one male with $Lrp4^{+/-};Lrp5^{-/-}$ genotype mated with a $Lrp4^{+/-};Lrp5^{+/-}$ female - referred to as *Lrp4;Lrp5*Δ (or *Lrp4;5*Δ) timed matings (Figure 4.4 D-F). I could show that *Lrp4;Lrp5* timed matings never produced *Lrp4;Lrp5* compound mutant embryos older than E10.5 (n=117) (Figure 4.4 C). Nonetheless, embryos of *Lrp4;Lrp5* timed matings that were analyzed at E10.5 or younger showed no significant difference to the expected ratio for *Lrp4;Lrp5* compound mutant embryos (n=77) (Figure 4.4 B). In accordance with these findings, embryos of *Lrp4;Lrp5*Δ timed matings that were analyzed at E10.5 or younger showed no discrepancy to the expected Mendelian ratio for $Lrp4^{-/-};Lrp5^{-/-}$ embryos (n=90) (Figure 4.4 E). Regarding embryos older than E10.5, *Lrp4;Lrp5*Δ timed matings also showed a significant difference to the expected genotype ratio for $Lrp4^{-/-};Lrp5^{-/-}$ embryos (n=46) (Figure 4.4 F). However, one $Lrp4^{-/-};Lrp5^{-/-}$ embryo at E12.5 resulted from a *Lrp4;Lrp5*Δ mating. Since this embryo showed no obvious differences to *wild type* littermates and further was the only $Lrp4^{-/-};Lrp5^{-/-}$ embryo observed older than E10.5 (out of n=163), the detected genotype might be the result of a genotyping error (see $Lrp4^{mitt}$ genotyping in Subsection 3.2.3.3). In conclusion, statistical analysis of the genotype distribution for embryo litter generated by $Lrp4^{+/-};Lrp5^{+/-}$ timed matings indicates that embryonic lethality occurs in *Lrp4;Lrp5* compound mutant embryos at around E10.5.

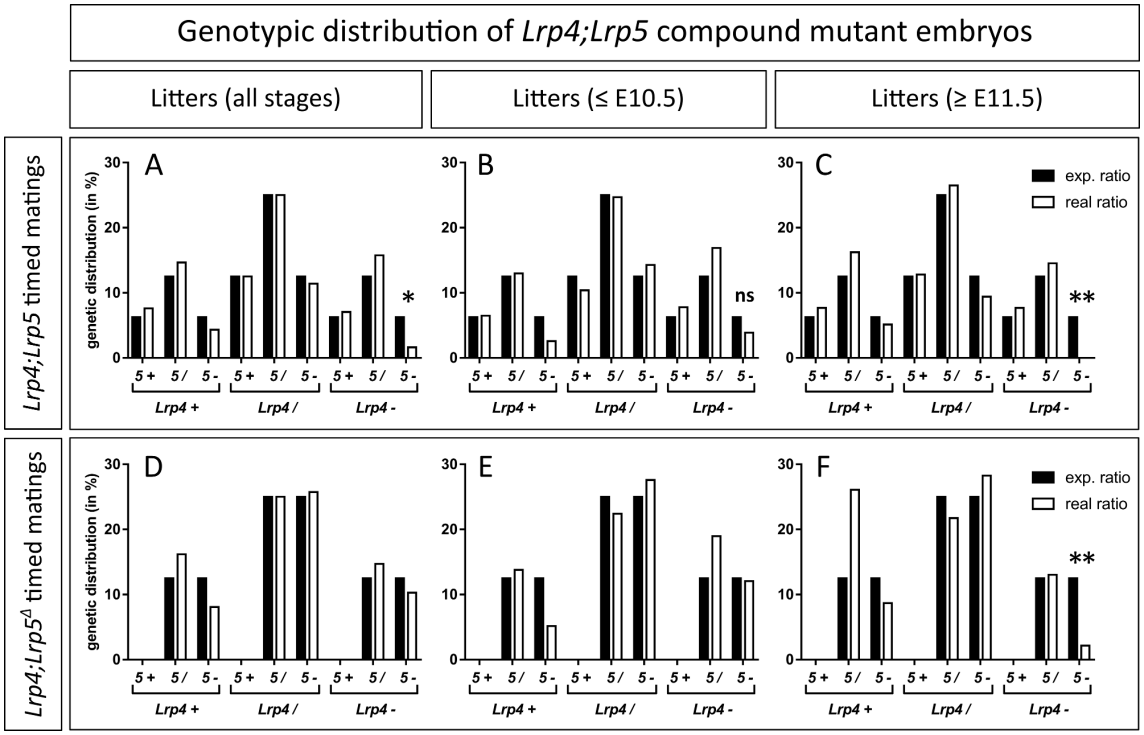

Figure 4.4: *Lrp4*$^{-/-}$*;Lrp5*$^{-/-}$ compound mutant embryos show a lethality phenotype at E10.5

(A) Genotype distribution of all litters (E8.5 - E16.5) generated from *Lrp4*$^{+/-}$*;Lrp5*$^{+/-}$ timed matings shows significantly less *Lrp4*$^{-/-}$*;Lrp5*$^{-/-}$ embryos compared to the expected Mendelian ratio (one sample t-test: * with p-value=0,0248, n=184). **(B)** At E10.5 and earlier there was no significant difference to the expected ratio for *Lrp4*$^{-/-}$*;Lrp5*$^{-/-}$ embryos (one sample t-test: n.s. with p-value=0,5183, n=77). **(C)** At later developmental stages ($\geq$ E11.5) *Lrp4*$^{-/-}$*;Lrp5*$^{-/-}$ compound mutants could no longer be detected (one sample t-test: ** with p-value=0,0061, n=117). **(D-F)** Data on the genetic distribution for litters of *Lrp4;Lrp5*Δ timed matings support the observed embryonic lethality [D: n.s. with p-value=0,5898, n=136. E: n.s. with p-value=0,9475, n=90. F: ** with p-value=0,0009, n=46 (for rate of *Lrp4*$^{-/-}$*;Lrp5*$^{-/-}$ in D-F the one sample t-test was used)].

4.2.2 Embryonic resorption of *Lrp4*$^{-/-}$*;Lrp5*$^{-/-}$ embryos occurs at E10.5

Based on the finding that *Lrp4*$^{-/-}$*;Lrp5*$^{-/-}$ embryos do not survive after E10.5, I concentrated on the analysis of *Lrp4*$^{-/-}$*;Lrp5*$^{-/-}$ embryos at E9.5 and E10.5. To determine the onset of resorption I used immunostaining for apoptosis marker cleaved-Caspase-3 on *Lrp4*$^{-/-}$*;Lrp5*$^{-/-}$ embryo sections. Whereas the majority of E9.5 *Lrp4;Lrp5* compound mutant embryos were not positive for cleaved-Caspase-3 (n=7), embryos at E10.5 (9 out of 15) showed a widespread staining for the apoptosis factor (Figure 4.5). *Wild type* littermate controls were void of cleaved-Caspase-3 staining (Figure 4.5). In addition, 73,34% of *Lrp4*$^{-/-}$*;Lrp5*$^{-/-}$ embryos at E10.5 had hemorrhages in the heart sac (Figure 4.5). Taken together these observations suggest that the onset of resorption of *Lrp4*$^{-/-}$*;Lrp5*$^{-/-}$ embryos is at E10.5.

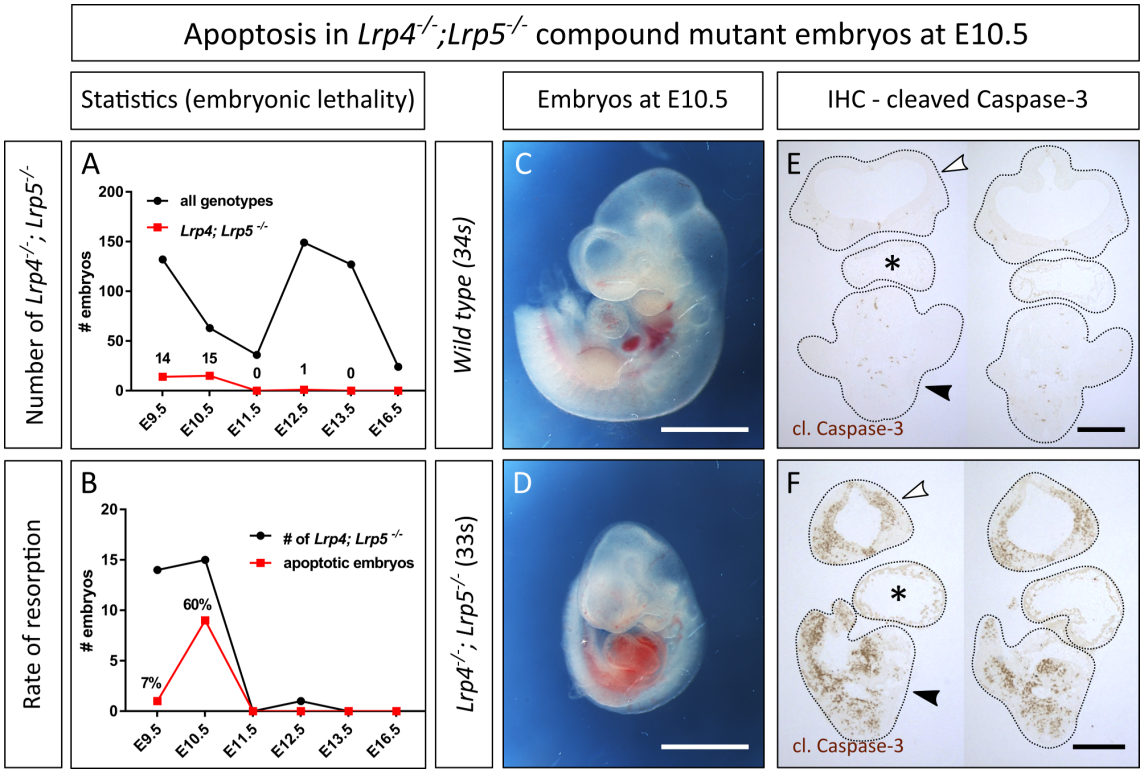

Figure 4.5: *Lrp4*$^{-/-}$*;Lrp5*$^{-/-}$ embryos have a high incidence of embryonic resorption at E10.5

(A) Later than E10.5 (n=200) *Lrp4*$^{-/-}$*;Lrp5*$^{-/-}$ compound mutants could not be detected, whereas at E9.5 and E10.5 *Lrp4*$^{-/-}$*;Lrp5*$^{-/-}$ embryos were observed. **(B)** At E10.5, *Lrp4*$^{-/-}$*;Lrp5*$^{-/-}$ embryos were apoptotic (9 out of 15). Resorption at E9.5: one-sample t-test, * with p=0,0271 (n=132). Resorption at E10.5: one-sample t-test, *** with p=0,0001 (n=63). **(C+D)** *Wild type* and *Lrp4*$^{-/-}$*;Lrp5*$^{-/-}$ embryo (apoptotic) at E10.5 (scalebar: 1mm). **(E+F)** Coronal sections at E10.5: Immunostaining with apoptosis marker cleaved Caspase-3. In *Lrp4*$^{-/-}$*;Lrp5*$^{-/-}$ resorption embryos cleaved Caspase-3 was detected [white arrowhead indicates the embryo head, asterisk marks the heart, black arrowhead illustrates the trunk (scalebar: 200 µm)].

4.2.3 *Lrp4;Lrp5* compound mutant embryos display a delayed neural tube closure

It has been reported that loss of LRP6 leads to neural tube closure defects (NTD) [61, 60], whereas NTD's have neither been described for LRP4 loss-of-function mutants nor for *Lrp5* null embryos. Nonetheless, I wanted to investigate whether neural tube closure in *Lrp4;Lrp5* compound mutant embryos might be affected. I found that at E9.5 *Lrp4*$^{-/-}$*;Lrp5*$^{-/-}$ embryos showed a delayed closure of the anterior neuropore. In *wild type* embryos, the anterior neuropore fuses between somite stage 16s-19s (Figure 4.6) [178]. At somite stage 20s the anterior neuropore of all analyzed *wild type*, *Lrp4*$^{-/-}$ and *Lrp5*$^{-/-}$ embryos was already entirely closed (Figure 4.6). In contrast, *Lrp4*$^{-/-}$*;Lrp5*$^{-/-}$ embryos at somite stage 20s to 23s still displayed an incomplete ANP closure (6 out of 9) (Figure 4.6). However, the dorsal neural tube of all

observed *Lrp4;Lrp5* compound embryos at E10.5 was completely fused (Figure 4.6). This indicates that loss of LRP4;LRP5 leads to a delayed closure of the ANP but not to a neural tube closure defect.

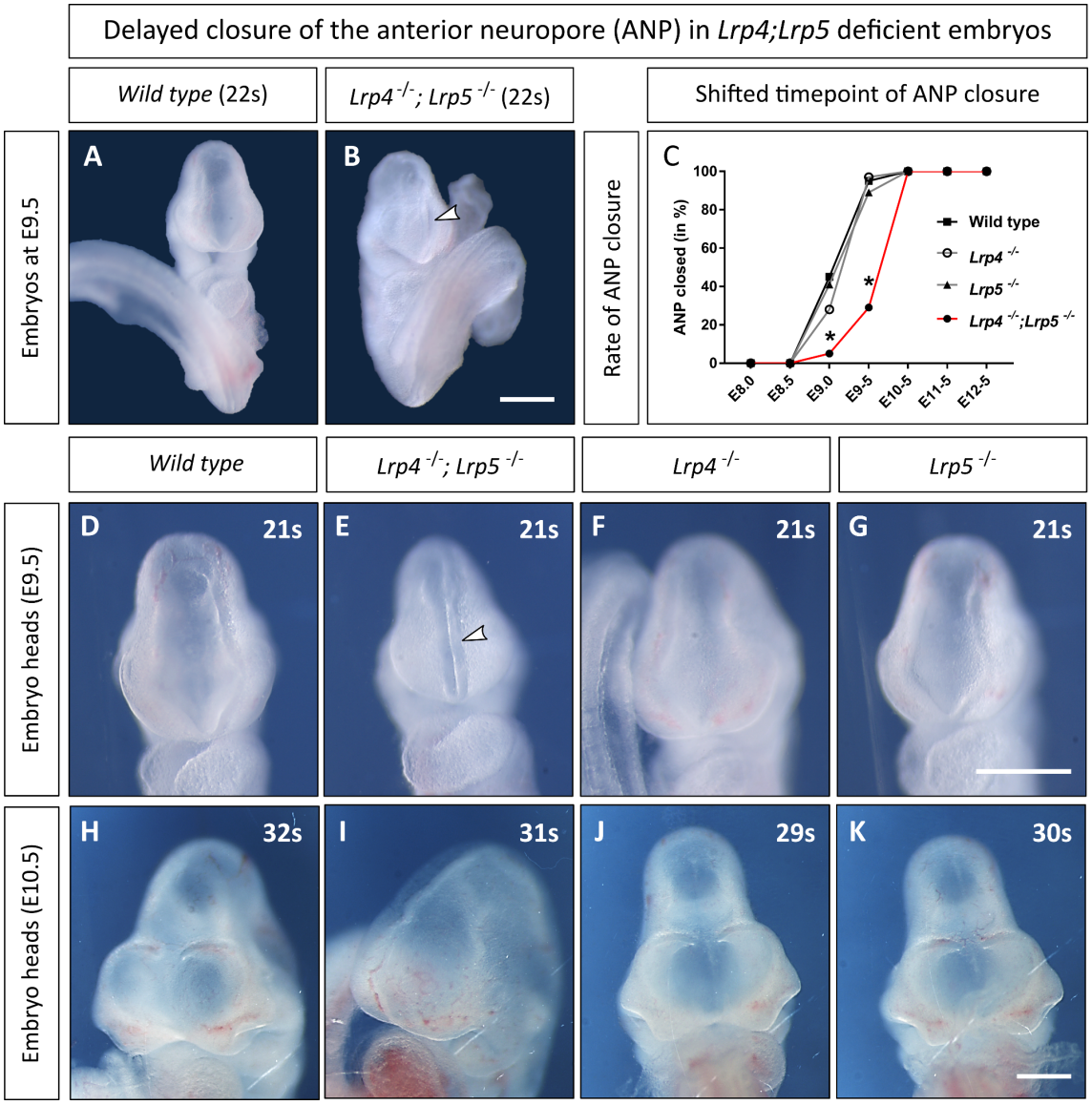

Figure 4.6: Loss of LRP4;LRP5 leads to a delayed closure of the anterior neuropore

(A+B) In contrast to *wild type* littermate controls, 71% of *Lrp4*$^{-/-}$*;Lrp5*$^{-/-}$ mutant embryos displayed an open anterior neuropore at E9.5 (frontal view of whole embryos, arrowhead indicates the ANP). **(C)** *Lrp4*$^{-/-}$*;Lrp5*$^{-/-}$ compound embryos have a significant delay in ANP closure [At E9.0: One-sample t-test, * with p=0,0188 (n=15). At E9.5: One-sample t-test, * with p=0,0164 (n=14)]. **(D+E)** Frontal view of *wild type* and *Lrp4*$^{-/-}$*;Lrp5*$^{-/-}$ embryo head (arrowhead indicates unclosed ANP). **(F+G)** *Lrp4*$^{-/-}$ and *Lrp5*$^{-/-}$ embryos do not have a delayed ANP closure. **(H-K)** At E10.5, the ANP of all dissected *Lrp4*$^{-/-}$*;Lrp5*$^{-/-}$ embryos was closed. Scalebars indicate 500 µm.

4.3 *Lrp6*$^{-/-}$ and *Lrp4*$^{-/-}$;*Lrp6*$^{-/-}$ embryos exhibit impaired growth

LRP5 shares a similar molecular structure with LRP6 [89, 98, 116] - see also Section 1.2.4. Many studies reported that both receptors have a functionally redundancy during embryo development [87, 89, 98]. Therefore, it was my intention to generate and investigate *Lrp4;Lrp6* compound mutant embryos in addition to the analysis of *Lrp4;Lrp5* compound mutants. By comparig both compound mutants, I intended to dissect common and distinct functions of LRP5 and LRP6 regarding WNT-related embryogenesis in interplay with LRP4. Further I was able to shed light on potential gene interaction of *Lrp4* and *Lrp6* during forebrain development.

4.3.1 Ratio of *Lrp4;Lrp6* compound mutants embryos matched the expected Mendelian ratio

I generated *Lrp4*$^{-/-}$;*Lrp6*$^{-/-}$ embryos by breeding mice that were double heterozygous for *Lrp4;Lrp6* - referred to as *Lrp4;Lrp6 (or Lrp4;6)* timed matings (Figure 4.7). Overall, 76 *Lrp4;Lrp6* timed matings spawned 521 embryos that were dissected between E8.5 and E11.5. For all analyzed developmental timepoints *Lrp4*$^{-/-}$;*Lrp6*$^{-/-}$ embryos could be generated. While the focus of *Lrp4*$^{-/-}$;*Lrp6*$^{-/-}$ mutant analysis was on developmental stage E10.5 and younger, I could show that generation of E11.5 *Lrp4;Lrp6* compound mutant embryos (n=2) was feasible (Figure 4.7 C). Both *Lrp4*$^{-/-}$;*Lrp6*$^{-/-}$ embryos at E11.5 showed no signs of apoptosis like *Lrp4*$^{-/-}$;*Lrp5*$^{-/-}$ mutant embryos $\geq$ E10.5 (see Figure 4.5). This supports the idea that unlike *Lrp4*$^{-/-}$;*Lrp5*$^{-/-}$ embryos, *Lrp4;Lrp6* compound mutant embryos are not embryonic lethal $\geq$ E10.5.

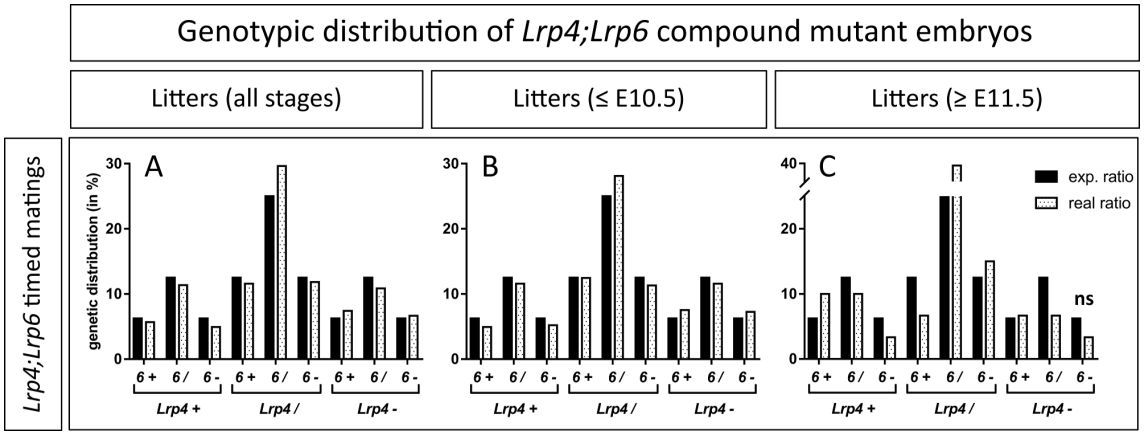

Figure 4.7: *Lrp4*$^{-/-}$*;Lrp5*$^{-/-}$ compound mutants $\leq$ E10.5 could be generated due to expected ratio

(A) Genotype distribution of all litters generated from *Lrp4*$^{+/-}$*;Lrp6*$^{+/-}$ timed matings showed no significant differences to the expected Mendelian ratios (one sample t-test: n.s. with p-value=0,8155, n=405). **(B)** Litters of *Lrp4*;6 timed matings $\leq$ E10.5 (one sample t-test: n.s. with p-value=0,6134, n=345) **(C)** Litters $\geq$ E11.5 showed a slightly decreased but not significant ratio of *Lrp4*$^{-/-}$*;Lrp6*$^{-/-}$ embryos [3.34% versus 6.25% expected ratio) (one sample t-test: n.s. with p-value=0,714, n=60).

4.3.2 *Lrp6*$^{-/-}$ neural tube closure defect is also exhibited in *Lrp4*$^{-/-}$*;Lrp6*$^{-/-}$ embryos

It was reported by others that loss-of-function mutation of *Lrp6* leads to severe neural tube closure defects [60, 146]. Since I could show that *Lrp4; Lrp5* compound mutant embryos have a delayed ANP closure (see Subsection 4.2.3), it was of particular interest to also investigate neural tube closure of *Lrp4; Lrp6* double deficient embryos. I found that at E9.5 68% of *Lrp6*$^{-/-}$ embryos (n=25) and only 30% of *Lrp4*$^{-/-}$*;Lrp6*$^{-/-}$ embryos (n=13) displayed a closed anterior neural tube, whereas the majority of *Lrp4*$^{-/-}$ and *wild type* littermates had an entirely closed neural tube (Figure 4.8). Therefore, *Lrp6*$^{-/-}$ as well as *Lrp4*$^{-/-}$*;Lrp6*$^{-/-}$ embryos showed a significant difference to *wild type* littermates regarding neural tube closure at E9.5. Interestingly, there was also a significant difference in neural tube closure at E9.5 between *Lrp6* single mutant embryos and *Lrp4; Lrp6* compound embryos in which the latter was more prone to display an open ANP. Nonetheless, at E10.5 approximately one fifth of both *Lrp6*$^{-/-}$ (n=40) and *Lrp4*$^{-/-}$*;Lrp6*$^{-/-}$ (n=11) embryos still showed an open (anterior) neural tube (Figure 4.8 A). The observations of *Lrp6*$^{-/-}$ and *Lrp4*$^{-/-}$*;Lrp6*$^{-/-}$ NTD at E10.5 is consistent with the reported rate of exencephalus phenotype in *Lrp6* loss-of-function mutants [61, 60, 146].

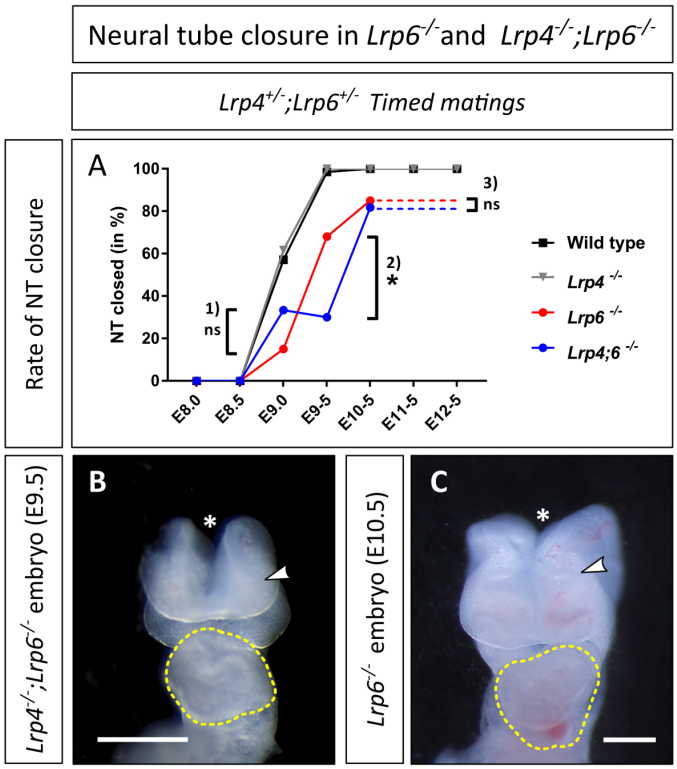

Figure 4.8: Neural tube closure deficit in *Lrp6*$^{-/-}$ embryos persists in *Lrp4*$^{-/-}$;*Lrp6*$^{-/-}$ embryos

(A) Statistics on neural tube closure of *Lrp6*$^{-/-}$ and *Lrp4*$^{-/-}$;*Lrp6*$^{-/-}$ embryos at the analyzed developmental stages (E8.5 to E10.5) **(B)** Open neural tube phenotype in *Lrp4*$^{-/-}$;*Lrp6*$^{-/-}$ embryo (16s) at E9.5 [frontal view: White arrowhead depicts the head, asterisk indicating the open neural tube (dorsal), yellow-dotted line contours the heart, scalebar: 500 µm]. **(C)** *Lrp6*$^{-/-}$ embryo (28s) at E10.5 displaying the open neural tube phenotype [frontal view: White arrowhead depicts the head, asterisk indicating the open neural tube (dorsal), yellow-dotted line contours the heart, scalebar: 500 µm].

Table 4.1: Statistical tests for data shown in Figure 4.8

1) For E9.0:	*Lrp6*$^{-/-}$ versus *Lrp4*$^{-/-}$;*Lrp6*$^{-/-}$:	one-sample t-test, n.s. with p=0,4646 (n=8)
	Lrp6-/- versus *wild type*:	one-sample t-test, * with p=0,0346 (n=14)
	Lrp4$^{-/-}$;*Lrp6*$^{-/-}$ versus *wild type*:	one-sample t-test, n.s. with p=0,3145 (n=12)
2) For E9.5:	*Lrp6*$^{-/-}$ versus *Lrp4*$^{-/-}$;*Lrp6*$^{-/-}$:	one-sample t-test, * with p=0,0188 (n=38)
	Lrp6$^{-/-}$ versus *wild type*:	one-sample t-test, * with p=0,0188 (n=91)
	Lrp4$^{-/-}$;*Lrp6*$^{-/-}$ versus *wild type*:	one-sample t-test, **** with p<0,00001 (n=79)
3) For E10.5:	*Lrp6*$^{-/-}$ versus *Lrp4*$^{-/-}$;*Lrp6*$^{-/-}$:	one-sample t-test, n.s. with p=0,8607 (n=51)
	Lrp6$^{-/-}$ versus *wild type*:	one-sample t-test, n.s. with p=0,2833 (n=98)
	Lrp4$^{-/-}$;*Lrp6*$^{-/-}$ versus *wild type*:	one-sample t-test, n.s. with p=0,2811 (n=69)

4.3.3 Somitogenesis phenotype of *Lrp6* single mutants persists in *Lrp4;Lrp6* compound mutant embryos

Embryos that are deficient for LRP6 show impaired somitogenesis, which ultimately leads to caudal truncation with a reduced number of somites [146]. This had to be taken into consideration for an accurate somite matched comparison between *Lrp6*$^{-/-}$ single mutant embryos (and also *Lrp4*$^{-/-}$;*Lrp6*$^{-/-}$ compound mutants) and littermate control embryos. Moreover, it was important to examine whether *Lrp4*$^{-/-}$;*Lrp6*$^{-/-}$ compound mutant embryos display the somitogenesis phenotype in same way as *Lrp6*$^{-/-}$ embryos. Therefore, I counted the somites of all embryos that were dissected and compared the somite number of the different genotypes (diagrams in Figure 4.9). It turned out that at E9.5 and E10.5 *Lrp6*$^{-/-}$ embryos and *Lrp4*$^{-/-}$;*Lrp6*$^{-/-}$ compound mutants showed somite count reduction to the same extent. *Lrp4*$^{-/-}$ embryos did not show a difference to the number of somites in *wild type* embryos (Figure 4.9). In order to match the developmental stage of the different genotypes according to the somite count, the reduction of somites in *Lrp6*$^{-/-}$ embryos and *Lrp4*$^{-/-}$;*Lrp6*$^{-/-}$ compound mutant embryos had to be considered. To reliably compare the embryos for all further experiments, I determined the mean difference of somites at E9.5 and E10.5 of affected embryos - with impaired somitogenesis (*Lrp6*$^{-/-}$ and *Lrp4*$^{-/-}$;*Lrp6*$^{-/-}$) - versus non-affected embryos (all other genotypes). At E9.5, I calculated a mean difference of 5,331 (± 0,8864) somites (n=104) and analogously at E10.5 a mean difference of 12,12 (± 0,9119) somites (n=113) was calculated (Figure 4.9 C). Based on these differences in somite count I matched *Lrp6*$^{-/-}$ embryos and *Lrp4*$^{-/-}$;*Lrp6*$^{-/-}$ compound mutants with littermate control embryos for all further analyses.

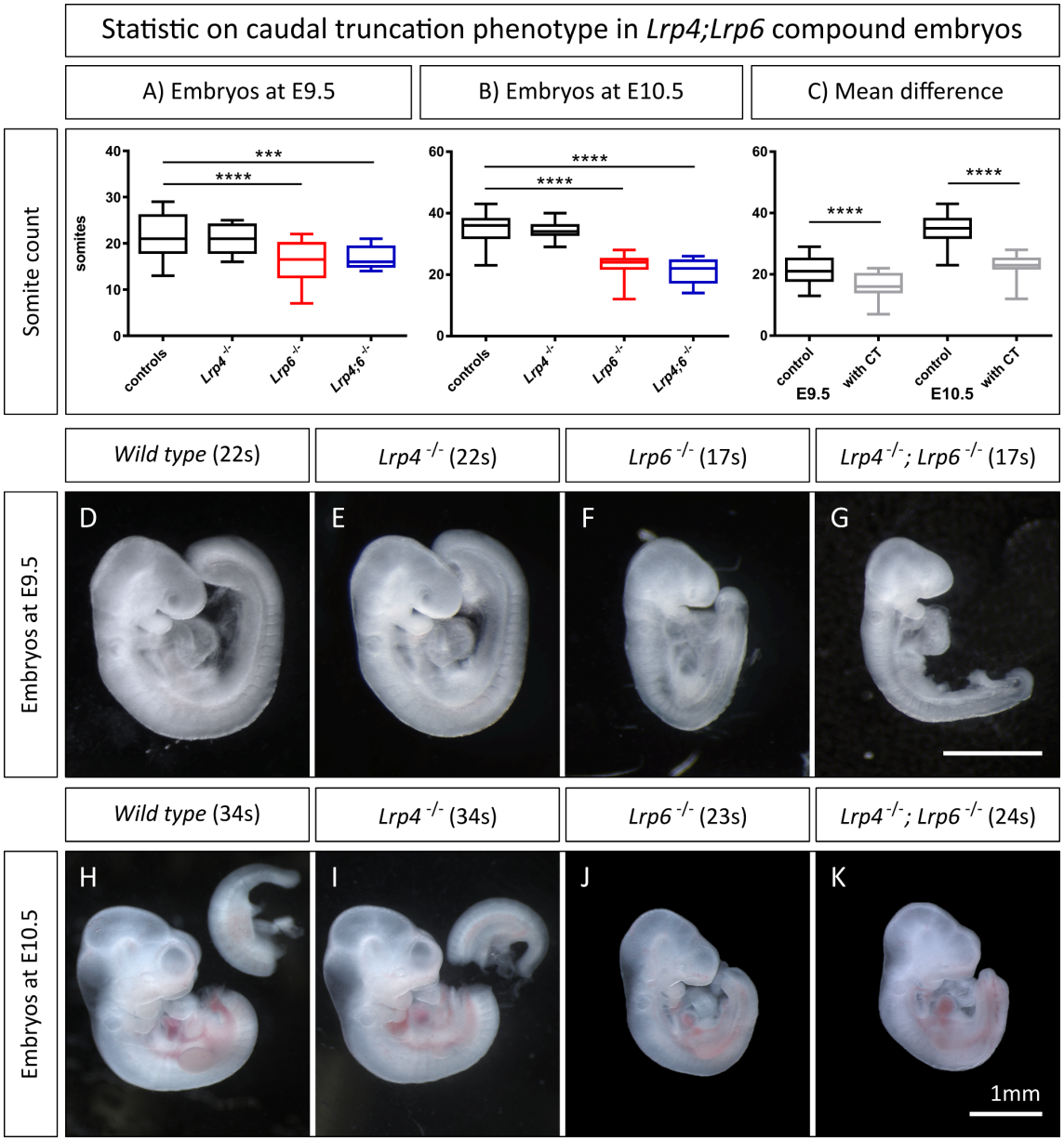

Figure 4.9: *Lrp6*$^{-/-}$ and *Lrp4*$^{-/-}$;*Lrp6*$^{-/-}$ embryos display a caudal truncation phenotype with a significant loss of somites

(A+B) Analysis of the somite count for *Lrp6*$^{-/-}$ and *Lrp4*;6-/- embryos at E9.5 and E10.5 revealed a significant decrease in somite number in these mutants compared to littermates with other genotypes. **(C)** Statistical analysis of affected embryos (*Lrp6*$^{-/-}$ and *Lrp4*$^{-/-}$;*Lrp6*$^{-/-}$) with caudal truncation phenotype (CT) and non-affected individuals (*wild type* and heterozygotes) revealed that mean values of the somite count differed with 5,331 (± 0,8864) somites for E9.5 and 12,12 (± 0,9119) somites for E10.5 **(D-G)** Embryos at E9.5 (lateral view) - Scalebar: 1mm. **(H-K)** Embryos at E10.5 (H+I: Tails of embryos were cut to align for taking lateral view pictures) - Scalebar: 1mm.

Table 4.2: Statistical tests for data shown in Figure 4.9

Graph A:	**E9.5 comparison of *Lrp6*$^{-/-}$ and controls**
	unpaired t-test: **** with p<0,0001
	mean ± SEM of controls: 21,89 ± 0,5355 (n=63)
	mean ± SEM of *Lrp6*$^{-/-}$: 16,11 ± 1,038 (n=18)
	E9.5 comparison of *Lrp4*$^{-/-}$;*Lrp6*$^{-/-}$ embryos and controls
	unpaired t-test: *** with p=0,0006
	mean ± SEM of controls: 21,89 ± 0,5355 (n=63)
Graph B:	**E10.5 comparison of *Lrp6*$^{-/-}$ and control embryos**
	unpaired t-test: **** with p<0,0001
	mean ± SEM of controls: 34,94 ± 0,5054 (n=68)
	mean ± SEM of *Lrp6*$^{-/-}$: 23,12 ± 0,8039 (n=17)
	E10.5 comparison of *Lrp4*$^{-/-}$;*Lrp6*$^{-/-}$ and control embryos
	unpaired t-test: **** with p<0,0001
	mean ± SEM of controls: 34,94 ± 0,5054 (n=68)
	mean ± SEM of *Lrp4*$^{-/-}$;*Lrp6*$^{-/-}$: 21,2 ± 1,985 (n=5)
Graph C:	**E9.5 difference (affected versus non-affected)**
	unpaired t-test: **** with p<0,0001
	mean ± SEM of non-affected embryos: 21,72 ± 0,4689 (n=76)
	mean ± SEM of affected embryos: 16,39 ± 0,7152 (n=28)
	E10.5 difference (affected versus non-affected)
	unpaired t-test: **** with p<0,0001
	mean ± SEM of non-affected embryos: 34,8 ± 0,4085 (n=91)
	mean ± SEM of affected embryos: 22,68 ± 0,7627 (n=22)

4.3.4 *Lrp6*$^{-/-}$ and *Lrp4*$^{-/-}$;*Lrp6*$^{-/-}$ mutants are smaller than littermate embryos

Besides the caudal truncation phenotype, I observed that *Lrp6*$^{-/-}$ embryos and *Lrp4*$^{-/-}$;*Lrp6*$^{-/-}$ compound mutants are much smaller compared to littermate embryos with a different genotype (see Figure 4.9 D-H & H-K). To quantify this observation, I measured several dimensions of the embryos that were dissected at E9.5 and E10.5. First, I measured the elongated body axis of the embryos referred to as rostro-caudal (R-C) dimension (see Figure 4.10 A). Further I wanted to address the scale of the embryo head (D-V: Dorsoventral dimension + A-P: Anteroposterior dimension), since I also intended to capture a dimension of the embryos that was not directly affected by the caudal truncation phenotype (described in Subsection 4.3.3). I could detect that elongation of the body axis is greatly reduced in *Lrp6*$^{-/-}$ embryos and *Lrp4*$^{-/-}$;*Lrp6*$^{-/-}$ compound mutants compared to *wild type* and *Lrp4*$^{-/-}$ embryos at E9.5 and E10.5. No significant difference was found for the R-C measure, when comparing *wild type* and *Lrp4*$^{-/-}$ embryos. Further, values for R-C measure in *Lrp6*$^{-/-}$ and *Lrp4*$^{-/-}$;*Lrp6*$^{-/-}$ embryos were also not

significantly different, which indicates that *Lrp4;Lrp6* compound mutant embryos are affected by caudal truncation to the same extent as *Lrp6* single mutant embryos (Figure 4.10 A). By quantification of the embryo head measures, I could show that also the extent of the D-V axis and the A-P axis of *Lrp6*$^{-/-}$ and *Lrp4*$^{-/-}$;*Lrp6*$^{-/-}$ embryo heads were significantly reduced at E9.5 and E10.5 compared to *wild type* (and *Lrp4*$^{-/-}$) embryos (Figure 4.10 B+C). To further analyze the measures of the R-C, D-V and A-P dimensions, I correlated the data to the somite count of the embryos to create somite stage related growth curves (Figure 4.11). Considering these growth curves, it becomes obvious that growth of *wild type* and *Lrp4*$^{-/-}$ embryos related to the somite number appears in a linear fashion (Figure 4.11 A-C & D-F). In contrast, *Lrp6*$^{-/-}$ and *Lrp4*$^{-/-}$;*Lrp6*$^{-/-}$ growth curves show a lower slope (Figure 4.11 G-I & J-L). To compare the growth curves of the different genotypes, I assembled the data in one coordinate system for each type of dimension (Figure 4.12 A-C). Further I calculated the linear regression for the growth curves (Figure 4.12 D-F) and incorporated the somite stage correction (see Subsection 4.3.3). Comparing the slopes for the linear regression of the growth curves for R-C dimension (body) and D-V/ A-P dimension (head) confirmed that there is a major growth deficit in *Lrp6*$^{-/-}$ and *Lrp4*$^{-/-}$;*Lrp6*$^{-/-}$ embryos compared to *wild type* and *Lrp4*$^{-/-}$ embryos (Figure 4.12 G-I).

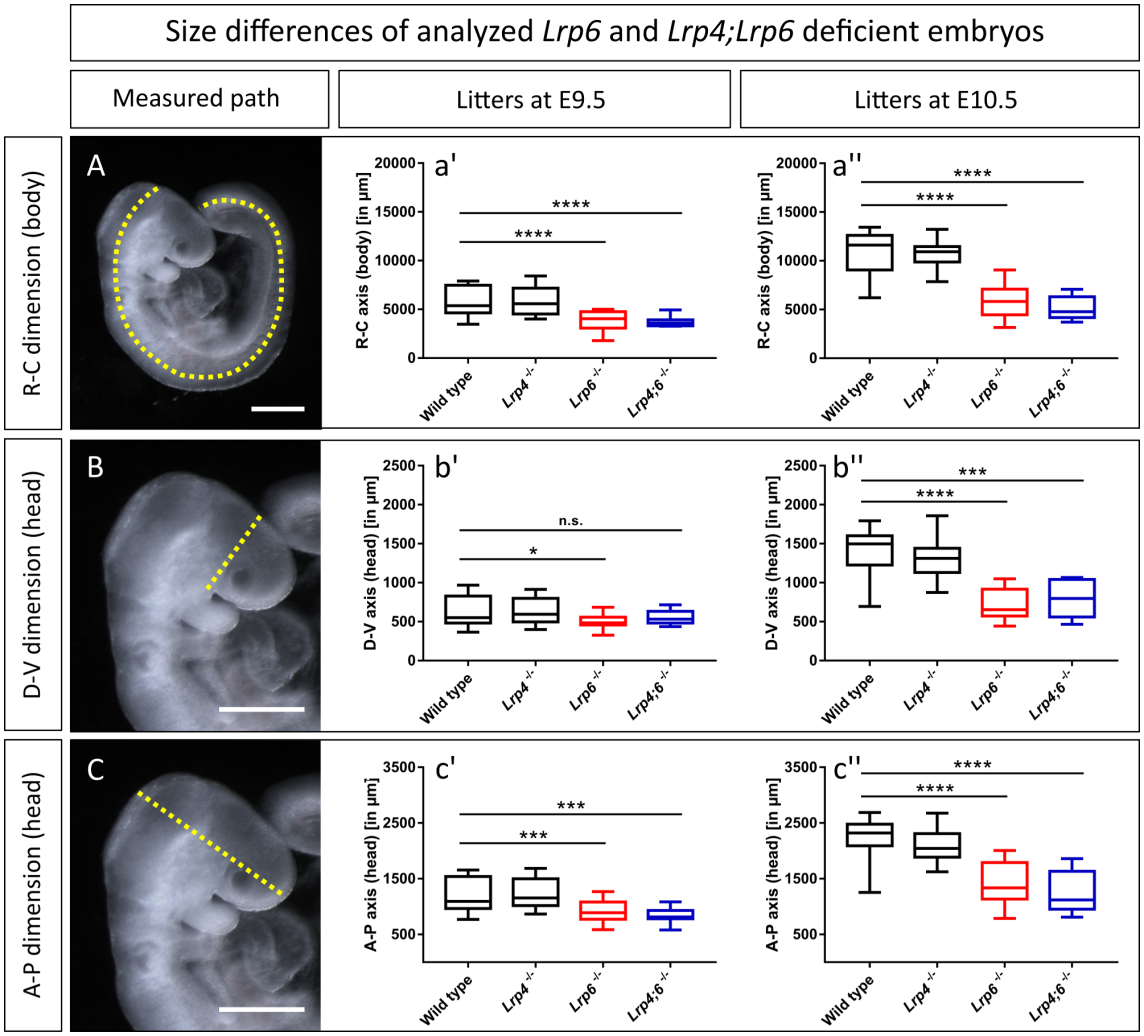

Figure 4.10: *Lrp6*$^{-/-}$ and *Lrp4*$^{-/-}$*;Lrp6*$^{-/-}$ embryos are significantly smaller than littermates

(A) The overall size (rostral to caudal dimension) of *Lrp6*$^{-/-}$ and *Lrp4*$^{-/-}$*;Lrp6*$^{-/-}$ embryos at E9.5 and E10.5 was significantly reduced compared to littermates with different genotypes. **(B+C)** The sizes of *Lrp6*$^{-/-}$ and *Lrp4*$^{-/-}$*;Lrp6*$^{-/-}$ embryos heads were also significantly decreased. The dorsoventral (D-V) dimension and the anteroposterior (A-P) dimension were measured The yellow-dotted line indicates the distance that was measured (Scalebars: 500 µm).

Table 4.3: Statistical tests for data shown in Figure 4.10 graph a' + a"

Graph a':	R-C dimension of *Lrp6*$^{-/-}$ embryos and controls at E9.5
	unpaired t-test: **** with p<0,0001
	mean ± SEM of controls: 5777 µm ± 260,3 (n=28)
	mean ± SEM of *Lrp6*$^{-/-}$: 3878 µm ±213,9 (n=21)
	R-C dimension of *Lrp4*$^{-/-}$*;Lrp6*$^{-/-}$ embryos and controls at E9.5
	unpaired t-test: **** with p<0,0001
	mean ± SEM of controls: 5777 µm ± 260,3 (n=28)
	mean ± SEM of *Lrp4*$^{-/-}$*;Lrp6*$^{-/-}$: 3755 µm ± 164,7 (n=12)
Graph a":	R-C dimension of *Lrp6*$^{-/-}$ embryos and controls at E10.5
	unpaired t-test: **** with p<0,0001
	mean ± SEM of controls: 10916 µm ± 481,1 (n=17)
	mean ± SEM of *Lrp6*$^{-/-}$: 5821 µm ± 329 (n=23)
	R-C dimension of *Lrp4*$^{-/-}$*;Lrp6*$^{-/-}$ embryos and controls at E10.5
	unpaired t-test: **** with p<0,0001
	mean ± SEM of controls: 10916 µm ± 481,1 (n=17)
	mean ± SEM of *Lrp4*$^{-/-}$*;Lrp6*$^{-/-}$: 5148 µm ± 563,7 (n=5)

Table 4.4: Statistical tests for data shown in Figure 4.10 graph b' + b"

Graph b':	D-V dimension (head) of *Lrp6*$^{-/-}$ embryos and controls at E9.5
	unpaired t-test: * with p=0,0109
	mean ± SEM of controls: 630,2 µm ± 35,65 (n=28)
	mean ± SEM of *Lrp6*$^{-/-}$: 511,5 µm ± 20,07 (n=21)
	D-V dimension (head) of *Lrp4*$^{-/-}$*;Lrp6*$^{-/-}$ embryos and controls at E9.5
	unpaired t-test: n.s. with p=0,1917
	mean ± SEM of controls: 630,2 µm ± 35,65 (n=28)
	mean ± SEM of *Lrp4*$^{-/-}$*;Lrp6*$^{-/-}$: 544 µm ± 25,88 (n=12)
Graph b":	D-V dimension (head) of *Lrp6*$^{-/-}$ embryos and controls at E10.5
	unpaired t-test: **** with p<0,0001
	mean ± SEM of controls: 1408 µm ± 67,95 (n=17)
	mean ± SEM of *Lrp6*$^{-/-}$: 727 µm ± 41,19 (n=23)
	D-V dimension (head) of *Lrp4*$^{-/-}$*;Lrp6*$^{-/-}$ embryos and controls at E10.5
	unpaired t-test: *** with p=0,0003
	mean ± SEM of controls: 1408 µm ± 67,95 (n=17)
	mean ± SEM of *Lrp4*$^{-/-}$*;Lrp6*$^{-/-}$: 799,2 µm ±111,8 (n=5)

Table 4.5: Statistical tests for data shown in Figure 4.10 graph c' + c"

Graph c':	A-P dimension (head) of *Lrp6*$^{-/-}$ embryos and controls at E9.5
	unpaired t-test: *** with p=0,0007;
	mean ± SEM of controls: 1200 µm ± 54,97 (n=28)
	mean ± SEM of *Lrp6*$^{-/-}$: 931,6 µm ± 43,98 (n=21)
	A-P dimension (head) of *Lrp4*$^{-/-}$*;Lrp6*$^{-/-}$ embryos and controls at E9.5
	unpaired t-test: *** with p=0,0003
	mean ± SEM of controls: 1200 µm ± 54,97 (n=28)
	mean ± SEM of *Lrp4*$^{-/-}$*;Lrp6*$^{-/-}$: 849,4 µm ± 40,07 (n=12)
Graph c":	A-P dimension (head) of *Lrp6*$^{-/-}$ embryos and controls at E10.5
	unpaired t-test: **** with p<0,0001
	mean ± SEM of controls: 2221 µm ± 87,13 (n=17)
	mean ± SEM of *Lrp6*$^{-/-}$: 1429 µm ± 78,88 (n=23)
	A-P dimension (head) of *Lrp4*$^{-/-}$*;Lrp6*$^{-/-}$ embryos and controls at E10.5
	unpaired t-test: **** with p=0,0001
	mean ± SEM of controls: 2221 µm ± 87,13 (n=17)
	mean ± SEM of *Lrp4*$^{-/-}$*;Lrp6*$^{-/-}$: 1257 µm ±177,4 (n=5)

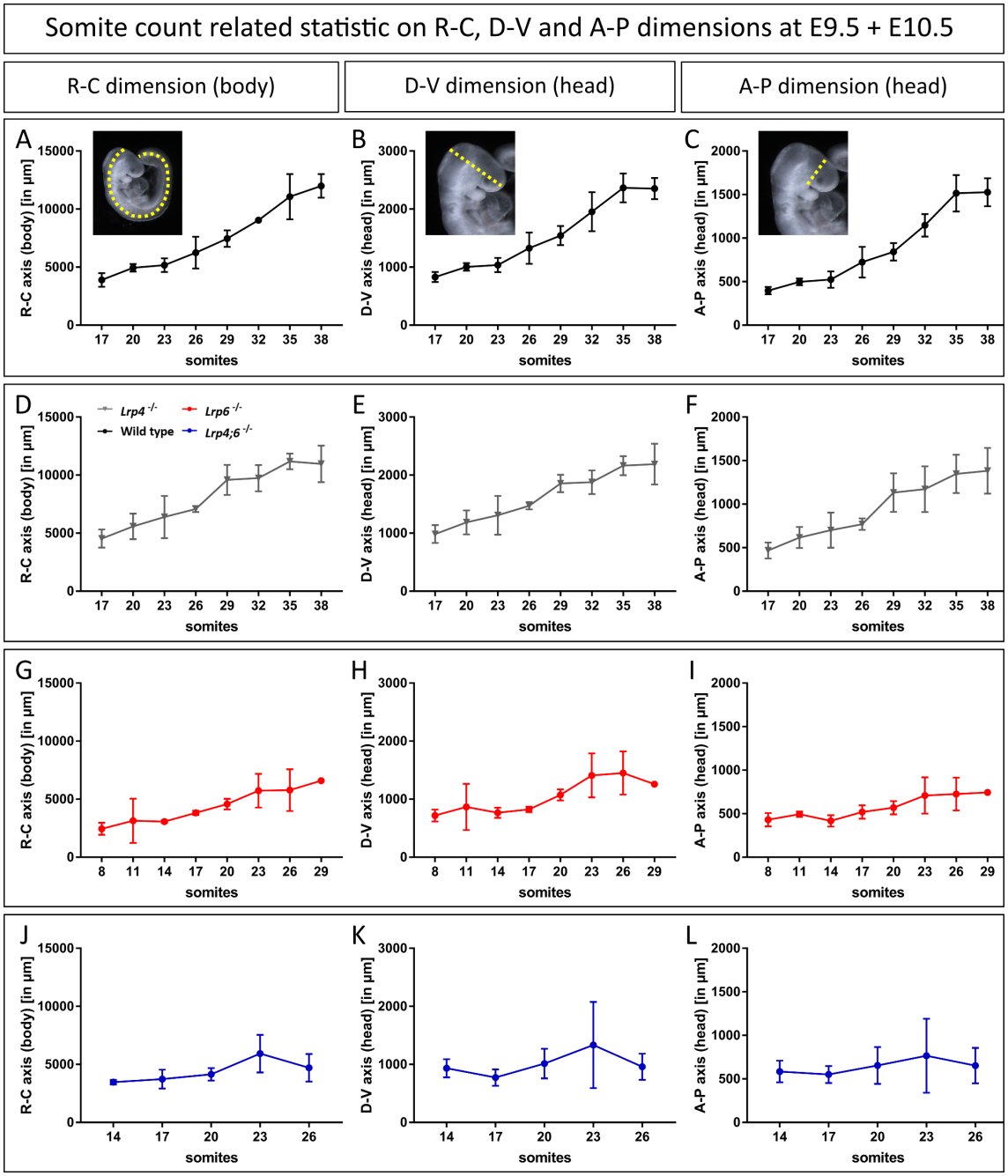

Figure 4.11: Somite related growth curves of *Lrp6*$^{-/-}$ and *Lrp4*$^{-/-}$;*Lrp6*$^{-/-}$ embryos reveal growth deficits at E9.5 and E10.5, whereas *Lrp4*$^{-/-}$ embryos show normal growth

Size measure data points (R-C, D-V and A-P dimension) of all embryos that were dissected at E9.5 and E10.5 are plotted in relation to their somite count. **(A-C)** *Wild type*: Black line (n=45). **(D-F)** *Lrp4*$^{-/-}$: Gray line (n=40). **(G-I)** *Lrp6*$^{-/-}$: Red line (n=44). **(J-L)** *Lrp4*$^{-/-}$;*Lrp6*$^{-/-}$: Blue line (n=22).

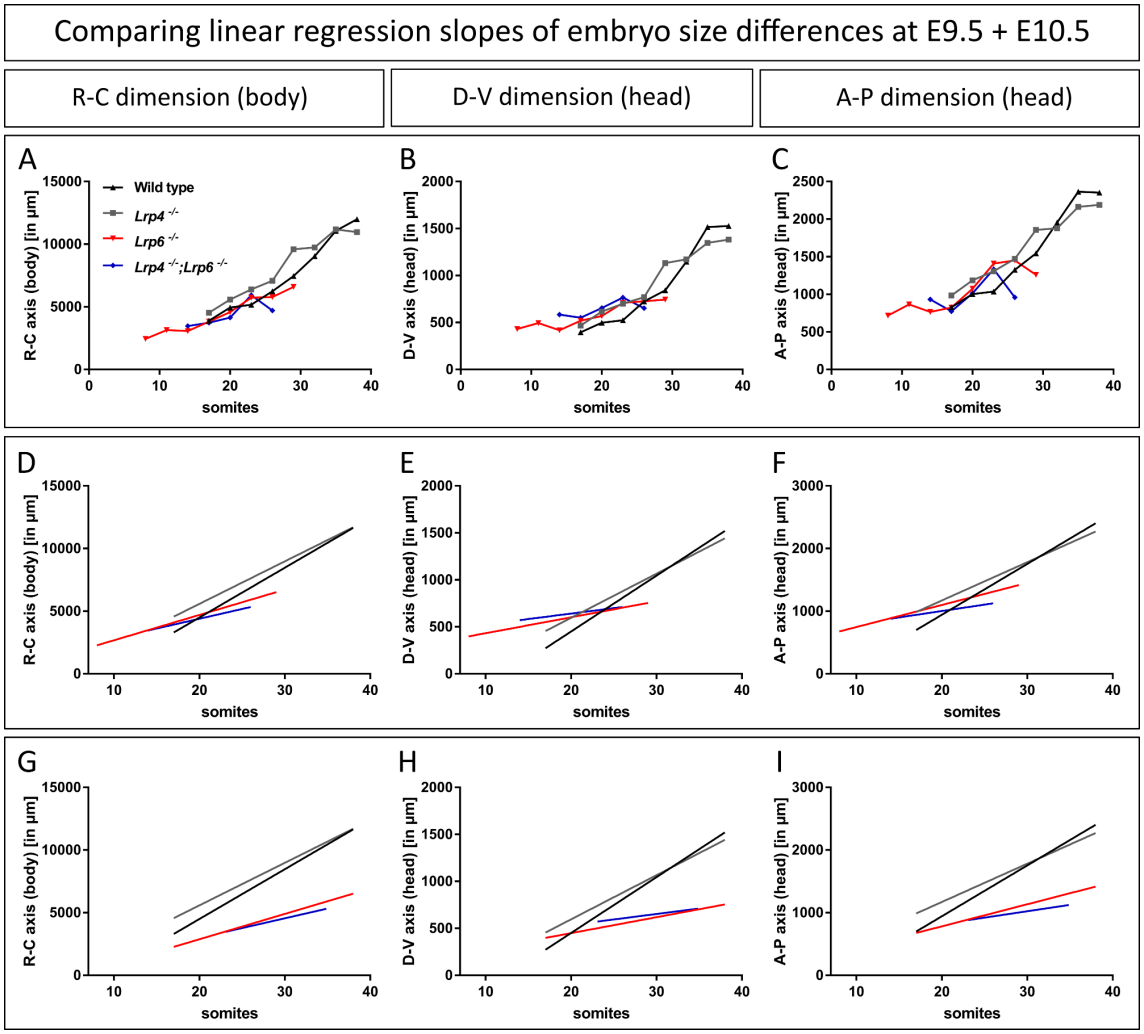

Figure 4.12: Comparing linear regression slopes of somite matched growth curves for embryos at E9.5 and E10.5

(A-C) Somite related growth curves for R-C, D-V and A-P dimension of all phenotypes combined (*Wild type*: Black line; *Lrp4*$^{-/-}$: Gray line; *Lrp6*$^{-/-}$: Red line; *Lrp4*$^{-/-}$*;Lrp6*$^{-/-}$: Blue line). **(D-E)** The linear regression curves of *Lrp6*$^{-/-}$ and *Lrp4*$^{-/-}$*;Lrp6*$^{-/-}$ are shifted to the right in relation to the curves of *wild type* and *Lrp4*$^{-/-}$ due to the caudal truncation phenotype (less somites). **(G-I)** When the curves of *Lrp6*$^{-/-}$ and *Lrp4*$^{-/-}$*;Lrp6*$^{-/-}$ are corrected (see Section_4.3.3) to match their littermate controls, it becomes obvious that the linear regression of *Lrp6*$^{-/-}$ and *Lrp4*$^{-/-}$*;Lrp6*$^{-/-}$ has a smaller slope compared to *wild type* and *Lrp4*$^{-/-}$.

Table 4.6: Linear regression values of curves shown in Figure 4.12

Linear regression slopes (best-fit values ± SE):		
R-C dimension (slope):	*Wild type*	397,5 µm (± 30,74)
	Lrp4$^{-/-}$	339,6 µm (± 29,94)
	Lrp6$^{-/-}$	202,3 µm (± 15,79)
	Lrp4$^{-/-}$*;Lrp6*$^{-/-}$	151 µm (± 77,47)
D-V dimension (slope):	*Wild type*	59,47 µm (± 6,179)
	Lrp4$^{-/-}$	46,99 µm (± 3,769)
	Lrp6$^{-/-}$	16,96 µm ± 2,637)
	Lrp4$^{-/-}$*;Lrp6*$^{-/-}$	11,66 µm (± 7,441)
A-P dimension (slope):	*Wild type*	81,18 µm (± 7,151)
	Lrp4$^{-/-}$	61,18 µm (± 4,099)
	Lrp6$^{-/-}$	35,26 µm (± 7,826)
	Lrp4$^{-/-}$*;Lrp6*$^{-/-}$	20,43 µm (± 22,07)

4.4 *Lrp4;Lrp6* compound mutants develop excrescences in the neuroepithelium

To refine the growth phenotype that was observed in *Lrp6*$^{-/-}$ embryos and *Lrp4*$^{-/-}$*;Lrp6*$^{-/-}$ compound mutant embryos at E9.5 and E10.5 (see Subsection 4.3.4), I examined embryos at these developmental stages in more detail. Since the heads of *Lrp6*$^{-/-}$ embryos and *Lrp4*$^{-/-}$*;Lrp6*$^{-/-}$ were much smaller compared to littermate controls, I further intended to analyze this growth deficit with respect to forebrain formation in *Lrp6*$^{-/-}$ and *Lrp4*$^{-/-}$*;Lrp6*$^{-/-}$ embryos. On that account, I conducted immunohistological experiments on coronal brain sections of E9.5 and E10.5 embryos that were generated by *Lrp4*;*Lrp*6 timed matings. I found that *Lrp4*$^{-/-}$*;Lrp6*$^{-/-}$ embryos develop excrescences within the neuroepithelium. I observed this phenotype exclusively in *Lrp4*$^{-/-}$*;Lrp6*$^{-/-}$ compound mutant embryos. Neither *Lrp4*$^{-/-}$ embryos nor *Lrp6*$^{-/-}$ embryos developed such neuroepithelial excrescences. In the following Sections, my finding are described in detail.

4.4.1 Neuroepithelial excrescences can be detected from E9.5 onwards

I defined the phenotype that was exclusively observed in *Lrp4*$^{-/-}$*;Lrp6*$^{-/-}$ compound mutant embryos as neuroepithelial excrescences, since there was a massive increase in thickness of the neuroepithelium along the apical-basal axis. The appearance of these excrescences was locally restricted and did not affect the entire neuroepithelium (Figure 4.13 B-D). Typically, the nature of the neuroepithelium in the early embryo is characterized by a pseudostratified

columnar epithelial shape (as described in Subsection 1.1.2). Thus, the extent of *wild type* neuroepithelium along the apical-basal axis is limited (to 100μm) to a certain extent - as shown for *wild type* embryos in 4.13 A (see also Subsection 1.1.2). However, more than 80% of the analyzed *Lrp4*$^{-/-}$*;Lrp6*$^{-/-}$ compound embryos at E9.5 (n=7) and at E10.5 (n=8) displayed excrescences in the neuroepithelium. The excrescences were first observed at E9.5. Although, *Lrp4*$^{-/-}$*;Lrp6*$^{-/-}$ embryos were analyzed at E8.5 (n=2) neuroepithelial excrescences could not detected (see expression of *Lrp4* in Subsection 4.1.1). A more detailed look at the cellular arrangement within the excrescences of *Lrp4*$^{-/-}$*;Lrp6*$^{-/-}$ embryos revealed that the organization as a pseudostratified columnar epithelium was disrupted (compare Figure 4.13 a'+a" with Figure 4.13 b'-d"). This seemed to be inevitable, since the extent of the excrescences along the apical-basal axis exceeded the normal thickness of single layered neuroepithelial cells. Further, it became obvious that within the neuroepithelial excrescences the number of cells (count of cell nuclei) was apparently highly increased (DAPI staining in Figure 4.13 a'-d').

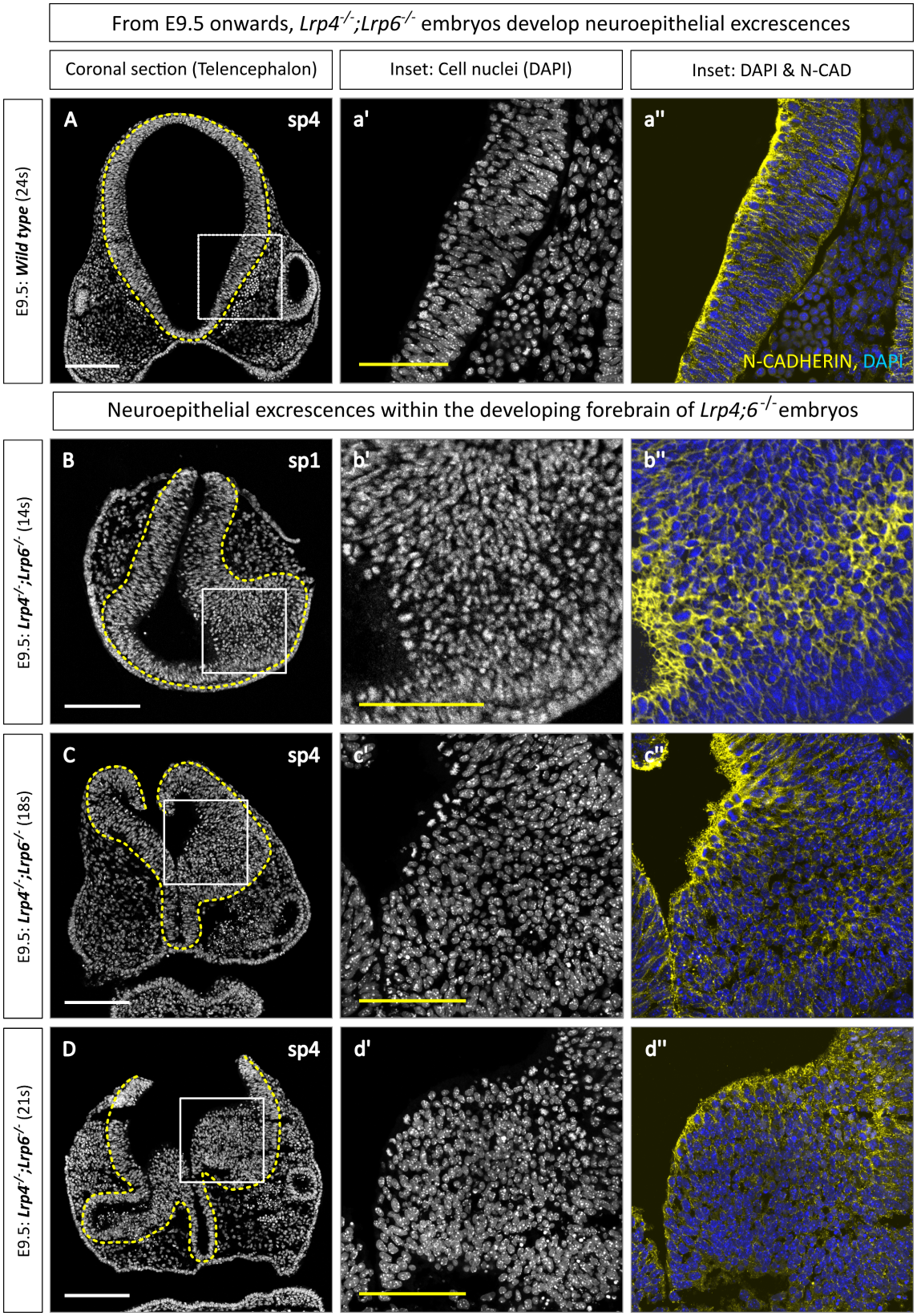

Figure 4.13: *Lrp4*$^{-/-}$;*Lrp6*$^{-/-}$ embryos develop neuroepithelial excrescences at E9.5

(A) Coronal section of a *wild type* at E9.5. **(a'+ a")** Insets (3x magnified) illustrate the cellular organization of the pseudostratified neuroepithelium. **(B+C)** Two examples of neuroepithelial excrescences in *Lrp4*$^{-/-}$*;Lrp6*$^{-/-}$ embryos at E9.5. **(b'- c")** Insets highlight the aberrant cellular organization within the excrescences. **(D)** *Lrp4*$^{-/-}$*;Lrp6*$^{-/-}$ embryo at E10.5, **(d'+ d")** show a magnified view of the neuroepithelial excrescence. White scalebar: 200 µm, yellow scalebar: 100 µm, yellow-dotted line indicates the basal boundary of the neuroepithelium.

4.4.2 The number of mitotic cells is increased in neuroepithelial excrescences

The apparent increase of cells within the neuroepithelial excrescences prompted me to analyze whether the proliferation of neuroepithelial cells was affected in *Lrp4;Lrp6* compound mutants. To corroborate the hypothesis that the observed excrescences display increased proliferation and potentially emerge due to local hyperproliferation, I intended to determine the number of mitotic cells on coronal brain sections of *Lrp4;Lrp6* compound mutants and littermate control embryos (Figure 4.14). I used immunostaining for the mitosis marker MPM-2 (marks all cell in M-Phase) to visualize and quantify mitotic cells within the neuroepithelium (see Subsection 3.5.1). In fact, I could detect a higher rate of mitotic cells in *Lrp4*$^{-/-}$*;Lrp6*$^{-/-}$ excrescences at E9.5 (Figure 4.14 G+g'+H and Figure 4.15). There was a significant increase of M-phase neuroepithelial cells in the excrescences compared to either regions of *Lrp4*$^{-/-}$*;Lrp6*$^{-/-}$ neuroepithelium that did not develop excrescences or to *wild type* littermate controls (Figure 4.15 D). The local increase in the neuroepithelial excrescences also lead to an overall increased count for M-phase cells in the neuroepithelium of *Lrp4*$^{-/-}$*;Lrp6*$^{-/-}$ compound mutant embryos (Figure 4.15 C). Interestingly, this was contrary to the observations made in *Lrp6*$^{-/-}$ embryos, which showed a markedly reduced number of mitotic cells in the neuroepithelium at E9.5 compared to the rate of M-phase cells in *wild type* embryos (Figure 4.15 E-F and Figure 4.15 C). The observed reduction of mitotic cells in the neuroepithelium of *Lrp6*$^{-/-}$ embryos at E9.5 was even greater than reported by others [60]. However, the rate of M-phase cells in *Lrp4*$^{-/-}$*;Lrp6*$^{-/-}$ neuroepithelium without incorporating the excrescences was not significantly different to *Lrp6*$^{-/-}$ embryos (Figure 4.15 E), indicating that the observed hyperproliferation of *Lrp4*$^{-/-}$*;Lrp6*$^{-/-}$ neuroepithelial cells just appeared locally. *Lrp4*$^{-/-}$ embryos showed no discrepancy to *wild type* regarding the count of mitotic cells within the neuroepithelium (Figure 4.15 C+D and Figure 4.15 C).

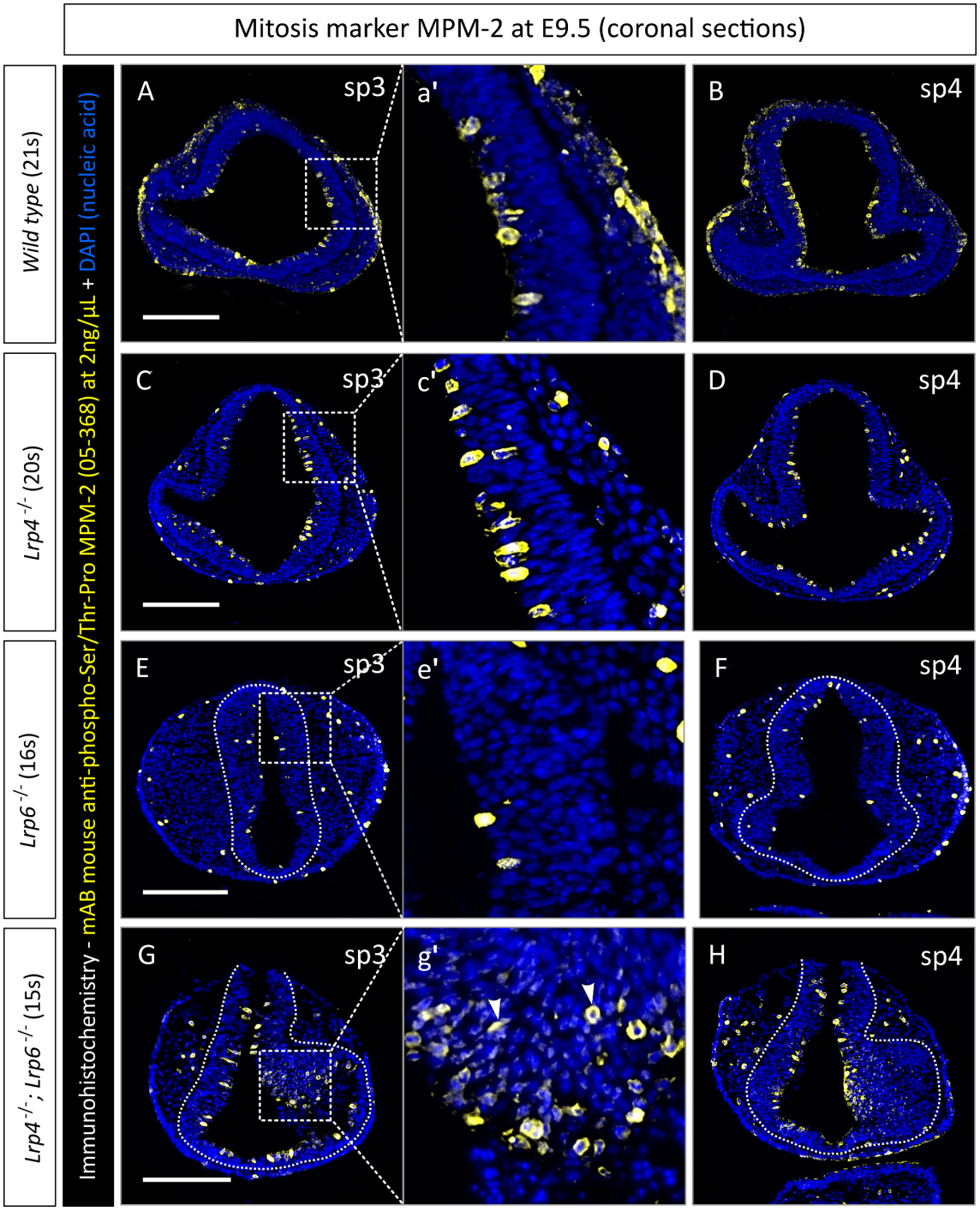

Figure 4.14: Neuroepithelial excrescences display an elevated rate of mitotic cells

(A-D) MPM-2 positive cell bodies are detected at the apical side of the neuroepithelium in the *wild type* and *Lrp4*$^{-/-}$ (n=4) embryos. **(E-F)** Less mitotic cells were observed in *Lrp4*$^{-/-}$ (n=7) at E9.5. **(G-H)** An increased count of MPM-2 positive cells could be visualized in neuroepithelial excrescences of E9.5 *Lrp4*$^{-/-}$*; Lrp6*$^{-/-}$ embryos (n=6). **(a'-g')** Insets are 4x magnified. Scalebars: 200 µm.

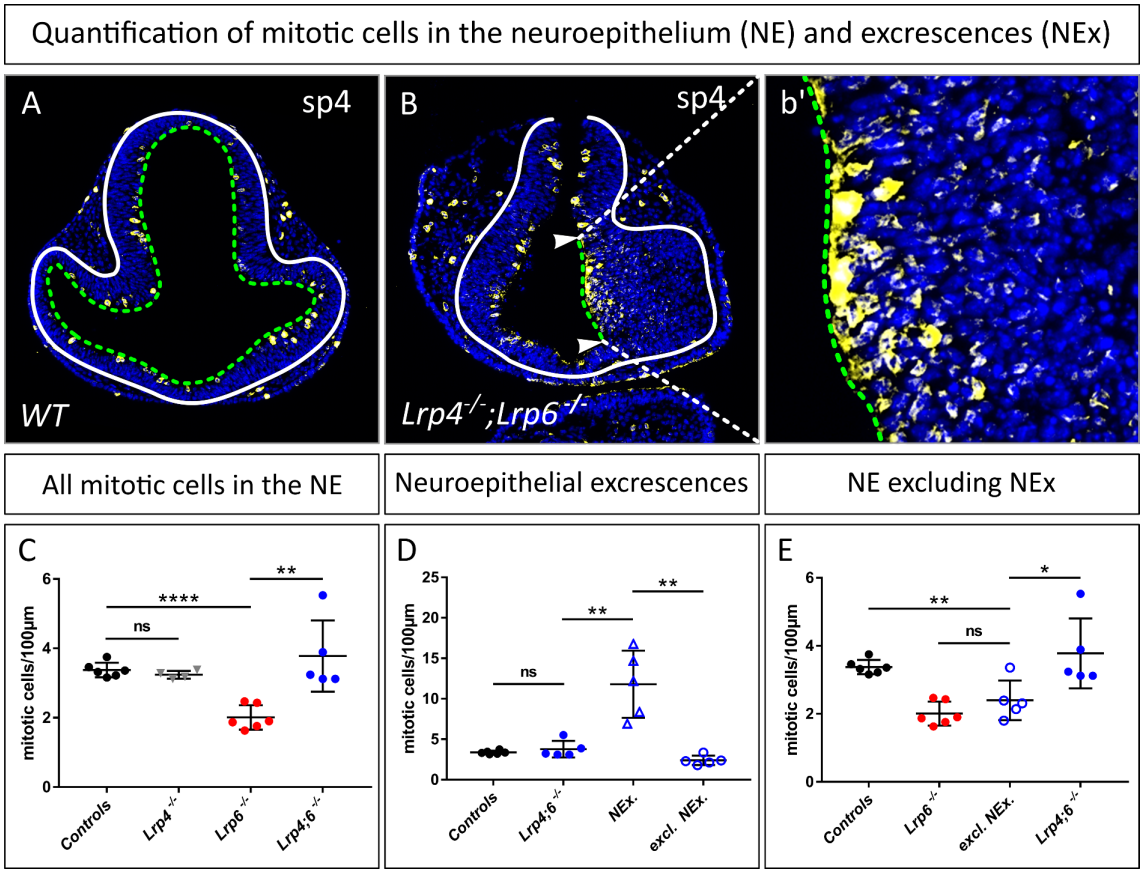

Figure 4.15: The rate of mitotic cells is increased within neuroepithelial excrescences

(A) The inner circumference of the neural tube (green-dotted line) was measured and set in relation to the count of mitotic cells (MPM-2 positive). **(B)** For *Lrp4*$^{-/-}$*;Lrp6*$^{-/-}$ embryos the neuroepithelial excrescences were also exclusively counted [indicated by green-dotted line within the white arrowheads – **(b')** magnified inset]. **(C)** Quantification of mitotic neuroepithelial cells in the forebrain of the different genotypes. **(D)** Comparison of mitotic rate within neuroepithelial excrescences of *Lrp4*$^{-/-}$*;Lrp6*$^{-/-}$ embryos. **(E)** MPM-2 positive cells in the neuroepithelium of *Lrp4*$^{-/-}$*;Lrp6*$^{-/-}$ embryos excluding the excrescences.

4.4.3 *Lrp6*$^{-/-}$ embryos and *Lrp4;Lrp6* compound mutants exhibit patches of apoptotic cells within the neuroepithelium

After observing that loss of LRP6 as well as loss of LRP4;6 had substantial impact on the proliferation of neural progenitors at E9.5, I decided to further investigate whether apoptosis was also affected in *Lrp6*$^{-/-}$ and *Lrp4*$^{-/-}$*;Lrp6*$^{-/-}$ embryos. To this end, I performed IHC experiments with an antibody against cleaved-Caspase-3, which plays a key role during the execution-phase of cell death (Figure 4.16). I found that *Lrp6*$^{-/-}$ embryos (n=4) and *Lrp4*$^{-/-}$*;Lrp6*$^{-/-}$ compound embryos (n=3) showed clusters of cells that stained positive for cleaved-Caspase-3. These ectopic sites of apoptosis appeared in a scattered fashion affecting neural as well as non-neuronal tissue (Figure 4.16 G-L). Besides natural loci of cell-death (like diencephalic

roof plate) *wild type* and *Lrp4*$^{-/-}$ embryos did not display other apoptotic clusters (Figure 4.16 A-F). To substantiate that the observed cleaved-Caspase-3 immunostaining was highlighting apoptotic cells rather than showing unspecific staining, I performed a TUNEL assay to detect apoptotic cells that undergo extensive DNA degradation. The performed TUNEL assay supported my findings and visualized apoptotic clusters in *Lrp6*$^{-/-}$ embryos (n=2) and *Lrp4*$^{-/-}$;*Lrp6*$^{-/-}$ compound mutants (n=2) to the same extent as seen by cleaved-Caspase-3 immunostaining.

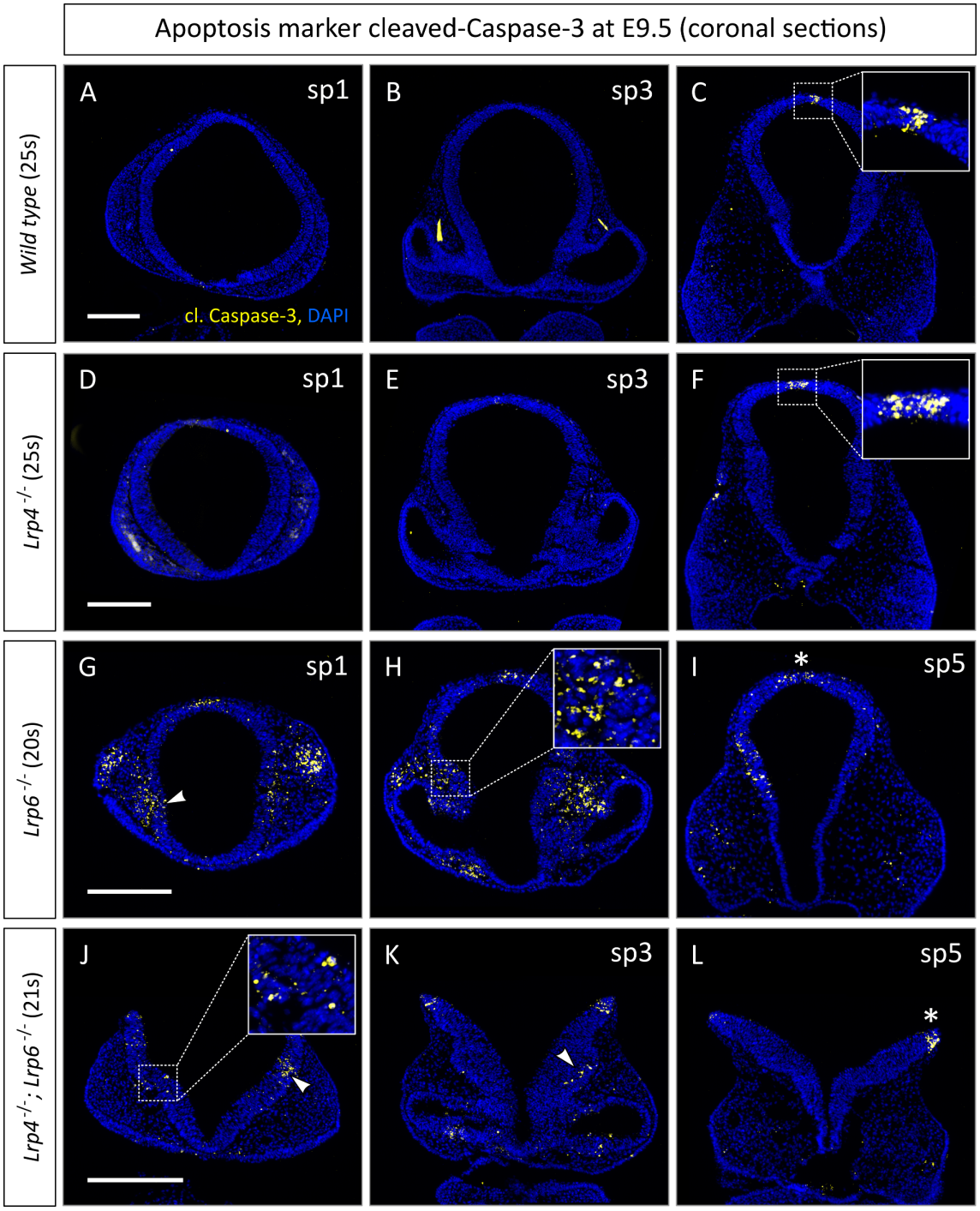

Figure 4.16: Immunohistological staining with cleaved-Caspase-3 highlights clusters of apoptotic cells in *Lrp6*$^{-/-}$ and *Lrp4*$^{-/-}$;*Lrp6*$^{-/-}$ embryos

(A-E) Apoptosis marker cleaved-Caspase-3 is not detectable on coronal forebrain sections of *Lrp4*$^{-/-}$ (n=3) and *wild type* embryos. **(C-F)** However, the genuine apoptosis site within the roof plate of the diencephalon contains apoptotic cells. **(G-L)** *Lrp6*$^{-/-}$ embryos (n=4) and *Lrp4*$^{-/-}$;*Lrp6*$^{-/-}$ embryos (n=3) display scattered sites of apoptosis (white arrowheads) including neural tissue. Asterisk indicates the natural apoptosis site in the roof plate (I+L). Scalebars: 200 µm.

4.4.4 Excrescences within the neuroepithelium were accompanied by structural abnormalities

As already mentioned the cellular organization of the neuroepithelium in *Lrp4;Lrp6* compound mutant embryos was affected because of the emerging neuroepithelial excrescences (Subsection 4.4.1). Since structural impairments are also reported for loss-of-function mutations of *Lrp6* [60, 146], I wanted to compare structural aberrations of *Lrp6*$^{-/-}$ embryos with the abnormal cellular organization observed in *Lrp4*$^{-/-}$*;Lrp6*$^{-/-}$ neuroepithelial excrescences. Therefore, I performed immunohistological experiments to highlight the structural order of neuroepithelial cells (Figure 4.17 and 4.18). First, I conducted IHC for β-catenin, which is also an important structural component of cadherin-based intermediate junctions [183]. I found that in *Lrp6*$^{-/-}$ embryos the shape of the neural tube sometimes appeared less defined compared to *wild type* littermate control embryos. Especially, on the apical side of the neuroepithelium cellular alignment appeared disorganized (Figure 4.17 F+f'). These disruptions in cellular organization of *Lrp6* single mutant embryos might result from deficits in cell-cell contact maintenance due to impaired non-canonical WNT signaling, as suggested by Gray and others [60]. Additional to disruptions in cellular organization observed in *Lrp6*$^{-/-}$ embryos, *Lrp4;Lrp6* compound mutant embryos displayed structural abnormalities in the neuroepithelium likely to be caused by locally increased proliferation (Figure 4.17 E-H). The locally restricted thickening of the neuroepithelium lead to abnormal protrusions and ectopic invaginations that were exclusively found in *Lrp4*$^{-/-}$*;Lrp6*$^{-/-}$ embryos (Figure 4.17 H+h'). I further performed immunostainings for the mesenchymal marker Vimentin, which is also expressed by radial glia cells [8]. By this, I was able to highlight the onset of gliogenesis, which was observed in the dorsal forebrain of *wild type* and *Lrp4*$^{-/-}$ embryos at E9.5 (depicted in Figure 4.18). By visualizing mesenchymal cells, I could determine the exact boundary between the neuroepithelium and the mesenchyme (indicated by red line in Figure 4.18 a'-d') to examine whether the cellular alignment of cells was disrupted similiar to the observation on the apical side of the neuroepithelium in *Lrp6*$^{-/-}$ embryos, *Lrp4*$^{-/-}$*;Lrp6*$^{-/-}$ compound mutant embryos as described above. However, it appears that cellular organization on the basal side of the neuroepithelium was not affected in *Lrp6*$^{-/-}$ and *Lrp4*$^{-/-}$*;Lrp6*$^{-/-}$ embryos since the basal boundary was clearly defined (Figure 4.18 C-d'). Interestingly, I detected Vimentin-positive cells in excrescences of *Lrp4*$^{-/-}$*;Lrp6*$^{-/-}$ embryos, which might indicate the onset of gliogenesis within the neuroepithelial protrusion (Figure 4.18 D+d'). *Lrp4*$^{-/-}$ embryos showed no structural discrepancies of the neuroepithelial organization compared to *wild type* littermate embryos (Figure 4.18 A-D and Figure 4.18 A+B).

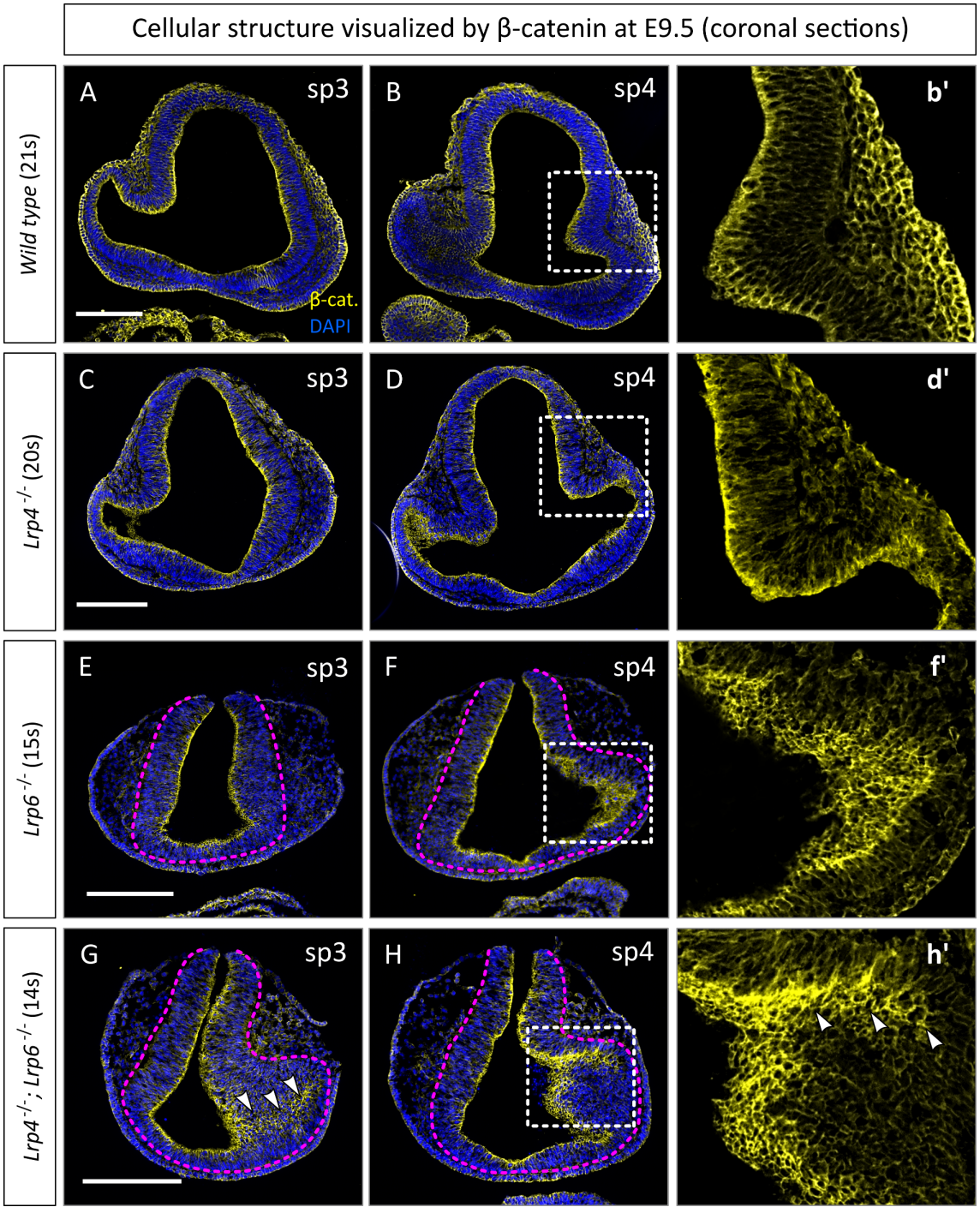

Figure 4.17: β-catenin staining reveals structural aberrations of *Lrp6*$^{-/-}$ and *Lrp4*$^{-/-}$;*Lrp6*$^{-/-}$ neuroepithelium

(A+B) IHC for β-catenin on E9.5 coronal forebrain sections depict neuroepithelial structure by illustrating cell-cell contacts. **(C+D)** *Lrp4*$^{-/-}$ embryos (n=3) do not display a diverging β-catenin staining compared to *wild type* embryos. **(E+F)** In *Lrp6*$^{-/-}$ embryos (n=5) β-catenin staining reveals structural disturbances within the neuroepithelium. **(G+H)** *Lrp4*$^{-/-}$;*Lrp6*$^{-/-}$ embryos (n=5) display a markedly altered neuroepithelial organization highlighted by β-catenin staining. White arrowheads indicate an ectopic invagination within the excrescence. **(b'-h')** Insets are 3x magnified and show only the β-catenin staining. Pink-dotted line indicate the basal neuroepithelial boundary. Scalebars: 200 µm.

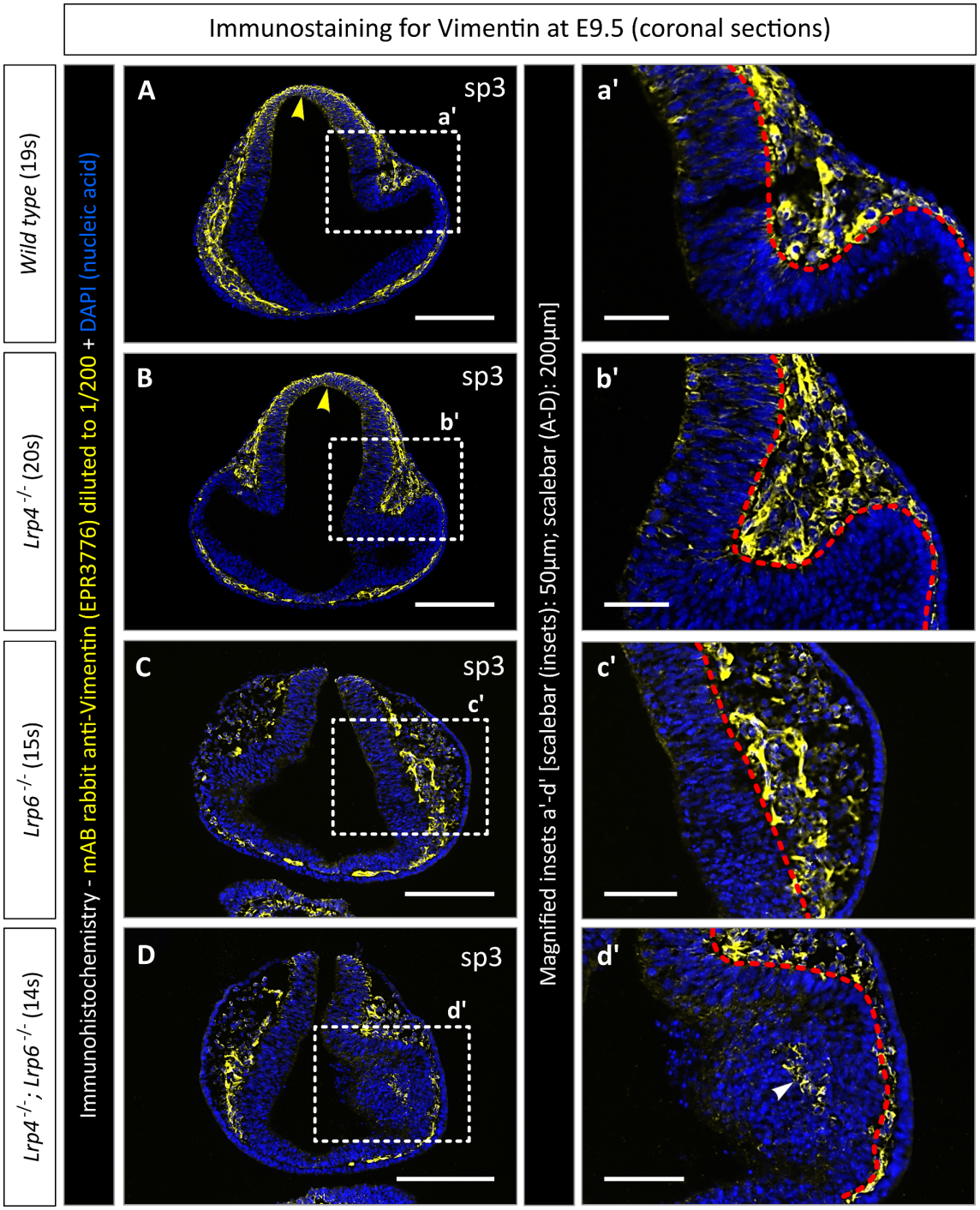

Figure 4.18: Vimentin can be detected in neuroepithelial excrescences of *Lrp4*$^{-/-}$;*Lrp6*$^{-/-}$ embryos

(A) At E9.5, Vimentin predominantly marks mesenchymal cells and begins to appear in radial glia cells in the dorsal neural tube (indicated by yellow arrowhead). **(B)** Vimentin pattern of *Lrp4*$^{-/-}$ (n=2) embryos is same as in *wild type*. **(C)** *Lrp6*$^{-/-}$ embryos (n=3) show positive Vimentin staining in mesenchymal cells. **(D)** Vimentin positive cells were also detected within neuroepithelial excrescence (white arrowhead) of *Lrp4*$^{-/-}$;*Lrp6*$^{-/-}$ embryos (n=2). Red-dotted line indicates the basal neuroepithelial boundary. **(a'-d')** Insets show 3x magnified section. Scalebars (A-D): 200 µm. Scalebars (a'-d'): 50 µm.

4.4.5 Columnar organization of the pseudostratified neuroepithelium is dispersed within *Lrp4$^{-/-}$;Lrp6$^{-/-}$* excrescences

To further study the structual changes that appear within the neuroepithelial excrescences of *Lrp4;Lrp6* compound mutant embryos, I performed immunostainings to detect the cell identity as well as cell orientation. In the early embryo the neuroepithelium is characterized by its well-defined organization as a pseudostratified columnar epithelial layer (see Subsection 1.1.2). As already stated in Subsection 1.1.2 this limits the thickness of the single-layered neuroepithelium to the span a neuronal progenitor cell, which is approximately 100 μm [126]. Since the neuroepithelial excrescences of *Lrp4;Lrp6* compound mutant embryos lead to a locally increased thickness of the neuroepithelium along the apical-basal axis, it is likely that the pseudostratified columnar epithelial organization can no longer be maintained. Thus, I intended to analyze the cellular composition of *Lrp4$^{-/-}$;Lrp6$^{-/-}$* neuroepithelial excrescences and further wanted to determine the alignment of the cells within the hyperproliferating structures. First, I performed immunostainings for the apical markers ZO-1 and ARL13b to examine whether the orientation of the neural progenitors is altered within *Lrp4$^{-/-}$;Lrp6$^{-/-}$* excrescences (Figure 4.19). ZO-1 (Zonula occludens-1) is a tight junction-associated protein and expressed at the apical side of neural progenitors. ARL13b (ADP-ribosylation factor-like protein 13B) is expressed in the primary cilium, which is also localized on the apical surface of cells in the neuroepithelium. By IHC for detecting these apically expressed proteins, I could show that the neuroepithelium of *Lrp4$^{-/-}$;Lrp6$^{-/-}$* exhibits a regular structural organization in regions that do not develop neuroepithelial excrescences (Figure 4.19 a'-c'). However, in those regions of the neuroepithelium where excrescences emerge show a disarranged cellular structure. The pseudostratified columnar epithelial layer that is highly polarized along the apical-basal axis is no longer discernible. Instead apical markers ARL13b and ZO-1 could be detected within the strucutre of the neuroepithelial excrescence, indicating that the cells are no longer orientend along the apical-basal axis but face in different directions (Figure 4.19 a"-c"). Thus, it became evident that the strucutre of the pseudostratified neuroepithelium is disrupted and cells loose their orientation within neuroepithelial excrescences of *Lrp4$^{-/-}$;Lrp6$^{-/-}$* embryos.

Since I could observe potentially gliogenic Vimentin-positive cells within a neuroepithelial excrescence of one *Lrp4$^{-/-}$;Lrp6$^{-/-}$* embryo at E9.5 (Figure 4.18), I wanted to analyse whether accumulating cells within excrescences retain their progenitor fate or prematurely differentiate. To assess the cellular composition of the excrescences, I conducted immunohistological

analysis with the neural stem cell marker SOX2 (or SRY: Sex determining region Y-box 2) to mark neural progenitor cells. Further, I used IHC to visualize neurogenic cells that stained positive for TUJ-1 (Neuron-specific class III β-tubulin). I found that at E9.5 all cells within *Lrp4*$^{-/-}$;*Lrp6*$^{-/-}$ excrescences (n=4) were positive for SOX2 (Figure 4.20 A+B). IHC at E10.5 revealed that TUJ-1 positive cells are detectable in neuroepithelial excrescences. However, they do not localize to the basal margin of the neuroepithelium and get stuck in the excrescence (Figure 4.20 C-c").

To sum up, I could reveal that the pseudostratified epithelial structure is disrupted in *Lrp4*$^{-/-}$;*Lrp6*$^{-/-}$ embryos and cells within the neuroepithelial excrescences loose their orientation along the apical-basal axis. Further, I could show that at E9.5 cells within neuroepithelial excrescences retain their fate as neural progenitor cells (expressing SOX2) and do not prematurely differentiate (see Section_INT_NE). This implies that during increased proliferation in the excrescences cells undergo symmetric cell division. However, at E10.5 asymmetric cell divison events can be detected (TUJ-1 positive neurogenic cells), whereas the differentiated cells irregularly migrate.

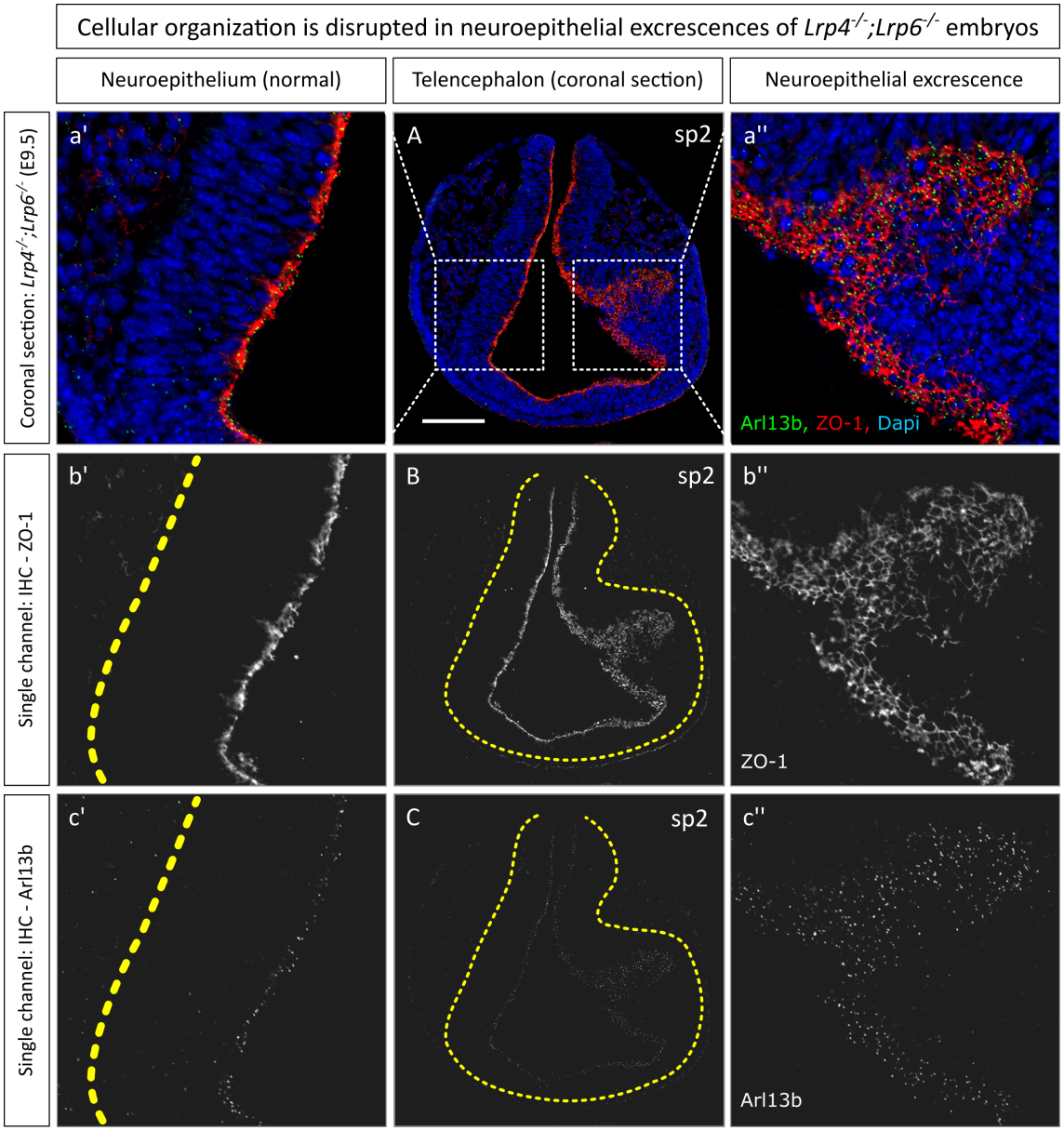

Figure 4.19: Pseudostratified neuroepithelial organization is lost in *Lrp4*$^{-/-}$;*Lrp6*$^{-/-}$ excrescences

(A) IHC with apical markers ZO-1 and Arl13b on coronal section of an E9.5 *Lrp4*$^{-/-}$;*Lrp6*$^{-/-}$ embryo **(a')** Left inset (3x magnified): Normal neuroepithelial structure **(a")** Right inset (3x magnified): Neuroepithelial excrescence. **(B)** Single channel micrograph for ZO-1 staining. **(C)** Single channel micrograph for Arl13b staining (b',b" and c',c" analogous to a',a"). Yellow-dotted line representing the basal boundary of the neuroepithelium. Scalebar: 100 µm.

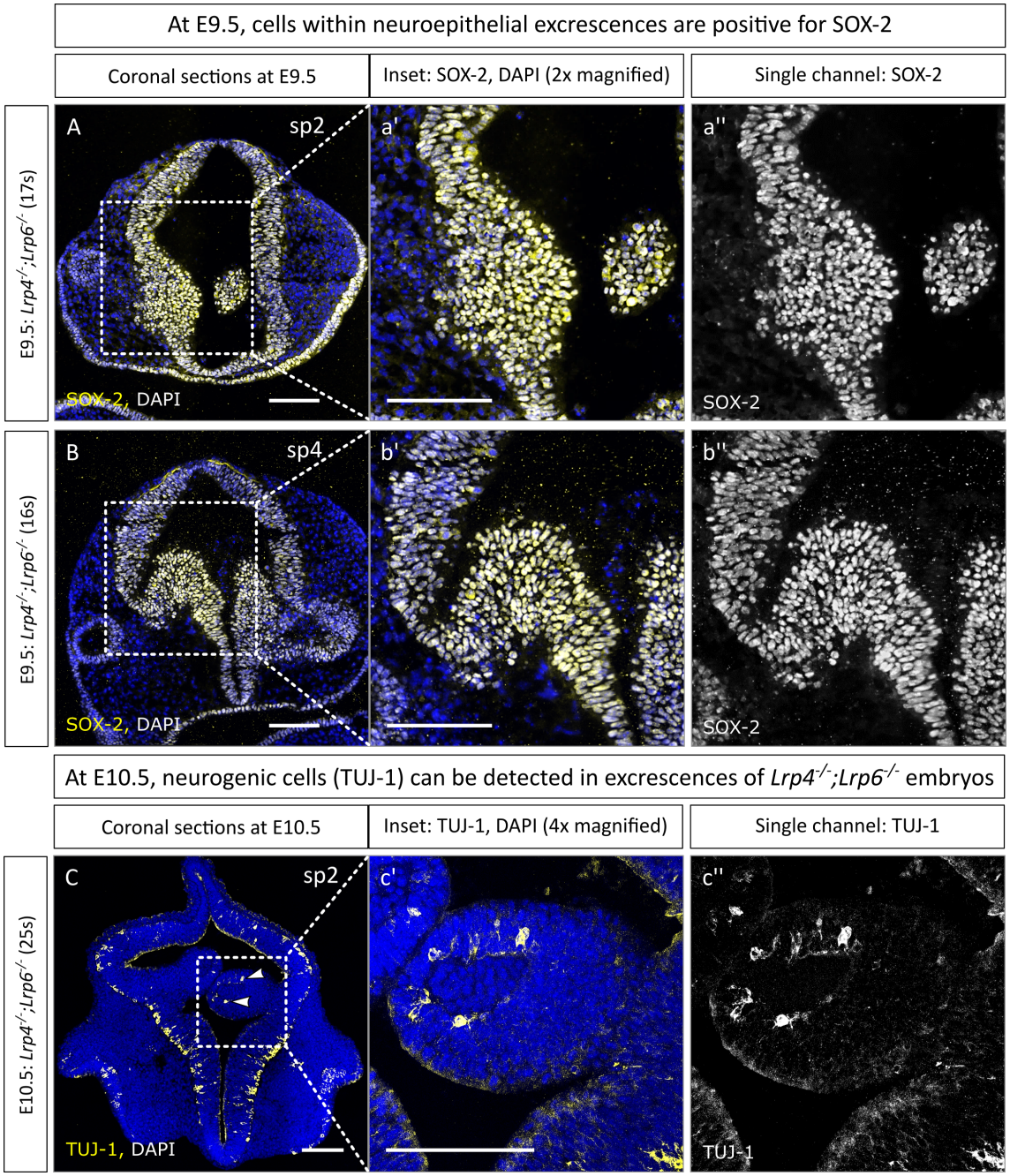

Figure 4.20: At E9.5, cells within neuroepithelial excrescences retain their progenitor character

(A+B) Coronal sections of *Lrp4*$^{-/-}$*;Lrp6*$^{-/-}$ embryos at E9.5 show immunostaining for neural stem cell marker SOX-2. **(a'- b")** Insets display (2x) magnified view of SOX-2 staining of neuroepithelial excrescences. **(C)** Immunostaining for neuronal lineage marker TUJ-1 illustrates neurogenic cells in excrescences of *Lrp4*$^{-/-}$*;Lrp6*$^{-/-}$ embryos at E10.5. **(c'+c")** Insets display a magnified view of the neuroepithelial excrescences at E10.5. Scalebar: 100 µm.

4.5 WNT signaling pathway is affected in the developing forebrain of *Lrp6* single mutants and *Lrp4;Lrp6* compound mutant embryos

Since LRP5/6 are co-receptors of Frizzled (FZD) and thus essential components of the WNT signal transduction cascade (Subsection 1.3.3), it was crucial importance to examine WNT factor expression and WNT target gene expression in the different *Lrp* mouse models that I used for my study. Further, I wanted to shed light on the role of LRP4 in WNT-related forebrain development and analyze potential gene interaction of *Lrp4* and *Lrp6*. Besides WNT signaling, forebrain development implies proper orchestration of various signaling pathways. Therfore, I also investigated expression of BMP and SHH signaling components in the prospective telencephalon of these embryos. However, I was limited on *Lrp4*$^{-/-}$*;Lrp6*$^{-/-}$ specimens and decided to concentrate on *Lrp4* and *Lrp6* single mutant embryos for the analyisis of BMP and SHH pathway components. Therefore, *Lrp4;Lrp6* compound mutants are not included in the ISH analysis of BMP, SHH components as well as for the detection of the WNT signaling center in the roof plate. Nonetheless, *Lrp4;Lrp6* compound mutant embryos were included in the ISH analysis of WNT downstream targets. I intended to reveal potential changes in WNT signal transduction that might contribute to the observed phenotype of emerging neuroepithelial excrescences in *Lrp4*$^{-/-}$*;Lrp6*$^{-/-}$ compound mutant embryos as WNT signaling has been tightly linked to proliferation activity [10, 35, 103]. To this end, I used *in situ* hybridization technique to detect the mRNA expression profiles of the mentioned signaling pathway components.

4.5.1 BMP4 signaling pathway is not affected in telencephalon of E10.5 *Lrp4*$^{-/-}$ embryos

Although BMP signaling was not primarily in the focus of my study, it was relevant to a certain extent to examine BMP signaling pathway components in the developing forebrain of *Lrp4*$^{-/-}$ embryos. It was previously shown that LRP4 can interact with proteins such as WISE that are involved in BMP4 signaling [138]. Moreover, it was reported that BMP4 acts as a telencephalic morphogen in the dorsal neural tube (Subsection 1.1.1). Therefore, I preformed ISH for *Bmp4* and its downstream target *Id3* to assess whether these expression patterns were altered in the forebrain of *Lrp4*$^{-/-}$ embryos. I could show that the *Bmp4* expressing domain in the roof plate of prospective telencephalon was not changed in *Lrp4*$^{-/-}$ embryos (n=3) compared to *wild type* littermate embryos at E10.5 (Figure 4.21 A-D). Expression of the BMP target gene *Id3* was detected in the dorsolateral domain adjacent to the BMP4 source. At E10.5, *Id3* expression in the prospective forebrain of *Lrp4*$^{-/-}$ embryos (n=4) was identical to the *Id3* transcript profile of *wild type* embryos (Figure 4.21 E-H). I could show that of loss LRP4 does neither lead to

abnormal expression of *Bmp4* nor BMP downstream target *Id3* in the developing forebrain.

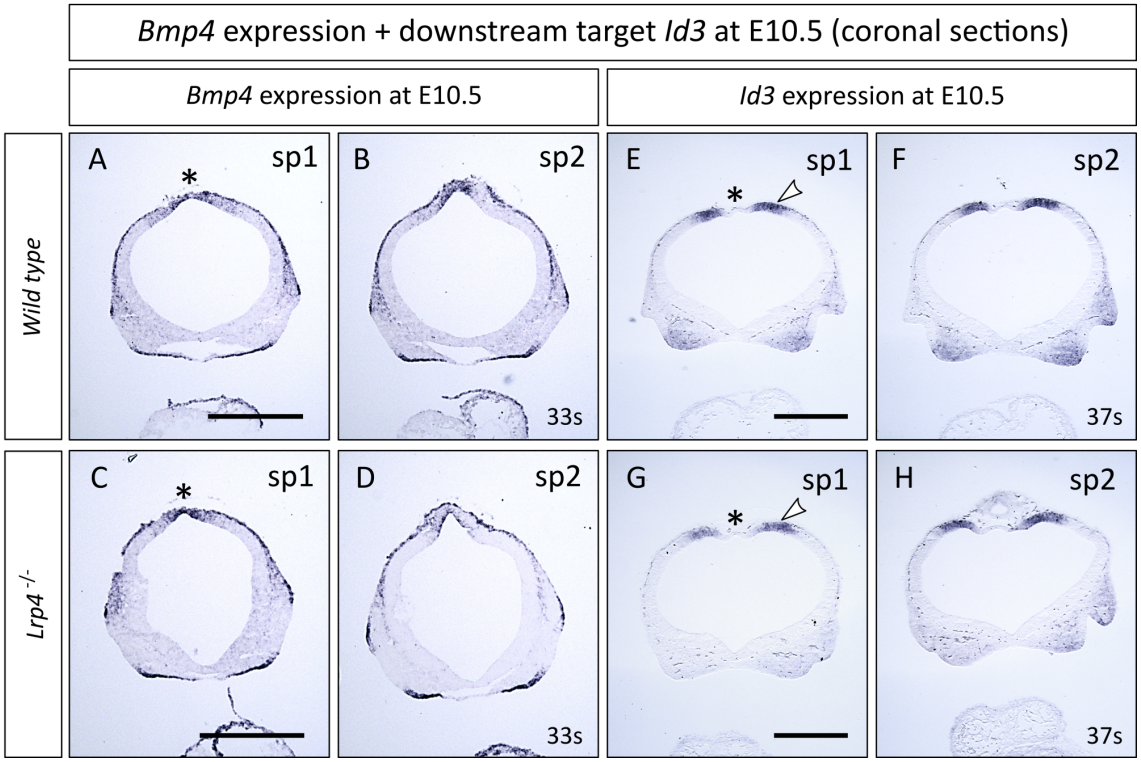

Figure 4.21: Expression of *Bmp4* and downstream target *Id3* is not altered in the prospective telencephalon of LRP4 deficient embryos

(A-D) *Bmp4* expression is restricted to the dorsal midline (indicated by black asterisk) of the developing forebrain. *Bmp4* expression profile in *Lrp4*$^{-/-}$ embryos (n=3) showed no difference to *wild type* embryos. **(E-H)** *Id3* - a direct target gene of BMP signaling - is expressed laterally (white arrowhead) to the BMP source in the roof plate (asterisk). Telencephalic *Id3* expression domain of LRP4 deficient embryos (n=4) is not changed compared to *wild type*. Scalebar: 500 µm.

4.5.2 SHH source in the floor plate and expression of downstream *Nkx2.1* is unchanged in *Lrp4*$^{-/-}$ and *Lrp6*$^{-/-}$ embryos

Another important pathway in terms of forebrain induction and patterning is the SHH pathway. *Shh* is a ventrally expressed morphogen that antagonizes dorsal morphogen signals like BMP or WNT [72, 147, 198]. Keeping the balance of these dorsal and ventral morphogen signals is important for cell fate decision of neural progenitor cells within the neural tube and therefore crucial for proper forebrain development [151, 198, 202]. Cells within the floor plate at the ventral midline of the developing telencephalon are the main source of SHH. High levels of SHH induce expression its downstream target *Nkx2.1*, which serves as a robust readout for SHH signal transduction [72, 147, 198]. To examine whether SHH signaling during development of the forebrain was altered by loss-of-function mutations for *Lrp4* or *Lrp6*, I conducted ISH experiments to determine mRNA expression profiles of *Shh* and *Nkx2.1*, respectively (Figure 4.22). I could show that the SHH source in the ventral midline is still intact in *Lrp4*$^{-/-}$ (n=3) and *Lrp6*$^{-/-}$ embryos (n=4) (Figure 4.22 A-F). However, I found that some LRP6 deficient embryos (2 out of 4) displayed a markedly reduced *Shh* expressing domain the *Zona limitans intrathalamica* (ZLI) (Figure 4.22 A-F). Nonetheless, the expression domain of *Nkx2.1* adjacent to the *Shh* expressing floor plate was present in both *Lrp4*$^{-/-}$ (n=3) and *Lrp6*$^{-/-}$ embryos (n=3) (Figure 4.22 G-L). Thus, I could show that the ventral *Shh* expressing domain in the floor plate was unaffected by loss of LRP4 or LRP6 and expression of downstream target *Nkx2.1* was unchanged. However, it remains to be elucidated why in some *Lrp6*$^{-/-}$ embryos the *Shh* expressing domain in the ZLI was reduced.

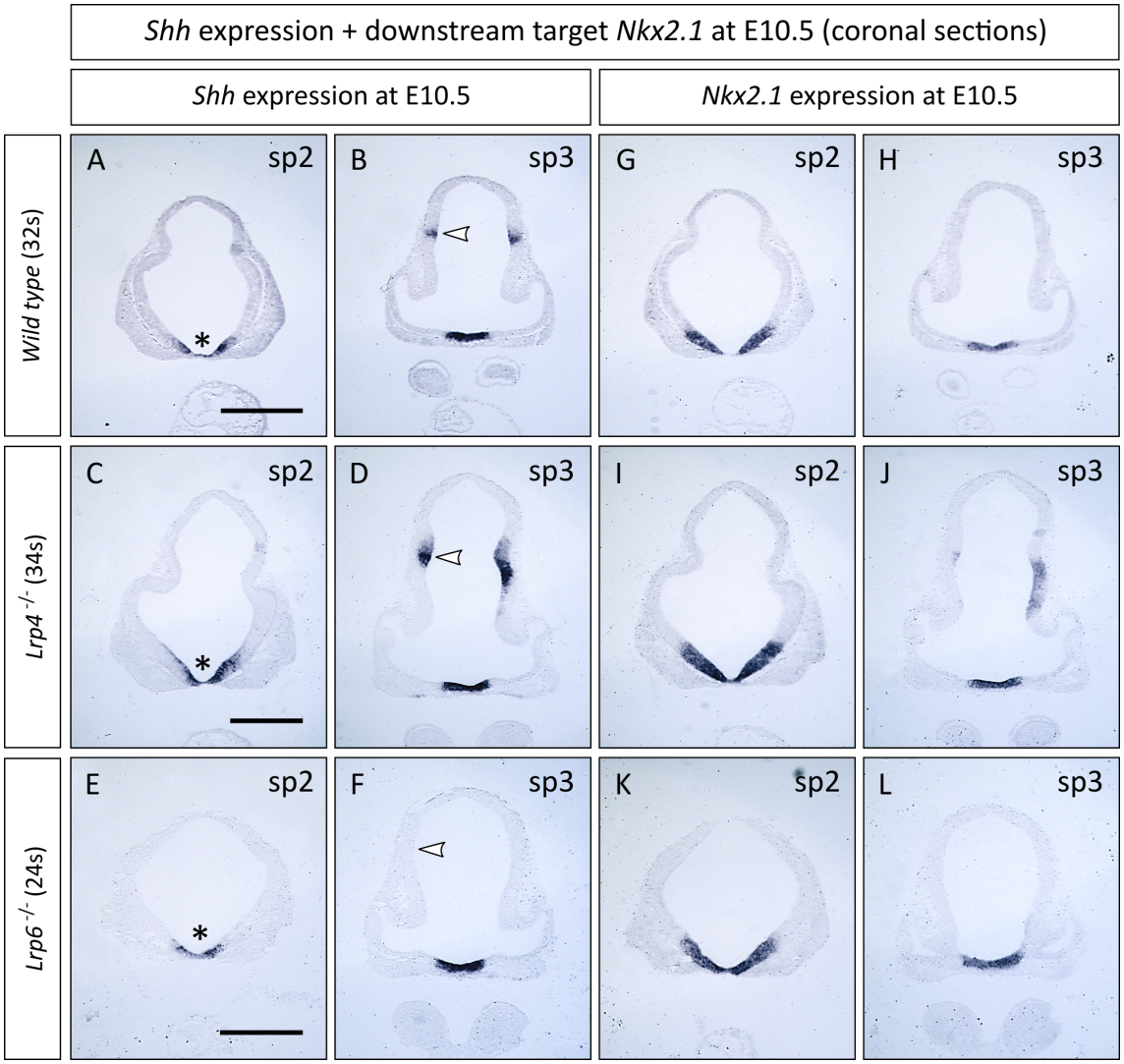

Figure 4.22: *Shh* expression in the floor plate and downstream target *Nkx2.1* are not altered in *Lrp4*$^{-/-}$ and *Lrp6*$^{-/-}$ embryos

(A-F) At E10.5, *Shh* is robustly expressed in the ventral midline of the developing forebrain. *Lrp4*$^{-/-}$ (n=3) and *Lrp6*$^{-/-}$ (n=4) embryos showed no alterations of *Shh* expression in floor plate cells. However, 2 out of 4 analyzed *Lrp6*$^{-/-}$ embryos at E10.5 showed a reduced expression of *Shh* in the ZLI (indicated by white arrowhead). **(G-L)** Expression of downstream target *Nkx2.1* is in the ventral lateral domain of the prospective telencephalon. Neither *Lrp4*$^{-/-}$ (n=3) nor *Lrp6*$^{-/-}$ (n=3) embryos showed aberrated *Nkx2.1* expression. Scalebar: 500 µm.

4.5.3 *Wnt1* and *Wnt3a* expressing domains are still present in embryos deficient for LRP6

Since LRP6 is a co-receptor of FZD and an essential component of the WNT signal transduction machinery (see Subsection 1.3.2), it was of great interest to test whether WNT signaling centers in the developing forebrain are also affected by loss of LRP6. On that account, I performed ISH experiments to examine whether expression of *Wnt1* and *Wnt3a* was still comparable to *wild types* in *Lrp6*$^{-/-}$ mutant embryos (Figure 4.23). At E9.5, *Wnt1* was strongly expressed by neural stem cells in the roof plate of the prospective forebrain of *wild types* (Figure 4.23 A+B). My results show that *Lrp4*$^{-/-}$ (n=3) and *Lrp6*$^{-/-}$ embryos (n=3) also express *Wnt1* in the dorsal midline (Figure 4.23 C-E). On the other hand, the *Wnt3a* expression domain is present in the dorsal midline and extends to dorsolateral regions of the neural tube (Figure 4.23 G+H). Like *wild type* embryos, all *Lrp4*$^{-/-}$ (n=3) and *Lrp6*$^{-/-}$ mutant embryos (n=3) that I observed displayed the dorsal *Wnt3a* expression profile in the roof plate (Figure 4.23 I-L). However, one out of three *Lrp6*$^{-/-}$ embryos displayed a narrowed *Wnt3a* expressing domain (Figure 4.23 K+L). In conclusion, I could show that the WNT signaling center in the roof plate of *Lrp4*$^{-/-}$ and *Lrp6*$^{-/-}$ embryos was present. This was the basis for testing WNT signal transduction in *Lrp6*$^{-/-}$ and *Lrp4*$^{-/-}$;*Lrp6*$^{-/-}$ embryos by examining expression of WNT downstream targets, which is described in the following Subsection.

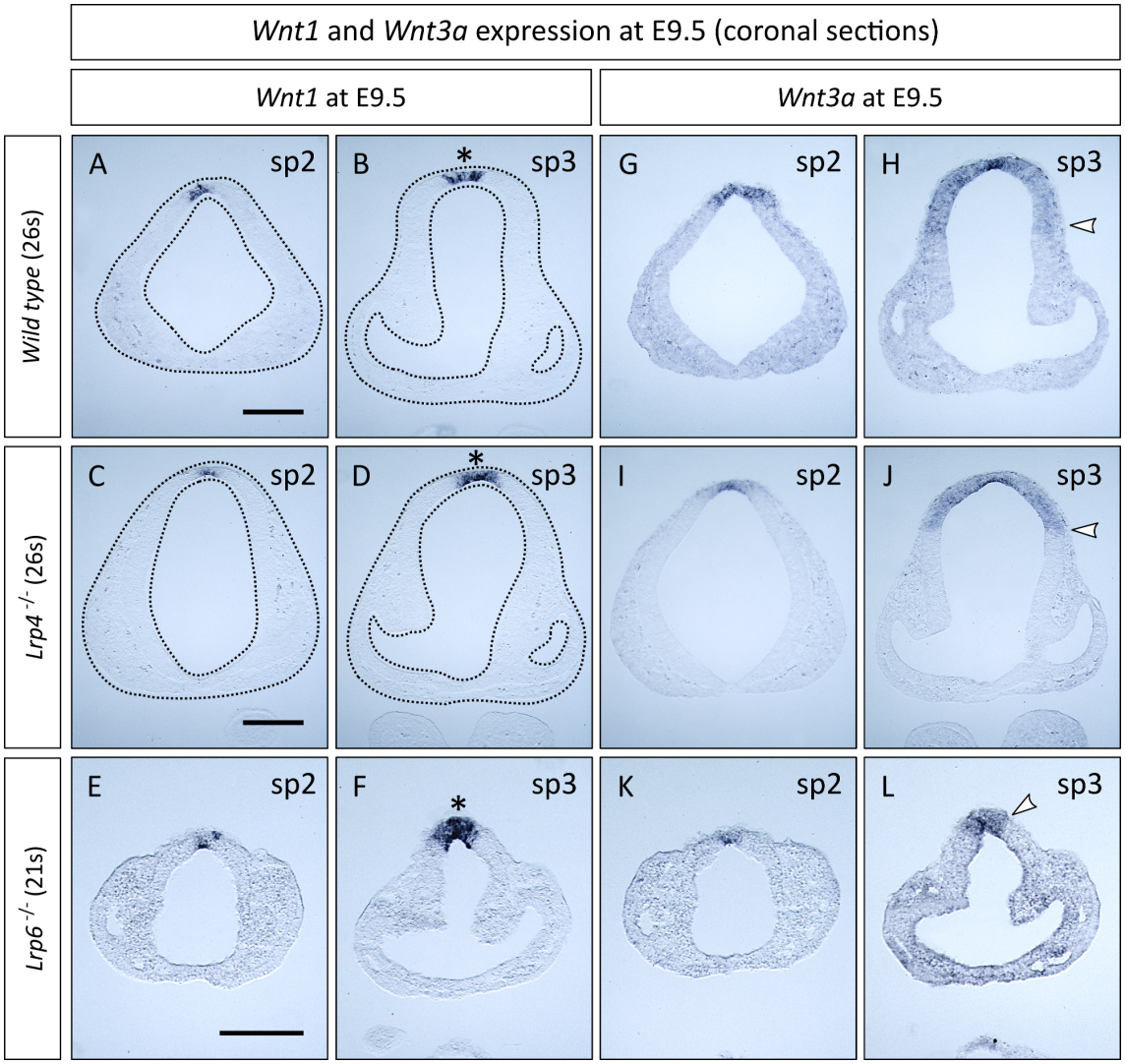

Figure 4.23: Loss of LRP4 or LRP6 does not affect the expression of *Wnt1* and *Wnt3a* in the dorsal midline of developing the forebrain

(A-D) At E9.5, *Wnt1* is expressed in the roof plate of the forebrain of the *wild type* and *Lrp4*$^{-/-}$ (n=3) embryos. **(E+F)** In *Lrp6*$^{-/-}$ (n=3) embryos *Wnt1* expression could also be detected in the dorsal midline. **(G-J)** *Wnt3a* is expression was found in the dorsolateral domain of the telencephalon of *Lrp4*$^{-/-}$ (n=3) and *wild type* embryos. **(K+L)** Embryos deficient for LRP6 also expressed *Wnt3a* though the expression domain occasionally appeared narrowed. The asterisk indicates the roof plate. White arrowhead marks the ventral boundary of *Wnt3a* expressing domain. Scalebar: 200 µm.

4.5.4 WNT target gene expression is downregulated in *Lrp6*$^{-/-}$ embryos and partially rescued in *Lrp4*$^{-/-}$;*Lrp6*$^{-/-}$ mutant embryos

To evaluate the implications on WNT signaling transduction by loss of LRP6 and potential gene interaction with *Lrp4* in *Lrp4;Lrp6* compound mutant embryos, it was important to assess the expression of WNT target genes. *Axin2* and *Lef1* are both WNT downstream target genes and start to be expressed in response to binding of WNT1 and WNT3a [84, 45, 162] Therefore, *Axin2* and *Lef1* expression levels represent an ideal readout for WNT signal transduction. I conducted ISH experiments on forebrain sections of *Lrp6*$^{-/-}$ embryos, *Lrp4;Lrp6* compound mutants and littermate control embryos to determine the efficiency of WNT signaling transduction (Figure 4.24 and Figure 4.25). *Axin2* expression was detected in the dorsal and lateral domain of the forebrain in *wild type* embryos (Figur 4.24 A-D). I observed that expression levels of *Axin2* were markedly reduced in *Lrp6* single mutant embryos (n=5), whereas no change in *Axin2* expression of was found in *Lrp4*$^{-/-}$ embryos (n=3) (Figure 4.24 A-L). Interestingly, I could reveal that in the dorsal forebrain of *Lrp4;Lrp6* compound mutant embryos (n=3) *Axin2* was expressed at comparatively higher levels than in *Lrp6*$^{-/-}$ embryos (Figure 4.24 M-P). Furthermore, I discovered that neuroepithelial cells within the excrescences of *Lrp4*$^{-/-}$;*Lrp6*$^{-/-}$ compound mutants also expressed *Axin2* (Figure 4.24 O+P). These findings were underpinned by the results of ISH experiments for Lef1 (Figure 4.25). Similar to *Axin2* expression, *Lef1* was found to be expressed in the dorsolateral domain in the developing telencephalon of *wild type* embryos at E10.5 (Figure 4.25 A+B). Embryos deficient for LRP4 displayed *Lef1* expression levels to the same extent as *wild type* controls (Figure 4.25 C+D). *Lef1* expression could be detected in the dorsal neural tube of *Lrp6*$^{-/-}$ mutant embryos (n=5), but was substantially decreased (Figure 4.25 E+F). However, *Lef1* expression in the prospective forebrain of *Lrp4*$^{-/-}$;*Lrp6*$^{-/-}$ embryos corroborated the finding of elevated *Axin2* expression levels. Compared to reduced *Lef1* transcript levels in *Lrp6*$^{-/-}$ embryos, *Lrp4;Lrp6* compound mutant embryos (n=3) showed increased *Lef1* levels in the dorsolateral telencephalon (Figure 4.25 G+H). In addition, *Lrp4*$^{-/-}$;*Lrp6*$^{-/-}$ neuroepithelial excrescences also showed elevated levels of *Lef1* expression (Figure 4.25 G+g'). After all, my result deliver evidence that WNT downstream target activation is markedly downregulated in the dorsal forebrain of *Lrp6* single mutant embryos. Intriguingly, in the telencephalon of *Lrp4;Lrp6* compound mutant embryos WNT target gene expression is apparently rescued at least in the dorsolateral domain.

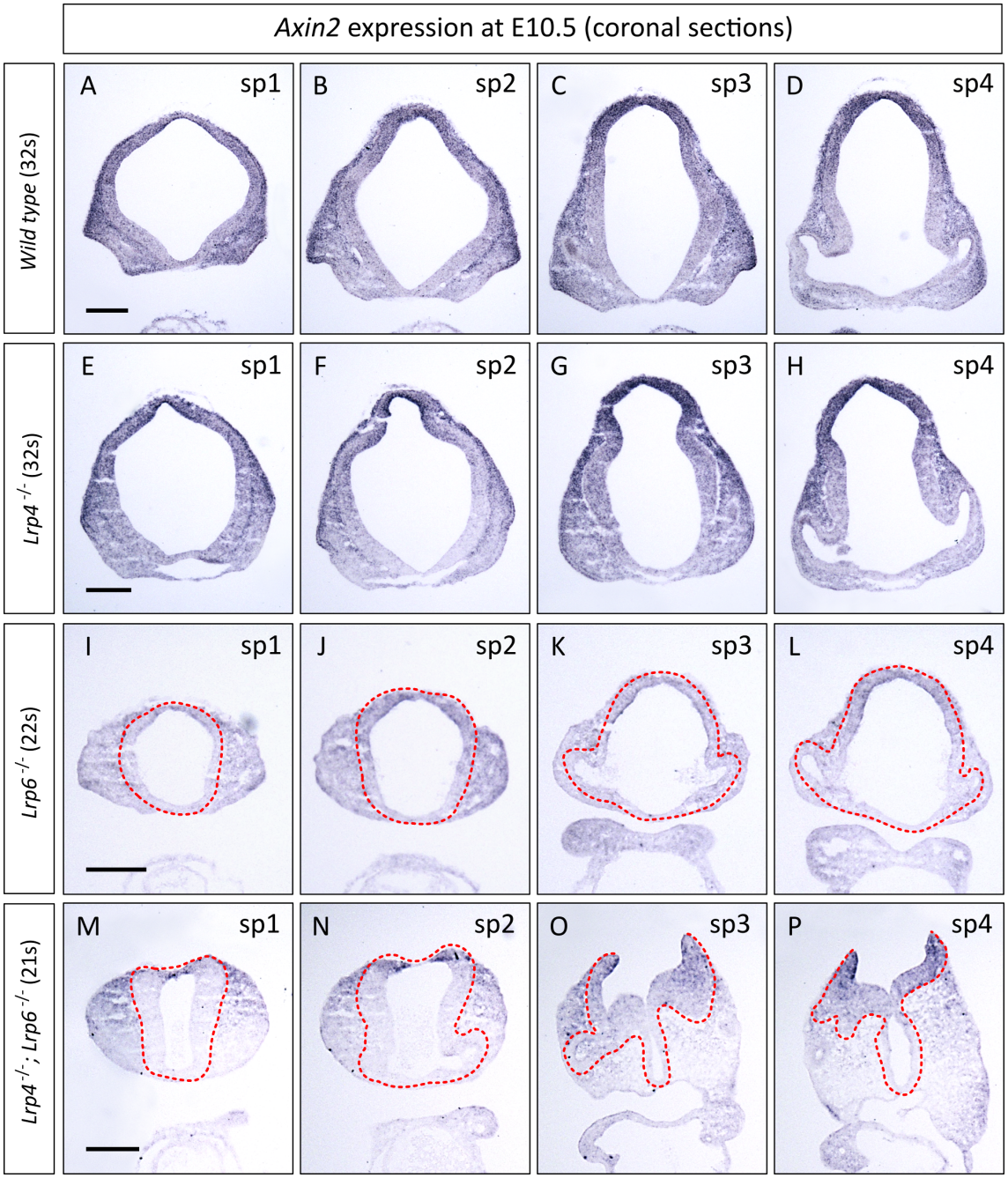

Figure 4.24: Reduction of *Axin2* expression levels in *Lrp6*$^{-/-}$ embryos is partially compensated in *Lrp4*$^{-/-}$;*Lrp6*$^{-/-}$ compound mutant embryos

(A-D) *In situ* hybridization at E10.5 shows *Axin2* expression in the dorsal part of the developing forebrain. **(E-H)** Compared to *wild types*, expression levels of *Axin2* are unchanged *Lrp4*$^{-/-}$ embryos (n=3). **(I-L)** However, *Axin2* expression in the developing telencephalon of *Lrp6*$^{-/-}$ embryos (n=5) is markedly decreased. **(M-P)** Compared to *Lrp6*$^{-/-}$ sections, *Lrp4*$^{-/-}$;*Lrp6*$^{-/-}$ compound mutant embryos (n=3) show elevated levels for *Axin2* expression in the dorsal forebrain. Scalebars: 200 µm.

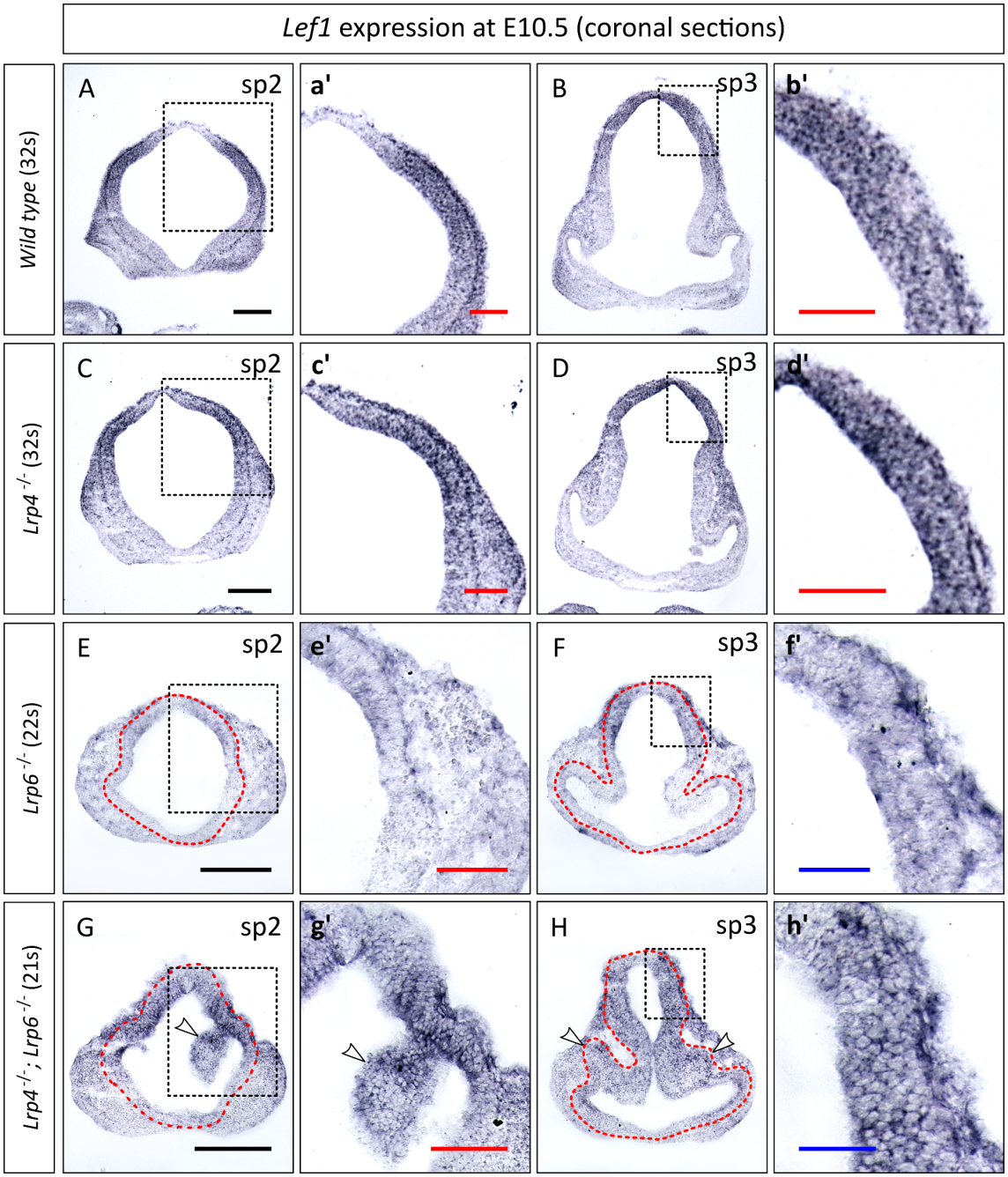

Figure 4.25: Expression of WNT downstream target *Lef1* is markedly reduced in *Lrp6* deficient embryos, whereas *Lrp4*$^{-/-}$;*Lrp6*$^{-/-}$ compound mutants show elevated levels of *Lef1* expression

(A+B) At E10.5, *Lef1* is expressed in the dorsal lateral region of the developing forebrain. **(C+D)** Expression of *Lef1* is not altered in *Lrp4*$^{-/-}$ embryos (n=4). **(E+F)** *Lrp6* deficient embryos (n=5) display a great reduction of *Lef1* expression in the neuroepithelium **(G+H)** In contrast, *Lrp4*$^{-/-}$;*Lrp6*$^{-/-}$ embryos (n=3) show elevated levels of *Lef1* transcripts compared to *Lrp6*$^{-/-}$ embryos. *Lef1* is expressed in neuroepithelial excrescences of *Lrp4;Lrp6* deficient embryos. **(a',c',e'+g')** Insets are 2x magnified. Red scalebars: 100 µm. **(b',d',f'+h')** Insets are 4x magnified. Blue scalebars: 50 µm. The red-dotted line delineates the basal neuroepithelial boundary. Black scalebars: 200 µm.

4.6 Immunostainings reveal further differences of *Lrp6*$^{-/-}$ and *Lrp4*$^{-/-}$;*Lrp6*$^{-/-}$ embryos in WNT target gene expression

4.6.1 WNT/ β-catenin downstream target cyclin-D1 is up-regulated in *Lrp4;Lrp6* compound mutants and severely down-regulated in *Lrp6*$^{-/-}$ embryos

I could show that gene expression of WNT downstream targets is drastically decreased in LRP6 deficient embryos and to a certain extent rescued in the forebrain of *Lrp4*$^{-/-}$;*Lrp6*$^{-/-}$ compound mutant embryos (Subsection 4.4.5.). To further support these findings, I performed immunohistochemistry stainings for cyclin D1, which is a downstream target of WNT/β-catenin signaling [162, 176]. In the developing telencephalon cyclin D1 is expressed in the ventrolateral region of the neural tube except for the dorsal midline (Figure 4.26 A and Figure 4.27 A-D). Whereas no changes of cyclin D1 protein levels could be observed in *Lrp4*$^{-/-}$ embryos (n=4) compared to *wild type* controls, *Lrp6*$^{-/-}$ mutant embryos (n=5) showed markedly reduced levels of cyclin D1 at E9.5 (Figure 4.26 B+C and Figure 4.27 D-F). Immunostaining on *Lrp4*$^{-/-}$;*Lrp6*$^{-/-}$ forebrain sections (n=5) revealed that cyclin D1 protein levels in dorsolateral neural progenitors were enhanced compared to dorsal regions of *Lrp6*$^{-/-}$ mutant neural tube (Figure 4.26 C+D and Figure 4.27 D-F versus G-I). Apparently the loss of cyclin D1 expression that was observed in the *Lrp6* single mutant forebrain was to some extent rescued in *Lrp4;Lrp6* compound mutant embryos leading to elevated cyclin D1 levels in the dorsolateral domain of the forebrain at E9.5. Interestingly, progenitor cells within the neuroepithelial excrescences of compound mutants displayed a positive staining for cyclin D1 at E9.5 (Figure 4.26 C+D). In concclusion, IHC for the WNT downstream target cyclin D1 revealed yet another WNT target gene that shows reduced expression in the dorsal domain of the *Lrp6*$^{-/-}$ forebrain. In concordance with the findings from ISH experiments (Subsection 4.5.4), this reduction in WNT target gene expression was paritally reverted in the dorsolateral domain of the telencephalon of *Lrp4;Lrp6* compound mutant embryos. Thus, additional loss of LRP4 on a *Lrp6*$^{-/-}$ background seems to affect WNT target gene activation in the dorsolateral domain of the forebrain.

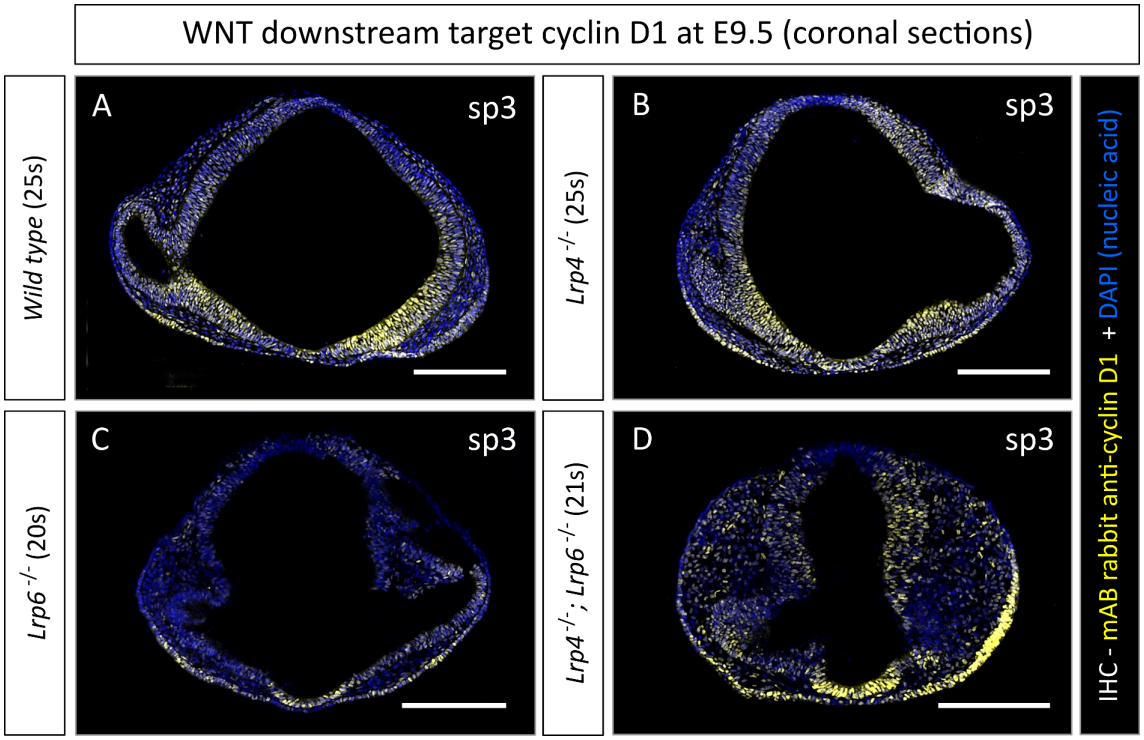

Figure 4.26: Wnt/β-catenin downstream target cyclin D1 is reduced in *Lrp6*$^{-/-}$ neuroepithelium but not in *Lrp4*$^{-/-}$;*Lrp6*$^{-/-}$ embryos at E9.5

(A+B) Immunostaining on E9.5 coronal brain sections shows broad expression of cyclin D1 within the prospective forebrain. Loss of LRP4 embryos (n=4) does not affect level of cyclin D1 in the neuroepithelium. **(C)** *Lrp6*$^{-/-}$ embryos (n=6) showed a great reduction of cyclin D1 protein in neural progenitors. **(D)** However, compared to *Lrp6* single mutants *Lrp4*$^{-/-}$;*Lrp6*$^{-/-}$ embryos (n=6) show rescued cyclin D1 protein levels in the dorsolateral domain of the telencephalon at E9.5. Scalebar: 200 µm.

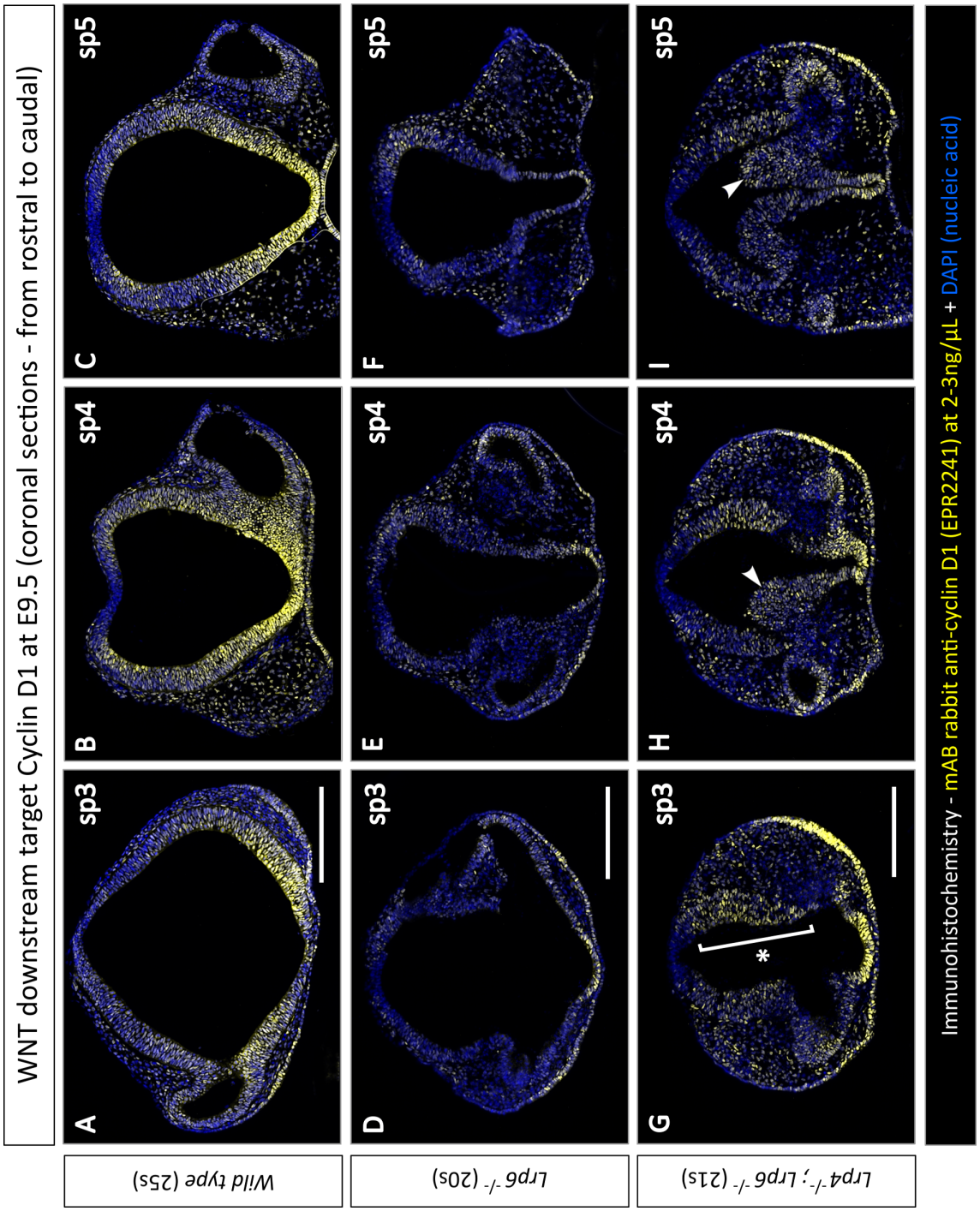

Figure 4.27: Cyclin D1 expression can be detected in neuroepithelial excrescences of in *Lrp4*$^{-/-}$*;Lrp6*$^{-/-}$ embryos

(A-C) Cyclin D1 expression in forebrain of *wild type* at E9.5 (sections A-C: from rostral to caudal). **(D-F)** In contrast, cyclin D1 levels are substantially reduced in *Lrp6*$^{-/-}$ embryos **(G-I)** Neuroepithelial excrescences (indicated by white arrowheads) of *Lrp4*$^{-/-}$*;Lrp6*$^{-/-}$ embryos (n=5) display elevated levels of cyclin D1 compared to *Lrp6*$^{-/-}$ embryos. Bracket/asterisk indicates dorsal region of the neuroepithelium with elevated cyclin D1 levels. Scalebars: 200 µm.

4.6.2 At E10.5, reduction of cyclin-D1 levels in the neuroepithelium of LRP6 deficient embryos is less pronounced

Immunohistochemistry analysis of cyclin D1 at E10.5 confirmed a ventrolateral distribution within the developing telencephalon (as observed at E9.5) in *wild type* and *Lrp4*$^{-/-}$ embryos (Figure 4.28 A+B). Although neuroepithelial levels of cyclin D1 were decreased in E9.5 *Lrp6*$^{-/-}$ mutant embryos (Subsection 4.6.1), at late E10.5 stages (n=3) a reduction in cyclin D1 expression was no longer discernible (Figure 4.28 A+C). Furthermore, the observed differences between *Lrp6*$^{-/-}$ embryos and *Lrp4*$^{-/-}$;*Lrp6*$^{-/-}$ compound mutants at E9.5 could not consistently be verified in E10.5 embryos. Neuroepithelial excrescences of *Lrp4*$^{-/-}$;*Lrp6*$^{-/-}$ embryos did not display an elevated expression of cyclin-D1 (Figure 4.28 D and Figure 4.29 D-F). However, cells within the excrescences expressed cyclin D1 (Figure 4.29 e'+g'). Curiously, my results on cyclin D1 expression suggest that *Lrp6* single mutants at E10.5 do not show discernible changes in cyclin D1, whereas at E9.5 I could robustly detect reduced cyclin D1 protein levels. This is not conclusive with my results from ISH experiments, where I could show a robust downregulation of WNT downstream targets *Lef1* and *Axin2* in *Lrp6*$^{-/-}$ embryos. Further analysis of cyclin D1 levels at E10.0 and E10.5 is required to confirm these findings.

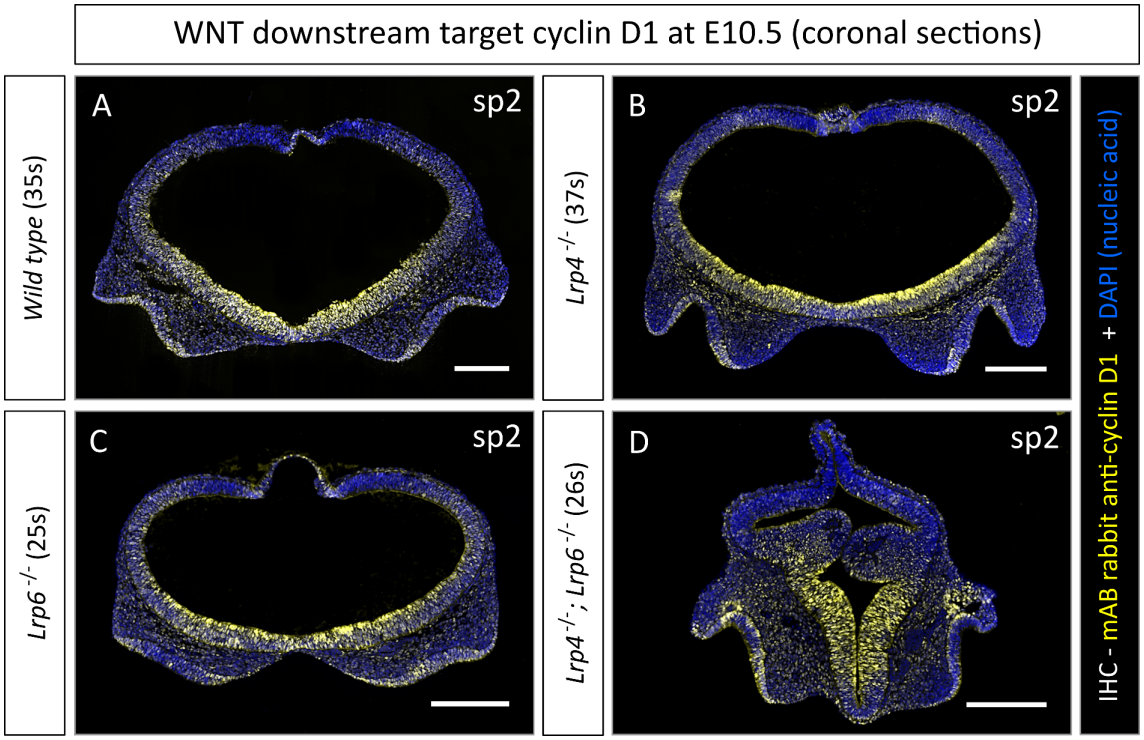

Figure 4.28: At E10.5, levels of cyclin D1 in *Lrp6*$^{-/-}$ embryos do not notably differ from *wild type* embryos

(A-C) At 10.5, cyclin-D1 expression of neural progenitor cells within the forebrain of *wild type*, *Lrp4*$^{-/-}$ embryos (n=2) and *Lrp6*$^{-/-}$ specimens (n=3) were all at comparable levels. **(C+D)** A discernible difference between *Lrp6*$^{-/-}$ and *Lrp4*$^{-/-}$*;Lrp6*$^{-/-}$ embryos (n=3) was not detectable. Scalebars: 100 µm.

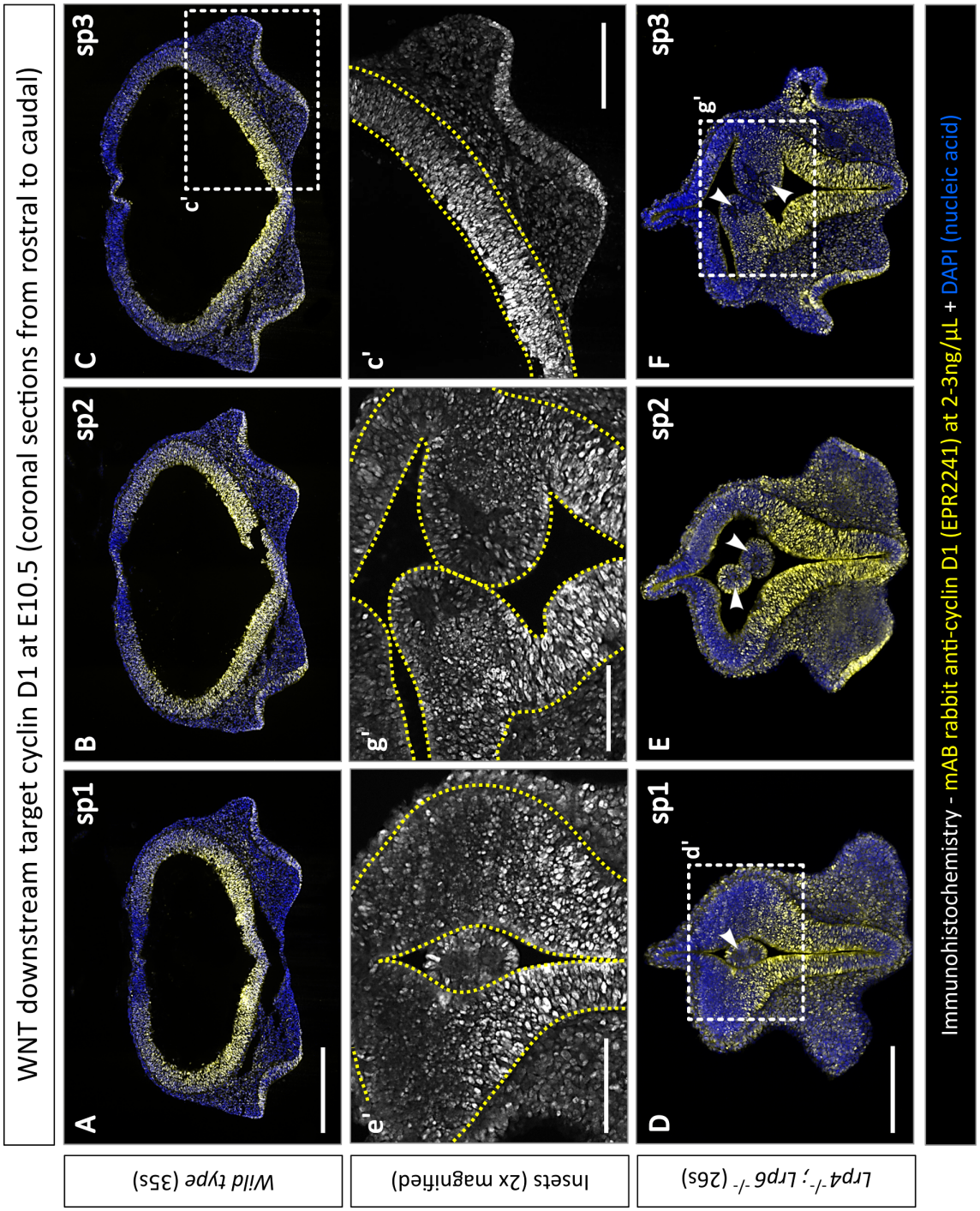

Figure 4.29: Neuroepithelial excrescences in *Lrp4*$^{-/-}$*;Lrp6*$^{-/-}$ embryos at E10.5 do not display enhanced cyclin D1 levels

(A-C) Throughout the ventrolateral telencephalon cyclin D1 is expressed in *wild type* at E10.5 **(D-F)** At E10.5, levels of cyclin D1 within the neuroepithelial excrescences (indicated by white arrowheads) of *Lrp4*$^{-/-}$*;Lrp6*$^{-/-}$ compound mutant embryos (n=3) are not elevated compared to respective regions of littermates with other genotypes. **(c',e'+g')** Magnified insets: Single channel micrograph of cyclin D1 (in white) IHC. Yellow-dotted line delineates margins of the neuroepithelium. Scalebars: 200 µm. Scalebars (insets): 100µm.

4.6.3 LRP6 deficient embryos show increased levels of PAX6 in the neuroepithelium

PAX6 (Paired box protein Pax-6) has been reported to be involved in WNT-related regulation of cell proliferation and differentiation in stem cells [41, 186, 190] . Recent studies also suggest PAX6 as a potential target of WNT signaling in the forebrain [53, 200]. Accordingly, I conducted immunohistochemistry stainings to detect PAX6 localization in the neuroepithelium of *Lrp6*$^{-/-}$ embryos, *Lrp4;Lrp6* compound mutants and littermate controls (Figure 4.30). Most neural progenitors located in dorsolateral regions of the developing forebrain stained positive for PAX6 in *wild type* and in *Lrp4*$^{-/-}$ embryos (n=3) - (Figure 4.30 A+B). Further, I could reveal differences in PAX6 staining intensity comparing *Lrp6*$^{-/-}$ and *Lrp4;Lrp6* compound mutant embryos. Interestingly, forebrain sections of LRP6 deficient embryos (n=4) always showed an increased PAX6 staining intensity, whereas this effect was not observed in *Lrp4*$^{-/-}$*;Lrp6*$^{-/-}$ embryos (n=3) (Figure 4.30 C+D). Examining the neuroepithelial excrescences of *Lrp4;Lrp6* compound mutant embryos, I found that cells within the excrescences were positive for PAX6 staining but did not show elevated protein levels (Figure 4.31 G-I). After all, I found consistently increased IHC staining intensity for PAX6 in the forebrain of *Lrp6* single mutant embryos compared to all other genotype littermate controls. However, whether the increased PAX6 levels in *Lrp6*$^{-/-}$ embryos can be correlated to impaired WNT signal transduction remains to be elucidated.

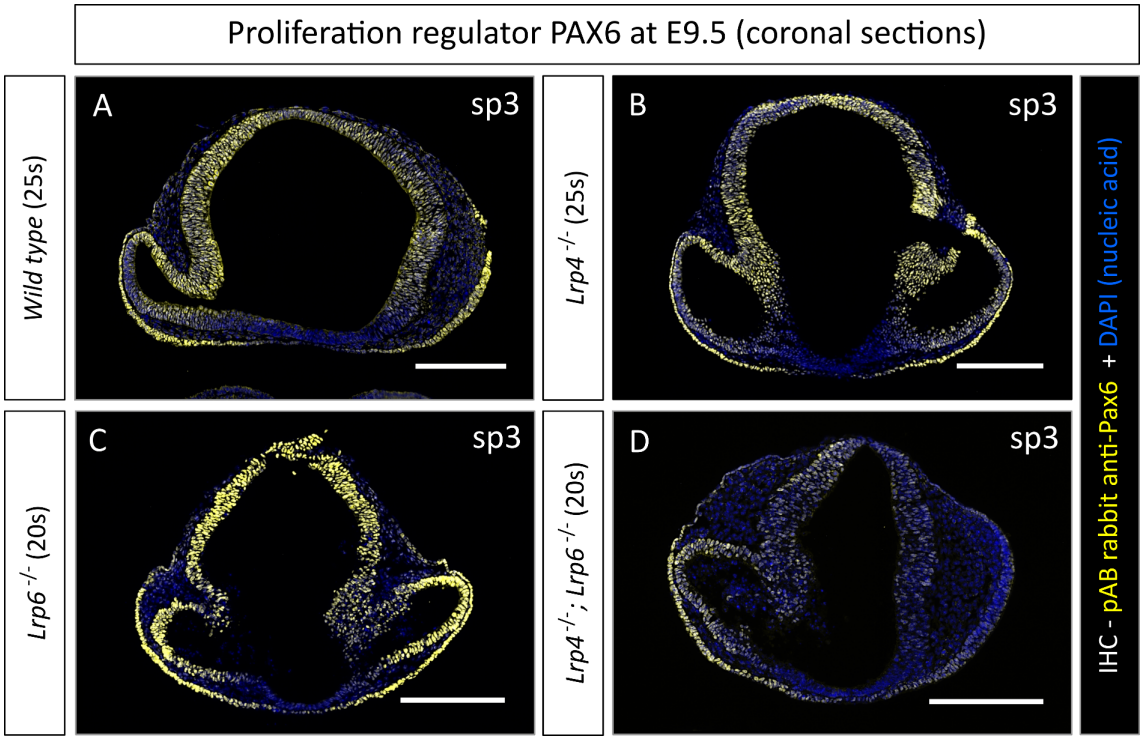

Figure 4.30: PAX6 levels were increased in *Lrp6*$^{-/-}$ neuroepithelial cells but not in *Lrp4*$^{-/-}$;*Lrp6*$^{-/-}$ embryos

(A) IHC for PAX6 on E9.5 coronal sections of the telencephalon showed a broad dorsolateral expression of PAX6 in *wild types*. **(B+C)** Whereas *Lrp4*$^{-/-}$ (n=3) showed PAX6 expression like *wild type* controls, *Lrp6*$^{-/-}$ embryos (n=4) always displayed a higher PAX6 staining intensity. **(D)** However, *Lrp4*$^{-/-}$;*Lrp6*$^{-/-}$ embryos (n=3) increased PAX6 staining was not observed at E9.5. Scalebar: 200 µm.

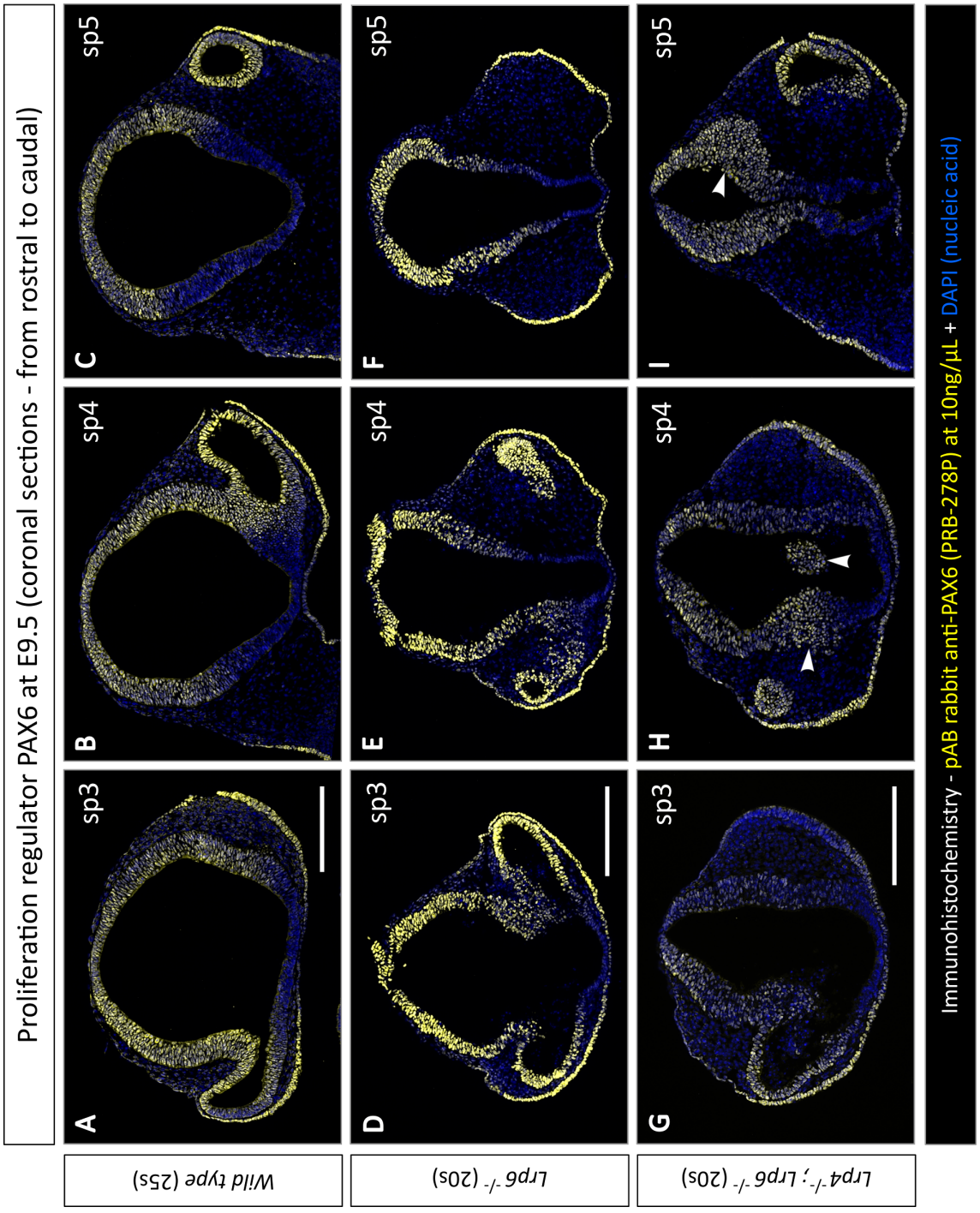

Figure 4.31: PAX6 can be detected in neuroepithelial excrescences of *Lrp4*$^{-/-}$*;Lrp6*$^{-/-}$ embryos

(A-C) *Wild type* sections of the forebrain (from rostral to caudal) at E9.5. **(D-F)** In all telencephalic sections of *Lrp6*$^{-/-}$ embryos (n=4) stronger PAX6 staining could be detected **(G-I)** In excrescences (indicated by white arrowheads) of *Lrp4*$^{-/-}$*;Lrp6*$^{-/-}$ embryos (n=3) PAX6 is also detectable. However, the intensity of PAX6 staining was less compared to sections of *Lrp6*$^{-/-}$ neural tube. Scalebar: 200 µm.

4.6.4 *TCF/Lef:H2B-GFP* reporter strain was crossed to the *Lrp* mouse lines to visualize Wnt/β-catenin signaling activity in the neuroepithelium

To find further evidence that in the neuroepithelium of *Lrp4;Lrp6* compound mutants the observed reduction of WNT-responsiveness in *Lrp6*$^{-/-}$ single mutant embryos is to a certain extent rescued, I crossed these *Lrp* mutants with a WNT activity reporter mouse line. *TCF/Lef:H2B-GFP* transgenic mice express GFP protein under the control of *Tcf/Lef* promoter (see Subsection 3.3.5). This reporter line is an ideal genetic tool to visualize WNT-responsiveness in cells that activated *Tcf/Lef* gene expression. By using this genetic approach, I found that most neural progenitor cells within the dorsal forebrain were GFP positive in the *wild type* (Figure 4.32 A+B). The extent of WNT-responsive progenitors in the dorsal and lateral neural tube of *Lrp4*$^{-/-}$ (n=3) was at comparable levels as in the *wild types* (Figure 4.32 A-D). In contrast, *Lrp6*$^{-/-}$ embryos displayed a substantially decreased count of GFP expressing cells in the neuroepithelium. Only few GFP-positive cells that were scattered within the dorsolateral forebrain could be detected (Figure 4.32 E+F). On the other hand, *Lrp4;Lrp6* compound mutant embryos exhibited a markedly increased number of GFP positive neural progenitor cells in the dorsolateral domain of the prospective telencephalon at E9.5 (Figure 4.32 G+H). In conclusion, my results on the *TCF/Lef:H2B-GFP* reporter activity in *Lrp6*$^{-/-}$ embryos and *Lrp4;Lrp6* compound mutant embryos confirmed my previous findings that *Lrp6* single mutants show reduced WNT target gene activation in the forebrain compared to *wild types*. However, WNT downstream targets and *Tcf/Lef* promoter activity are elevated in the dorsal forebrain of *Lrp4*$^{-/-}$*;Lrp6*$^{-/-}$ embryos - here visualized by GFP expressing NPCs.

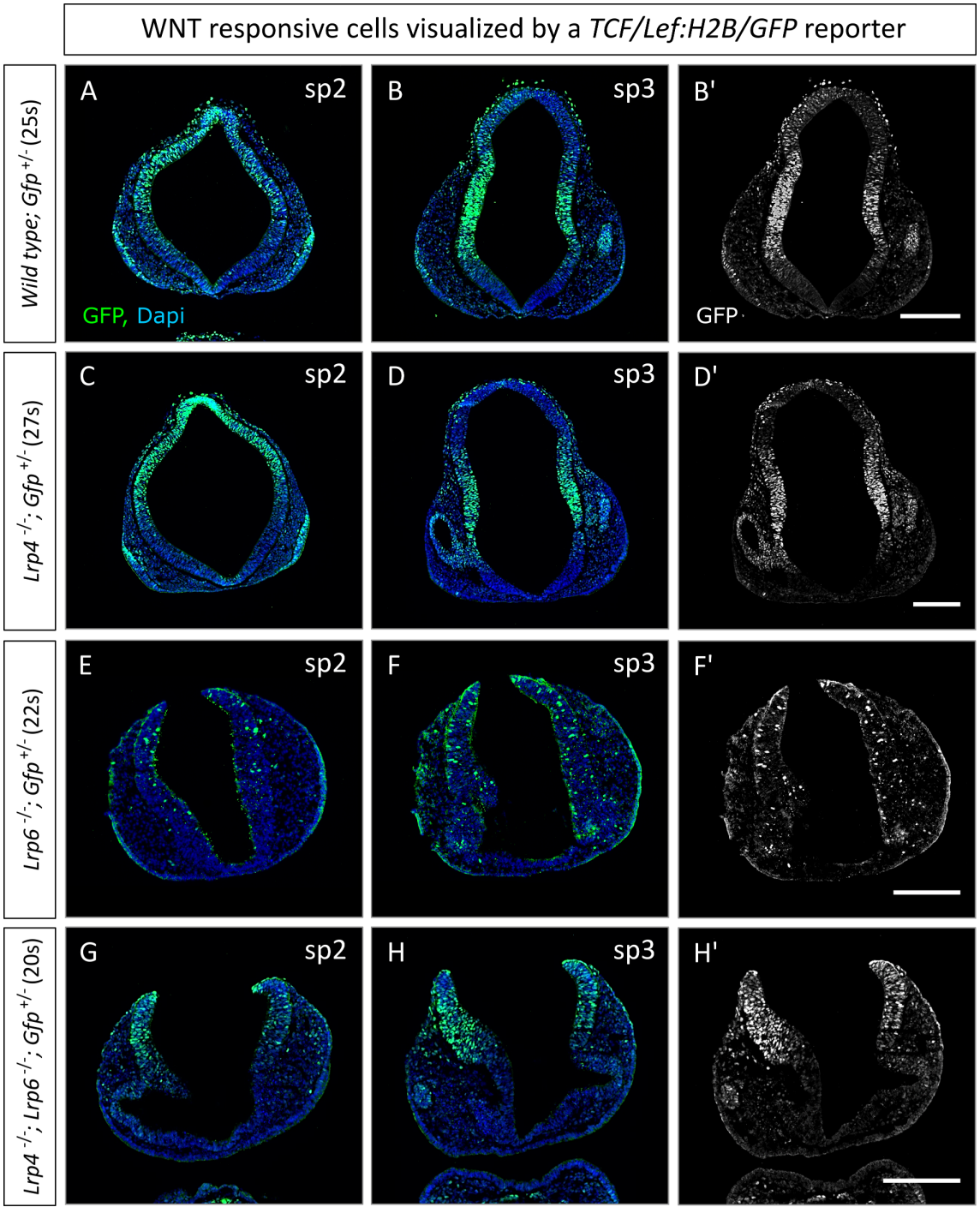

Figure 4.32: Less WNT-responsive neuroepithelial cells were found in *Lrp6*$^{-/-}$ embryos at E9.5, whereas *Lrp4*$^{-/-}$*;Lrp6*$^{-/-}$ compound mutants had more GFP+ cells in the dorsal neural tube

(A-D) Visualizing WNT-responsive neural progenitor cells by crossing with a TCF/Lef:H2B-GFP reporter line confirmed that there are no obvious differences in the number of WNT-responsive cells in *Lrp4*$^{-/-}$ embryos (n=3) compared *wild type* littermate controls. **(E+F)** *Lrp6*$^{-/-}$ embryos (n=4) showed a greatly reduced number of GFP-positive cells in the developing forebrain. **(G+H)** In contrast, more GFP positive cells were detected in dorsal regions of the neural tube of E9.5 *Lrp4*$^{-/-}$*;Lrp6*$^{-/-}$ embryos (n=2). (b',d',f'+h') Single channel micrographs of GFP immunostaining (in white). Scalebars: 200 µm.

4.7 WNT3a uptake is markedly reduced in *Lrp6*$^{-/-}$ embryos

My results demonstrated that WNT signaling response was reduced in LRP6 deficient mice. In contrast, WNT signaling was less affected in *Lrp4;Lrp6* compound mutant embryos. Next, I wanted to dissect whether reduced ligand binding could explain the observed implications in WNT signal transduction. Furthermore, I intended to examine whether WNT binding efficacy and/or uptake of WNT could deliver an explanation for the appearance of neuroepithelial excrescences in *Lrp4*$^{-/-}$*;Lrp6*$^{-/-}$ embryos. There are several lines of evidence that WNT3a is tightly linked with regulation of proliferation in stem cells [85, 103, 124, 160]. Moreover, it was shown that WNT3a can bind to LRP6 to activate the WNT pathway [12, 24, 28]. Therefore, WNT3a was a prominent candidate to further dissect its capability to bind to neuroepithelial cells during critical stages of forebrain development. To this end, I established a whole embryo culture (WEC) assay (see Subsection 3.3.11) to test binding and uptake of WNT3a in the neuroepithelium of *Lrp6*$^{-/-}$ embryos and *Lrp4;Lrp6* compound mutants.

4.7.1 At E8.5 the uptake of WNT3a in dramatically reduced in LRP6 deficient embryos

At first, whole embryo culture experiments with Alexa488-labeled WNT3a were conducted at E8.5. I tested *Lrp6*$^{-/-}$ embryos and *wild type* embryos to examine whether loss of LRP6 alone leads to implications of binding and uptake of WNT3a (Figure 4.33). First, I could demonstrate that the WEC assay was an adequate tool for detecting the uptake of WNT3a *ex vivo*. E8.5 *wild type* embryos exhibited binding and uptake of WNT3a-A488 at total length of the neural folds (Figure 4.33 C and Figure 4.34 A+A*). I could show that binding and uptake in neural progenitors of *Lrp6*$^{-/-}$ embryos was significantly reduced (Figure 4.33 E and Figure 4.34 C+C*). Interestingly, *Lrp6*$^{+/-}$ embryos also showed a slightly decreased uptake rate (not significant) of labeled WNT3a compared to *wild types* (Figure 4.33 D and Figure 4.34 B+B*). I quantified the absolute count of WNT3a-A488 positive vesicles within the neural folds as well as the area of vesicles and the relative count per area (µm²), respectively (Figure 4.34). I could demonstrate that *Lrp6*$^{-/-}$ embryos showed a significant decrease compared to *wild type* littermate embryos in all these analyses (see Table_20).

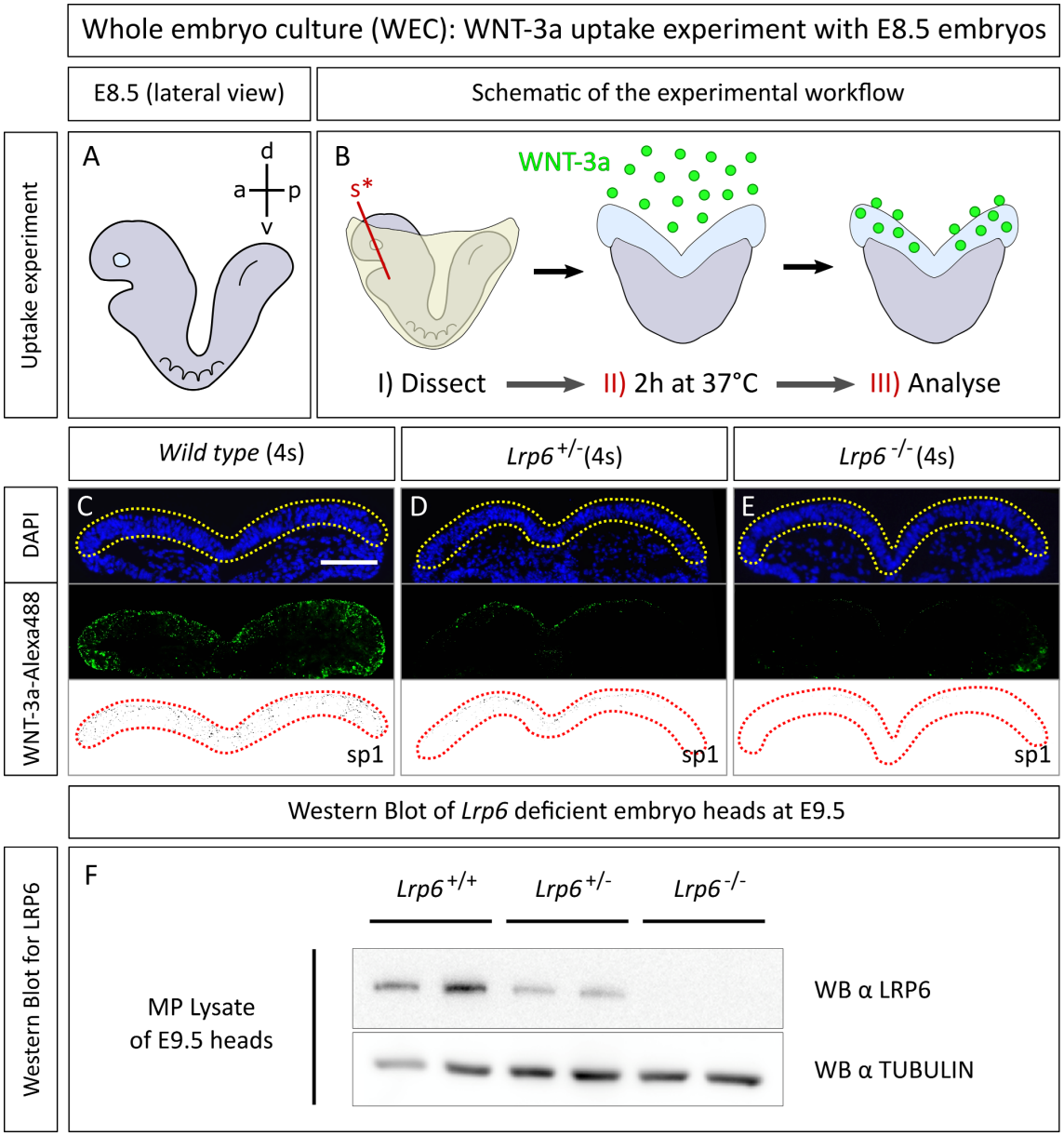

Figure 4.33: WNT3a uptake of neuroepithelium is significantly reduced in *Lrp6*$^{-/-}$ embryos at E8.5

(A) Schematic of E8.5 embryo - lateral view [anteroposterior-axis (a-p) and dorsoventral-axis (d-v)]. **(B)** Schematic of the experimental workflow (s* - red line indicate section plane of II and III). **(C)** In *wild type* embryos (n=4) uptake of fluorophore-labeled WNT3a could be verified by detecting Alexa-488 positive vesicles within the neuroepithelium. **(D)** Uptake of WNT3a-A488 was almost abolished in *Lrp6*$^{-/-}$ embryos (n=3). **(E)** Interestingly, uptake was even impaired in neuroepithelium of *Lrp6*$^{+/-}$ embryos (n=7). **(C-E)** Coronal sections at E8.5, three panels display 1.) DAPI staining in blue 2.) WNT3a-Alexa488 signal in green 3.) inverted monochrome image of the analyzed neuroepithelial area. Yellow-/red-dotted lines indicate neural folds/ measured area of the neuroepithelium. **(F)** Western blot analysis of embryo heads revealed reduced receptor levels in *Lrp6*$^{+/-}$ embryos at E9.5. Scalebar: 50 µm.

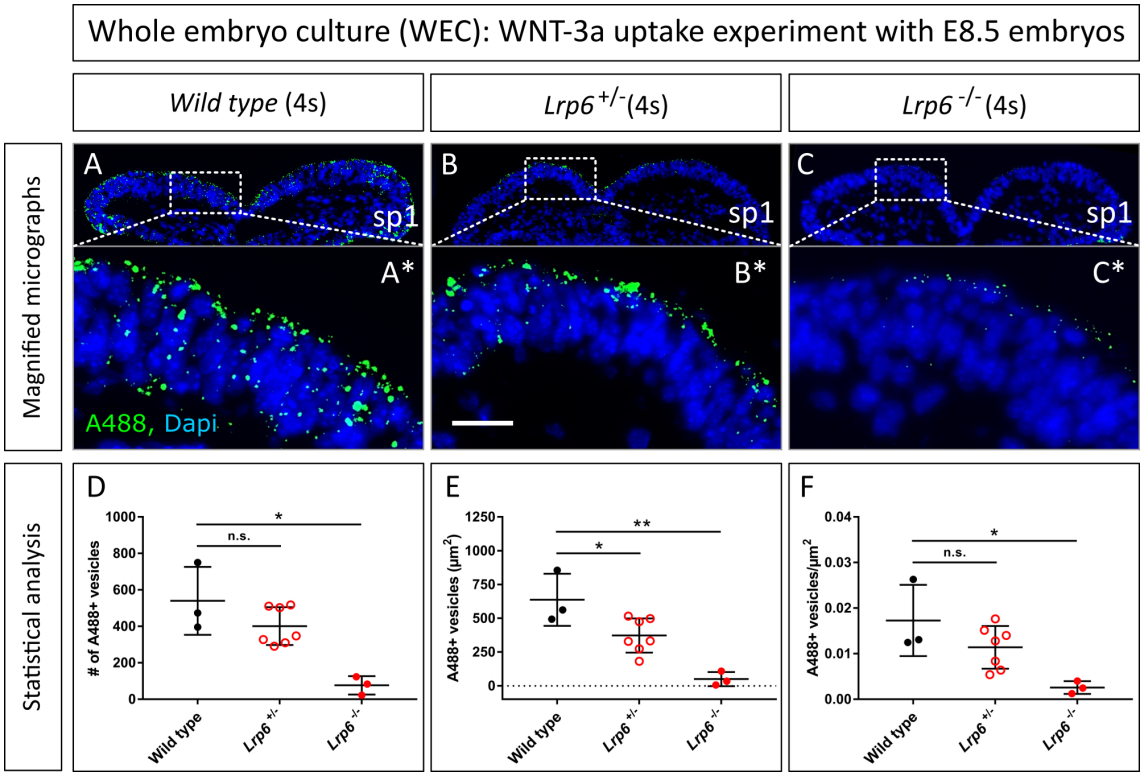

Figure 4.34: WEC experiments at E8.5 revealed lessened WNT3a uptake even in *Lrp6*$^{+/-}$ embryos

(A-C) Coronal sections of neural folds of *wild type*, *Lrp6*$^{+/-}$ and *Lrp6*$^{-/-}$ embryos at E8.5 after uptake experiment. **(A*-C*)** Insets display 5x magnified section of the neural folds with A488 positive vesicles. **(D)** Quantification of counted Alexa488 positive vesicles. **(E)** Area (in µm²) of Alexa488 positive vesicles within the neural folds **(F)** Number of Alexa488 positive vesicles per µm² (relative values).

Table 4.7: Statistical tests for data shown in Figure 4.34'

Diagram D:	*Wild type* versus *Lrp6*$^{+/-}$	
	unpaired t-test:	mean ± SEM of *WT*: 540 ± 107,4 (n=4)
	n.s. with p=0,1591	mean ± SEM of *Lrp6*$^{+/-}$: 401,4 ± 39,23 (n=7)
	Wild type versus *Lrp6*$^{-/-}$	
	unpaired t-test:	mean ± SEM of *WT*: 540 ± 107,4 (n=4)
	* with p=0,0141	mean ± SEM of *Lrp6*$^{-/-}$: 76,67 ± 29,33 (n=3)
Diagram E:	*Wild type* versus *Lrp6*$^{+/-}$	
	unpaired t-test:	mean ± SEM of *WT*: 637,1 µm² ± 111,3 (n=4)
	* with p=0,0306	mean ± SEM of *Lrp6*$^{+/-}$: 372,6 µm² ± 47,98 (n=7)
	Wild type versus *Lrp6*$^{-/-}$	
	unpaired t-test:	mean ± SEM of *WT*: 637,1 µm² ± 111,3 (n=4)
	** with p=0,007	mean ± SEM of *Lrp6*$^{-/-}$: 49,79 µm² ± 30,39 (n=3)
Diagram F:	*Wild type* versus *Lrp6*$^{+/-}$	
	unpaired t-test:	mean ± SEM of *WT*: 0,017 ± 0,00452 (n=4)
	n.s. with p=0,1686	mean ± SEM of *Lrp6*$^{+/-}$: 0,01141 ± 0,001772 (n=7)
	Wild type versus *Lrp6*$^{-/-}$	
	unpaired t-test:	mean ± SEM of *WT*: 0,017 ± 0,00452 (n=4)
	* with p=0,0328	mean ± SEM of *Lrp6*$^{-/-}$: 0,002585 ± 0,0008058 (n=3)

4.7.2 While WNT3a uptake at E9.5 is still impaired in *Lrp6*$^{-/-}$ embryos, *Lrp4;Lrp6* compound mutants exhibit increased uptake of WNT3a

Since *Lrp4* starts to be expressed between E8.5 and E9.5 (see Subsection 4.1.1), it was important to establish WEC uptake experiments also for E9.5 embryos. Since the neural tube of most embryos at E9.5 is already closed, I had to cut the diencephalon dorsally to make neuroepithelial tissue accessible for labeled WNT3a medium during incubation time (Figure 4.35 B) - (also see Subsection 3.3.11). I could successfully perform WNT3a uptake experiments at E9.5 and assess neuroepithelial WNT3a-A488 binding and uptake. I found that in *wild types* all progenitor cells within the neuroepithelium could bind and absorb labeled WNT3a (Figure 4.35 C+C*). Whereas *Lrp4*$^{-/-}$ embryos did not show a difference in uptake efficacy to *wild type* controls, *Lrp6*$^{-/-}$ embryos displayed a significantly decreased rate of WNT3a uptake (Figure 4.35 D-E*). Strikingly, *Lrp4;Lrp6* compound embryos exhibited increased uptake of WNT3a-A488 at E9.5. Especially in neuroepithelial excrescences more (and bigger) vesicles that contained Alexa488-labeled WNT3a were found (Figure 4.35 F+F*). I quantified the data for all WEC WNT3a-A488 uptake experiments at E9.5 as described in Subsection 3.5.1 (Figure 4.36). Compared to a markedly reduced uptake efficacy in *Lrp6*$^{-/-}$ neuroepithelium, the overall rate of WNT3a binding and uptake in *Lrp4;Lrp6* compound mutant embryos was increased and even reached levels similar to *wild type* embryos (Figure 4.36). *Wild type* littermate embryos served as negative controls and were incubated with Alexa488 fluorophore containing medium. None of the negative control embryos showed any signs of Alexa488 positive vesicles or spots 4.35(Figure 4.35 G). After all, WNT3a uptake experiments represent a great *ex vivo* tool to examine the uptake of WNT3a proteins in E8.5 and E9.5 embryos. My experiments revealed that WNT3a binding and uptake was significantly reduced in *Lrp6* single mutant embryos compared to *wild types*. Further, I could reveal that *Lrp4;Lrp6* compound mutant embryos showed an increased WNT3a uptake, especially in the neuroepithelial excrescences. This would indicate that binding of WNT3a could be the key to unravel the observed phenotypes of changed WNT target gene expression in the dorsolateral forebrain of *Lrp6* single mutants and *Lrp4;Lrp6* compound mutant embryos.

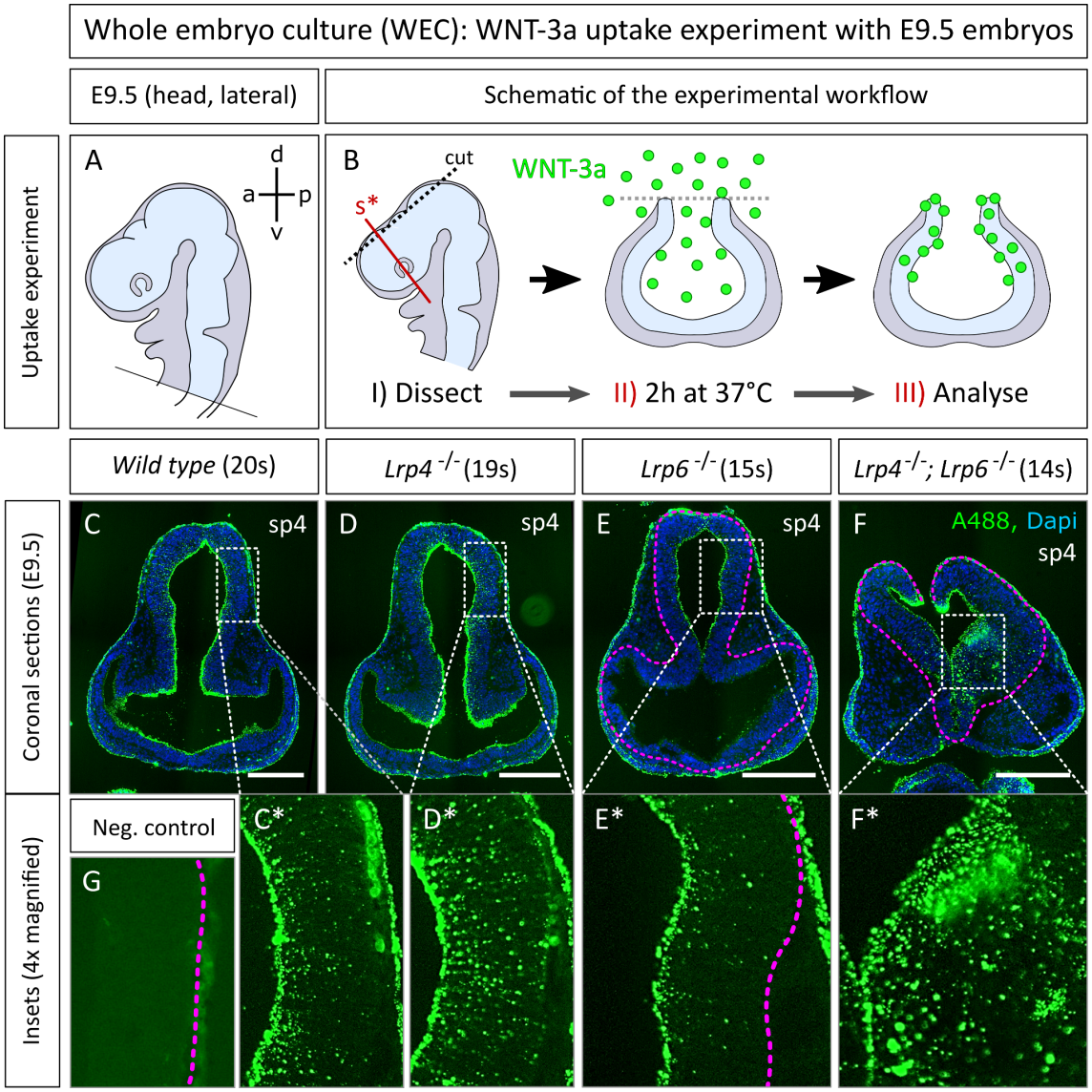

Figure 4.35: An increased uptake of WNT3a-A488 is detected in the neuroepithelial excrescences

(A) Lateral view of E9.5 embryo head (schematic), anteroposterior-axis (a-p) and dorsoventral-axis (d-v) are indicated] **(B)** At E9.5 embryo heads had to be cut open at dorsally to ensure WNT3a-Alexa488 penetration to neuroepithelial tissue. **(C-D)** No significant difference for uptake of the labeled ligand in *Lrp4* deficient embryos was observed at E9.5. **(E)** In contrast, *Lrp6*$^{-/-}$ embryos still showed a significantly decreased capability to absorb WNT3a. **(F)** The uptake of WNT3a-A488 was strikingly increased at the sites of the excrescences in the neuroepithelium of *Lrp4*$^{-/-}$*; Lrp6*$^{-/-}$ embryos. **(G)** As negative controls served *wild type* embryos that were incubated with Alexa-488 label, which was not linked to recombinant WNT3a. **(C*-F*)** Insets show 5x magnified sections of the neuroepithelium. Pink-dotted lines indicate the basal neuroepithelial boundary. Scalebars: 200 µm.

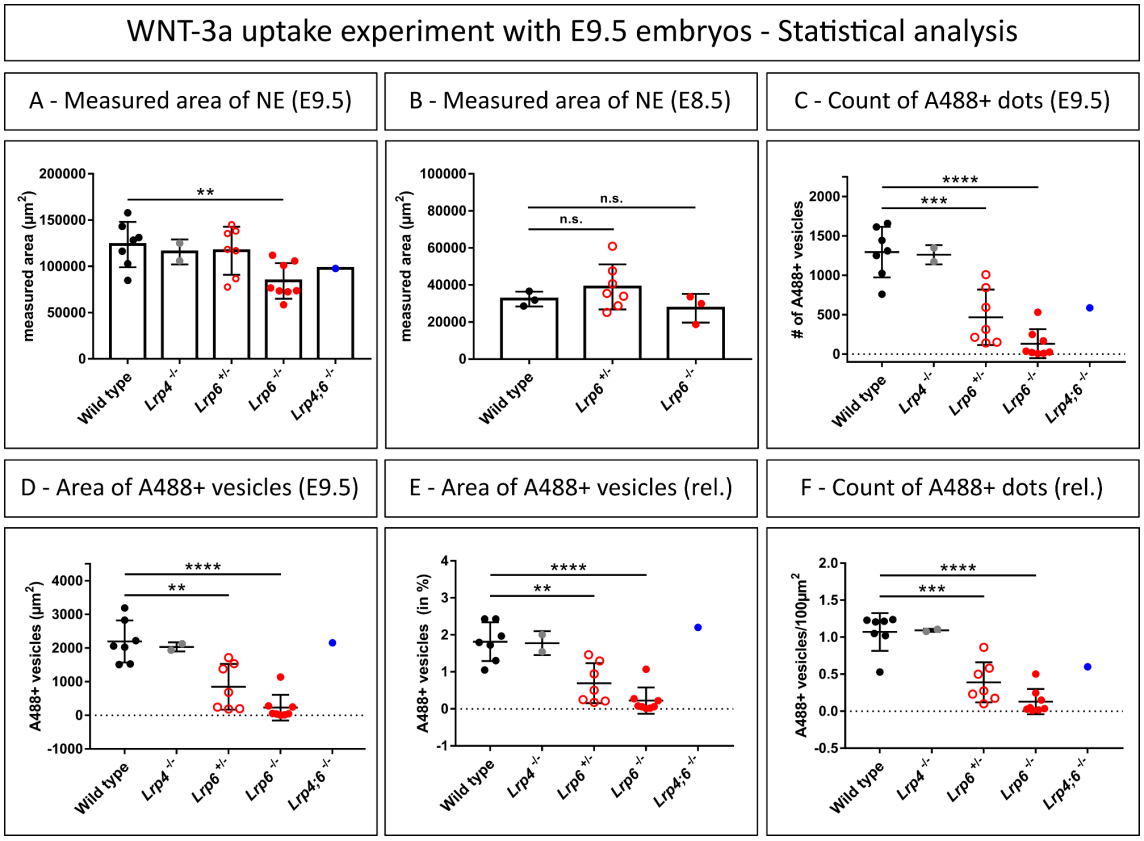

Figure 4.36: Reduction/loss of LRP6 receptor leads to impaired uptake of WNT3a, which was not reflected in *Lrp4*$^{-/-}$*;Lrp6*$^{-/-}$ embryos

(A) Measured area of neuroepithelial tissue was smaller in *Lrp6*$^{-/-}$ embryos, whereas no significant differences were observed at E8.5. **(B-F)** *Wild type* (black dots) and *Lrp4*$^{-/-}$ embryos exhibited the same rate of neuroepithelial WNT3a uptake at E9.5. In contrast, a significant reduction of WNT3a uptake was observed for *Lrp6*$^{+/-}$ (red hollow dots) and *Lrp6*$^{-/-}$ (red dots) embryos. Analyzing the relative values for *Lrp6* heterozygotes and LRP6 deficient embryos supported these observations. So far, the sample size of *Lrp4*$^{-/-}$*;Lrp6*$^{-/-}$ (blue dots) genotype (n=1) is too low to include in the statistical analysis, but so far, the observations suggest a higher rate of WNT3a uptake in the excrescences of *Lrp4*$^{-/-}$*;Lrp6*$^{-/-}$ embryos.

Table 4.8: Statistical tests for data shown in Figure 4.36

Diagram A:	*Wild type* versus *Lrp6*$^{-/-}$	
	unpaired t-test:	mean ± SEM of *WT*: 123596 µm² ± 9287, (n=7)
	** with p=0,0041	mean ± SEM of *Lrp6*$^{+/-}$: 84294 µm² ± 6810, (n=8)
Diagram B:	*Wild type* versus *Lrp6*$^{+/-}$	
	unpaired t-test:	mean ± SEM of *WT*: 32371 µm² ± 2321 (n=4)
	n.s. with p=0,4005	mean ± SEM of *Lrp6*$^{+/-}$: 38960 µm² ± 4611, (n=7)
	Wild type versus *Lrp6*$^{-/-}$	
	unpaired t-test:	mean ± SEM of *WT*: 32371 µm² ± 2321 (n=4)
	n.s. with p= 0,3824	mean ± SEM of *Lrp6*$^{-/-}$: 27428 ± 4476, (n=3)
Diagram C:	*Wild type* versus *Lrp6*$^{+/-}$(absolute count of vesicles)	
	unpaired t-test:	mean ± SEM of *WT*: 1295 ± 121,2, (n=7)
	*** with p=0,0006	mean ± SEM of *Lrp6*$^{+/-}$: 467 ± 133,3, (n=7)
	Wild type versus *Lrp6*$^{-/-}$ (absolute count of vesicles)	
	unpaired t-test:	mean ± SEM of *WT*: 1295 ± 121,2, (n=7)
	**** with p<0,0001	mean ± SEM of *Lrp6*$^{-/-}$: 131,7 ± 65,17, (n=8)
Diagram D:	*Wild type* versus *Lrp6*$^{+/-}$ (area of the detected A488+ vesicles)	
	unpaired t-test:	mean ± SEM of *WT*: 2195 µm² ± 237,1, (n=7)
	** with p= 0,0023	mean ± SEM of *Lrp6*$^{+/-}$: 849,6 µm² ± 256,1, (n=7)
	Wild type versus *Lrp6*$^{-/-}$ (area of the detected A488+ vesicles)	
	unpaired t-test:	mean ± SEM of *WT*: 2195 µm² ± 237,1, (n=7)
	**** with p<0,0001	mean ± SEM of *Lrp6*$^{-/-}$: 229,5 ± 135, (n=8)
Diagram E:	*Wild type* versus *Lrp6*$^{+/-}$ (area of A488+ vesicles in relation to the measured area)	
	unpaired t-test:	mean ± SEM of *WT*: 1,816 % ± 0,1971, (n=7)
	** with p=0,0019	mean ± SEM of *Lrp6*$^{+/-}$: 0,6955 ± 0,2042, (n=7)
	Wild type versus *Lrp6*$^{-/-}$ (area of A488+ vesicles in relation to the measured area)	
	unpaired t-test:	mean ± SEM of *WT*: 1,816 % ± 0,1971, (n=7)
	**** with p<0,0001	mean ± SEM of *Lrp6*$^{-/-}$: 0,2258 % ± 0,1258, (n=8)
Diagram F:	*Wild type* versus *Lrp6*$^{+/-}$ (count of A488+ vesicles per area)	
	unpaired t-test:	mean ± SEM of *WT*: 1,071 ± 0,09618, (n=7)
	*** with p=0,0004	mean ± SEM of *Lrp6*$^{+/-}$: 0,3902 ± 0,1024, (n=7)
	Wild type versus *Lrp6*$^{-/-}$(count of A488+ vesicles per area)	
	unpaired t-test:	mean ± SEM of *WT*: 1,071 ± 0,09618, (n=7)
	**** with p<0,0001	mean ± SEM of *Lrp6*$^{-/-}$: 0,1302 ± 0,06057, (n=3)

In conclusion, my results show that *Lrp4;Lrp5* and *Lrp4;Lrp6* compound mutant embryos are good models to study common and distinct functions of LRP5 and LRP6 through phenotypic analysis of compound mutant embryos. I could show that *Lrp4;Lrp5* compound mutant embryos are embryonic lethal at E10.5, whereas *Lrp4;Lrp6* compound mutant embryos are viable at least until E11.5 (analysis of older embryos need to be elucidated). Further, my results deliver several lines of evidence that LRP4 and LRP6 are involved in WNT signal transduction during early forebrain development. With different methodological approaches, I revealed that *Lrp6* single mutant embryos show decreased levels of WNT target gene activation, whereas *Lrp4;Lrp6* compound mutant embryos display elevated levels of WNT downstream targets in the dorsolaterl domain of the developing forebrain. Finally, I could show that WNT3a is a promising canditate to mediate the observed WNT signal transduction phenotypes in *Lrp5* single mutants and *Lrp4;Lrp6* compound mutant embryos.

5 Discussion

WNT signal transduction represents one of the main regulatory pathways of development and orchestrates various processes that are involved in body formation throughout the animal kingdom. Since the very first WNT protein was discovered by Nusse and Varmus 35 years ago [135], understanding of the WNT pathway for developmental processes and its complexity has steadily risen. It is therefore not surprising that WNT signaling also plays a pivotal role during formation of the mammalian forebrain, which is one of the most complex developmental processes [66, 192]. Various studies performed loss-of-function and gain-of-function experiments to shed light on the involvement of WNT pathway related proteins in respect of their role during brain development [60, 105, 119, 123]. Crucial for proper WNT signal transduction is the docking site of WNT proteins, which comprises the transmembrane receptors Frizzled (FZD) and LRP5/6 [116]. Whereas many scientific publications highlight the role of FZD receptors during brain development [18, 46], only a limited number of studies addressed the question to what extent LRP5 and LRP6 are involved in WNT-related mammalian forebrain formation. My study delivers supporting evidence that besides LRP5/6 also LRP4 - another candidate of the LDL-receptor protein family - plays an important role for WNT signal transduction during early telencephalic development. Whereas the concept that WNT binding to the FZD-LRP receptor complex leading to activation of WNT downstream targets is well-understood, less is known about the mechanism how this ligand-receptor interaction can be modulated to alter WNT signal interpretation [9, 134]. However, there is growing evidence that modulation of the FZD co-receptor complex plays an important role in regulating WNT target gene expression [3, 4, 92, 208]. It was reported before that LRP4 in interplay with the WNT inhibiting protein WISE can modulate the function of LRP5/6 during the development of non-neuronal tissue [3, 4, 137, 138]. My study provides genetic evidence that the concept of LRP5/6 modulation by LRP4 can also be adopted for WNT target gene expression during mouse forebrain development. Furthermore, this modulation of WNT signal transduction seems to be essential in keeping the balance of proliferation and differentiation of neural progenitor cells within the prospective forebrain.

5.1 *Lrp4;Lrp5* and *Lrp4;Lrp6* compound mutant embryos serve as models to study common and distinct functions of LRP4 and LRP5/6 during forebrain development

To study the function of LRP4 and LRP5/6 and their implications during forebrain formation in detail, it was of crucial relevance to obtain a comprehensive understanding of their spatial and temporal distribution at critical stages of murine telencephalic development. Since it was not possible to visualize LRP4 and LRP5/6 protein abundance with immunohistochemical methods (due to lack of functional antibodies), *in situ* hybridization experiments shed light on the spatial and temporal aspect of expression for these LRP-candidates. Looking at the onset of expression for all three LRP members, it becomes apparent that at first *Lrp6* expression can be detected and it is ubiquitously expressed at E8.5 [98]. *Lrp5* starts to be expressed in the neural folds at E8.5 and *Lrp5* transcripts can also be detected in the secondary heart field (Figure 4.2). This also pinpoints the moment of *Lrp5* and *Lrp6* co-expression in the neural folds. Further, I could show that *Lrp4* mRNA expression was induced a little bit later at E9.0-E9.5 in the dorsolateral neural tube, whereas the ventral midline was void of *Lrp4* transcripts. Therefore, I could verify that *Lrp4* and *Lrp5/6* are co-expressed in most of the neural progenitors (NPC's) within the developing forebrain from E9.5 onwards (Figure 4.1-4.3). Previous work by Ahn et al. suggested a modulatory role of LRP4 acting on LRP5/6 during mammary placode development [3]. I wanted to examine whether this concept of LRP4 acting on LRP5/6 function could also be applied to dorsolateral regions of the neural tube during early forebrain development. I decided to generate compound loss-of-function mutants of either *Lrp4;Lrp5* and *Lrp4;Lrp6* to examine the role of LRP4 and LRP5/6 in more detail. The phenotypic analysis was completed by comparing observations with single loss-of-function mutant embryos for *Lrp4*, *Lrp5* and *Lrp6*, respectively. Compound mutants for *Lrp5;Lrp6* were not part of the study, since they display an implantation phenotype and do not develop past embryonic stage E4.5 [98]. All three LRP members have been shown to act in a WNT-dependent manner at different sites during embryogenesis. For instance, in limb development as well as in the mouse mammary stem cell niche [3, 107, 137]. Since I could show that *Lrp4* and *Lrp5/6* are co-expressed in the forebrain at E9.5, I intended to prove their involvement in WNT-related development of the telencephalon by analyzing single and compound mutant embryos. On the one hand, this enabled me to highlight common and distinct functions of LRP5 and LRP6 by comparing observations in *Lrp4;Lrp5* with *Lrp4;Lrp6* compound mutant embryos (see Subsection 5.2). This is of relevance, since single loss-of-function mutants for *Lrp5* display only minor

phenotypic abnormalities affecting the bone mineral density (BMD), due to a compensation by the highly homologous LRP6 receptor [73, 87]. Whereas *Lrp6* loss-of-function mutants display several WNT-related phenotypes such as skeletal malformations, tailbud truncation and impaired kidney development, indicating that LRP5 cannot fully compensate [73, 87, 146]. However, developmental defects that also affect morphology of the forebrain and synapsis formation have been reported for *Lrp6* loss-of-function mutants [60, 83, 110, 212]. In addition, *Lrp6* single mutants embryos are susceptible for developing neural tube closure defects (NTDs) [61, 60] and show impairments for induction of certain neuronal subtypes such as dopaminergic neurons in the midbrain [21]. In contrast, only little is known about developmental forebrain defects in *Lrp4* loss-of-function mutant embryos, although LRP4 seems to be involved in establishing synaptic intergration of the hippocampus [148]. Therefore, I intended to shed light on potential gene interations of *Lrp4* and *Lrp5/6* by generating *Lrp4;Lrp5* and *Lrp4;Lrp6* compound mutants to reveal functional relationships and syngergies during forebrain formation. In relation to already published data where it could be shown that LRP4 acts inhibitory on LRP5/6 to modulate WNT signal transduction in non-neuronal tissue [2, 138], I decided to concentrate my analysis on WNT-related early forebrain development at E9.5 and E10.5 (when *Lrp4* and *Lrp5/6* are co-expressed).

5.2 Generation of *Lrp4;Lrp5* compound mutants revealed embryonic lethality at E10.5 and delayed closure of the anterior neuropore

It has been reported that *Lrp4* loss-of-function mutation leads to perinatal lethality, because *Lrp4* is required to establish the neuromuscular synapse and thus the newborn mice cannot breathe on their own [7, 191]. In contrast, *Lrp5* loss-of-function mutants are viable and show a rather mild phenotype merely affecting the BMD due to compensation by LRP6 [73, 87]. Interestingly, I could show that *Lrp4;Lrp5* compound mutant embryos die at around E10.5 (Figure 4.4) and most *Lrp4;Lrp5* compound mutants were completely apoptotic at E10.5 (Figure 4.5). A critical point in embryogenesis is the onset of fetal circulation, which emerges between E8.5 and E9.5. Malformations of the blood vessel system or the heart of the embryo usually lead to the degeneration of the fetus. To probe the cause of an embryonic lethal phenotype it is important to pinpoint the tissue in which the mutated genes are likely to have an effect. Although, evaluation of transcript expression for *Lrp4* and *Lrp5* in the cardiovascular systems was not part of my study, others showed that these genes seem to play a role in establishing the cardiovascular system. Tomita et al. could show that *Lrp4* is highly expressed

in the murine heart [179] and another study revealed that LRP4 is involved in cardiovascular formation [209]. On the other hand, several studies linked LRP5 function with vascularization defects in the brain and in the retina [114, 203]. Moreover, various *Lrp5* mutations in humans could be linked to different heart diseases [19, 152]. Since I could show that *Lrp5* starts to be expressed in the secondary heart field of mouse embryos, it will be worthwhile to look in more detail into the role of LRP5 during cardiogenesis. *Lrp4;Lrp5* compound mutants might serve as the ideal model system to study the implications of LRP4 and LRP5 in murine heart development. Interestingly, the well-known WNT inhibitors DKK1 and DKK2 play a major role in heart formation [145] and several studies showed that LRP4 and LRP5 can bind these inhibitors [2, 26, 188]. To identify the cause of *Lrp4;Lrp5* compound mutant lethality, examining WNT-dependent involvement of LRP4 and LRP5 represents a promising endeavor. This is of special interest, because the observed embryonic lethality for *Lrp4;Lrp5* compound mutant embryos was not seen in *Lrp4;Lrp6* double mutants (Figure 4.7). Therefore, one could also reveal distinct functions of LRP5 and LRP6 by examining the cause of *Lrp4;Lrp5* compound mutant lethality.

Another aspect that I could observe in *Lrp4;Lrp5* compound mutant embryos was a delayed neural tube closure affecting the rostral neuropore. According to Theiler stage 14 definition (13-20 somites), the formation and closure of the anterior neuropore (ANP) occurs during the period when 15-19 somites have already formed and in any case the folds are closed at 19 somites [159, 178]. This corresponds with my observations in *wild type* C57Bl/6N mouse embryos at E9.5, where all embryos showed a completely closed ANP at 19 somites. Neither loss of LRP4 nor LRP5 alone affected the timing of neurulation and ANPs of $Lrp4^{-/-}$ and $Lrp5^{-/-}$ embryos were closed at latest with 20 somites. However, in *Lrp4;Lrp5* compound mutant embryos the ANP closure was delayed and it was still not completely closed when 21-23 somites had already formed (Figure 4.6). This phenotype of deferred ANP closure in *Lrp4;Lrp5* compound mutants was restricted to embryos that were dissected at E9.5. All embryos that were examined at E10.5 displayed a fully closed ANP (Figure 4.6). Thus, one could state that it is rather a delay of ANP closure and not a complete failure of rostral neural tube closure.Interestingly, it was reported before for *Lrp6* loss-of-function mutations as well as for gain-of-function mutated mice that show neurulation defects to a certain extent [60, 146]. Pinson and others reported that a certain percentage of *Lrp6* null embryos develop an anterior neural tube closure defect that will ultimately lead to an exencephalus phenotype [146]. My analysis of *Lrp6* single mutants and *Lrp4;Lrp6* compound mutant embryos supported this finding and about one fifth of *Lrp6* and *Lrp4;Lrp6* mutant embryos had still an open neural

tube at E10.5. Interestingly, *Lrp4;Lrp6* compound mutant embryos were more prone to display an open ANP at E9.5 compared to *Lrp6* single mutant embryos, whereas this was not reflected at E10.5 (Figure 4.8). However, this has to be carefully evaluated, since *Lrp4;Lrp6* compound mutant embryos also develop structural abnormalities in the neural tube, which are discussed further in Subsection 5.4. Nevertheless, the observed ANP closure delay in *Lrp4;Lrp5* compound mutant embryos might be an intersting subject for further studies. Albeit, it has to be considered that the embryonic lethality phenotypse might interfere with the analysis of *Lrp4;Lrp5* compound mutants at E9.5 and conditional compound mutants would have to be generated.

5.3 *Lrp6*$^{-/-}$ embryos and *Lrp4;Lrp6* compound mutants have a growth deficit

Pinson and others were the first to report the phenotype of *Lrp6* loss-of-function mice and they could show that *Lrp6*$^{-/-}$ embryos displayed a size reduction of the tailbud starting from at E8.5 onwards [146]. Along with this axial truncation a reduction of the somite count was reported. I could show that this somite reduction affected *Lrp6*$^{-/-}$ embryos at E9.5 and E10.5. Whereas at E9.5 there was an average loss of five somites compared to *wild type* littermate control embryos, somite count reduction at E10.5 was between 10-12 somites (Figure 4.9). The axial truncation phenotype was also present in *Lrp4;Lrp6* compound mutant embryos and no significant difference was observed compared to the somites count of *Lrp6* single mutant embryos (Figure 4.9). This axial truncation phenotype is very likely due to impaired WNT3a binding, because *Wnt3a* loss-of-function mutations lead to a similar phenotype with even broader manifestation [205]. Several studies showed that WNT3a can bind to LRP6 and it is therefore important for WNT3a signal transduction [24, 28]. Given that *Lrp4;Lrp6* compound mutant embryos display the same axial truncation phenotype and the somite count of *Lrp4* single mutants is not different to *wild types*, indicates that *Lrp4* does not seem to play a major role in WNT-signaling dependent somitogenesis.

A fundamental hallmark of the WNT factors is their function as growth stimulatory factors [131]. As a consequence, impaired WNT signal transduction can also lead to deficits in tissue growth [89]. Therefore, I assessed the embryo growth of *Lrp4;Lrp6* compound mutant embryos and *Lrp4* and *Lrp6* single mutant embryos at E9.5 and E10.5 (Figure 4.10). Besides the axial truncation phenotype which of course negatively affected the overall size of the embryos along the longitudinal axis, I could show that *Lrp6*$^{-/-}$ and *Lrp4*$^{-/-}$*;Lrp6*$^{-/-}$ embryos at

E9.5 and E10.5 displayed significantly reduced head dimensions (Figure 4.10). By measuring the dorsoventral and anteroposterior length of the embryo heads of all dissected embryos at E9.5 and E10.5, I could reveal that there is a significant reduction in head size for *Lrp6*$^{-/-}$ and *Lrp4*$^{-/-}$*;Lrp6*$^{-/-}$, but not for *Lrp4*$^{-/-}$ mutant embryos (Figure 4.10 B-C). This was also reflected in the growth curves that illustrate the growth increment of the respective dimension (Figure 4.11). Whereas the growth curves of *wild type* and *Lrp4*$^{-/-}$ embryos display steady growth in correlation to somite accumulation, *Lrp6*$^{-/-}$ and *Lrp4*$^{-/-}$*;Lrp6*$^{-/-}$ embryos show markedly impaired growth for R-C, D-V and A-P dimension (Figure 4.11). It was important to consider the axial truncation phenotype of *Lrp6* single mutants and *Lrp4;Lrp6* compound mutant embryos when comparing size measurements and growth curves. Taking this into account, I calculated the linear regression for the growth curves and adjusted the somite count (Figure 4.12 G-H). In doing so I could reveal that the growth deficit displayed by *Lrp6*$^{-/-}$ and *Lrp4*$^{-/-}$*;Lrp6*$^{-/-}$ embryos is an actual growth phenotype and not only a delay in embryonic growth. This can be documented by comparison of the linear regression values for the growth curves. A delayed embryo growth would show the same/similar slope values for the linear regression of *Lrp6*$^{-/-}$ and *Lrp4*$^{-/-}$*;Lrp6*$^{-/-}$ growth curves compared to *wild type* (see Subsection 4.3. However, the slope values for all measured dimensions in *Lrp6* single mutants and *Lrp4;Lrp6* compound mutant embryos are drastically reduced compared to *wild type* and *Lrp4*$^{-/-}$ embryos. The concept that WNT proteins can act as growth factors and positively regulate proliferation has been demonstrated for various tissues [10, 35, 91, 103, 118]. Disrupted WNT signal transduction can therefore lead to proliferation defects that imply impaired growth of tissue and organs. Since LRP6 is an essential component of the FZD-LRP receptor complex for WNT proteins and it is ubiquitously expressed from E8.5 to E10.5 (Figure 4.3), it seems plausible that loss of LRP6 leads to impaired proliferation and thus to smaller embryos at E9.5 and E10.5. By investigating the gross morphology, I could reveal that *Lrp6* single mutants and *Lrp4;Lrp6* compound mutant embryos displayed impaired growth of the head region, which implied that the formation of the forebrain might also be affected. On the other hand, my data did not reveal obvious differences in the gross morphology of *Lrp6*$^{-/-}$ mutants and *Lrp4;Lrp6* compound embryos, which prompted me to depict potential differences on a histological level.

5.4 *Lrp4;Lrp6* compound mutant embryos develop neuroepithelial excrescences

My observations revealed that *Lrp4;Lrp6* compound mutant embryos showed growth deficits at E9.5 and E10.5 to the same extent as *Lrp6* single mutant embryos (Figure 4.12). This affected the embryo length (R-C dimension) as well as the overall dimension of the embryo head (A-P and D-V dimension). Since it was my purpose to study implications of LRP4 on LRP5/6 during forebrain formation, a reduced head size was the first evident indication that telencephalic development could be affected in *Lrp6*$^{-/-}$ and *Lrp4*$^{-/-}$*;Lrp6*$^{-/-}$ embryos. Consequently, I examined the proliferation rate with MPM-2 immunostaining as a mitosis-specific marker [175] on forebrain sections of E9.5 embryos (Figure 4.14+4.15). I could show that *Lrp6*$^{-/-}$ embryos have a significantly reduced rate of actively proliferating progenitor cells within the neuroepithelium of the prospective forebrain (Figure 4.15 C). This is in line with already published data from Gray and others that showed a reduced rate of phospho-Histone H3 (another M-Phase marker) positive neural progenitors in the neuroepithelium of *Lrp6*$^{-/-}$ embryos at E9.0 [60]. Remarkably, I could show that *Lrp4;Lrp6* compound mutant embryos develop bulges of neural progenitor cells (referred to as neuroepithelial excrescences) that occur as locally restricted protuberances of the neuroepithelium (Figure 4.14 G+H). These tumor-like structures within the neuroepithelium were exclusively observed in *Lrp4;Lrp6* compound mutant embryos, neither *Lrp4*$^{-/-}$ nor *Lrp6*$^{-/-}$ showed comparable malformations. The progenitor cells within the neuroepithelial excrescences displayed an increased rate of proliferation compared to non-affected neuroepithelial regions, leading to an assymmetric appearance of the neural tube (Figure 4.15). Similiar assymmetrical structural defects of the neural tube have been reported by Draganova and others, where they could show that aberrant β-catenin signaling led to local increase of neural progenitors in the developing cortex [38, 90]. Yet another study reported a similiar phenotype caused by disuption of Tulp3, a protein involved in Shh pathway inhibition [80].

As a consequence of the localized thickening of the neuroepithelium the cellular organization as a pseudostratified columnar epithelium was disrupted - [79, 199]. Occasionally, ectopic invaginations could be observed within the neuroepithelial excrescences and the cell density seemed to be increased (Figure 4.19 and Figure 4.20). On the other hand, the overall proliferation rate of *Lrp4;Lrp6* compound mutants excluding the neuroepithelial excrescences was not significantly higher compared to the proliferation rate of *Lrp6*$^{-/-}$ NPCs (Figure 4.15 E). Given the fact that increased proliferation of neural progenitor cells led to a prema-

turely thickening of the neuroepithelium, the primary question was whether the cells undergo symmetric division (proliferative division) or that they already turn neurogenic (asymmetric division) - [58, 74]. To test this, I compared immunostainings of neural progenitor marker SOX-2 [59] with immunostainings of Vimentin as a marker for gliogenesis [185] and TUJ-1 (see Subsection 3.1.6), which appears in newly generated immature postmitotic neurons (Figure 4.18+4.20). I could show that at E9.5 the cells within the neuroepithelial excrescences were primarily positive for SOX-2. This implies that the increased proliferation does not lead to a prematurely asymmetric cell division as it naturally occurs at E10.0/E10.5 in the prospective forebrain [20]. While the proliferating NPCs at E9.5 mainly divided symmetrically, I could detect one exception where a cluster of Vimentin positive cells appeared in a neuroepithelial excrescence (Figure 4.18). At E10.5, when asymmetric cell division starts to occur in the murine forebrain and NPCs undergo neurogenic division, I could show that postmitotic cells (TUJ-1 positive) could be detected in neuroepithelial excrescences although they did not migrate to the basal side, which might also be a secondary effect of the excrescences formation as ectopic structures (Figure 4.17).

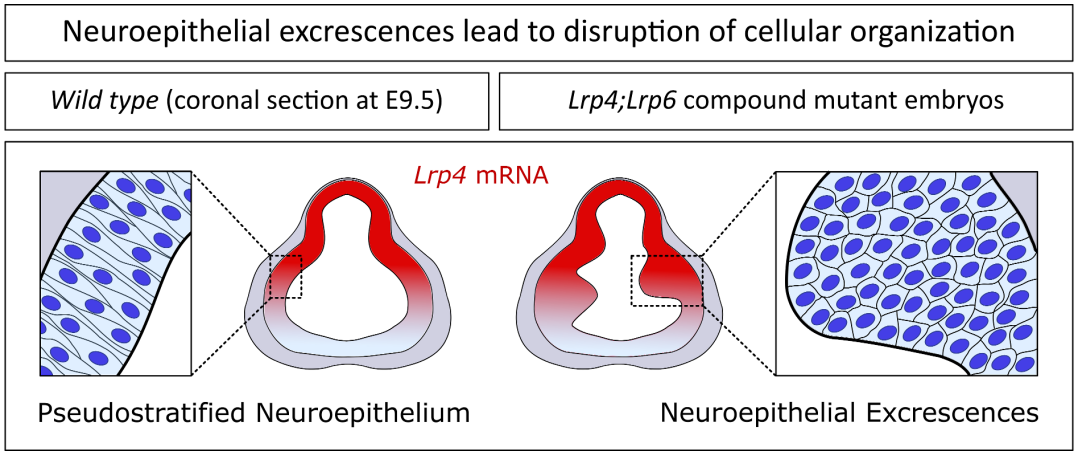

Figure 5.1: Schematic of neuroepithelial excrescences leading to disruption of the cellular organisation in the pseudostratifed NE

This schematic shows a coronal section of the forebrain at E9.5 (left side) with *Lrp4* expression highlighted in red. On the right side, a section of an *Lrp4;Lrp6* compound mutant embryo is illustrated. Neuroepithelial excrescences always appeared in the regions where *Lrp4* was expressed. Insets: On the left side a schematic of the pseudostratified NE structure is shown with NPCs spanning from the apical to basal side of the NE. On the right side the disorganized celluar alignment within an excrescence is depicted. The cells are no longer capable of spanning the whole apical-basal distance of the NE.

When examining phenotypes that affect proliferation, it is also advisable to consider implications on cell survival and apoptosis. Especially, since various studies reported that the WNT pathway is tightly linked to regulation of proliferation, cell survival and apoptosis during development of many tissues [10, 11, 23, 143]. Pharmacological studies found evidence that LRP6 is crucial for cell survival and inhibition of LRP6 leads to apoptosis and impaired proliferation [10, 103, 113]. Keeping this in mind, I performed immunostainings for apoptosis factor cleaved-Caspase-3 and TUNEL assays to examine whether cell survival and apoptosis was affected in *Lrp6*$^{-/-}$ and *Lrp4*$^{-/-}$*;Lrp6*$^{-/-}$ embryos. I could consistently detect patches of apoptotic cells within the neuroepithelium of *Lrp6* single mutant embryos and *Lrp4;Lrp6* compound mutants at E9.5 (Figure 4.16). This is in contrast with findings of Gray and others who investigated LRP6 loss-of-function and gain-of-function embryos at E9.0 [60]. One potential explanation could be the different mouse strains on which the mutations were maintained. Gray and others used A-strain and C3H/HeJ mice for their studies, whereas I kept my mouse models exclusively on a C57Bl/6N background. However, my results could deliver evidence that LRP4 in combination with LRP6 is required to maintain the balance of proliferation and cell survival in the neuroepithelium of E9.5 embryos [60].

5.5 WNT pathway is affected in *Lrp6* single mutants and *Lrp4;Lrp6* compound mutant embryos but not in *Lrp4*$^{-/-}$

To prove the assumption that in *Lrp6* single mutants WNT signal transduction is affected in the developing forebrain and further to find evidence that *Lrp4;Lrp6* compound mutant embryos might display a divergent WNT target gene expression, I performed *in situ* hybridization experiments. Moreover, I intended to analyze other major pathways that are involved in formation of the telencephalon (Subsection 1.1.1). For this, I conducted ISH experiments of the appropriate morphogens and their corresponding gene targets (Subsection 4.5). My results show that neither BMP signaling nor SHH signaling pathway was affected on the level of morphogen expression and activation of respective target gene expression (Subsection 4.5.1+4.5.2). Unfortunately, I had not enough samples of *Lrp4;Lrp6* compound mutant embryos to include sufficient number of sections into the ISH analysis addressing BMP and SHH signaling pathway gene expression. However, my study was focused to address the question to what extent LRP4 contributes to WNT-LRP mediated WNT signal transduction. And since the observed phenotype of developing neuroepithelial excrescences in *Lrp4;Lrp6* compound mutant embryos could likely be linked to the effect of WNT factors, which act as

growth factors [131] , I concentrated on the transcript expression analysis of WNT signaling components (Subsection 4.5.4). I could show that *Wnt1* and *Wnt3a* expressing domains were present in the dorsal midline of *Lrp6* single mutant forebrains (Figure 4.5.3), this was essential to verify since Pinson and others reported that *Wnt3a* expression in the tail of *Lrp6* loss-of-function mutants is lost [146]. However, since it was shown that LRP6 plays a role in WNT signal transduction, it was critical to examine WNT downstream target gene expression in the prospective forebrain of $Lrp6^{-/-}$ and $Lrp4^{-/-};Lrp6^{-/-}$ embryos. I could show that loss of LRP6 leads to a markedly reduced expression of WNT downstream targets *Lef1* [45, 77] and *Axin2* [84, 115] in neuroepithelial cells of the prospective forebrain. Thus, my results deliver supporting evidence that LRP6 is essential for proper WNT signal transduction in NPCs during forebrain development. Conversely, my results deliver evidence that in the neuroepithelium of *Lrp4;Lrp6* compound mutant embryos expression of WNT downstream target genes *Lef1* and *Axin2* was partially restored (Figure 4.5.4). In dorsolateral regions of the prospective forebrain, where *Lrp4* is normally expressed transcripts of *Lef1* and *Axin2* could be detected and clearly exceeded the expression levels of $Lrp6^{-/-}$ embryos (Figure 4.5.4). Interestingly, $Lrp4^{-/-}$ embryos seem to express *Axin2* and *Lef1* to same extent as *wild type* littermate control embryos. Although, staining intensity of ISH sometimes appeared a bit stronger in *Lrp4* single mutant embryos (more quantitative methods would be necessary to validate this impression) - (Figure 4.5.4). After all, I found evidence that additional loss of LRP4 on a *Lrp6* loss-of-function background leads to a partial compensation of reduced WNT target gene expression in the neuroepithelium of the developing forebrain.

5.6 Further evidence that WNT readout is reduced in $Lrp6^{-/-}$ and to some extent compensated in $Lrp4^{-/-};Lrp6^{-/-}$ neuroepithelium of the prospective forebrain

To find further evidence that *Lrp6* single mutants show a reduction of WNT downstream targets and *Lrp4;Lrp6* compound mutants might transduce WNT signaling more effciently in the developing forebrain, I additionally performed immunostainings for cyclin D1 and PAX6. On the one hand, it was reported that cyclin D1 expression is initiated upon β-catenin accumulation in the nucleus [176] and activated by direct WNT target LEF1 transcription factor which can bind to the promoter region of cyclin D1 [162]. On the other hand, cyclin D1 is well-known for its function as a regulator of proliferation and was shown to be increasingly expressed in proliferating tissues [130, 149, 169]. Therefore, cyclin D1 represented an ade-

quate read-out to first examine WNT target gene activation and second to study proliferative capacity of NPCs in the neuroepithelium of *Lrp6*$^{-/-}$ and *Lrp4*$^{-/-}$;*Lrp6*$^{-/-}$ embryos. I could show that cyclin D1 expression was massively downregulated in the neuroepithelium of *Lrp6* single mutant embryos at E9.5. As depicted in Figure 4.26-C the dorsal region of the forebrain is almost void of cyclin D1 positive NPCs and further the neuroepithelium appears to be thinner than in *wild type* littermate embryos. In a variety of *Lrp6*$^{-/-}$ embryos at E9.5, I observed this phenomenon which could be a secondary effect of the reduced proliferation rate of NPCs (Figure 4.27). I observed higher expression levels of cyclin D1 in dorsal regions of the forebrain at E9.5 in *Lrp4;Lrp6* compound mutant embryos (Figure 4.27). Moreover, the neuroepithelial excrescences of *Lrp4*$^{-/-}$;*Lrp6*$^{-/-}$ embryos were also positive for cylclin D1 immunostaining. This might be an indication that higher levels of cyclin D1 could contribute to the imbalanced regulation of NPC proliferation and ultimately facilitating the emergence of excrescences in the neuroepithelium of *Lrp4*$^{-/-}$;*Lrp6*$^{-/-}$ embryos (Figure 4.27). However, the analysis of E10.5 *Lrp6* single mutants and *Lrp4;Lrp6* compound embryos revealed that cyclin D1 was still expressed in neuroepithelial excrescences, but cyclin D1 levels of *Lrp6*$^{-/-}$ embryos in the prospective forebrain were no longer dramatically reduced compared to *wild type* or *Lrp4*$^{-/-}$ littermate control embryos (Figure 4.28). The cause of the observed differences in cyclin D1 levels in the neuroepithelium of *Lrp6* single mutant embryos at E9.5 and E10.5 remain to be elucidated. However, I could deliver supporting evidence that another WNT downstream target is differentially expressed in the developing forebrain of *Lrp6*$^{-/-}$ and *Lrp4*$^{-/-}$;*Lrp6*$^{-/-}$ embryos.

PAX6 is a transcription factor that is also tightly linked to the regulation of proliferation and cell cycle progression and was reported to play a prominent role in balancing proliferation and differentiation in NPCs [41, 186, 190, 210]. Recent publications also suggested PAX6 as a bona fida WNT/β-catenin downstream target, but it is not yet reliably proved to act in such manner [53, 200]. Nonetheless, I included immunostaining of PAX6 to my E9.5 *Lrp6*$^{-/-}$ and *Lrp4*$^{-/-}$;*Lrp6*$^{-/-}$ forebrain analysis. I found that in the dorsal neuroepithelium of *Lrp6* single mutant embryos immunostaining of PAX6 consistently appeared stronger compared to littermate control embryos (Figure 4.30+4.31). Gray and other reported in their studies that on a transcriptional level *Pax6* was expressed in a broader domain of the neuroepithelium of E9.0 embryos [60]. In contrast, this elevated PAX6 immunostaining was not reflected in *Lrp4;Lrp6* compound mutant embryos (Figure 4.31). Considering PAX6 as target of WNT signal transduction would be in contradiction with the findings that WNT target genes were less active in *Lrp6*$^{-/-}$ NPCs (Subsection 5.5). Regarding proliferation regulation of PAX6, several studies could show that high PAX6 levels have a negative effect on proliferation. Mi et al. and Du-

parc et al. revealed that loss of PAX6 increases proliferation of neural progenitors and that overexpression of *Pax6* leads to repression of cellular proliferation respectively [41, 125, 190]. This would be in line with my findings that *Lrp6*$^{-/-}$ embryos have elevated PAX6 levels and show decreased proliferation of NPC in the neuroepithelium. On the other hand, PAX6 levels appeared to be less in *Lrp4;Lrp6* compound mutants, when compared to *Lrp6*$^{-/-}$ embryos (Figure 4.31). The fact that neuroepithelial excrescences admittedly contained PAX6 positive NPCs but showed lower staining intensity than *Lrp6*$^{-/-}$ samples, could represent a connection to the observed hyperproliferation within the neuroepithelial excrescences.

One of the best read-outs for active WNT signaling and proper WNT signal transduction is the distribution of β-catenin (Subsection 1.3.2). Translocation of β-catenin into the nucleus indicates active WNT signaling. Unfortunately, immunostainings with β-catenin antibodies on embryo sections do not depict precise localization of β-catenin on a cellular level (Figure 4.17). Nonetheless, I found indirect evidence that WNT signal transduction in the forebrain of *Lrp6* single mutants and *Lrp4;Lrp6* compound mutants is affected and thus intracellular β-catenin levels are changed. Further evidence for the activation of WNT downstream targets were found by examining *Gfp* expression of the *TCF/Lef:H2B-GFP* reporter strain (Subsection 3.3.5). Thus, I could monitor *Tcf/Lef* promoter activity downstream of WNT/β-catenin in *Lrp6* single mutants and *Lrp4;Lrp6* compound mutant embryos (Figure 4.32). My results on *TCF/Lef:H2B-GFP* reporter activity in the neuroepithelium of the developing forebrain revealed that the number of WNT responsive NPCs in *Lrp6*$^{-/-}$ embryos is greatly reduced, whereas in *Lrp4;Lrp6* compound mutant embryos I could detect many dorsolareally located GFP-positive NPCs in the prospective forebrain (Figure 4.32). Thus, I could deliver further evidence that WNT signals are more efficiently transduced in dorsal NPCs of *Lrp4*$^{-/-}$*;Lrp6*$^{-/-}$ E9.5 embryos compared to a markedly reduced WNT signal transduction in *Lrp6* single mutants.

5.7 WNT3a uptake of *Lrp6* single mutant embryos is markedly reduced, whereas WNT3a binding reduction seems to be reversed in *Lrp4;Lrp6* compound mutants

Various WNT proteins are expressed in the prospective forebrain at E9.5 [66, 142]. Whereas WNT1 and WNT3a are expressed in the dorsal midline, which is a rather restricted domain (Figure 4.23), other WNT proteins - such as WNT7a and Wnt7b - show broader domains of expression in the developing forebrain [75, 142, 150]. Furthermore, distinct WNT factors seem to play diverse roles during formation of the central nervous system. For instance,

Megason and others could show that WNT1 and WNT3a have a mitogenic effect on neural precursor cells, whereas other WNT proteins (e.g. WNT3, WNT4, WNT7a, WNT7b) do not affect proliferation of NPCs [124]. It has been shown that WNT1 and WNT3a are tightly linked to proliferative activity of neural progenitor cells [85, 141, 160]. Initially, loss-of-function experiments revealed that major parts of the brain were not forming in mice that were deficient for *Wnt1* and *Wnt3a* [105, 123]. *Wnt1/Wnt3a* compound mutants display even additional reduction of brain mass, showing that WNT1 and WNT3a - even though their expression domains overlap (see also Figure 4.23) - have a synergistic effect on proliferative activity in the developing brain [81]. On the other hand, artificially increased levels of WNT1 and WNT3a cause ectopic proliferation of progenitor cells [52, 141].

To prove whether the observed proliferation phenotype in *Lrp6*$^{-/-}$ and *Lrp4*$^{-/-}$*;Lrp6*$^{-/-}$ embryos (Subsection 4.4.1+4.4.2) can be linked to WNT1 or WNT3a signaling, I performed *ex vivo* uptake experiments (Subsection 4.7). Unfortunately, I could not establish uptake experiments with murine WNT1, since either the recombinant ligand could not be labeled or the embryos did not bind labeled WNT1 (data not shown). For that reason, I had to concentrate on uptake experiments with labeled WNT3a (Subsection 4.7.1). On the other hand, it has been reported that the extracellular domain of LRP6 contains binding sites for WNT3a [12, 28]. WNT3a also seemed to be a promising candidate for causing the observed proliferation defects in *Lrp6*$^{-/-}$ and *Lrp4*$^{-/-}$*;Lrp6*$^{-/-}$ embryos. Various studies delivered lines of evidence that WNT3a is a potent activator of proliferation [34, 67, 85, 160, 189]. With my *ex vivo* uptake experiments, I could show for the first time that WNT3a binding and uptake is significantly reduced in *Lrp6* single mutant embryos (Subsection 4.7.1). This delivers strong evidence that defective WNT3a signal transduction could be the cause for the observed reduction in proliferation activity in the neuroepithelium of *Lrp6* single mutants at E9.5 (Subsection 4.7.2). In contrast, one would expect the exact opposite namely elevated WNT3a levels to explain the observed hyperproliferative areas in the neuroepithelium of *Lrp4;Lrp6* compound mutant embryos (Subsection 4.7.2). Although, I could analyze only one *Lrp4;Lrp6* compound mutant embryo at E9.5 in a WNT3a uptake assay so far. This *Lrp4*$^{-/-}$*;Lrp6*$^{-/-}$ embryo showed indeed a strikingly increased binding and uptake of fluorophore-labeled WNT3a compared to *Lrp6* single mutants. Especially, in the regions of the neuroepithelium that displayed excrescences, the number of internalized WNT3a-A488 positive vesicles was increased (Figure 4.35). Nevertheless, further uptake experiments with *Lrp4;Lrp6* compound mutants are required to verify that elevated WNT3a levels are causative for the observed neuroepithelial excrescences.

So far, this leads to the presumption that in absence of LRP6, WNT3a binding is dramat-

ically impaired. But when both LRP6 and LRP4 are missing, impairment of WNT3a binding is reversed (reflecting my observations of WNT downstream target activation in *Lrp6*$^{-/-}$ and *Lrp4*$^{-/-}$*; Lrp6*$^{-/-}$ embryos - described in Subsection 4.5+4.6. This would require two inferences: First, LRP4 needs to have an inhibitory effect on WNT3a binding and signaling (either direct or indirect). This would be in line with the proposed function of LRP4 in WNT-dependent signal transduction models for other tissues [3, 137] - see also Subsection 1.3.4. Secondly, another receptor besides LRP6 (likely LRP5) would be capable of transducing (though to a limited extent) WNT3a signals, but it is repressed from binding WNT3a in presence of LRP4.

Other studies correlated altered WNT3a signal transduction to malformations and disorganization in neural tissue. For instance, Munji and others could show that ectopic WNT3a expression in embryonic cortical tissue leads to increased proliferation of NPCs, formation of ectopic neural bulges (referred to as nodules) and tissue dysplasia [128]. Megason and others could reveal by electroporation experiments in chick embryos that WNT3a overexpression causes markedly increased NPC proliferation, which ultimately leads to ectopic invaginations of the neural tube [124]. Thus, the observed growth-related phenotypes in *Lrp6*$^{-/-}$ and *Lrp4*$^{-/-}$*;Lrp6*$^{-/-}$ embryos, including formation of neuroepithelial excrescences and ectopic invaginations might be a direct or indirect consequence of modified WNT3a signal transduction.

5.8 Summary and hypothetical models for WNT pathway regulation in the neuroepithelium during early embryonic forebrain development

My results deliver lines of evidence that LRP4 and LRP6 are essential for keeping the balance of proliferation and cell survival in neuroepithelial progenitor cells during critical stages of embryonic forebrain development. Impaired WNT signal transduction accompanied by reduced proliferative activity of NPCs in the neuroepithelium of *Lrp6*$^{-/-}$ embryos shows that LRP6 is essential to transduce WNT signals in neural precursor cells in the prospective forebrain. Further, I could show that binding of WNT3a is significantly reduced in *Lrp6*$^{-/-}$embryos and that the impaired WNT3a binding capacity might lead to the observed reduction of mitogenic activity in NPC in the prospective forebrain. This is supported by the finding that in the neuroepithelium of *Lrp4;Lrp6* compound mutant embryos the WNT downstream targets are expressed at higher levels compared to *Lrp6*$^{-/-}$ embryos, which is associated with the appearance of ectopic NPC proliferation leading to the formation of neuroepithelial excrescences. These findings suggest that LRP4 has an inhibitory effect on WNT signal transduction in the developing forebrain. In *Lrp4;Lrp6* compound mutants, when LRP4 function is lost on

a *Lrp6*$^{-/-}$ background the inhibitory effect on the FZD-LRP receptor complex is relieved and WNT signals are more effectively transduced compared to *Lrp6*$^{-/-}$ embryos where the LRP4 inhibition is present. It remains to be elucidated whether the inhibitory effect of LRP4 on WNT signal transduction during forebrain formation is of a direct nature or in combination with other WNT inhibiting factors. Ahn and others reported on multiple modes of WNT-related modulation by LRP4 and inhibition in interplay with WNT antagonist WISE or SOSTDC1 in non-neural tissue [3, 4]. Since WISE is not expressed in the neuroepithelium early but can be detected at later stages (E13.5) in the brain [32], the inhibition of LRP4 in early forebrain development might be in interaction with a different WNT antagonist – referred to as WNT inhibiting facor X.

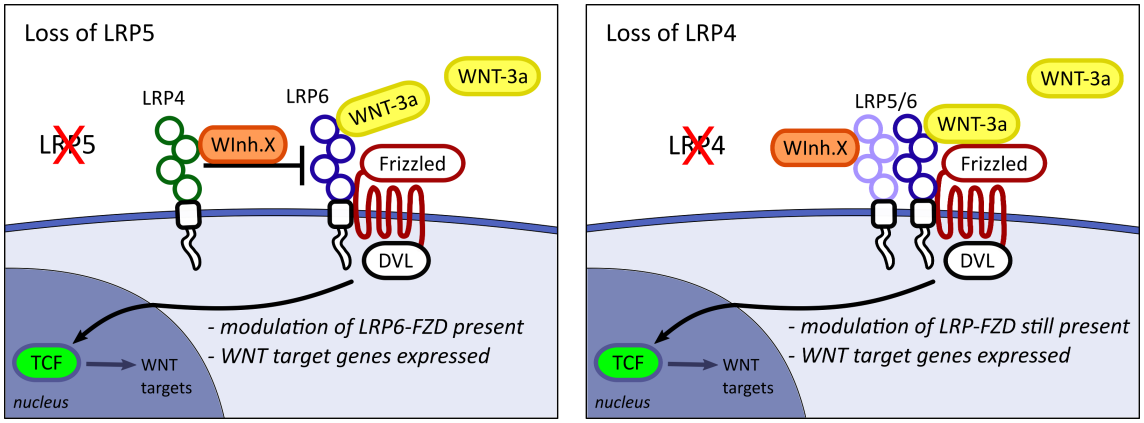

Figure 5.2: Schematics for LRP-FZD modulation: WNT downstream target activation in the prospective forebrain of LRP5 and LRP4 loss-of-function mutant embryos

(Loss of LRP5) In absence of LRP5, LRP6 can fully compensate the loss of LRP5 function in the developing forebrain. Therefore, this schematic also represents the wild type situation. LRP4 modulates the WNT signal transduction in interplay with WNT inhibitor X (WInh.X) by inhibiting WNT3a binding to the LRP-FZD receptor complex. **(Loss of LRP4)** In absence of LRP4, WNT inhibitor X can still bind to the LRP-FZD receptor complex (at least to a certain extent) so that expression of WNT downstream targets is not affected.

My findings contribute to lay the foundation of a model how LRP4 can modulate WNT signal transduction in a LRP5/6 dependent manner during early forebrain development. However, further experiments need to be performed to establish a profound model of how LRP4 is acting on the efficiency of signal transduction by the FZD-LRP receptor complex. Nevertheless, I want to illustrate my findings in hypothetical models to propose theoretical support to understand the observed phenotypes of the different mouse models that I analyzed.

Assuming LRP4 acts in an inhibitory fashion in interplay with another WNT antagonist during early forebrain development to modulate LRP-FZD function, could lead to the following

hypothetical models (following the proposed model from Ahn et al. [3, 4]. LRP4 with WNT inhibitor X acts in a modulatory manner on the WNT binding capacity of LRP5/6 and thus acting on the WNT signal transduction efficiency (illustrated in Figure 5.2). Loss of LRP5 does not lead to significant changes in this model, because LRP6 can fully compensate. Since I could not quantify any changes of WNT downstream target expression in *Lrp4* single mutant embryos (perhaps more quantitative analyzing methods could potentially reveal differences in WNT target gene activation of *Lrp4* single mutants compared to *wild types*) , I would propose that in absence of LRP4 the WNT inhibiting factor X alone can still (at least to a certain extent) bind to the LRP-FZD complex and thus modulate WNT readout – WNT downstream target expression is not different compared to *wild type* embryos (Figure 5.2). In contrast, WNT downstream target expression is greatly reduced when LRP6 function is lost. LRP5 cannot fully compensate for the loss of LRP6 and on top of that LRP4 with WNT inhibitor X represses WNT binding capacity of LRP5 leading to a markedly decreased WNT signal transduction (Figure 5.3). In *Lrp4;Lrp6* compound mutants, LRP4 can no longer present WNT inhibitor factor X to LRP5 and without LRP6 being present, WNT inhibiting factor X cannot bind to LRP5 effectively. Therefore, WNT binding capacity of LRP5 is greater when LRP4+LRP6 are absent compared to absence of LRP6 alone, leading to elevated expression levels of WNT downstream targets (compared to the situation in *Lrp6* single mutant embryos).

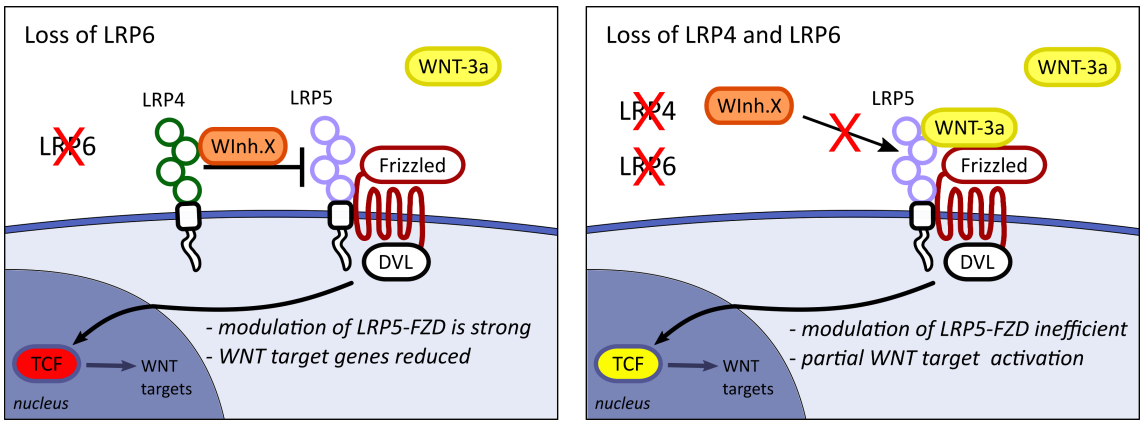

Figure 5.3: Schematics for LRP-FZD modulation: WNT downstream target activation in the prospective forebrain of LRP6 single mutants and LRP4;LRP6 compound mutant embryos

(Loss of LRP6) When LRP6 function is lost, LRP5 cannot fully compensate and binding of WNT3a is impaired which leads to great reduction of WNT target gene expression. In addition, LRP4 inhibition in interplay with WNT inhibiting factor X acts on the LRP5-FZD complex. WNT signal transduction is markedly reduced. **(Loss of LRP4;LRP6)** In Lrp4;6 compound mutants, LRP4 can no longer present WNT inhibitor X to the LRP-FZD complex and LRP5 binding of WInh.X is too weak to have an inhibiting effect on binding of WNT3a. Therefore, WNT downstream targets are expressed to a higher extent compared to LRP6 loss-of-function situation.

Although these models still need to be verified (or refined) by further experiments, they can deliver a theoretical attempt to explain the observed phenotypes in the neuroepithelium of the analyzed mouse models during early forebrain development. In the next section, I critically assess the findings and propose further experiments to support my data.

5.9 Critical assessment of the results and future perspectives

My findings deliver clear indications that LRP4 is implicated in WNT signaling transduction and regulation of NPC proliferation during early forebrain development. However, it is not conclusive why *Lrp4* loss-of-function mutant embryos do not reveal increased levels of WNT downstream targets, when LPR4 has an inhibitory function on the LRP-FZD receptor complex. On the one hand, there might be slightly higher levels of downstream targets in *Lrp4*$^{-/-}$ embryos, but the methods (i.e. IHC and ISH) that were used in my study might be not precise enough to detect these differences compared to *wild type* embryos. This could be tested with more quantitative methods such as protein immunoblots or by real-time PCR. On the other hand, lack of LRP4 could be compensated (as suggested in Figure 5.3) by sufficient binding of WNT antagonists to LRP5/6, but not to LRP5 alone. However, there are slight indications in my results that loss of LRP4 alone could lead to changes in WNT downstream target expression. In Figure 4.25-C+c', the *Lef1* expressing domain in Lrp4 mutants appears to extend into the roof plate, whereas it is void of *Lef1* in the *wild type* (Figure 4.25-A+a'). A similar effect can be seen Figure 4.32-C, the *Lrp4*$^{-/-}$ embryo appears to have a little more GFP-positive cells in the dorsal domain compared to the *wild type* (Figure 4.32-A). Nonetheless, these are just hints that *Lrp4*$^{-/-}$ embryos could have slightly increased WNT target gene activation in the forebrain and further experiments that are more sensitive (quantitative) to reveal even slight differences are required.

Another aspect that remains unresolved is the observation that hyperproliferation in *Lrp4;Lrp6* compound mutant embryos does not affect all sites of the neuroepithelium where *Lrp4* is naturally expressed. Instead, neuroepithelial excrescences appear locally restricted in an unpredictable manner. As already mentioned, I could neither detect neuroepithelial excrescences in *Lrp4*$^{-/-}$ nor *Lrp6* single mutant embryos. However, I observed a high variability in manifestation of the phenotype affecting forebrain morphology in *Lrp6* single mutant embryos – this was also reported by Gray and others [60]. This might also explain why the *Lrp4;Lrp6* compound mutant phenotype appears in different ways including discrete appearance of neuroepithelial excrescences within the neuroepithelium.

A general limitation to the progress of my studies was the low rate of generating *Lrp4;Lrp6* compound mutant embryos. Certainly, *in vivo* experiments are advantageous compared to *ex vivo* or *in vitro* assays in regard of natural physiological/environmental conditions. However, to further investigate the modulatory role of LRP4 on the LRP-FZD receptor complex in NPCs, it might be beneficial to establish an *in vitro* system to recapitulate the observed proliferation phenotypes and WNT transduction modulation. Another possibility to increase the number of LRP4;LRP6 deficient embryos could be the pharmacological inactivation of LRP6 in E8.5 or E9.5 *Lrp4*$^{-/-}$ embryos *ex vivo* – several agents to inactivate LRP6 function are reported [10, 104, 113].

In summary, my results lay a profound basis of *in vivo* observations that reveal the implications of LRP4 and LRP6 in transducing WNT signals and regulating proliferation in NPCs during early forebrain development. However, to fully understand the mechanism how LRP4 modulates the LRP-FZD complex in respect of WNT binding and transduction capacity in the developing telencephalon further experiments are required.

A Appendix

A.1 List of Algorithms

List of Algorithms

1 Equation to calculate amount of restriction enzyme for DNA cutting 25

2 Formula to calculate amount of insert DNA for ligation 26

3 Script for quantification of WNT3a-A488 positive vesicles 41

A.2 List of Figures

List of Figures

1.1 Signaling centers during early forebrain development 3

1.2 Cellular organization of the pseudostratified neuroepithelium 4

1.3 The low density lipoprotein receptor (LDLR) family 6

1.4 Schematic model of WNT signaling transduction 14

1.5 Schematic of proposed model for LRP4 modulation of the LRP-FZD complex 16

3.1 Schematic of the experimental design for the *in vitro* uptake assay of WNT3a-A488 34

3.2 Schemtic overview of coronal section planes along the anterior-posterior axis 36

4.1 *Lrp4* starts to be expressed between E8.5 and E9.5 in the neural tube 44

4.2 *Lrp5* starts to be expressed at E8.5 in the neural folds 46

4.3 *Lrp6* is ubiquitously expressed in neural tissue between E8.5 and E12.5 47

4.4 $Lrp4^{-/-}; Lrp5^{-/-}$ compound mutant embryos show a lethality phenotype at E10.5 . 49

4.5 $Lrp4^{-/-}; Lrp5^{-/-}$ embryos have a high incidence of embryonic resorption at E10.5 . 50

4.6 Loss of LRP4; LRP5 leads to a delayed closure of the anterior neuropore 51

4.7 $Lrp4^{-/-}; Lrp5^{-/-}$ compound mutants $\leq$ E10.5 could be generated due to expected ratio 53

4.8 Neural tube closure deficit in $Lrp6^{-/-}$ embryos persists in $Lrp4^{-/-}; Lrp6^{-/-}$ embryos 54

4.9 $Lrp6^{-/-}$ and $Lrp4^{-/-}; Lrp6^{-/-}$ embryos display a caudal truncation phenotype with a significant loss of somites 56

4.10 $Lrp6^{-/-}$ and $Lrp4^{-/-}; Lrp6^{-/-}$ embryos are significantly smaller than littermates . . . 59

4.11 Somite related growth curves of $Lrp6^{-/-}$ and $Lrp4^{-/-}; Lrp6^{-/-}$ embryos reveal growth deficits at E9.5 and E10.5, whereas $Lrp4^{-/-}$ embryos show normal growth 62

4.12 Comparing linear regression slopes of somite matched growth curves for embryos at E9.5 and E10.5 63
4.13 *Lrp4*$^{-/-}$;*Lrp6*$^{-/-}$ embryos develop neuroepithelial excrescences at E9.5 66
4.14 Neuroepithelial excrescences display an elevated rate of mitotic cells 68
4.15 The rate of mitotic cells is increased within neuroepithelial excrescences 69
4.16 Immunohistological staining with cleaved-Caspase-3 highlights clusters of apoptotic cells in *Lrp6*$^{-/-}$ and *Lrp4*$^{-/-}$;*Lrp6*$^{-/-}$ embryos 71
4.17 β-catenin staining reveals structural aberrations of *Lrp6*$^{-/-}$ and *Lrp4*$^{-/-}$;*Lrp6*$^{-/-}$ neuroepithelium 73
4.18 Vimentin can be detected in neuroepithelial excrescences of *Lrp4*$^{-/-}$;*Lrp6*$^{-/-}$ embryos 74
4.19 Pseudostratified neuroepithelial organization is lost in *Lrp4*$^{-/-}$;*Lrp6*$^{-/-}$ excrescences 77
4.20 At E9.5, cells within neuroepithelial excrescences retain their progenitor character 78
4.21 Expression of *Bmp4* and downstream target *Id3* is not altered in the prospective telencephalon of LRP4 deficient embryos 80
4.22 *Shh* expression in the floor plate and downstream target *Nkx2.1* are not altered in *Lrp4*$^{-/-}$ and *Lrp6*$^{-/-}$ embryos 82
4.23 Loss of LRP4 or LRP6 does not affect the expression of *Wnt1* and *Wnt3a* in the dorsal midline of developing the forebrain 84
4.24 Reduction of *Axin2* expression levels in *Lrp6*$^{-/-}$ embryos is partially compensated in *Lrp4*$^{-/-}$;*Lrp6*$^{-/-}$ compound mutant embryos 86
4.25 Expression of WNT downstream target *Lef1* is markedly reduced in *Lrp6* deficient embryos, whereas *Lrp4*$^{-/-}$;*Lrp6*$^{-/-}$ compound mutants show elevated levels of *Lef1* expression 87
4.26 Wnt/β-catenin downstream target cyclin D1 is reduced in *Lrp6*$^{-/-}$ neuroepithelium but not in *Lrp4*$^{-/-}$;*Lrp6*$^{-/-}$ embryos at E9.5 89
4.27 Cyclin D1 expression can be detected in neuroepithelial excrescences of in *Lrp4*$^{-/-}$;*Lrp6*$^{-/-}$ embryos 90
4.28 At E10.5, levels of cyclin D1 in *Lrp6*$^{-/-}$ embryos do not notably differ from *wild type* embryos 92
4.29 Neuroepithelial excrescences in *Lrp4*$^{-/-}$;*Lrp6*$^{-/-}$ embryos at E10.5 do not display enhanced cyclin D1 levels 93
4.30 PAX6 levels were increased in *Lrp6*$^{-/-}$ neuroepithelial cells but not in *Lrp4*$^{-/-}$;*Lrp6*$^{-/-}$ embryos 95
4.31 PAX6 can be detected in neuroepithelial excrescences of *Lrp4*$^{-/-}$;*Lrp6*$^{-/-}$ embryos 96

4.32 Less WNT-responsive neuroepithelial cells were found in *Lrp6*$^{-/-}$ embryos at E9.5, whereas *Lrp4*$^{-/-}$;*Lrp6*$^{-/-}$ compound mutants had more GFP+ cells in the dorsal neural tube 98
4.33 WNT3a uptake of neuroepithelium is significantly reduced in *Lrp6*$^{-/-}$ embryos at E8.5 100
4.34 WEC experiments at E8.5 revealed lessened WNT3a uptake even in *Lrp6*$^{+/-}$ embryos 101
4.35 An increased uptake of WNT3a-A488 is detected in the neuroepithelial excrescences 104
4.36 Reduction/loss of LRP6 receptor leads to impaired uptake of WNT3a, which was not reflected in *Lrp4*$^{-/-}$;*Lrp6*$^{-/-}$ embryos 105
5.1 Schematic of neuroepithelial excrescences leading to disruption of the cellular organisation in the pseudostratifed NE 116
5.2 Schematics for LRP-FZD modulation: WNT downstream target activation in the prospective forebrain of LRP5 and LRP4 loss-of-function mutant embryos 123
5.3 Schematics for LRP-FZD modulation: WNT downstream target activation in the prospective forebrain of LRP6 single mutants and LRP4; LRP6 compound mutant embryos 124

A.3 List of Tables

List of Tables

1.1 (a) List of loss-of-function models of LDLR protein family 8
1.2 (b) List of loss-of-function models of LDLR protein family 9
3.1 List of technical equipment 19
3.2 List of consumables and kits 19
3.3 List of chemicals and reagents 20
3.4 List of buffers and solutions 21
3.5 List of media 22
3.6 List of primary antibodies 22
3.7 List of secondary antibodies 22
3.8 List of primers 23
3.9 List of ISH riboprobes 23
3.10 PCR programs for genotyping *Lrp4 and Lrp5* samples 30
3.11 PCR programs for genotyping *Lrp6 and TCF/Lef1-GFP* samples 30
4.1 Statistical tests for data shown in Figure 4.8 54
4.2 Statistical tests for data shown in Figure 4.9 57
4.3 Statistical tests for data shown in Figure 4.10 graph a' + a" 60
4.4 Statistical tests for data shown in Figure 4.10 graph b' + b" 60
4.5 Statistical tests for data shown in Figure 4.10 graph c' + c" 61
4.6 Linear regression values of curves shown in Figure 4.12 64
4.7 Statistical tests for data shown in Figure 4.34' 102
4.8 Statistical tests for data shown in Figure 4.36 106

A.4 Curriculum vitae (CV)

Due to privacy protection the CV is not included in the online-version.

Der Lebenslauf ist in der Online-Version aus Gründen des Datenschutzes nicht enthalten.

A.5 Bibliography

References

[1] Eeva Aaku-Saraste, Andrea Hellwig, and Wieland B. Huttner. Loss of Occludin and Functional Tight Junctions, but Not ZO-1, during Neural Tube Closure Remodeling of the Neuroepithelium Prior to Neurogenesis. *Developmental Biology*, 180(2):664–679, 1996.

[2] Victoria E. Ahn, Matthew Ling Hon Chu, Hee Jung Choi, Denise Tran, Arie Abo, and William I. Weis. Structural basis of Wnt signaling inhibition by Dickkopf binding to LRP5/6. *Developmental Cell*, 21(5):862–873, 2011.

[3] Youngwook Ahn, Carrie Sims, Jennifer M Logue, Scott D Weatherbee, and Robb Krumlauf. Lrp4 and Wise interplay controls the formation and patterning of mammary and other skin appendage placodes by modulating Wnt signaling. *Development (Cambridge, England)*, 140(3):583–93, 2013.

[4] Youngwook Ahn, Carrie Sims, Megan J. Murray, Paige K. Kuhlmann, Jesús Fuentes-Antrás, Scott D. Weatherbee, and Robb Krumlauf. Multiple modes of Lrp4 function in modulation of Wnt/β-catenin signaling during tooth development. *Development*, (July):dev.150680, 2017.

[5] Nuno Andrade, Vukoslav Komnenovic, Sophia M Blake, Yves Jossin, Brian Howell, Andre Goffinet, Wolfgang J Schneider, and Johannes Nimpf. ApoER2/VLDL receptor and Dab1 in the rostral migratory stream function in postnatal neuronal migration independently of Reelin. *Proceedings of the National Academy of Sciences of the United States of America*, 104(20):8508–13, 2007.

[6] Nisha M. Badders, Shruti Goel, Rod J. Clark, Kristine S. Klos, Soyoung Kim, Anna Bafico, Charlotta Lindvall, Bart O. Williams, and Caroline M. Alexander. The Wnt receptor, Lrp5, is expressed by mouse mammary stem cells and is required to maintain the basal lineage. *PLoS ONE*, 4(8), 2009.

[7] A. Barik, Y. Lu, A. Sathyamurthy, A. Bowman, C. Shen, L. Li, W.-c. Xiong, and L. Mei. LRP4 Is Critical for Neuromuscular Junction Maintenance. *Journal of Neuroscience*, 34(42):13892–13905, 2014.

[8] Denis Barry and Hieran McDermott. Differentiation of radial glia from radial precursor cells and transformation into astrocytes in the developing rat spinal cord. *Glia*, 50(3):187–197, 2005.

[9] P Bhanot, M Brink, C H Samos, J C Hsieh, Y Wang, J P Macke, D Andrew, J Nathans, and R Nusse. A new member of the frizzled family from Drosophila functions as a Wingless receptor., 1996.

[10] Birdal Bilir, Omer Kucuk, and Carlos S Moreno. Wnt signaling blockage inhibits cell proliferation and migration, and induces apoptosis in triple-negative breast cancer cells. *Journal of translational medicine*, 11(1):280, 2013.

[11] Peter V N Bodine. Wnt signaling control of bone cell apoptosis. *Cell research*, 18(2):248–253, 2008.

[12] Eric Bourhis, Christine Tam, Yvonne Franke, J. Fernando Bazan, James Ernst, Jiyoung Hwang, Mike Costa, Andrea G. Cochran, and Rami N. Hannoush. Reconstitution of a Frizzled8 Wnt3a LRP6 signaling complex reveals multiple Wnt and Dkk1 binding sites on LRP6. *Journal of Biological Chemistry*, 285(12):9172–9179, 2010.

[13] Kym M Boycott, Shauna Flavelle, Alexandre Bureau, Hannah C Glass, T Mary Fujiwara, Elaine Wirrell, Krista Davey, Albert E Chudley, James N Scott, D Ross McLeod, and Jillian S Parboosingh. Homozygous deletion of the very low density lipoprotein receptor gene causes autosomal recessive cerebellar hypoplasia with cerebral gyral simplification. *American journal of human genetics*, 77(3):477–483, 2005.

[14] Michael S Brown, Joachim Herz, and Joseph L Goldstein. LDL-receptor structure: Calcium cages, acid baths and recycling receptors. *Nature*, 388(August):629–630, 1997.

[15] M Brown, Michael S, Goldstein. The Cholesterol Quartet. *Science*, 292(May):1310–1313, 2001.

[16] Bryan T. MacDonald; Keiko Tamai and Xi He. Wnt/β-catenin signaling: components, mechanisms, and diseases Bryan. *Developmental biology*, 17(1):9–26, 2010.

[17] Hideaki Bujo, T Yamamoto, Kozo Hayashi, Marcela Hermann, Johannes Nimpf, and Wolfgang Johann Schneider. Mutant oocytic low density lipoprotein receptor gene family member causes atherosclerosis and female sterility. *Proceedings of the National Academy of Sciences of the United States of America*, 92(21):9905–9909, 1995.

[18] C J Burns, J Zhang, E C Brown, A M Van Bibber, J Van Es, H Clevers, T O Ishikawa, M M Taketo, M L Vetter, and S Fuhrmann. Investigation of Frizzled-5 during embryonic neural development in mouse. *Dev Dyn*, 237(6):1614–1626, 2008.

[19] Frank C. Caira, Stuart R. Stock, Thomas G. Gleason, Edwin C. McGee, Jie Huang, Robert O. Bonow, Thomas C. Spelsberg, Patrick M. McCarthy, Shahbudin H. Rahimtoola, and Nalini M. Rajamannan. Human Degenerative Valve Disease Is Associated With Up-Regulation of Low-Density Lipoprotein Receptor-Related Protein 5 Receptor-Mediated Bone Formation. *Journal of the American College of Cardiology*, 47(8):1707–1712, 2006.

[20] Kenneth Campbell and Magdalena Götz. Radial glia: Multi-purpose cells for vertebrate brain development. *Trends in Neurosciences*, 25(5):235–238, 2002.

[21] Gonçalo Castelo-Branco, Emma R. Andersson, Eleonora Minina, Kyle M. Sousa, Diogo Ribeiro, Chikara Kokubu, Kenji Imai, Nilima Prakash, Wolfgang Wurst, and Ernest Arenas. Delayed dopaminergic neuron differentiation in Lrp6 mutant mice. *Developmental Dynamics*, 239(1):211–221, 2010.

[22] Minyong Chen, Melanie Philipp, Jiangbo Wang, Richard T. Premont, Tiffany R. Garrison, Marc G. Caron, Robert J. Lefkowitz, and Wei Chen. G protein-coupled receptor kinases phosphorylate LRP6 in the Wnt pathway. *Journal of Biological Chemistry*, 284(50):35040–35048, 2009.

[23] Shaoqiong Chen, Denis C Guttridge, Zongbing You, Zhaochen Zhang, Andrew Fribley, Marty W Mayo, Jan Kitajewski, and Cun-yu Wang. Wnt-1 Signaling Inhibits Apoptosis by Activating ß-Catenin/T Cell Factor-mediated Transcription. 152(1):87–96, 2001.

[24] Shuo Chen, Doryen Bubeck, Bryan T. MacDonald, Wen Xue Liang, Jian Hua Mao, Tomas Malinauskas, Oscar Llorca, A. Radu Aricescu, Christian Siebold, Xi He, and E. Yvonne Jones. Structural and functional studies of LRP6 ectodomain reveal a platform for Wnt signaling. *Developmental Cell*, 21(5):848–861, 2011.

[25] W-J Chen, J L Goldstein, and M S Brown. NPXY, a sequence often found in cytoplasmic tails, is required for coated-pit mediated internalization of the low density lipoprotein receptor. *Journal of Biological Chemistry*, 265(6):3116–3123, 1990.

[26] Hong Y. Choi, Marco Dieckmann, Joachim Herz, and Andreas Niemeier. Lrp4, a novel receptor for dickkopf 1 and sclerostin, is expressed by osteoblasts and regulates bone growth and turnover In Vivo. *PLoS ONE*, 4(11), 2009.

[27] Annabel Christ, Anna Christa, Esther Kur, Oleg Lioubinski, Sebastian Bachmann, Thomas E. Willnow, and Annette Hammes. LRP2 Is an Auxiliary SHH Receptor Required to Condition the Forebrain Ventral Midline for Inductive Signals. *Developmental Cell*, 22(2):268–278, 2012.

[28] Matthew Ling Hon Chu, Victoria E. Ahn, Hee Jung Choi, Danette L. Daniels, Roel Nusse, and William I. Weis. Structural studies of wnts and identification of an LRP6 binding site. *Structure*, 21(7):1235–1242, 2013.

[29] C.T. Chung and Roger H. Miller. A rapid and convenient mehtod for preparation and storage of competent bacterial cells. *Nucleic Acids Research*, 16(2):999–1008, 1988.

[30] Hans Clevers. Wnt/β-Catenin Signaling in Development and Disease. *Cell*, 127(3):469–480, 2006.

[31] Nicole M. Collette, Damian C. Genetos, Deepa Murugesh, Richard M. Harland, and Gabriela G. Loots. Genetic evidence that SOST inhibits WNT signaling in the limb. *Developmental Biology*, 342(2):169–179, 2010.

[32] Nicole M. Collette, Cristal S. Yee, Deepa Murugesh, Aimy Sebastian, Leila Taher, Nicholas W. Gale, Aris N. Economides, Richard M. Harland, and Gabriela G. Loots. Sost and its paralog Sostdc1 coordinate digit number in a Gli3-dependent manner. *Developmental Biology*, 383(1):90–105, 2013.

[33] Gabriella D'Arcangelo, Ramin Homayouni, Lakhu Keshvara, Dennis S. Rice, Michael Sheldon, and Tom Curran. Reelin is a ligand for lipoprotein receptors. *Neuron*, 24(2):471–479, 1999.

[34] Monica D. David, Carles Cantí, and Judit Herreros. Wnt-3a and Wnt-3 differently stimulate proliferation and neurogenesis of spinal neural precursors and promote neurite outgrowth by canonical signaling. *Journal of Neuroscience Research*, 88(14):3011–3023, 2010.

[35] Jan de Boer, Hong Jun Wang, and Clemens van Blitterswijk. Effects of Wnt Signaling on Proliferation and Differentiation of Human Mesenchymal Stem Cells. *Tissue engineering*, 10(3-4):393–401, 2004.

[36] Martin F Dietrich, Louise van der Weyden, Haydn M Prosser, Allan Bradley, Joachim Herz, and David J Adams. Ectodomains of the LDL receptor-related proteins LRP1b and LRP4 have anchorage independent functions In Vivo. *PLoS ONE*, 5(4), 2010.

[37] Patrick DiMario and Anthony Mahowald. Female sterile (1) yolkless : A Recessive Female Sterile Mutation in Drosophila melanogaster with Depressed Numbers of Coated Pits and Coated Vesicles within the Developing Oocytes. (1):199–206, 1986.

[38] K Draganova, M Zemke, L Zurkirchen, T Valenta, C Cantu, M Okoniewski, M-T Schmid, R Hoffmanns, M Goetz, K Basler, and L Sommer. Tissue Specific Stem Cells: Wnt / b -Catenin Signaling Regulates Sequential Fate Decisions of Murine Cortical Precursor Cells. pages 170–182, 2015.

[39] Cord Drögemüller, Tosso Leeb, Barbara Harlizius, Imke Tammen, Ottmar Distl, Martin Höltershinken, Arcangelo Gentile, Amandine Duchesne, and André Eggen. Congenital syndactyly in cattle: four novel mutations in the low density lipoprotein receptor-related protein 4 gene (LRP4). 12:1–12.

[40] A Duchesne, M Gautier, S Chadi, C Grohs, S Floriot, Y Gallard, G Caste, A. Ducos, and A. Eggen. Identification of a doublet missense substitution in the bovine LRP4 gene as a candidate causal mutation for syndactyly in Holstein cattle. *Genomics*, 88(5):610–621, 2006.

[41] Robert Hugues Duparc, Mohamed Abdouh, Jocelyn David, Mireille Lépine, Nicolas Tétreault, and Gilbert Bernier. Pax6 controls the proliferation rate of neuroepithelial progenitors from the mouse optic vesicle. *Developmental Biology*, 301(2):374–387, 2007.

[42] Gerald W. Eagleson and Ryan D. Dempewolf. The role of the anterior neural ridge and Fgf-8 in early forebrain patterning and regionalization in Xenopus laevis. *Comparative Biochemistry and Physiology - B Biochemistry and Molecular Biology*, 132(1):179–189, 2002.

[43] Marie Fernandes, Grigoriy Gutin, Heather Alcorn, Susan K McConnell, and Jean M Hébert. Mutations in the BMP pathway in mice support the existence of two molecular classes of holoprosencephaly. *Development (Cambridge, England)*, 134(21):3789–94, 2007.

[44] Anna Ferrer-Vaquer, Anna Piliszek, Guangnan Tian, Robert J Aho, Daniel Dufort, and Anna-Katerina Hadjantonakis. A sensitive and bright single-cell resolution live imaging reporter of Wnt/ß-catenin signaling in the mouse. *BMC Developmental Biology*, 10(1):121, 2010.

[45] Mohammed Filali, Ningli Cheng, Duane Abbott, Vladimir Leontiev, and John F. Engelhardt. Wnt-3A/β-catenin signaling induces transcription from the LEF-1 promoter. *Journal of Biological Chemistry*, 277(36):33398–33410, 2002.

[46] T. Fischer, J. Guimera, W. Wurst, and N. Prakash. Distinct but redundant expression of the Frizzled Wnt receptor genes at signaling centers of the developing mouse brain. *Neuroscience*, 147(3):693–711, 2007.

[47] Ann C. Foley and Claudio Stern. Evolution of vertebrate forebrain development: how many different mechanisms, 2001.

[48] Vassiliki Fotaki, Osmany Larralde, Shaoju Zeng, David McLaughlin, Jennifer Nichols, David J. Price, Thomas Theil, and John O. Mason. Loss of Wnt8b has no overt effect on hippocampus development but leads to altered wnt gene expression levels in dorsomedial telencephalon. *Developmental Dynamics*, 239(1):284–296, 2010.

[49] Marc Fuccillo, Alexandra L Joyner, and Gord Fishell. Morphogen to mitogen: the multiple roles of hedgehog signalling in vertebrate neural development. *Nature reviews. Neuroscience*, 7(10):772–83, 2006.

[50] Takahiro Fujino, Hiroshi Asaba, Man-jong Kang, Yukio Ikeda, ..., Masashi Yanagisawa, Juro Sakai, and Tokuo T Yamamoto. Low-density lipoprotein receptor-related protein 5 (LRP5) is essential for normal cholesterol metabolism and glucose-induced insulin secretion. *Proceedings of the National Academy of Sciences of the United States of America*, 100(1):229–34, 2003.

[51] J Galceran, E M Miyashita-Lin, E Devaney, J L Rubenstein, and R Grosschedl. Hippocampus development and generation of dentate gyrus granule cells is regulated by LEF1. *Development (Cambridge, England)*, 127(3):469–482, 2000.

[52] Lisa M. Galli, Karl Willert, Roel Nusse, Zipora Yablonka-Reuveni, Tsutomu Nohno, Wilfred Denetclaw, and Laura W. Burrus. A proliferative role for Wnt-3a in chick somites. *Developmental Biology*, 269(2):489–504, 2004.

[53] Qini Gan, Albert Lee, Ryusuke Suzuki, Takashi Yamagami, Arjun Stokes, Bao Cahu Nguyen, David Pleasure, Junjiang Wang, Hong-Wu Chen, and Chengji J. Zhou. Pax6 Mediates ß-Catenin Signaling for Self-Renewal and Neurogenesis by Neocortical Radial Glial Stem Cells. 32(1)(January 2014):45–58, 2014.

[54] Shruti Goel, Emily N. Chin, Saja A. Fakhraldeen, Scott M. Berry, David J. Beebe, and Caroline M. Alexander. Both LRP5 and LRP6 receptors are required to respond to physiological Wnt ligands in mammary epithelial cells and fibroblasts. *Journal of Biological Chemistry*, 287(20):16454–16466, 2012.

[55] Joseph L Goldstein and Michael S Brown. The LDL receptor locus and the genetics of familial hypercholesterolemia. *Annual review of genetics*, 13:259–89, 1979.

[56] Andrea M. Gomez, Robert C. Froemke, and Steven J. Burden. Synaptic plasticity and cognitive function are disrupted in the absence of Lrp4. *eLife*, 3:e04287, 2014.

[57] Yaoqin Gong, Roger B Slee, Naomi Fukai, ..., Bjorn R Olsen, and Matthew L Warman. LDL receptor-related protein 5 (LRP5) affects bone accrual and eye development. *Cell*, 107(4):513–523, 2001.

[58] Magdalena Götz and Wieland B Huttner. The cell biology of neurogenesis. *Nat Rev Mol Cell Biol*, 6(10):777–788, 2005.

[59] Victoria Graham, Jane Khudyakov, Pamela Ellis, and Larysa Pevny. SOX2 functions to maintain neural progenitor identity. *Neuron*, 39(5):749–765, 2003.

[60] Jason D. Gray, Stanislav Kholmanskikh, Bozena S. Castaldo, Alex Hansler, Heekyung Chung, Brian Klotz, Shawn Singh, Anthony M C Brown, and M. Elizabeth Ross. LRP6 exerts non-canonical effects on Wnt signaling during neural tube closure. *Human Molecular Genetics*, 22(21):4267–4281, 2013.

[61] Jason D. Gray, Ghunwa Nakouzi, Bozena Slowinska-Castaldo, Jean Eudes Dazard, J. Sunil Rao, Joseph H. Nadeau, and M. Elizabeth Ross. Functional interactions between the LRP6 WNT co-receptor and folate supplementation. *Human Molecular Genetics*, 19(23):4560–4572, 2010.

[62] Tamara L. Greco, Shinji Takada, Matthew M. Newhouse, Jill A. McMahon, Andrew P. McMahon, and Sally A. Camper. Analysis of the vestigial tail mutation demonstrates that Wnt-3a gene dosage regulates mouse axial development. *Genes and Development*, 10(3):313–324, 1996.

[63] Grigoriy Gutin, Marie Fernandes, Laura Palazzolo, Hunki Paek, Kai Yu, David M Ornitz, Susan K McConnell, and Jean M Hébert. FGF signalling generates ventral telencephalic cells independently of SHH. *Development (Cambridge, England)*, 133(15):2937–2946, 2006.

[64] Iris Hack, Sabine Hellwig, Dirk Junghans, Bianka Brunne, Hans H Bock, Shanting Zhao, and Michael Frotscher. Divergent roles of ApoER2 and Vldlr in the migration of cortical neurons. *Development*, 134(21):3883–3891, 2007.

[65] Annette Hammes, Thomas K. Andreassen, Robert Spoelgen, Jens Raila, Norbert Hubner, Herbert Schulz, Jochen Metzger, Florian J. Schweigert, Peter B. Luppa, Anders Nykjaer, and Thomas E. Willnow. Role of endocytosis in cellular uptake of sex steroids. *Cell*, 122(5):751–762, 2005.

[66] Susan J. Harrison-Uy and Samuel J. Pleasure. Wnt signaling and forebrain development. *Cold Spring Harbor Perspectives in Biology*, 4(7):1–11, 2012.

[67] Sha He, Yi Lu, Xia Liu, Xin Huang, Evan T. Keller, Chao Nan Qian, and Jian Zhang. Wnt3a: functions and implications in cancer. *Chinese journal of cancer*, 34(12):554–562, 2015.

[68] Xi He, Mikhail Semenov, Keiko Tamai, and Xin Zeng. LDL receptor-related proteins 5 and 6 in Wnt/beta-catenin signaling: arrows point the way. *Development (Cambridge, England)*, 131(8):1663–77, 2004.

[69] Xi He, Keiko Tamai, Mikhail Semenov, Yoichi Kato, Rebecca Spokony, Chunming Liu, Yu Katsuyama, Fred Hess, and Jean-Pierre Saint-Jeannet. LDL-receptor-related proteins in Wnt signal transduction. *Nature*, 407(6803):530–535, 2000.

[70] J Herz and H H Bock. Lipoprotein receptors in the nervous system. 71:405–434, 2002.

[71] Joachim Herz, David E. Clouthier, and Robert E. Hammer. LDL receptor-related protein internalizes and degrades uPA-PAI-1 complexes and is essential for embryo implantation. *Cell*, 71(3):411–421, 1992.

[72] Karen S. Ho and Matthew P. Scott. Sonic hedgehog in the nervous system: Functions, modifications and mechanisms. *Current Opinion in Neurobiology*, 12(1):57–63, 2002.

[73] Sheri L Holmen, Troy a Giambernardi, Cassandra R Zylstra, Bree D Buckner-Berghuis, James H Resau, J Fred Hess, Vaida Glatt, Mary L Bouxsein, Minrong Ai, Matthew L

Warman, and Bart O Williams. Decreased BMD and limb deformities in mice carrying mutations in both Lrp5 and Lrp6. *Journal of bone and mineral research : the official journal of the American Society for Bone and Mineral Research*, 19(12):2033–40, 2004.

[74] C C Homem, M Repic, and J A Knoblich. Proliferation control in neural stem and progenitor cells. *Nat Rev Neurosci*, 16(11):647–659, 2015.

[75] Zachi Horn, Panagiotis Papachristou, Maria Shariatmadari, Julie Peyronnet, Beatrice Eriksson, and Thomas Ringstedt. Wnt7a overexpression delays beta-tubulin III expression in transgenic mouse embryos. *Brain research*, 1130(1):67–72, 2007.

[76] Corinne Houart, M. Westerfield, and Stephen W Wilson. A small population of anterior cells patterns the forebrain during zebrafish gastrulation. *Nature*, 391(6669):788–792, 1998.

[77] K Hovanes, T W Li, J E Munguia, T Truong, T Milovanovic, J Lawrence Marsh, R F Holcombe, and M L Waterman. Beta-catenin-sensitive isoforms of lymphoid enhancer factor-1 are selectively expressed in colon cancer. *Nature genetics*, 28(1):53–57, 2001.

[78] Waterham H.R., Wijburg F.A., Hennekam R.C.M., Vreken P., Poll-The B.T., Dorland L., Duran M., Jira P.E., Smeitink J.A.M., Wevers R.A., and Wanders R.J.A. Smith-Lemli-Opitz syndrome is caused by mutations in the 7- dehydrocholesterol reductase gene. pages 329–338, 1998.

[79] Wieland B. Huttner and Michael Brand. Asymmetric division and polarity of neuroepithelial cells. *Current Opinion in Neurobiology*, 7(1):29–39, 1997.

[80] Akihiro Ikeda, Sakae Ikeda, Thomas Gridley, Patsy M. Nishina, and Jürgen K. Naggert. Neural tube defects and neuroepithelial cell death in Tulp3 knockout mice. *Human Molecular Genetics*, 10(12):1325–1334, 2001.

[81] M Ikeya, S M Lee, J E Johnson, a P McMahon, and S Takada. Wnt signalling required for expansion of neural crest and CNS progenitors. *Nature*, 389(6654):966–970, 1997.

[82] T Ishikawa, Y Tamai, A M Zorn, H Yoshida, M F Seldin, S Nishikawa, and M M Taketo. Mouse Wnt receptor gene Fzd5 is essential for yolk sac and placental angiogenesis. *Development (Cambridge, England)*, 128:25–33, 2001.

[83] Myong-Ho Jeong, Seok-Man Ho, Tuan Anh Vuong, Shin-Bum Jo, Guizhong Liu, Stuart a Aaronson, Young-Eun Leem, and Jong-Sun Kang. Cdo suppresses canonical Wnt signalling via interaction with Lrp6 thereby promoting neuronal differentiation. *Nature communications*, 5:5455, 2014.

[84] Eek-hoon Jho, Tong Zhang, Claire Domon, Choun-Ki Joo, Jean-Noel Freund, and Frank Costantini. Wnt/beta-catenin/Tcf signaling induces the transcription of Axin2, a negative regulator of the signaling pathway. *Molecular and cellular biology*, 22(4):1172–83, 2002.

[85] Liwei Jia, Jiaxi Zhou, Sha Peng, Juxue Li, Yujing Cao, and Enkui Duan. Effects of Wnt3a on proliferation and differentiation of human epidermal stem cells. *Biochemical and Biophysical Research Communications*, 368(3):483–488, 2008.

[86] Yong Ri Jin, Taryn J. Turcotte, Alison L. Crocker, Xiang Hua Han, and Jeong Kyo Yoon. The canonical Wnt signaling activator, R-spondin2, regulates craniofacial patterning and morphogenesis within the branchial arch through ectodermal-mesenchymal interaction. *Developmental Biology*, 352(1):1–13, 2011.

[87] Kyu Sang Joeng, Cassie A. Schumacher, Cassandra R. Zylstra-Diegel, Fanxin Long, and Bart O. Williams. Lrp5 and Lrp6 redundantly control skeletal development in the mouse embryo. *Developmental Biology*, 359(2):222–229, 2011.

[88] Eric B. Johnson, David J. Steffen, Kristen W. Lynch, and Joachim Herz. Defective splicing of Megf7/Lrp4, a regulator of distal limb development, in autosomal recessive mulefoot disease. *Genomics*, 88(5):600–609, 2006.

[89] Danese M. Joiner, Jiyuan Ke, Zhendong Zhong, H. Eric Xu, and Bart O. Williams. LRP5 and LRP6 in development and disease. *Trends in Endocrinology and Metabolism*, 24(1):31–39, 2013.

[90] Dirk Junghans, Iris Hack, Michael Frotscher, Verdon Taylor, and Rolf Kemler. Beta-Catenin-Mediated Cell-Adhesion Is Vital for Embryonic Forebrain Development. *Developmental Dynamics*, 233(2):528–539, 2005.

[91] Ulf D Kahlert, Abigail K Suwala, Katharina Koch, Manabu Natsumeda, Brent A Orr, Masanori Hayashi, Jarek Maciaczyk, and Charles G Eberhart. Pharmacologic Wnt Inhibition Reduces Proliferation, Survival, and Clonogenicity of Glioblastoma Cells. *Journal of neuropathology and experimental neurology*, 74(9):889–900, 2015.

[92] Satoshi Kakugawa, Paul F Langton, Matthias Zebisch, Steven A Howell, Tao-Hsin Chang, Yan Liu, Ten Feizi, Ganka Bineva, Nicola O'Reilly, Ambrosius P Snijders, E Yvonne Jones, and Jean-Paul Vincent. Notum deacylates Wnt proteins to suppress signalling activity. *Nature*, 519(7542):187–92, 2015.

[93] Darren M. Kamikura and Jonathan A. Cooper. Lipoprotein receptors and a Disabled family cytoplasmic adaptor protein regulate EGL-17/FGF export in C. elegans. *Genes and Development*, 17(22):2798–2811, 2003.

[94] Sibel Kantarci, Lihadh Al-gazali, R Sean Hill, ..., Christopher A Walsh, Patricia K Donahoe, and Barbara R Pober. Mutations in LRP2, which encodes the multiligand receptor megalin, cause Donnai-Barrow and facio-oculo-acoustico-renal syndromes. 39(8):957–959, 2010.

[95] Courtney M. Karner, Martin F. Dietrich, Eric B. Johnson, Natalie Kappesser, Christian Tennert, Ferda Percin, Bernd Wollnik, Thomas J. Carroll, and Joachim Herz. Lrp4 regulates initiation of ureteric budding and is crucial for kidney formation - a mouse model for cenani-lenz syndrome. *PLoS ONE*, 5(4), 2010.

[96] Masaki Kato, Millan S. Patel, Regis Levasseur, Ivan Lobov, Benny H J Chang, Donald A. Glass, Christine Hartmann, Lan Li, Tae Ho Hwang, Cory F. Brayton, Richard A. Lang, Gerard Karsenty, and Lawrence Chan. Cbfa1-independent decrease in osteoblast proliferation, osteopenia, and persistent embryonic eye vascularization in mice deficient in Lrp5, a Wnt coreceptor. *Journal of Cell Biology*, 157(2):303–314, 2002.

[97] Olga Kazanskaya, Andrei Glinka, and Christof Niehrs. The role of Xenopus dickkopf1 in prechordal plate specification and neural patterning. *Development (Cambridge, England)*, 127(22):4981–92, 2000.

[98] Olivia G Kelly, Kathy I Pinson, and William C Skarnes. The Wnt co-receptors Lrp5 and Lrp6 are essential for gastrulation in mice. *Development (Cambridge, England)*, 131:2803–2815, 2004.

[99] Natalie Kim, Amy L. Stiegler, Thomas O. Cameron, Peter T. Hallock, Andrea M. Gomez, Julie H. Huang, Stevan R. Hubbard, Michael L. Dustin, and Steven J. Burden. Lrp4 Is a Receptor for Agrin and Forms a Complex with MuSK. *Cell*, 135(2):334–342, 2008.

[100] Elisabeth Knust and Wieland B. Huttner. Cell Polarity from Cell Division. *Developmental Cell*, 12(5):664–666, 2007.

[101] Esther Kur, Anna Christa, Kerry N Veth, Chandresh R Gajera, Miguel A Andrade, Jingjing Zhang, Jason R Willer, Ronald G Gregg, Salim Abdelilah-seyfried, Sebastian Bachmann, Brian A Link, Annette Hammes, and Thomas E Willnow. Loss of Lrp2 in zebrafish disrupts pronephric tubular clearance but not forebrain development. 240(6):1567–1577, 2012.

[102] Oleg V. Lagutin, Changqi C. Zhu, Daisuke Kobayashi, Jacek Topczewski, Kenji Shimamura, Luis Puelles, Helen R.C. Russell, Peter J. McKinnon, Lilianna Solnica-Krezel, and Guillermo Oliver. Six3 repression of Wnt signaling in the anterior neuroectoderm is essential for vertebrate forebrain development. *Genes and Development*, 17(3):368–379, 2003.

[103] Hyung Chul Lee, Sumi Lim, and Jae Yong Han. Wnt/β-catenin signaling pathway activation is required for proliferation of chicken primordial germ cells in vitro. *Scientific reports*, 6(May):34510, 2016.

[104] Jung Sun Lee, Man Wook Hur, Seong Kyung Lee, Won Il Choi, Young Guen Kwon, and Chae Ok Yun. A novel sLRP6E1E2 inhibits canonical Wnt signaling, epithelial-to-mesenchymal transition, and induces mitochondria-dependent apoptosis in lung cancer. *PLoS ONE*, 7(5), 2012.

[105] S M Lee, S Tole, E Grove, and a P McMahon. A local Wnt-3a signal is required for development of the mammalian hippocampus. *Development*, 127(3):457–467, 2000.

[106] Yonghe Li, Judy Cam, and Guojun Bu. Low-Density Lipoprotein Receptor Family; Endocytosis and Signal Transduction. *Molecular Neurobiology*, 23(1):53–67, 2001.

[107] Yun Li, Barbara Pawlik, Nursel Elcioglu, ..., Peter Nürnberg, Joachim Herz, Samia A. Temtamy, and Bernd Wollnik. LRP4 Mutations Alter Wnt/β-Catenin Signaling and Cause Limb and Kidney Malformations in Cenani-Lenz Syndrome. *American Journal of Human Genetics*, 86(5):696–706, 2010.

[108] Charlotta Lindvall, Nicole C. Evans, Cassandra R. Zylstra, Yi Li, Caroline M. Alexander, and Bart O. Williams. The Wnt signaling receptor Lrp5 is required for mammary ductal stem cell activity and Wnt1-induced tumorigenesis. *Journal of Biological Chemistry*, 281(46):35081–35087, 2006.

[109] C X Liu, S Musco, N M Lisitsina, S Y Yaklichkin, and N a Lisitsyn. Genomic organization of a new candidate tumor suppressor gene, LRP1B. *Genomics*, 69(2):271–274, 2000.

[110] Chia-Chen Liu, Chih-Wei Tsai, Ferenc Deak, Justin Rogers, Michael Penuliar, You Me Sung, James Nicholas Maher, Yuan Fu, Xia Li, Huaxi Xu, Steven Estus, Hyang-Sook Hoe, John D. Fryer, Takahisa Kanekiyo, and Guojun Bu. Deficiency in LRP6-mediated Wnt Signaling Contributes to Synaptic Abnormalities and Amyloid Pathology in Alzheimer's Disease. *Neuron*, 84(1)(October 2014):63–77, 2012.

[111] Pentao Liu, Maki Wakamiya, Martin J Shea, Urs Albrecht, Richard R Behringer, and Allan Bradley. Requirement for Wnt3 in vertebrate axis formation. *Nature genetics*, 22(4):361–365, 1999.

[112] Catriona Y. Logan and Roel Nusse. the Wnt Signaling Pathway in Development and Disease. *Annual Review of Cell and Developmental Biology*, 20(1):781–810, 2004.

[113] Desheng Lu, Michael Y Choi, Jian Yu, Januario E Castro, Thomas J Kipps, and Dennis A Carson. Salinomycin inhibits Wnt signaling and selectively induces apoptosis in chronic lymphocytic leukemia cells. *Proceedings of the National Academy of Sciences of the United States of America*, 108(32):13253–7, 2011.

[114] Ulrich F O Luhmann, John Neidhardt, Barbara Kloeckener-Gruissem, Nikolaus F. Schäfer, Esther Glaus, Silke Feil, and Wolfgang Berger. Vascular changes in the cerebellum of Norrin/Ndph knockout mice correlate with high expression of Norrin and Frizzled-4. *European Journal of Neuroscience*, 27(10):2619–2628, 2008.

[115] Barbara Lustig, Boris Jerchow, Martin Sachs, Sigrid Weiler, Torsten Pietsch, Uwe Karsten, Marc van de Wetering, Hans Clevers, Peter M Schlag, Walter Birchmeier, and Jürgen Behrens. Negative feedback loop of Wnt signaling through upregulation of conductin/axin2 in colorectal and liver tumors. *Molecular and cellular biology*, 22(4):1184–93, 2002.

[116] Bryan T Macdonald and Xi He. Frizzled and LRP5 / 6 Receptors for Wnt / β Â Catenin Signaling. *Cold Spring Harbor Perspectives in Biology*, pages 1–12, 2016.

[117] Arya Mani, Jayaram Radhakrishnan, He Wang, Alaleh Mani, Mohammad-Ali Mani, Carol Nelson-Williams, Khary S Carew, Shrikant Mane, Hossein Najmabadi, Dan Wu, and Richard P Lifton. LRP6 mutation in a family with early coronary disease and metabolic risk factors. *Science*, 315(5816):1278–1282, 2007.

[118] T Néstor H Masckauchán, Carrie J Shawber, Yasuhiro Funahashi, Chi-Ming Li, and Jan Kitajewski. Wnt/beta-catenin signaling induces proliferation, survival and interleukin-8 in human endothelial cells. *Angiogenesis*, 8(1):43–51, 2005.

[119] Benjamin Mattes, Sabrina Weber, João Peres, Qing Chen, Gary Davidson, Corinne Houart, and Steffen Scholpp. Wnt3 and Wnt3a are required for induction of the mid-diencephalic organizer in the caudal forebrain. *Neural Development*, 7(1):12, 2012.

[120] Petra May, Hans H Bock, and Joachim Herz. Integration of endocytosis and signal transduction by lipoprotein receptors. *Science's STKE : signal transduction knowledge environment*, 2003(176):PE12, 2003.

[121] Petra May and Joachim Herz. LDL receptor-related proteins in neurodevelopment. *Traffic (Copenhagen, Denmark)*, 4:291–301, 2003.

[122] A. P. McMahon, A. L. Joyner, A. Bradley, and J. A. McMahon. The midbrain-hindbrain phenotype of Wnt-1- Wnt-1- mice results from stepwise deletion of engrailed-expressing cells by 9.5 days postcoitum. *Cell*, 69(4):581–595, 1992.

[123] Andrew P. McMahon and Allan Bradley. The Wnt-1 (int-1) proto-oncogene is required for development of a large region of the mouse brain. *Cell*, 62(6):1073–1085, 1990.

[124] Sean G Megason and Andrew P McMahon. A mitogen gradient of dorsal midline Wnts organizes growth in the CNS. *Development (Cambridge, England)*, 129(9):2087–2098, 2002.

[125] Da Mi, CatherineB Carr, Petrina A. Georgala, Yu Ting Huang, Martine N. Manuel, Emily Jeanes, Emi Niisato, Stephen N. Sansom, Frederick J. Livesey, Thomas Theil, Kerstin Hasenpusch-Theil, T. Ian Simpson, John O. Mason, and David J. Price. Pax6 Exerts regional control of cortical progenitor proliferation via direct repression of Cdk6 and Hypophosphorylation of pRb. *Neuron*, 78(2):269–284, 2013.

[126] Takaki Miyata. Development of three-dimensional architecture of the neuroepithelium: Role of pseudostratification and cellular 'community'. *Development Growth and Differentiation*, 50(SUPPL. 1), 2008.

[127] Kary B. Mullis and Fred A. Faloona. Specific synthesis of DNA in vitro via a polymerase-catalyzed chain reaction. *Methods in Enzymology*, 155(C):335–350, 1987.

[128] Roeben N. Munji, Youngshik Choe, Guangnan Li, Julie A. Siegenthaler, and Samuel J.Pleasure. Wnt signaling regulates neuronal differentiation of cortical intermediate progenitors Roeben. *J Neuroscience*, 31(5):1676–1687, 2011.

[129] M Nakayama, D Nakajima, T Nagase, N Nomura, N Seki, and O Ohara. Identification of high-molecular-weight proteins with multiple EGF-like motifs by motif-trap screening. *Genomics*, 51(1):27–34, 1998.

[130] Christopher J. Nelsen, David G. Rickheim, Melissa M. Tucker, Linda K. Hansen, and Jeffrey H. Albrecht. Evidence that cyclin D1 mediates both growth and proliferation downstream of TOR in hepatocytes. *Journal of Biological Chemistry*, 278(6):3656–3663, 2003.

[131] Christof Niehrs and Sergio P Acebron. Mitotic and mitogenic Wnt signalling. *The EMBO Journal*, 31(12):2705–2713, 2012.

[132] U Nordstrom, T M Jessell, and T Edlund. Progressive induction of caudal neural character by graded Wnt signaling. *Nat Neurosci*, 5(6):525–532, 2002.

[133] R. Nusse, C. Fuerer, W. Ching, K. Harnish, C. Logan, A. Zeng, D. Ten Berge, and Y. Kalani. Wnt signaling and stem cell control. *Cold Spring Harbor Symposia on Quantitative Biology*, 73:59–66, 2008.

[134] Roel Nusse and Hans Clevers. Wnt/β-Catenin Signaling, Disease, and Emerging Therapeutic Modalities. *Cell*, 169(6):985–999, 2017.

[135] Roel Nusse and Harold E. Varmus. Many tumors induced by the mouse mammary tumor virus contain a provirus integrated in the same region of the host genome. *Cell*, 31(1):99–109, 1982.

[136] Molly K Nyholm, Shan-Fu Wu, Richard I Dorsky, and Yevgenya Grinblat. The zebrafish zic2a-zic5 gene pair acts downstream of canonical Wnt signaling to control cell proliferation in the developing tectum. *Development (Cambridge, England)*, 134(4):735–746, 2007.

[137] Atsushi Ohazama, Eric B. Johnson, Masato S. Ota, Hong J. Choi, Thantrira Porntaveetus, Shelly Oommen, Nobuyuki Itoh, Kazuhiro Eto, Amel Gritli-Linde, Joachim Herz, and Paul T. Sharpe. Lrp4 modulates extracellular integration of cell signaling pathways in development. *PLoS ONE*, 3(12), 2008.

[138] Atsushi Ohazama, Thantrira Porntaveetus, Masato S. Ota, Joachim Herz, and Paul T. Sharpe. Lrp4: A novel modulator of extracellular signaling in craniofacial organogenesis. *American Journal of Medical Genetics, Part A*, 152 A(12):2974–2983, 2010.

[139] María Cristina Ortega, Olivier Cases, Paloma Merchán, Renata Kozyraki, Diego Clemente, and Fernando De Castro. Megalin mediates the influence of sonic hedgehog on oligodendrocyte precursor cell migration and proliferation during development. *Glia*, 60(6):851–866, 2012.

[140] Tayfun Ozcelik, Nurten Akarsu, Elif Uz, Safak Caglayan, Suleyman Gulsuner, Onur Emre Onat, Meliha Tan, and Uner Tan. Mutations in the very low-density lipoprotein receptor VLDLR cause cerebellar hypoplasia and quadrupedal locomotion in humans. *Proceedings of the National Academy of Sciences of the United States of America*, 105(11):4232–6, 2008.

[141] Markus Panhuysen, Daniela M. Vogt Weisenhorn, Veronique Blanquet, Claude Brodski, Ulrich Heinzmann, Wolfgang Beisker, and Wolfgang Wurst. Effects of Wnt1 signaling on proliferation in the developing mid-/hindbrain region. *Molecular and Cellular Neuroscience*, 26(1):101–111, 2004.

[142] B A Parr, M J Shea, G Vassileva, and A P McMahon. Mouse Wnt genes exhibit discrete domains of expression in the early embryonic CNS and limb buds. *Development*, 119(1):247–261, 1993.

[143] Nives Pećina-Slaus. Wnt signal transduction pathway and apoptosis: a review. *Cancer cell international*, 10(1):22, 2010.

[144] A. Perea-Gomez, M. Rhinn, and S. L. Ang. Role of the anterior visceral endoderm in restricting posterior signals in the mouse embryo. *International Journal of Developmental Biology*, 45(1):311–320, 2001.

[145] Matthew D. Phillips, Mahua Mukhopadhyay, M. Cristina Poscablo, and Heiner Westphal. Dkk1 and Dkk2 Regulate Epicardial Specification during Mouse Heart Development. *Int J Cardiol.*, 150(2)(July 2011):186–192, 2011.

[146] K I Pinson, J Brennan, S Monkley, B J Avery, and W C Skarnes. An LDL-receptor-related protein mediates Wnt signalling in mice. *Nature*, 407(6803):535–538, 2000.

[147] Marysia Placzek and James Briscoe. The floor plate: multiple cells, multiple signals. *Nature reviews. Neuroscience*, 6(3):230–40, 2005.

[148] Theresa Pohlkamp, Murat Durakoglugil, Courtney Lane-Donovan, Xunde Xian, Eric B. Johnson, Robert E. Hammer, and Joachim Herz. Lrp4 domains differentially regulate limb/brain development and synaptic plasticity. *PLoS ONE*, 10(2):1–11, 2015.

[149] Chaolin Qiu, Qiuhua Xie, Dongqing Zhang, Qing Chen, Jinhui Hu, and Limin Xu. GM-CSF induces cyclin D1 expression and proliferation of endothelial progenitor cells via PI3K and MAPK signaling. *Cellular Physiology and Biochemistry*, 33(3):784–795, 2014.

[150] Robyn Quinlan, Manuela Graf, Ivor Mason, Andrew Lumsden, and Clemens Kiecker. Complex and dynamic patterns of Wnt pathway gene expression in the developing chick forebrain. *Neural development*, 4(1):35, 2009.

[151] Robyn Quinlan, Manuela Graf, Ivor Mason, Andrew Lumsden, and Clemens Kiecker. Complex and dynamic patterns of Wnt pathway gene expression in the developing chick forebrain. *Neural development*, 4(1):35, 2009.

[152] Nalini M. Rajamannan, Malayannan Subramaniam, Frank Caira, Stuart R. Stock, and Thomas C. Spelsberg. Atorvastatin inhibits hypercholesterolemia-induced calcification in the aortic valves via the Lrp5 receptor pathway. *Circulation*, 112(9 SUPPL.), 2005.

[153] Anton J M Roebroek, Sara Reekmans, Annick Lauwers, Nathalie Feyaerts, Liesbet Smeijers, and Dieter Hartmann. Mutant Lrp1 knock-in mice generated by recombinase-mediated cassette exchange reveal differential importance of the NPXY motifs in the intracellular domain of LRP1 for normal fetal development. *Molecular and cellular biology*, 26(2):605–16, 2006.

[154] Jill A. Rosenfeld, Blake C. Ballif, Donna M. Martin, Arthur S. Aylsworth, Bassem A. Bejjani, Beth S. Torchia, and Lisa G. Shaffer. Clinical characterization of individuals with deletions of genes in holoprosencephaly pathways by aCGH refines the phenotypic spectrum of HPE. *Human Genetics*, 127(4):421–440, 2010.

[155] Gabby Rudenko. Structure of the LDL Receptor Extracellular Domain at Endosomal pH. *Science*, 298(5602):2353–2358, 2002.

[156] W L Russell, E M Kelly, P R Hunsicker, J W Bangham, S C Maddux, and E L Phipps. Specific-locus test shows ethylnitrosourea to be the most potent mutagen in the mouse. *Proceedings of the National Academy of Sciences of the United States of America*, 76(11):5818–5819, 1979.

[157] T. W. Sadler. Embryology of neural tube development. *American Journal of Medical Genetics - Seminars in Medical Genetics*, 135 C(1):2–8, 2005.

[158] R K Saiki, D H Gelfand, S Stoffel, S J Scharf, R Higuchi, G T Horn, K B Mullis, and H a Erlich. Primer-directed enzymatic amplification of DNA with a thermostable DNA polymerase. *Science (New York, N.Y.)*, 239(4839):487–491, 1988.

[159] Yoshio Sakai. Neurulation in the mouse: Manner and timing of neural tube closure. *The Anatomical Record*, 223(2):194–203, 1989.

[160] Yan-chang Shang, Shu-hui Wang, Fu Xiong, Cui-ping Zhao, Fu-ning Peng, Shan-wei Feng, and Cheng Zhang. Wnt3a signaling promotes proliferation, myogenic differentiation, and migration of rat bone marrow mesenchymal stem cells 1. *Acta Pharmacol Sin*, 28(11):1761–1774, 2007.

[161] S Shanmugalingam, C Houart, a Picker, F Reifers, R Macdonald, a Barth, K Griffin, M Brand, and S W Wilson. Ace/Fgf8 is required for forebrain commissure formation and patterning of the telencephalon. *Development (Cambridge, England)*, 127(12):2549–2561, 2000.

[162] M Shtutman, J Zhurinsky, I Simcha, C Albanese, M D'Amico, R Pestell, and a Ben-Ze'ev. The cyclin D1 gene is a target of the beta-catenin/LEF-1 pathway. *Proceedings of the National Academy of Sciences of the United States of America*, 96(10):5522–5527, 1999.

[163] Dominique Simon-Chazottes, Sylvie Tutois, Michael Kuehn, Martin Evans, Franck Bourgade, Sue Cook, Muriel T. Davisson, and Jean Louis Guénet. Mutations in the gene encoding the low-density lipoprotein receptor LRP4 cause abnormal limb development in the mouse. *Genomics*, 87(5):673–677, 2006.

[164] Jodi L. Smith and Gary C. Schoenwolf. Neurulation: Coming to closure. *Trends in Neurosciences*, 20(11):510–517, 1997.

[165] Lanying Song, Yunhong Li, Kai Wang, Ya-Zhou Wang, Andrei Molotkov, Lifang Gao, Tianyu Zhao, Takashi Yamagami, Yongping Wang, Qini Gan, David E Pleasure, and Chengji J Zhou. Lrp6-mediated canonical Wnt signaling is required for lip formation and fusion. *Development*, 136(18):3161–3171, 2009.

[166] Lanying Song, Yunhong Li, Kai Wang, and Chengji J. Zhou. Cardiac neural crest and outflow tract defects in Lrp6 mutant mice. *Developmental Dynamics*, 239(1):200–210, 2010.

[167] I Sonoda, I Imoto, J Inoue, T Shibata, Y Shimada, K Chin, M Imamura, T Amagasa, J W Gray, S Hirohashi, and J Inazawa. Frequent silencing of low density lipoprotein receptor-related protein 1B (LRP1B) expression by genetic and epigenetic mechanisms in esophageal squamous cell carcinoma. *Cancer Res*, 64(11):3741–3747, 2004.

[168] Robert Spoelgen, Annette Hammes, Uwe Anzenberger, Dietmar Zechner, Olav M Andersen, Boris Jerchow, and Thomas E Willnow. LRP2/megalin is required for patterning of the ventral telencephalon. *Development (Cambridge, England)*, 132(2):405–414, 2005.

[169] Dennis W. Stacey. Cyclin D1 serves as a cell cycle regulatory switch in actively proliferating cells. *Current Opinion in Cell Biology*, 15(2):158–163, 2003.

[170] Claudio D. Stern. Induction and initial patterning of the nervous system - The chick embryo enters the scene. *Current Opinion in Genetics and Development*, 12(4):447–451, 2002.

[171] Sebastian Stuebner, Theresa Faus-Kessler, Thomas Fischer, Wolfgang Wurst, and Nilima Prakash. Fzd3 and Fzd6 deficiency results in a severe midbrain morphogenesis defect. *Developmental Dynamics*, 239(1):246–260, 2010.

[172] S Swarup and E Verheyen. Wnt / Wingless Signaling in Drosophila Wnt / Wingless Signaling in Drosophila. *Cold Spring Harbor perspectives in biology*, 4(6):1–16, 2012.

[173] S Takada, K L Stark, M J Shea, G Vassileva, Jill A McMahon, and Andrew P. McMahon. Wnt-3a regulates somites and tailbud formation in the mouse embryo. *Genes and Development*, 8:174–189, 1994.

[174] Keiko Tamai, Xin Zeng, Chunming Liu, Xinjun Zhang, Yuko Harada, Zhijie Chang, and Xi He. A Mechanism for Wnt Coreceptor Activation. *Molecular Cell*, 13(1):149–156, 2004.

[175] Coya Tapia, Heinz Kutzner, Thomas Mentzel, Spasenija Savic, Daniel Baumhoer, and Katharina Glatz. Two mitosis-specific antibodies, MPM-2 and phospho-histone H3 (Ser28), allow rapid and precise determination of mitotic activity. *The American journal of surgical pathology*, 30(1):83–89, 2006.

[176] O Tetsu and F McCormick. Beta-catenin regulates expression of cyclin D1 in colon carcinoma cells. *Nature*, 398(6726):422–426, 1999.

[177] Thomas Theil, Elena Dominguez-Frutos, and Thomas Schimmang. Differential requirements for Fgf3 and Fgf8 during mouse forebrain development. *Developmental Dynamics*, 237(11):3417–3423, 2008.

[178] Karl Theiler. The House Mouse: Atlas of Embryonic Development, 1989.

[179] Yasuhiro Tomita, Dong-ho Kim, Kenta Magoori, and Tokuo T Yamamoto. A Novel Low-Density Lipoprotein II Membrane Structure Is Abundant Protein in Heart1 with Type. 789:784–789, 1998.

[180] Carmel Toomes, Helen M Bottomley, Richard M Jackson, Katherine V Towns, Sheila Scott, David a Mackey, Jamie E Craig, Li Jiang, Zhenglin Yang, Richard Trembath, Geoffrey Woodruff, Cheryl Y Gregory-Evans, Kevin Gregory-Evans, Michael J Parker, Graeme C M Black, Louise M Downey, Kang Zhang, and Chris F Inglehearn. Mutations in LRP5 or FZD4 underlie the common familial exudative vitreoretinopathy locus on chromosome 11q. *American journal of human genetics*, 74(4):721–730, 2004.

[181] M. Trommsdorff, M. Gotthardt, T. Hiesberger, J. Shelton, W. Stockinger, J. Nimpf, R. E. Hammer, J. A. Richardson, and J. Herz. Reeler/disabled-like disruption of neuronal migration in knockout mice lacking the VLDL receptor and ApoE receptor 2. *Cell*, 97(6):689–701, 1999.

[182] Justin H Trotter, South Florida, E Fletcher Ave, Martin Klein, South Florida, E Fletcher Ave, Florida E Fletcher, Ave Tampa, Chad A Dickey, Fletcher Ave Tampa, Jeremy Tharkur, N C Jindongsmtpdukeedu, Kirstin G Locke, David G Birch, South Florida, E Fletcher Ave, and Joachim Herz. ApoER2 Function in the Establishment and Maintenance of Retinal Synaptic Connectivity. 31(40):14413–14423, 2012.

[183] Tomas Valenta, George Hausmann, and Konrad Basler. The many faces and functions of β-catenin. *The EMBO Journal*, 31(12):2714–2736, 2012.

[184] Kerry N. Veth, Jason R. Willer, Ross F. Collery, Matthew P. Gray, Gregory B. Willer, Daniel S. Wagner, Mary C. Mullins, Ava J. Udvadia, Richard S. Smith, Simon W M John, Ronald G. Gregg, and Brian A. Link. Mutations in zebrafish Lrp2 result in adult-onset ocular pathogenesis that models myopia and other risk factors for glaucoma. *PLoS Genetics*, 7(2), 2011.

[185] Oliver Von Bohlen Und Halbach. Immunohistological markers for proliferative events, gliogenesis, and neurogenesis within the adult hippocampus. *Cell and Tissue Research*, 345(1):1–19, 2011.

[186] T Walcher, Q Xie, J Sun, M Irmler, J Beckers, T Ozturk, D Niessing, A Stoykova, A Cvekl, J Ninkovic, and M Gotz. Functional dissection of the paired domain of Pax6 reveals molecular mechanisms of coordinating neurogenesis and proliferation. *Development*, 140(5):1123–1136, 2013.

[187] Jianbo Wang, Tanvi Sinha, and Anthony Wynshaw-Boris. Wnt signaling in mammalian development: Lessons from mouse genetics. *Cold Spring Harbor Perspectives in Biology*, 4(5):6, 2012.

[188] Ke Wang, Yazhou Zhang, Xiaofeng Li, Lijun Chen, He Wang, Jianguo Wu, Jie Zheng, and Dianqing Wu. Characterization of the Kremen-binding site on Dkk1 and elucidation of the role of Kremen in Dkk-mediated Wnt antagonism. *Journal of Biological Chemistry*, 283(34):23371–23375, 2008.

[189] Ya-Zhou Wang, Takashi Yamagami, Qini Gan, Yongping Wang, Tianyu Zhao, Salaheddin Hamad, Paul Lott, Nikolai Schnittke, James E Schwob, and Chengji J Zhou. Canonical Wnt signaling promotes the proliferation and neurogenesis of peripheral olfactory stem cells during postnatal development and adult regeneration. *Journal of cell science*, 124:1553–1563, 2011.

[190] N Warren, D Caric, T Pratt, J a Clausen, P Asavaritikrai, J O Mason, R E Hill, and D J Price. The transcription factor, Pax6, is required for cell proliferation and differentiation in the developing cerebral cortex. *Cerebral cortex (New York, N.Y. : 1991)*, 9:627–635, 1999.

[191] Scott D Weatherbee, Kathryn V Anderson, and Lee A Niswander. LDL-receptor-related protein 4 is crucial for formation of the neuromuscular junction. *Development (Cambridge, England)*, 133(24):4993–5000, 2006.

[192] Scott D Weatherbee, Kathryn V Anderson, and Lee A Niswander. LDL-receptor-related protein 4 is crucial for formation of the neuromuscular junction. *Development (Cambridge, England)*, 133(24):4993–5000, 2006.

[193] M Wehrli, S T Dougan, K Caldwell, L O'Keefe, S Schwartz, D Vaizel-Ohayon, E Schejter, a Tomlinson, and S DiNardo. arrow encodes an LDL-receptor-related protein essential for Wingless signalling. *Nature*, 407(6803):527–530, 2000.

[194] Grzegorz Wicher and Håkan Aldskogius. Megalin deficiency induces critical changes in mouse spinal cord development. *Neuroreport*, 19(5):559–63, 2008.

[195] T E Willnow, J Hilpert, S A Armstrong, A Rohlmann, R E Hammer, D K Burns, and Joachim Herz. Defective forebrain development in mice lacking gp330/megalin. *Proceedings of the National Academy of Sciences of the United States of America*, 93(16):8460–8464, 1996.

[196] Thomas E Willnow, Annabel Christ, and Annette Hammes. Endocytic receptor-mediated control of morphogen signaling. *Development (Cambridge, England)*, 139(23):4311–9, 2012.

[197] Thomas E Willnow, Annette Hammes, and Suzanne Eaton. Lipoproteins and their receptors in embryonic development: more than cholesterol clearance. *Development (Cambridge, England)*, 134(18):3239–3249, 2007.

[198] Stephen W. Wilson and Corinne Houart. Early steps in the development of the forebrain. *Developmental Cell*, 6(2):167–181, 2004.

[199] Andreas Wodarz and Wieland B. Huttner. Asymmetric cell division during neurogenesis in Drosophila and vertebrates. *Mechanisms of Development*, 120(11):1297–1309, 2003.

[200] Qing Xie, Ying Yang, Jie Huang, Jovica Ninkovic, Tessa Walcher, Louise Wolf, Ariel Vitenzon, Deyou Zheng, Magdalena Götz, David C. Beebe, Jiri Zavadil, and Ales Cvekl. Pax6 Interactions with Chromatin and Identification of Its Novel Direct Target Genes in Lens and Forebrain. *PLoS ONE*, 8(1), 2013.

[201] G. Bu Y. Li, P. van Kerkhof, M. P. Marzolo, G. J. Strous. Identification of a Major Cyclic AMP-Dependent Protein Kinase A Phosphorylation Site within the Cytoplasmic Tail of the Low-Density Lipoprotein Receptor-Related Protein : Implication for Receptor-Mediated Endocytosis. *Molecular and Cellular Biology*, 21(4):1185–1195, 2001.

[202] Yu Ping Yang and John Klingensmith. Roles of organizer factors and BMP antagonism in mammalian forebrain establishment. *Developmental Biology*, 296(2):458–475, 2006.

[203] Xin Ye, Yanshu Wang, Hugh Cahill, Minzhong Yu, Tudor C. Badea, Philip M. Smallwood, Neal S. Peachey, and Jeremy Nathans. Norrin, Frizzled-4, and Lrp5 Signaling in Endothelial Cells Controls a Genetic Program for Retinal Vascularization. *Cell*, 139(2):285–298, 2009.

[204] J Yochem, S Tuck, I Greenwald, and M Han. A gp330/megalin-related protein is required in the major epidermis of Caenorhabditis elegans for completion of molting. *Development (Cambridge, England)*, 126:597–606, 1999.

[205] Y Yoshikawa, T Fujimori, a P McMahon, and S Takada. Evidence that absence of Wnt-3a signaling promotes neuralization instead of paraxial mesoderm development in the mouse. *Developmental biology*, 183(2):234–242, 1997.

[206] Huimin Yu, Xin Ye, Nini Guo, and Jeremy Nathans. Frizzled 2 and frizzled 7 function redundantly in convergent extension and closure of the ventricular septum and palate: evidence for a network of interacting genes. *Development (Cambridge, England)*, 139(23):4383–94, 2012.

[207] Bin Zhang, Shiwen Luo, Qiang Wang, Tatsuo Suzuki, Wen C Xiong, and Lin Mei. LRP4 Serves as a Coreceptor of Agrin. *Neuron*, 60(2):285–297, 2008.

[208] Q Zhang, M B Major, S Takanashi, N D Camp, N Nishiya, E C Peters, M H Ginsberg, X Jian, P A Randazzo, P G Schultz, R T Moon, and S Ding. Small-molecule synergist of the Wnt/beta-catenin signaling pathway. *Proceedings of the National Academy of Sciences of the United States of America*, 104(18):7444–7448, 2007.

[209] Shu Xing Zhang, Eduardo Garcia-Gras, Diane R. Wycuff, Suzanne J. Marriot, Nijiati Kadeer, Wei Yu, Eric N. Olson, Daniel J. Garry, Michael S. Parmacek, and Robert J. Schwartz. Identification of direct serum-response factor gene targets during Me 2SO-induced P19 cardiac cell differentiation. *Journal of Biological Chemistry*, 280(19):19115–19126, 2005.

[210] Xiaoting Zhao, Wentao Yue, Lina Zhang, Li Ma, Wenyun Jia, Zhe Qian, Chunyan Zhang, and Yue Wang. Downregulation of PAX6 by shRNA inhibits proliferation and cell cycle progression of human non-small cell lung cancer cell lines. *PLoS ONE*, 9(1):1–10, 2014.

[211] Hou Feng Zheng, Jon H. Tobias, Emma Duncan, ..., Claes Ohlsson, J. Brent Richards, and Mattias Lorentzon. WNT16 influences bone mineral density, cortical bone thickness, bone strength, and osteoporotic fracture risk. *PLoS Genetics*, 8(7), 2012.

[212] C.-J. Zhou. Severe Defects in Dorsal Thalamic Development in Low-Density Lipoprotein Receptor-Related Protein-6 Mutants. *Journal of Neuroscience*, 24(35):7632–7639, 2004.

[213] C.-J. Zhou. Wnt Signaling Mutants Have Decreased Dentate Granule Cell Production and Radial Glial Scaffolding Abnormalities. *Journal of Neuroscience*, 24(1):121–126, 2004.

[214] C. J. Zhou, U. Borello, J. L R Rubenstein, and S. J. Pleasure. Neuronal production and precursor proliferation defects in the neocortex of mice with loss of function in the canonical Wnt signaling pathway. *Neuroscience*, 142(4):1119–1131, 2006.

[215] Cheng Ji Zhou, Andrei Molotkov, Lanying Song, Yunhong Li, David E. Pleasure, Samuel J Pleasure, and Ya Zhou Wang. Ocular coloboma and dorsoventral neuroretinal patterning defects in Lrp6 mutant eyes. *Developmental Dynamics*, 237(12):3681–3689, 2008.

[216] Chengji J Zhou. Ocular Coloboma and Dorsoventral Neuroretinal Patterning Defects in Lrp6 Mutant Eyes. *Am J Hypertens*, 24(7):724–732, 2011.